

Research Highlight

Increased asynchronous GABA release causes more inhibition in human epileptic brain?

Qi FANG, Zhong CHEN*

Acta Pharmacologica Sinica (2012) 33: 859–860; doi: 10.1038/aps.2012.92

When an action potential (AP) propagates to the presynaptic terminals, Ca^{2+} influx through voltage-gated Ca^{2+} channels triggers rapid synchronous transmitter release within milliseconds, which is then followed by a so-called asynchronous release with a prolonged time course of tens or hundreds of milliseconds at both excitatory and inhibitory synapses^[1–3]. Fast synchronous release is well-known as the foundation of precise neuronal communication, whereas the characteristics and functions of asynchronous release in central nervous system, especially in human brain, are largely unexplored. Jiang *et al*^[4] now report that asynchronous release occurs in all GABAergic synapses of fast-spiking (FS) interneurons, and the strength of asynchronous GABA release increases in human epileptic neocortex, which may contribute to the regulation of epileptiform activities.

In central nervous system, individual neurons receive both excitatory and inhibitory synaptic transmission. Proper and dynamic balance between the excitatory and inhibitory inputs are essential for precise information coding in complex neuronal network^[5], whereas dis-

ruption of this balance may cause severe neurological diseases, such as epilepsy^[6]. GABA is the predominant inhibitory neurotransmitter which is released from GABAergic axon terminals and consequently activates postsynaptic and extrasynaptic GABA receptors. Besides fast synchronous GABA release tightly coupled with AP, asynchronous GABA release has been recently demonstrated in the avian nucleus magnocellularis neurons and rat hippocampal interneuron–principal neuron synapse, which generates long-lasting inhibition and may contribute to the control of postsynaptic target neurons^[2, 7]. Therefore, it will be interesting to study the functional role of this asynchronous GABA release in both physiological and pathological conditions.

In this report, Jiang *et al* performed simultaneous recordings from inhibitory FS neurons and excitatory pyramidal neurons (PC) in human epileptic or non-epileptic cortical slices. They demonstrate for the first time that single AP- or AP train-evoked asynchronous GABA release from FS interneuron occur at all GABAergic synapses, including FS autapses (synapses formed by the axon of the FS interneuron on its own dendrites), FS-FS and FS-PC synapses in human brain, among which FS autapses show the strongest asynchronous release. Moreover, the duration and total number of asynchronous release increase when enhancing the frequency or the number of presynaptic APs, dem-

onstrating the dependence of asynchronous release strength on the intensity of presynaptic stimulation. Most interestingly, elevated asynchronous release from FS autapses was found in human epileptic cortical slices as compared with that in non-epileptic peri-tumor tissue. To confirm this phenomenon, authors examined the asynchronous release from FS autapses and FS-PC synapse in the rat pilocarpine model of status epilepsy, which mimics human temporal-lobe epilepsy. Consistent with what is observed in human brain, AP train induces asynchronous release both at FS autapses and FS-PC synapses, with its strength depending on the intensity of presynaptic stimulation. Meanwhile, FS autapses exhibited significantly stronger asynchronous release than FS-PC synapse in both control and pilocarpine-treated rats, which showing that the strength of asynchronous release tightly depend on the type of synaptic connection. Notably, asynchronous GABA release at both FS autapses and FS-PC synapse in pilocarpine-treated rats were remarkably increased as compared with those in control rats. The enhanced asynchronous GABA release at FS neuron synapses in both epileptic human brain and epileptic animal model provide scientific insight that the long-lasting inhibition mediated by increased asynchronous GABA release may contribute to the regulation of epileptiform activities.

Decades ago, asynchronous release was found as a “delayed” phase char-

Department of Pharmacology, Key Laboratory of Medical Neurobiology of Ministry of Health of China, Zhejiang Province Key Laboratory of Neurobiology, College of Pharmaceutical Sciences, School of Medicine, Zhejiang University, Hangzhou 310058, China

Correspondence to: Prof Zhong CHEN (chenzhong@zju.edu.cn)

acterized by a much smaller but long-lasting elevation of quantal release rate following the rapid synchronous release^[8,9]. Similar to fast synchronous release, asynchronous release also depends on presynaptic Ca^{2+} . Different Ca^{2+} sensor and the distance between the Ca^{2+} source and the sensor of exocytosis have been considered as the mechanism underlying the distinct properties of these two types of transmitter release^[10]. According to this report, blocking background Ca^{2+} by EGTA-AM, a membrane-permeable Ca^{2+} chelator, almost completely abolishes the asynchronous release at FS autapses, FS-FS and FS-PC synapses. This result confirms the Ca^{2+} dependence of asynchronous GABA release from FS neurons in human brain. Does the enhanced asynchronous GABA release in epileptic human brain or pilocarpine-treated animal model relate to the presynaptic Ca^{2+} ? In pilocarpine-treated rats, the authors found that the train stimulus-induced APs in presynaptic neuron exhibited larger peak amplitude and integrated area than those in control rats. Meanwhile, proper reduction of presynaptic AP amplitude by a low concentration of TTX (100 nmol/L) significantly decreased the strength of asynchronous release from FS neurons.

Therefore, Jiang *et al* hypothesized that increased AP amplitude may cause more Ca^{2+} entry and consequently enhance asynchronous GABA release from FS synapses. Although more evidence should be provided, it's still worth to examine the related channels and Ca^{2+} sensors that may be involved in the underlying mechanism.

This study by Jiang *et al* is important because it confirms the existence of asynchronous release in human brain, and reveals the enhanced asynchronous GABA release from FS interneuron in human epileptic brain and pilocarpine-treated rats. Consider the fact that asynchronous GABA release in FS autapses is significantly stronger than that in FS-PC synapse, it is noticeable that asynchronous GABA release in FS autapses can actually lead to self-inhibition and consequently excites its target neurons. Therefore, further works are needed to test whether or not the increased asynchronous GABA release really causes more inhibition in the epileptic brain. Except asynchronous GABA release, the properties and functional role of excitatory asynchronous release in the epileptic brain are also attractive. At last, it's would be anticipated, yet interesting, to uncover the regulation effect of asyn-

chronous release on the neurological diseases, such as epilepsy.

- 1 Atluri PP, Regehr WG. Delayed release of neurotransmitter from cerebellar granule cells. *J Neurosci* 1998; 18: 8214–27.
- 2 Lu T, Trussell LO. Inhibitory transmission mediated by asynchronous transmitter release. *Neuron* 2000; 26: 683–94.
- 3 Goda Y, Stevens CF. Two components of transmitter release at a central synapse. *Proc Natl Acad Sci U S A* 1994; 91: 12942–6.
- 4 Jiang M, Zhu J, Liu Y, Yang M, Tian C, Jiang S, *et al*. Enhancement of asynchronous release from fast-spiking interneuron in human and rat epileptic neocortex. *PLoS Biol* 2012; 10: e1001324.
- 5 Haider B, Duque A, Hasenstaub AR, McCormick DA. Neocortical network activity *in vivo* is generated through a dynamic balance of excitation and inhibition. *J Neurosci* 2006; 26: 4535–45.
- 6 Marco P, Sola RG, Pulido P, Aljarde MT, Sanchez A, Ramon y Cajal S, *et al*. Inhibitory neurons in the human epileptogenic temporal neocortex. An immunocytochemical study. *Brain* 1996; 119: 1327–47.
- 7 Hefft S, Jonas P. Asynchronous GABA release generates long-lasting inhibition at a hippocampal interneuron-principal neuron synapse. *Nat Neurosci* 2005; 8: 1319–28.
- 8 Rahamimoff R, Yaari Y. Delayed release of transmitter at the frog neuromuscular junction. *J Physiol* 1973; 228: 241–57.
- 9 Barrett EF, Stevens CF. The kinetics of transmitter release at the frog neuromuscular junction. *J Physiol* 1972; 227: 691–708.
- 10 Yao J, Gaffaney JD, Kwon SE, Chapman ER. Doc2 is a Ca^{2+} sensor required for asynchronous neurotransmitter release. *Cell* 2011; 147: 666–77.

Original Article

Atorvastatin enhances neurite outgrowth in cortical neurons *in vitro* via up-regulating the Akt/mTOR and Akt/GSK-3 β signaling pathways

Ying JIN*, Hai-juan SUI, Yan DONG, Qi DING, Wen-hui QU, Sheng-xue YU, Ying-xin JIN

Department of Pharmacology, Liaoning Medical University, Jinzhou 121001, China

Aim: To investigate whether atorvastatin can promote formation of neurites in cultured cortical neurons and the signaling mechanisms responsible for this effect.

Methods: Cultured rat cerebral cortical neurons were incubated with atorvastatin (0.05–10 $\mu\text{mol/L}$) for various lengths of time. For pharmacological experiments, inhibitors were added 30 min prior to addition of atorvastatin. Control cultures received a similar amount of DMSO. Following the treatment period, phase-contrast digital images were taken. Digital images of neurons were analyzed for total neurite branch length (TNBL), neurite number, terminal branch number, and soma area by SPOT Advanced Imaging software. After incubation with atorvastatin for 48 h, the levels of phosphorylated 3-phosphoinoside-dependent protein kinase-1 (PDK1), phospho-Akt, phosphorylated mammalian target of rapamycin (mTOR), phosphorylated 4E-binding protein 1 (4E-BP1), p70S6 kinase (p70S6K), and glycogen synthase kinase-3 β (GSK-3 β) in the cortical neurons were evaluated using Western blotting analyses.

Results: Atorvastatin (0.05–10 $\mu\text{mol/L}$) resulted in dose-dependent increase in neurite number and length in these neurons. Pretreatment of the cortical neurons with phosphatidylinositol 3-kinase (PI3K) inhibitors LY294002 (30 $\mu\text{mol/L}$) and wortmannin (5 $\mu\text{mol/L}$), Akt inhibitor triciribine (1 $\mu\text{mol/L}$) or mTOR inhibitor rapamycin (100 nmol/L) blocked the atorvastatin-induced increase in neurite outgrowth, suggesting that atorvastatin promoted neurite outgrowth via activating the PI3K/Akt/mTOR signaling pathway. Atorvastatin (10 $\mu\text{mol/L}$) significantly increased the levels of phosphorylated PDK1, Akt and mTOR in the cortical neurons, which were prevented by LY294002 (30 $\mu\text{mol/L}$). Moreover, atorvastatin (10 $\mu\text{mol/L}$) stimulated the phosphorylation of 4E-BP1 and p70S6K, the substrates of mTOR, in the cortical neurons. In addition, atorvastatin (10 $\mu\text{mol/L}$) significantly increased the phosphorylated GSK-3 β level in the cortical neurons, which was prevented by both LY294002 and triciribine.

Conclusion: These results suggest that activation of both the PI3K/Akt/mTOR and Akt/GSK-3 β signaling pathways is responsible for the atorvastatin-induced neurite outgrowth in cultured cortical neurons.

Keywords: statin; atorvastatin; cortical neurons; neuritogenesis; PI3-kinase; GSK-3 β

Acta Pharmacologica Sinica (2012) 33: 861–872; doi: 10.1038/aps.2012.59; published online 18 Jun 2012

Introduction

Neurons form functional networks by extending axons and dendrites (collectively termed neurites) that can connect via synapses to other neurons and cells. Molecules that promote effective neurite growth may have therapeutic potential in the treatment of a wide variety of disorders of the human nervous system. The statins are important cholesterol lowering agents for patients at risk of cardiovascular disease. However, many studies show that statins may have additional neuroprotective properties independent of their effect on cholesterol synthesis. Statins can reduce the region of focal cerebral ischemia^[1]

and protect cortical neurons from excitotoxicity^[2]. Recent studies reported that statins can preventively and therapeutically attenuate traumatic brain injury and spinal cord injury. These beneficial effects of statins include upregulation of brain-derived neurotrophin factor (BDNF) and vascular endothelial growth factor (VEGF) and activation of the Akt-mediated signaling pathways^[3–5]. Epidemiological studies have established a link between the use of statins and a lowered risk of developing Alzheimer's disease (AD)^[6]. While it is unclear exactly how statin treatment leads to a reduction in risk, there is significant evidence to suggest that statins affect amyloid precursor protein (APP) processing and consequently reduce plaque formation^[7–10]. In addition, the treatment of cells in culture with statins induces a number of striking morphological changes. For example, statin treatment has been reported to

* To whom correspondence should be addressed.

E-mail: yjjinying@yahoo.com.cn

Received 2011-10-05 Accepted 2012-04-28

promote neurite outgrowth^[11–14]. Furthermore, enhancement of neurite outgrowth by statins treatment is probably mediated by inhibition of Rho isoprenylation, a cholesterol-independent mechanism^[12]. In addition to the Rho family of proteins, the serine/threonine kinase Akt, also known as protein kinase B, has also been revealed as a key mediator of several aspects of neurite outgrowth. Akt is the major effector of the phosphatidylinositol 3-kinase (PI3K) signaling pathway. Downstream of Akt, several substrates have been identified that are likely to play key roles in Akt-mediated neurite outgrowth, such as mammalian target of rapamycin (mTOR) and glycogen synthase kinase 3 β (GSK-3 β)^[15]. mTOR is a serine/threonine protein kinase that regulates multiple cellular functions including neurite outgrowth. PI3K/Akt/mTOR signaling has been shown to promote growth and branching in hippocampal neurons^[16]. The serine/threonine protein kinase GSK-3 β is a key substrate. Activated Akt phosphorylates at GSK-3 β at Ser-9 to inactivate its kinase activity^[17]. It has been reported that statins can induce the phosphorylation of Akt^[3, 18, 19]. These observations suggest the possibility that statins can affect neurite outgrowth by activation of the Akt signaling pathway. In the present study, we examine the effects of the widely employed hydrophilic statin atorvastatin on neurite growth in primary cultured cortical neurons and investigate in more detail the major signaling pathways that mediate these effects. Our data demonstrate that atorvastatin promotes neurite outgrowth. The mechanism mediating this effect involves the PI3K/Akt/mTOR and PI3K/Akt/GSK-3 β signaling pathways.

Materials and methods

Atorvastatin was obtained from LKT Laboratories, Inc (St Paul, MN, USA). LY294002 and wortmannin (PI3K inhibition), LY303511 (inactive analogue of LY294002), PD98059 and U0126 (MEK inhibition), and rapamycin (mTOR inhibition) were from Calbiochem (Darmstadt, Germany). SB415286 (GSK3 β inhibition) and triciribine (TCBN; Akt inhibition) were from Santa Cruz Biotechnology, Inc (Santa Cruz, CA, USA).

Primary cortical neuron cultures

Primary cultures were obtained from the cerebral cortex of 0- to 24-h-old Sprague-Dawley rats. After removal of the meninges and white matter, the cerebral cortex was collected in Hanks' solution without Ca²⁺ and Mg²⁺ (D-Hanks). The cortex was then mechanically fragmented, transferred to D-Hanks' solution containing 0.125% trypsin, and incubated for 15 min at 37°C. Following trypsinization, cells were washed twice with DMEM and re-suspended in DMEM/F12 medium containing 10% heat-inactivated fetal bovine serum, 10% horse serum, glutamine (3 mg/mL), insulin (0.25 mg/mL), penicillin (50 U/mL), and streptomycin (50 mg/mL). The cells were then plated onto 35-mm cell culture dishes (~150 cells/mm²) or 6-well culture plates pre-coated with poly-L-lysine (0.1 g/L, Sigma, St Louis, MO, USA) and kept at 37°C in a humidified atmosphere of 5% CO₂/95% O₂. Forty-eight hours after plating, the media were removed and replaced with DMEM containing glutamine (3 mg/mL), B-27 (2%; Life Technolo-

gies, Gaithersburg, MD, USA) and cytosine arabinofuranoside (final concentration 5 μ mol/L, Sigma) to inhibit the proliferation of non-neuronal cells. After 4 d in culture, the cells were incubated for various lengths of time in media containing atorvastatin (0.05–10 μ mol/L). For pharmacological experiments, inhibitors were added 30 min prior to addition of atorvastatin. Control cultures received a similar amount of DMSO, which was the organic solvent for all inhibitors. Microtubule-associated protein immunostaining indicated that about 90% of the cells were neurons after arabinofuranoside treatment for 3 d.

Immunofluorescence for MAP-2

To examine the effect of treatment on neurite outgrowth, neurons were incubated with media containing the appropriate test compound for an appropriate period of time. Following the treatment period, neurons were fixed with 4% paraformaldehyde/PBS at room temperature for 30 min and permeabilized in 0.2% Triton X-100/PBS for 5 min. Following washes with PBS, the neurons were incubated for 1 h in blocking solution (TBS containing 5% BSA at room temperature). Mouse monoclonal anti MAP-2 antibody (1:500, Abcam Inc, Cambridge, MA, USA) diluted in the blocking buffer was applied and incubated overnight at 4°C. After extensive washes, Cy3-conjugated anti-mouse secondary antibody (Life Technologies, Gaithersburg, MD, USA) was applied and incubated at 37°C for 1 h.

Neuronal imaging and analysis

Neuronal morphology was analyzed using an Olympus CKX41SF microscope, a Universal Imaging SPOT CCD camera and the SPOT Advanced Imaging software. Briefly, images of neurons were analyzed for total neurite branch length (TNBL), neurite number, terminal branch number, and soma area. TNBL and soma area were calculated using image measuring software, whereas neurite number and terminal branch number were counted manually. Five to six fields per well were chosen at random and only neurons distinguishable from neighboring neurons were evaluated to ensure the precision of the measurements; approximately 50–60 neurons were quantified per treatment group per experiment. The experimental group was kept blind until all analysis was done, and then the data from the same group of experiments were pooled together. Each experiment was performed in triplicate, unless otherwise noted.

Western blot analyses

Cells treated with atorvastatin or inhibitor described above were lysed in RIPA Lysis Buffer [Beyotime Institute of Biotechnology; 50 mmol/L Tris (pH 7.4), 150 mmol/L NaCl, 1% Triton X-100, 1% sodium deoxycholate, 0.1% SDS, 1 mmol/L sodium orthovanadate, 10 mmol/L sodium fluoride, 1 mmol/L phenylmethylsulphonyl fluoride, and 1 \times Halt protease inhibitor cocktail], after which detergent-insoluble materials were removed by centrifugation at 12000 \times g for 10 min. Protein concentration in the soluble fraction was measured using an Enhanced BCA protein assay kit (Beyotime

Institute of Biotechnology, Haimen, China). Equal amounts of protein were then separated by SDS-PAGE, transferred onto nitrocellulose membranes, and probed with primary antibodies against the following proteins: rabbit anti-phospho-PDK1 (Ser241), rabbit anti-PDK1, rabbit anti-phospho-Akt (Ser473), rabbit anti-Akt, rabbit anti-phospho-PTEN (Ser380) (phosphatase and tensin homolog deleted on chromosome 10), rabbit anti-PTEN, rabbit anti-phospho-mTOR (Ser2448), rabbit anti-mTOR, rabbit anti-phospho-p70S6K (Thr389), rabbit anti-p70S6K, rabbit anti-phospho-4EBP1 (Thr37/46), anti-4EBP1, rabbit anti-phospho-GSK-3 β (Ser9), and anti-GSK-3 β (all from Cell Signaling Technology, Beverly, MA, USA and diluted 1:1000). Bound antibodies were detected with horseradish peroxidase-conjugated anti-rabbit immunoglobulin G (IgG) (Cell Signaling Technology) each diluted 1:2000 and Supersignal West Pico chemiluminescence substrate (Pierce, Rockford, IL, USA). Staining intensity was quantified from four blots derived from four independent experimental trials. The density of each band was quantified with Image J software and normalized to total kinase or β -actin expression. The protein levels reported in the figures were obtained as a ratio between the band intensity for the protein of interest and the band intensity of total kinases or β -actin (Sigma), used as loading control.

Statistical analysis

Statistical analyses were conducted using multifactor ANOVA including appropriate variables or *t*-test when suitable. Values represent mean \pm SEM. *P* values <0.05 were considered statistically significant.

Results

Atorvastatin increases neurite outgrowth and soma size in cortical neurons

To test the effects of atorvastatin on neurite outgrowth, we used dissociated postnatal cortical neuronal cultures as our model system. The initial set of experiments was designed to investigate whether atorvastatin affects neurite outgrowth in cultured cortical neurons. Atorvastatin (0.05–10 μ mol/L) was added to cultures of cortical neurons at 4 DIV, at a stage in which neurites mature by elongating and branching. TNBL, neurite number, terminal branch number, and soma area were measured after an additional 48 h. As shown in Figure 1, incubation of cortical neurons with atorvastatin (0.05–10 μ mol/L) for 48 h resulted in a dose-dependent increase in the soma size. Both the neurite number and terminal branch number were significantly increased, resulting in a net increase of TNBL. The maximum dose of atorvastatin was 10 μ mol/L for neurite outgrowth. Therefore, we chose this treatment protocol to identify the underlying mechanisms of this event in all subsequent experiments. In our culture of cortical neurons, cells were classified as pyramidal or nonpyramidal on the basis of morphological features. However, there was no difference in the effect of atorvastatin on pyramidal and nonpyramidal neurons. In a time course analysis, increased TNBL and terminal branch number were detected as early as 12 h

after atorvastatin treatment (Figure 2A and 2B). A significant increase in neurite number was detected at 24 h after atorvastatin treatment (Figure 2C). A significant increase in soma area was detected at 48 h after atorvastatin treatment (Figure 2D).

Atorvastatin promotes neurite outgrowth via the PI3K-Akt pathway in cortical neurons

Having established that atorvastatin treatment stimulated neurite outgrowth, we next sought to determine the specific signaling pathways that contribute to these effects. At first, we focused on the PI3K-Akt and MEK-MAPK signaling pathways which have recently been shown to be important for the control of neurite outgrowth. In addition, statins are reported to activate the PI3K pathway, resulting in the phosphorylation of Akt^[20] in endothelial cells. Therefore, the requirement for PI3K activation was first examined. Pretreatment of the cortical neurons with the specific PI3K inhibitor LY294002 (30 μ mol/L) significantly blocked atorvastatin-induced neurite outgrowth as reflected by neurite number, terminal branch number and soma area (Figure 3). Similar results were also observed with the use of another structurally unrelated PI3K inhibitor, wortmannin (5 μ mol/L) (data not shown). In contrast the inactive analogue of LY294002, LY303511 (20 μ mol/L) did not affect the effect of atorvastatin (data not shown). These results show that the activation of PI3K is required for atorvastatin-induced increases in neurite outgrowth in cultured cortical neurons. Pretreatment of the cortical neurons with the specific MEK inhibitor U0126 (10 μ mol/L) also partly blocked the atorvastatin-induced increase in TNBL, terminal branch number, and neurite number. PD98059 (30 μ mol/L; MEK inhibitor) showed similar results. Remarkably, the atorvastatin-induced increase in soma area was blocked by LY294002 but not by U0126 (Figure 3E). Concurrent application of LY294002 and U0126 to block both the PI3K and MAPK signaling pathways completely blocked atorvastatin-induced increases in neurite outgrowth. Interestingly, neither LY294002 nor U0126 changed any of the neurite parameters in control neurons (Figure 3). Together, the data reported above indicate that atorvastatin promotes neurite outgrowth and branching through both the PI3K/Akt and MAPK pathways, whereas atorvastatin increases soma area through only the PI3K/Akt pathway.

Pretreatment of the cortical neurons with triciribine, which blocks all Akt isoforms (Akt1, Akt2, and Akt3) without inhibiting known upstream activators PDK1 and PI3K, completely eliminated the effects of atorvastatin on TNBL, terminal branch number, neurite number, and soma size. Interestingly, triciribine alone also reduced soma size in control neurons (Figure 3).

To further ascertain the requirement for the activation of the PI3K/Akt signaling pathway in the atorvastatin-induced increases in neurite outgrowth, we used phospho-specific antibodies to measure the relative levels of phosphorylated, active forms of the protein kinases phosphoinositide-dependent kinase-1 (PDK1) and Akt after cultured neurons were treated with atorvastatin. For PDK1, we used an antibody specific for

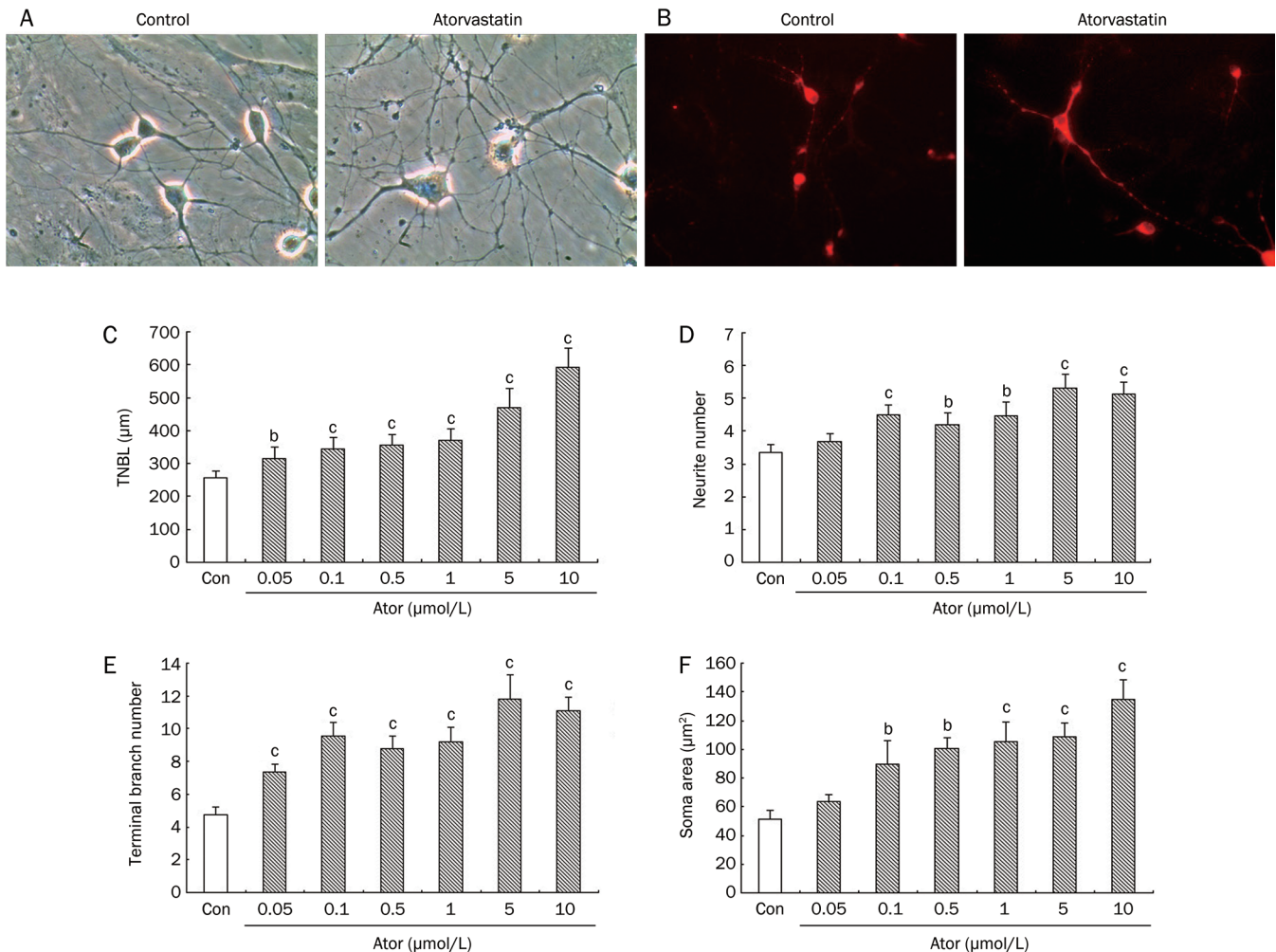


Figure 1. Atorvastatin (Ator) promotes neurite growth in rat cortical neurons in a dose-dependent manner. (A) Examples of neurons taken using phase-contrast microscopy depicting cortical neurons either in the absence (left panel) or presence of 10 μmol/L atorvastatin (right panel). (B) Dendritic structures are confirmed by immunostaining for the dendritic marker MAP-2. Cultured cortical cells were treated at 4 DIV either with vehicle solution (Control, 0.1% DMSO) or with 10 μmol/L atorvastatin for 48 h. Following the treatment period, phase-contrast digital images of the cells were taken using a phase-contrast microscope. The graphs show mean±SEM for TNBL (C), neurite number (D), terminal branch number (E), and soma area (F). Data are from at least three independent experiments (n=50–60 cells). ^bP<0.05, ^cP<0.01 demonstrates statistical significance by one-way ANOVA, followed by least significant difference (LSD)'s *post-hoc* test.

phosphorylated serine 241, which is on the activation loop of PDK1 and is essential for kinase activity. For Akt, we used antibody specific for phosphorylated serine 473, which is necessary for maximal activation of Akt^[21]. As expected, incubation of cultured cortical neurons at 4 DIV with atorvastatin (0.1, 1, and 10 μmol/L) for 48 h caused marked increases in phospho-PDK1 and phospho-Akt (Ser473) in a concentration-dependent manner without a concurrent increase in the total levels of PDK1 and Akt as measured on Western blots of lysates of neurons (Figure 4A). Next, to further confirm that the observed effect of atorvastatin on neurite outgrowth is mediated by elevated level of PIP3, we tested whether atorvastatin treatment can downregulate the PIP3 phosphatase PTEN, which is a negative regulator of the PI3K signaling pathway. The results showed that atorvastatin treatment did not affect

the levels of phospho-PTEN (Ser380) expression (Figure 4A). In a time course analysis, increased phospho-PDK1 levels were detected as early as 6 h and leveled off between 48 to 96 h after atorvastatin treatment (Figure 4B). It is well documented that PDK1 is downstream of PI3K, therefore, we determined whether LY294002 (30 μmol/L) or wortmannin (5 μmol/L) could block the atorvastatin-induced increases in the phosphorylation of PDK1 and Akt. We found that LY294002 (30 μmol/L) significantly blocked the increases in PDK1 and Akt phosphorylation induced by atorvastatin. Similar results were also observed with the use of wortmannin (5 μmol/L) (data not shown). LY303511 (20 μmol/L) did not affect this action of atorvastatin. None of LY294002, wortmannin, or LY303511 alone altered the basal levels of phosphorylated PDK1 and Akt (Figure 4C and 4D). Neither PD98059 (10 μmol/L) nor U0126

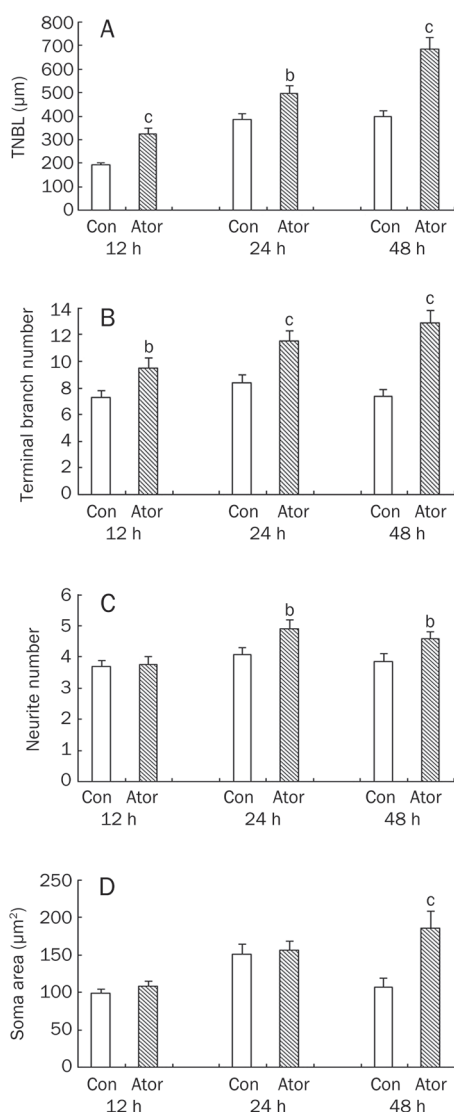


Figure 2. Atorvastatin (10 $\mu\text{mol/L}$) significantly enhanced neurite outgrowth after 12, 24, and 48 h of treatment. The graphs show mean \pm SEM for TNBL (A), terminal branch number (B), neurite number (C), and soma area (D). Data are from at least three independent experiments ($n=50-60$ cells). ^b $P<0.05$, ^c $P<0.01$ demonstrates statistical significance by one-way ANOVA, followed by least significant difference (LSD)'s *post-hoc* test.

pretreatment blocked the action of atorvastatin on phosphorylated PDK1 and Akt (data not shown). Pretreatment of cortical neurons with triciribine (1 $\mu\text{mol/L}$) for 30 min completely blocked atorvastatin-induced increases in phospho-Akt levels. Triciribine (1 $\mu\text{mol/L}$) alone inhibited the basal levels of phosphorylated Akt (Figure 4D). Together, these results indicate that PI3K mediates the action of atorvastatin on PDK1 and Akt levels.

Atorvastatin-induced neurite outgrowth is mTOR-dependent

mTOR is an important downstream node in the PI3K-Akt pathway. We next asked whether the increase in neurite

outgrowth by atorvastatin occurs through an mTOR-coupled mechanism. We used rapamycin, a highly specific mTOR inhibitor, to further elucidate the downstream signaling mechanisms. This treatment decreased the phosphorylation of p70S6K on Thr389, which depends on mTOR activity^[22]. As shown in Figure 5A-5E, pretreatment of cortical neurons with rapamycin (100 nmol/L) almost completely blocked atorvastatin-increased neurite outgrowth and soma size, indicating that a rapamycin-sensitive pathway is involved. We conclude therefore that atorvastatin stimulates neurite outgrowth in cultured cortical neurons in a rapamycin-sensitive manner.

To further ascertain the requirement for mTOR pathway activation in atorvastatin-induced neurite outgrowth, we used phospho-specific mTOR antibody (Ser2448), which has been shown to be important in the control of mTOR activity^[23-25], to measure the relative levels of phosphorylated, active forms of mTOR. As expected, atorvastatin (10 $\mu\text{mol/L}$) induced a significant increase in phosphorylated mTOR without a concurrent increase in the total level of this kinase (Figure 5F). Next, we tested the dependence of atorvastatin-induced mTOR phosphorylation on PI3K/Akt pathway. The results showed that LY294002 (30 $\mu\text{mol/L}$) and triciribine (1 $\mu\text{mol/L}$) completely blocked the atorvastatin-induced increase in phosphorylated mTOR (Figure 5F).

Atorvastatin stimulates the phosphorylation of p70S6K and 4E-BP1

mTOR stimulates translation by activating p70S6K, a kinase that increases synthesis of several components of the translation machinery^[24]. The suppression of p70S6K impairs dendrite branching similarly to inhibition of mTOR^[16, 26]. We then asked if the atorvastatin-induced increases in neurite outgrowth are p70S6K-dependent by examining the phosphorylation state of p70S6K after atorvastatin treatment. We used an antibody specific for phosphorylated threonines 389, a site whose phosphorylation is vital for p70S6K activation^[27]. When cultured cortical neurons were treated with atorvastatin (10 $\mu\text{mol/L}$) for 48 h, the phosphorylation of p70S6K was significantly increased. Furthermore, the atorvastatin-induced increases in the phosphorylation of p70S6K were completely blocked by LY294002 (30 $\mu\text{mol/L}$) and rapamycin (100 nmol/L) pretreatment, respectively (Figure 6A).

In addition, because activation of mTOR can also contribute to translational initiation by phosphorylation of 4E-binding protein 1 (4E-BP1), which binds to and represses the function of the cap-binding translation factor eIF4E, we asked if this regulatory protein may have a role in atorvastatin-induced neurite outgrowth. We used an antibody specific for phosphorylated threonines 37/46, a site whose phosphorylation is required for the inactivation of 4E-BP1 and its dissociation from the eIF4E complex^[28]. Incubation of the cultured cortical neurons with atorvastatin (10 $\mu\text{mol/L}$) for 48 h increased the phosphorylation of 4E-BP1. Furthermore, atorvastatin-induced increases in the phosphorylation of 4E-BP1 was completely blocked by LY294002 (30 $\mu\text{mol/L}$) and rapamycin

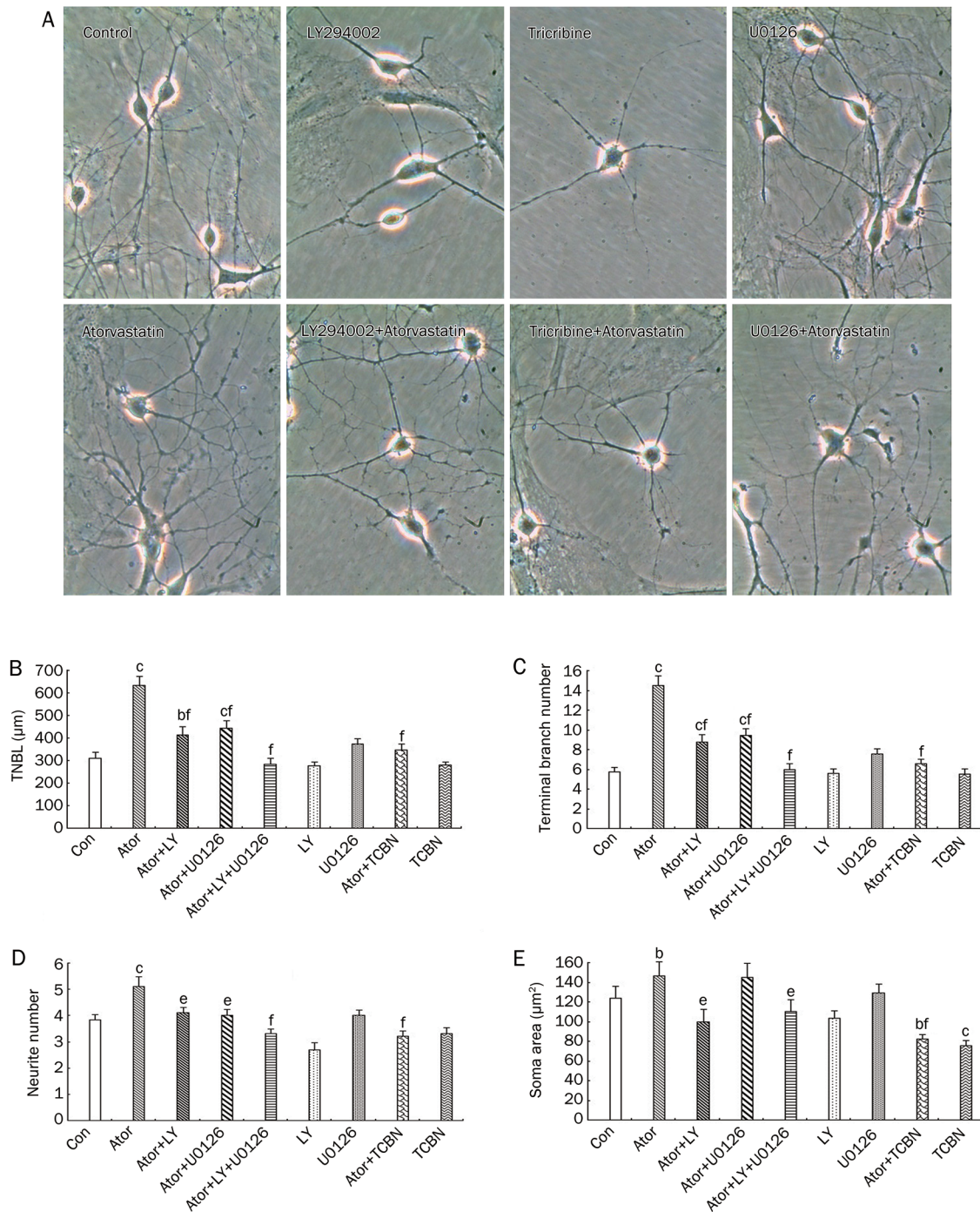


Figure 3. Atorvastatin (Ator) increases neurite outgrowth and soma size through PI3K/Akt and MAPK pathways. (A) Cultured neurons at 4 DIV were pretreated with vehicle, LY294002 (LY, 30 µmol/L), U0126 (10 µmol/L), or tricribine (TCBN, 1 µmol/L) for 30 min and then exposed to atorvastatin (10 µmol/L) for 48 h in the presence of vehicle or inhibitor. Following the treatment period, phase-contrast digital images of the cells were taken using a phase-contrast microscope. The graphs show mean±SEM for TNBL (B), terminal branch number (C), neurite number (D), and soma area (E). Quantifications were performed from at least three independent experiments ($n=50-60$ neurons). ^b $P<0.05$, ^c $P<0.01$ compared with control group; ^e $P<0.05$, ^f $P<0.01$ compared with 10 µmol/L atorvastatin group.

(100 nmol/L) pretreatment, respectively (Figure 6B). These results support the suggestion that activation of both p70S6K

and 4E-BP1 are required for atorvastatin-induced neurite outgrowth.

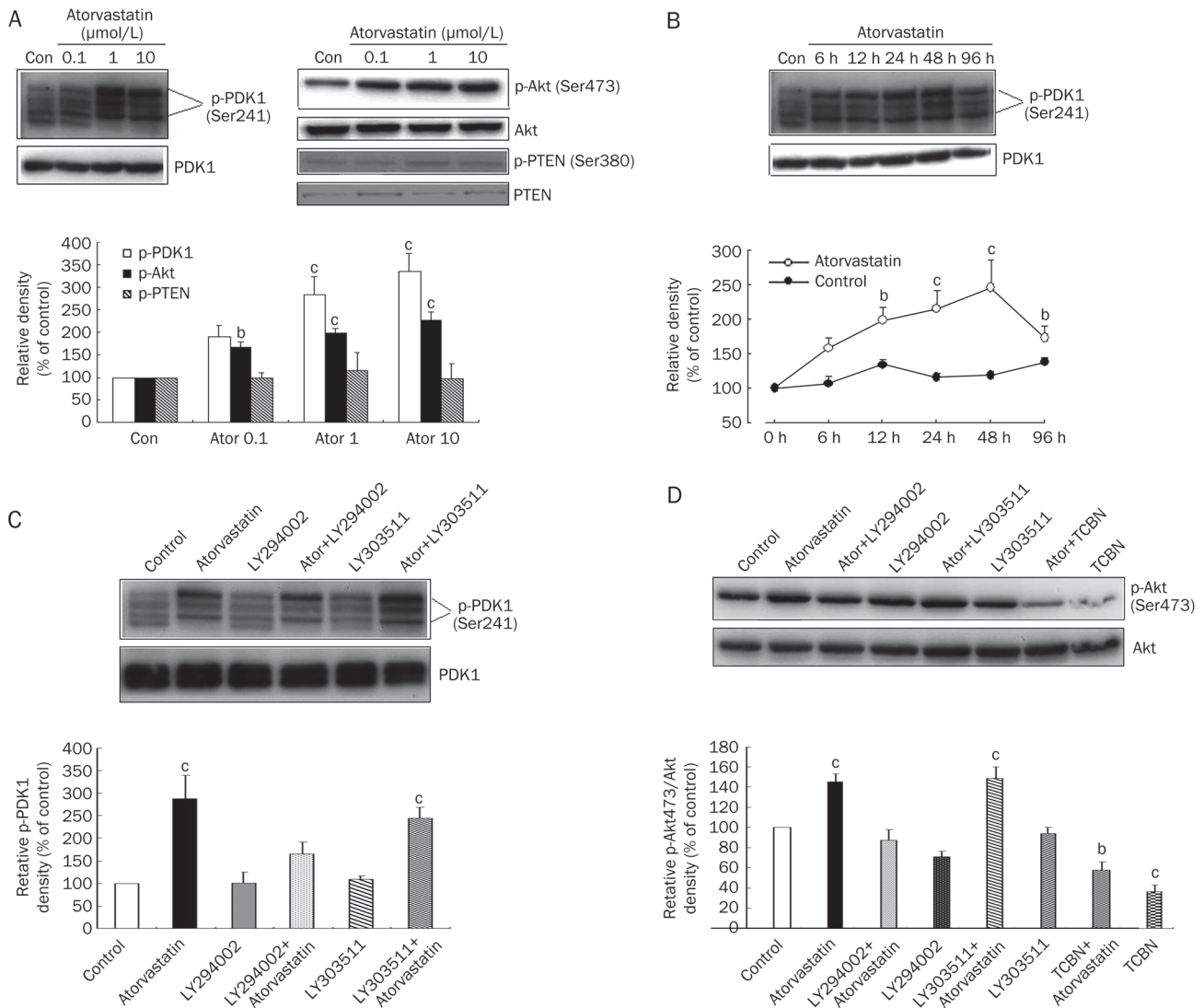


Figure 4. (A) Representative Western blot showing that atorvastatin induced increases in phosphorylation of PDK1 and Akt in a concentration-dependent manner, whereas atorvastatin did not have significant effects on phospho-PTEN. Group data showing the normalization of phospho-PDK1, phospho-Akt, and phospho-PTEN proteins to total PDK1, Akt, and proteins was determined in each group of four experiments. (B) Representative Western blot showing the level of phospho-PDK1 taken at different times after adding atorvastatin (10 μmol/L). Group data showing the normalization of phospho-PDK1 proteins to total PDK1 protein was determined in each group of four experiments. (C) Representative Western blot showing that LY294002 inhibited atorvastatin-induced increases in phosphorylation of PDK1, whereas LY303511 did not have an effect. Group data showing the normalization of phospho-PDK1 to total PDK1 protein was determined in each group of four experiments. (D) Representative Western blot showing that both LY294002 and triciribine inhibited atorvastatin-induced increases in phosphorylation of Akt (Ser473). Group data showing normalization of phosphorylated Akt to total kinase was determined in each group of four experiments. Mean±SEM. ^b*P*<0.05, ^c*P*<0.01 compared with control group.

Atorvastatin increases neurite outgrowth through the Akt/GSK3β pathway

Signaling via the Akt/GSK-3β pathway can regulate neurite morphology by regulating phosphorylation of MAP2^[17]. Akt phosphorylates GSK-3β to inactivate it. Inactivation of GSK-3β leads to decreased phosphorylation of MAP2 and its increased binding and stabilization of microtubules. To test whether GSK-3β mediates the effects of atorvastatin on neurite outgrowth, we treated cultured cortical neurons with SB415286, a specific GSK-3β inhibitor. GSK-3β inhibition by

SB415286 (5 μmol/L) caused an increase in TNBL, terminal branch number, neurite number, and soma area. Treatment of neurons with a combination of atorvastatin (10 μmol/L) and SB415286 (5 μmol/L) caused an additive effect on TNBL, neurite number, terminal branch number, and soma area (Figure 7A–7E). To further test whether atorvastatin can promote neurite growth by regulating the Akt/GSK-3β pathway in cultured cortical neurons, we tested for phosphorylation of GSK-3β in cells treated with atorvastatin. Phosphorylation of GSK-3β increased in response to treatment with atorvastatin

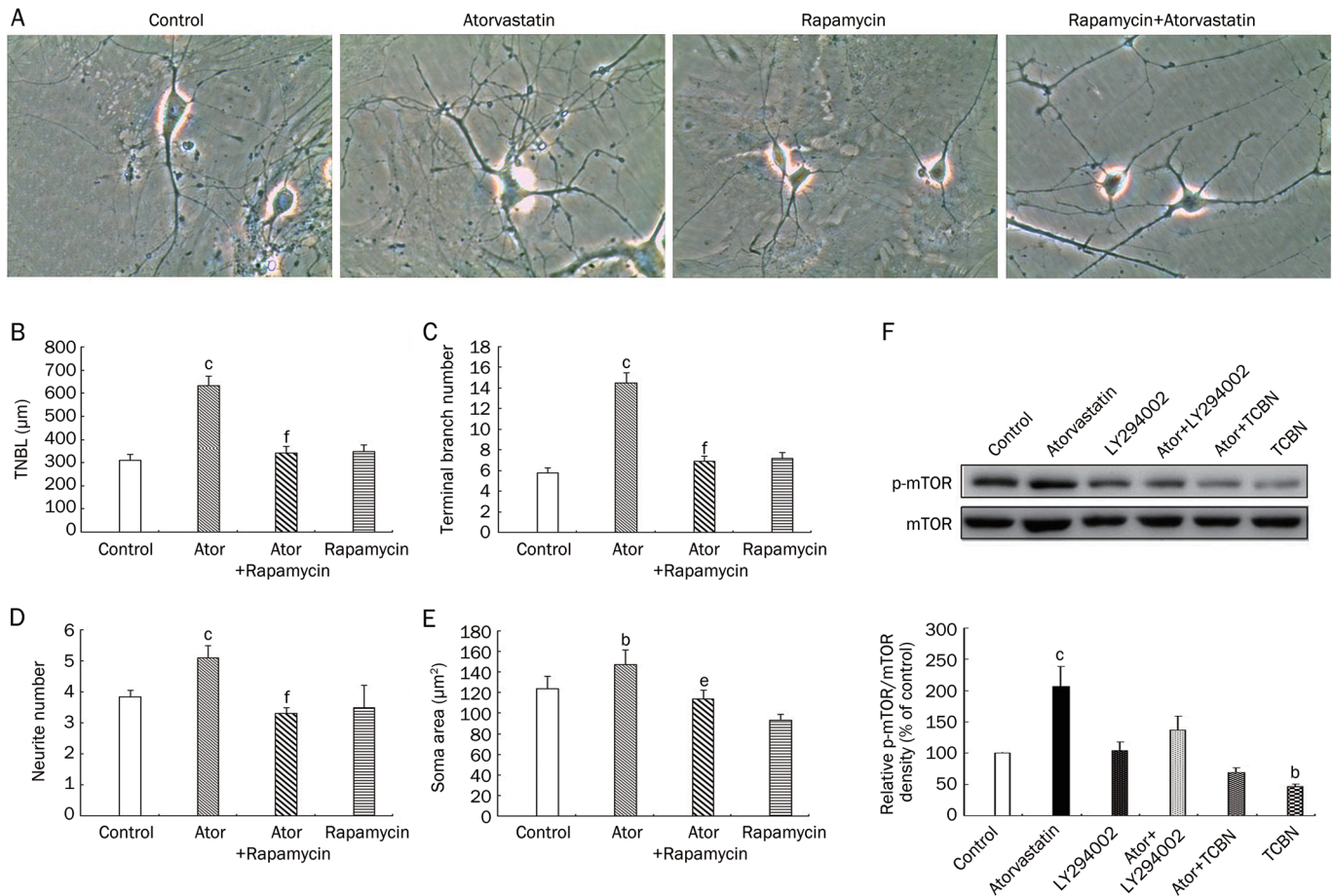


Figure 5. Atorvastatin enhances neurite outgrowth as well as soma size in an mTOR-dependent manner. (A) Cultured neurons at 4 DIV were pretreated with vehicle, rapamycin (100 nmol/L) for 30 min and then exposed to atorvastatin (10 μmol/L) for 48 h in the presence of vehicle or inhibitor. Following the treatment period, phase-contrast digital images of the cells were taken using a phase-contrast microscope. The graphs show mean±SEM for TNBL (B), terminal branch number (C), neurite number (D), and soma area (E). Quantifications were performed from at least three independent experiments ($n=50-60$ neurons in each experiment). ^b $P<0.05$, ^c $P<0.01$ compared with control group; ^e $P<0.05$, ^f $P<0.01$ compared with 10 μmol/L atorvastatin group. (F) Representative Western blot showing both LY294002 and triciribine inhibited atorvastatin-induced increases in phosphorylation of mTOR (Ser2448). Group data showing normalization of phosphorylated mTOR to total kinase was determined in each group of four experiments. Mean±SEM. ^b $P<0.05$, ^c $P<0.01$ compared with control group.

(10 μmol/L) (Figure 7F). To confirm that GSK-3β mediates the effect of atorvastatin on neurite outgrowth, we treated cultured cortical neurons with either LY294002 or triciribine. Pre-treatment with LY294002 (30 μmol/L) or triciribine (1 μmol/L) before adding atorvastatin completely blocked atorvastatin-induced phosphorylation of GSK-3β (Figure 7F). These treatments did not affect GSK-3β protein levels. Together, these results suggest that atorvastatin enhances neurite outgrowth through the Akt/GSK-3β pathway.

Discussion

This study demonstrates that atorvastatin promotes neurite outgrowth by activating the PI3K/Akt/mTOR and Akt/GSK-3β signal pathways in cultured cortical neurons. Our findings are consistent with previous reports that statins significantly induce neurite outgrowth in cultured hippocampal

neurons^[12], explants of rat embryonic cortex and post-natal spinal cord^[13] and PC12 cells^[11]. In contrast, statins have also been reported to inhibit neurite outgrowth in cultured cortical neurons, either by reducing cholesterol levels^[29] or by inhibition of isoprenylation^[30]. However, these studies started statin treatment within 24 h of plating primary neuronal cells. In the present study, we grew the neurons in culture for 4 d before starting treatment to better understand the effect that statin treatment might have on more developmentally mature neurons. A possible explanation for this discrepancy is increased sensitivity of immature neurons to toxicity induced by inhibition of mevalonate synthesis. Comparison of these results also suggests that statins may either stimulate or inhibit neuronal growth, depending on the stage of neuronal development. How can enhancement of neurite outgrowth by atorvastatin be explained? Our results are summarized in Figure 8, which

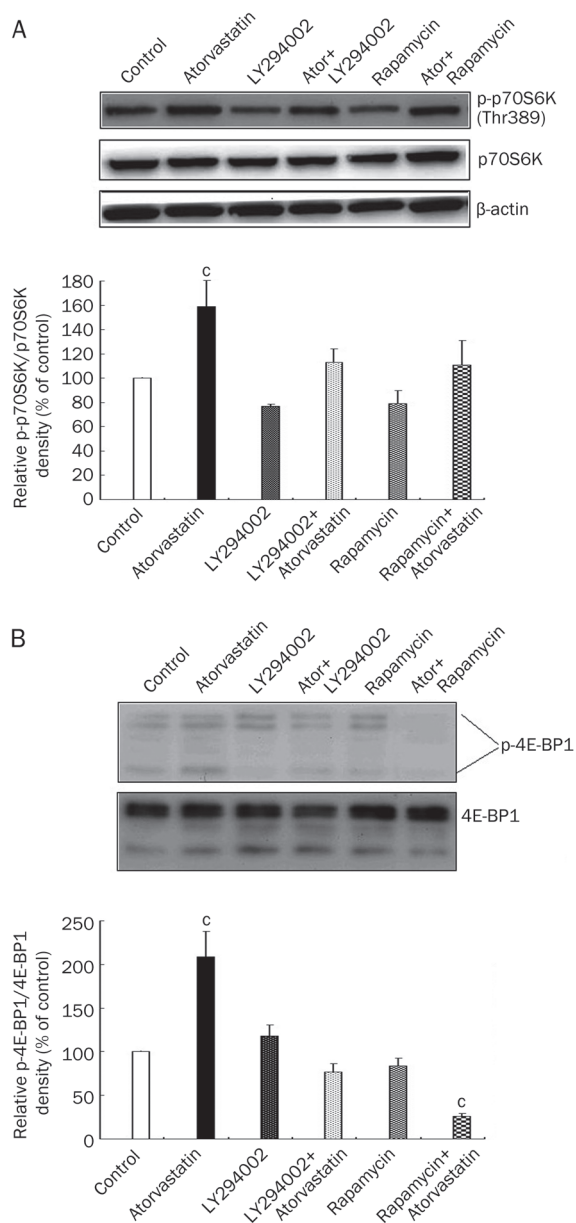


Figure 6. Atorvastatin-induced increases in the phosphorylation of p70S6K and 4E-BP1 are PI3K- and mTOR-dependent. Cultured cortical neurons at 4 DIV were pretreated with vehicle, LY294002 (30 $\mu\text{mol/L}$) or rapamycin (100 nmol/L) for 30 min and then exposed to atorvastatin (10 $\mu\text{mol/L}$) for 48 h in the presence of vehicle or inhibitor. (A) Representative Western blot showing both LY294002 and rapamycin inhibited atorvastatin-induced increases in phosphorylation of p70S6K (Thr389). Group data showing normalization of phosphorylated p70S6K to total kinase was determined in each group of four experiments. (B) Representative Western blot showing both LY294002 and rapamycin inhibited atorvastatin-induced increases in phosphorylation of 4E-BP1 (Thr70). Group data showing normalization of phosphorylated 4E-BP1 to total kinase was determined in each group of four experiments. Mean \pm SEM. ^c $P < 0.01$ compared with control group.

will serve as a guide to the discussion. A previous report has demonstrated that pravastatin's stimulation of neurite out-

growth is mediated by reduction of RhoA signaling via inhibition of geranylgeranylation^[12]. In addition to the Rho family proteins^[31], Akt has been revealed as a key mediator of several aspects of neurite outgrowth, including elongation, branching and caliber^[15]. Several *in vitro* and *in vivo* studies provided evidence that statins activate the PKB/Akt pathway^[3, 32, 33]. Though the mechanism of Akt activation by statins is not known, a study on mammalian endothelial cells demonstrated that simvastatin activates Akt in these cells, while treatment with wortmannin or LY294002 blocked this activation of Akt, suggesting that PI3-kinase signaling is involved^[33]. Our study is the first demonstration to our knowledge that the PI3K/Akt pathway is involved in enhancement of neurite outgrowth by atorvastatin because this process was blocked by wortmannin or LY294002. Furthermore, Western blotting reveals that atorvastatin increased PDK1 and Akt phosphorylation. Therefore, activation of Akt by atorvastatin as demonstrated here is one explanation for the effect of the drug on neurite outgrowth in cortical neurons. The question remains of how atorvastatin activates specific protein kinase such as Akt. The involvement of Ras in the activation of PI3K has been reported^[34]. It has been reported that lovastatin stimulates rapid activation of Ras, which associates with and activates PI3K in the plasma membrane, which in turn regulates Akt^[35]. Based on these previous reports, we propose the hypothesis that atorvastatin activates Akt through activation of Ras and further facilitates neurite outgrowth in cortical neurons. We need to further clarify the specific downstream signal of Akt that promotes neurite outgrowth in the presence of atorvastatin.

Akt phosphorylates or interacts with a number of proteins that may positively influence the development of neuronal morphology. The PI3K/Akt pathway is known to regulate the mTOR pathway, and mTOR has been shown to be a direct substrate of Akt. PI3K/Akt/mTOR signaling has been shown to promote growth and branching in hippocampal neurons^[16]. In recent reports, mTOR promoted axonal regeneration in the adult central nervous system and increased the axonal growth of injured peripheral nerves^[36, 37]. In our experiment, atorvastatin increased the activation of mTOR and p70S6K while rapamycin, an inhibitor of mTOR, decreased the effect of atorvastatin on neurite outgrowth. These results implicated mTOR as a signal of neurite outgrowth in neurons stimulated by atorvastatin. Akt is the main upstream regulator of mTOR in many cellular functions^[38], and in our experiments the inhibition of PI3K-dependent Akt activation by LY294002 decreased the activation of mTOR. In addition, both LY294002 and Akt inhibitor blocked neurite outgrowth facilitated by atorvastatin. Based on these results, we believe that atorvastatin increases the phosphorylation of mTOR and neurite outgrowth through PI3K and Akt. The PI3K pathway to mTOR is mediated by Akt and results in inhibition of tuberlin, a GAP (GTPase-activating protein) for Rheb (Ras homolog enriched in brain); elevated GTP-bound Rheb then stimulates mTOR^[39-41]. In addition, atorvastatin may activate the mTORC2 complex, thereby stimulating phosphorylation of Akt at Ser473^[42, 43]. mTOR activation stimulated transla-

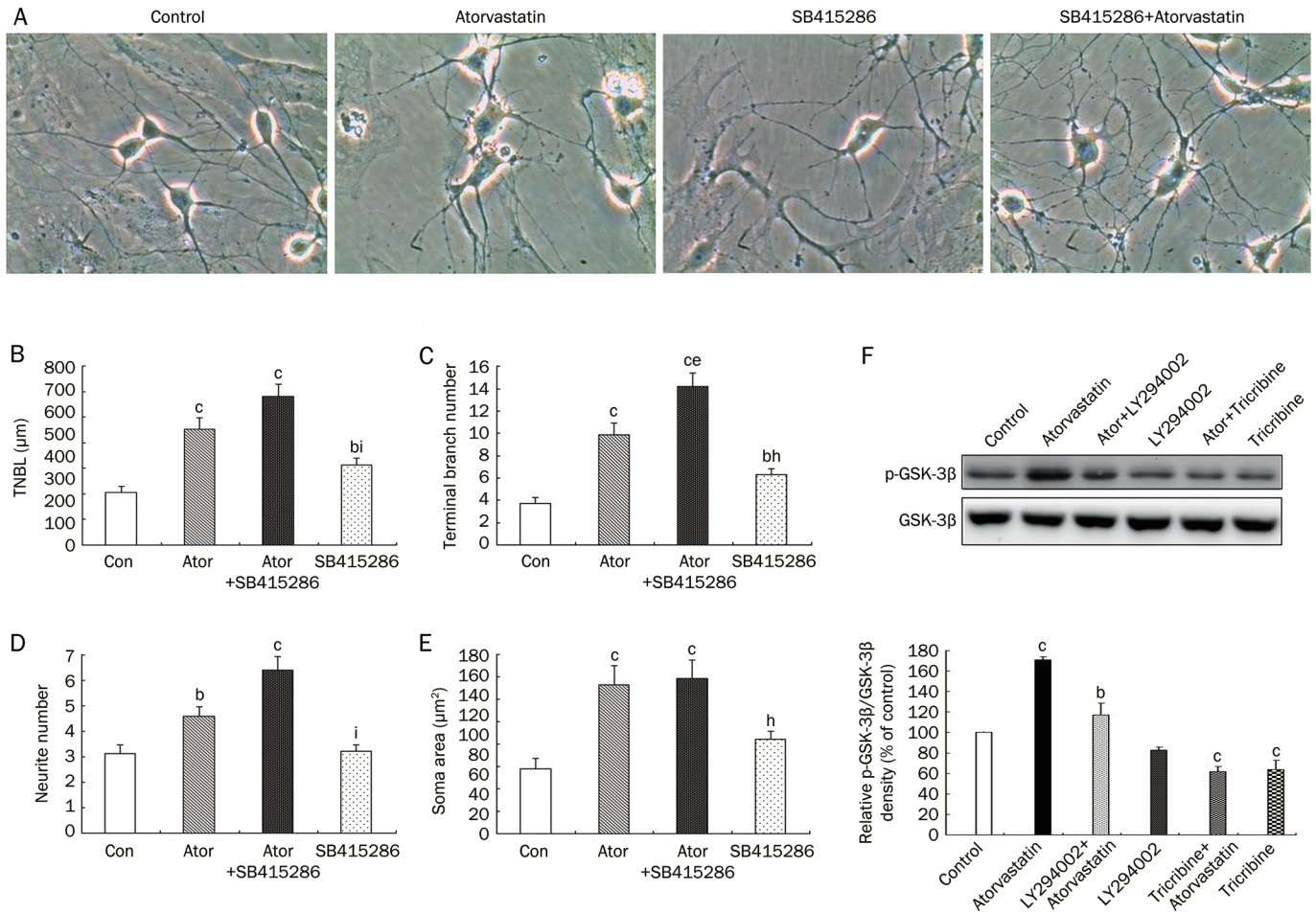


Figure 7. Atorvastatin enhances neurite outgrowth through the PI3K/Akt/GSK-3 β pathway. (A) Cultured neurons at 4 DIV were pretreated with vehicle or SB415286 (5 μ mol/L) for 30 min and then exposed to atorvastatin (10 μ mol/L) for 48 h in the presence of vehicle or inhibitor. Following the treatment period, phase-contrast digital images of the cells were taken using a phase-contrast microscope. The graphs show mean \pm SEM for TNBL (B), terminal branch number (C), neurite number (D), and soma area (E). Quantifications were performed from at least three independent experiments ($n=50-60$ neurons). ^b $P<0.05$, ^c $P<0.01$ compared with control group; ^e $P<0.05$ compared with 10 μ mol/L atorvastatin group. ^h $P<0.05$, ⁱ $P<0.01$ compared with atorvastatin+SB415286 group. (F) Representative Western blot showing both LY294002 and triciribine inhibited atorvastatin-induced increases in phosphorylation of GSK-3 β (Ser9). Group data showing normalization of phosphorylated GSK-3 β to total kinase was determined in each group of four experiments. Mean \pm SEM. ^b $P<0.05$, ^c $P<0.01$ compared with control group.

tional initiation involving both 4E-BP1 and p70S6K^[22], which stimulate translation of 5' capped and 5'TOP (5'-terminal oligopyrimidine tract) mRNAs, respectively^[24, 44]. mTOR and its substrates 4E-BP1 and p70S6Ks are present in dendrites^[45]. p70S6Ks requires hierarchical phosphorylation by mTOR and MAPK for optimal activation^[46]. Similarly, 4E-BP1 is also phosphorylated by mTOR and MAPK at multiple sites^[47]. These might be partially accountable for the involvement of both PI3K and MAPK in neurite formation. The phosphorylated 4E-BP1 is replaced by eIF4G, a scaffolding translation factor that assembles several critical components of the cap-dependent translation initiation complex on the mRNA via its interaction with cap-bound eIF4E^[48]. The activated p70S6K then phosphorylates ribosomal protein S6, which can result in enhanced translation of 5'-oligopyrimidine tract-containing mRNAs that encode numerous components of translation

machinery^[48]. In our study, atorvastatin treatment leads to increased phosphorylation of 4E-BP1 and p70S6K, both of which are inhibited by rapamycin. Thus, activation of mTOR by atorvastatin may enhance both cap-dependent translation (eIF4E pathway) and initiation of 5'-oligopyrimidine tract-containing mRNAs (p70S6K-ribosomal protein S6 pathway). It has been shown that suppression of p70S6K or overexpression of 4E-BP1 impairs dendrite branching similarly to inhibition of mTOR^[16]. Additional investigation into the potential role of p70S6K and 4E-BP1 in atorvastatin-induced neurite outgrowth would be of great interest.

Activated Akt phosphorylates GSK-3 β at Ser9 to inactivate its kinase activity^[17]; thus, GSK-3 β activity is inversely correlated with PI3K/Akt signaling activity^[49]. Some studies have observed GSK-3 β phosphorylation following Akt activation and subsequently neurite outgrowth^[50, 51]. Our study

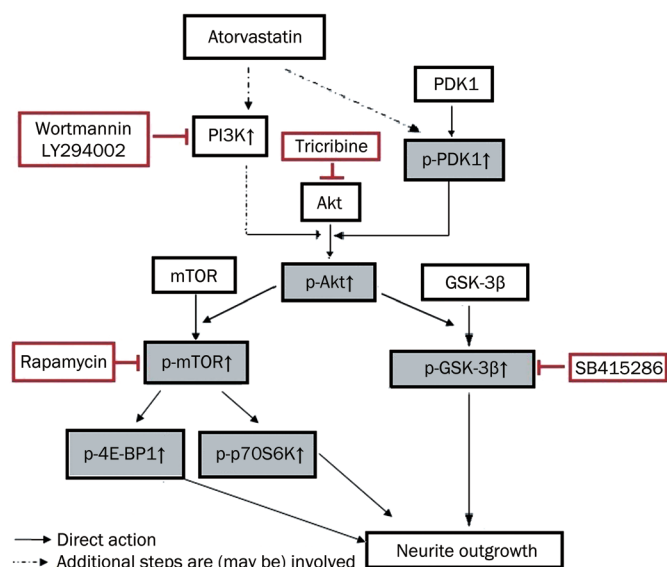


Figure 8. Schematic view of the effects of atorvastatin on PI3K pathways. Findings based on the present study are in bold and highlighted by shaded boxes. The inhibitors used in the study are boxed in red.

demonstrates that treatment of cultured cortical neurons with atorvastatin increased phosphorylation of GSK-3 β (Ser9). Inhibiting PI3K with LY294002 or directly inhibiting Akt with triciribine blocked the atorvastatin-induced increase in phosphorylated GSK-3 β (Ser9). Another study also demonstrates that simvastatin increases phosphorylation of GSK-3 β (Ser9) in the hippocampus in rats after traumatic brain injury^[3]. GSK-3 β , which is inactivated upon phosphorylation by Akt, is implicated in the regulation of microtubule dynamics by phosphorylating MAPs, including adenomatous polyposis coli (APC), MAP1, and MAP2^[52]. Phosphorylation of MAPs is a key step in the regulation of neurite initiation, growth, and branching in hippocampal neurons^[17]. Decreased activity of GSK-3 β reduces phosphorylation of MAP2, a step that can enhance microtubule polymerization and dendritic growth^[53].

Taken together, we have shown for the first time that atorvastatin can regulate neurite outgrowth via the PI3K/Akt/mTOR and PI3K/Akt/GSK-3 β pathways in cultured cortical neurons. It will be important to investigate the effects of atorvastatin on neurite growth *in vivo*. We believe that statins have great potential for treating several nervous disorders. Our results indicate a novel cholesterol-independent effect of statins and call for further studies to reveal the responsible mechanisms.

Acknowledgements

This work was supported by grant from Education Commission of Liaoning Province (LT2010064).

Author contribution

Ying JIN designed the research; Hai-juan SUI, Yan DONG, Qi DING, Wen-hui QU, Sheng-xue YU, and Ying-xin JIN performed the research; Hai-juan SUI and Wen-hui QU analyzed

the data; and Ying JIN wrote the paper.

References

- Asahi M, Huang Z, Thomas S, Yoshimura S, Sumii T, Mori T, et al. Protective effects of statins involving both eNOS and tPA in focal cerebral ischemia. *J Cereb Blood Flow Metab* 2005; 25: 722–9.
- Bosel J, Gandor F, Harms C, Synowitz M, Harms U, Djoufack PC, et al. Neuroprotective effects of atorvastatin against glutamate-induced excitotoxicity in primary cortical neurones. *J Neurochem* 2005; 92: 1386–98.
- Wu H, Lu D, Jiang H, Xiong Y, Qu C, Li B, et al. Simvastatin-mediated upregulation of VEGF and BDNF, activation of the PI3K/Akt pathway, and increase of neurogenesis are associated with therapeutic improvement after traumatic brain injury. *J Neurotrauma* 2008; 25: 130–9.
- Mahmood A, Goussev A, Kazmi H, Qu C, Lu D, Chopp M. Long-term benefits after treatment of traumatic brain injury with simvastatin in rats. *Neurosurgery* 2009; 65: 187–91.
- Han X, Yang N, Xu Y, Zhu J, Chen Z, Liu Z, et al. Simvastatin treatment improves functional recovery after experimental spinal cord injury by upregulating the expression of BDNF and GDNF. *Neurosci Lett* 2011; 487: 255–9.
- Fonseca AC, Resende R, Oliveira CR, Pereira CM. Cholesterol and statins in Alzheimer's disease: current controversies. *Exp Neurol* 2010; 223: 282–93.
- Fassbender K, Simons M, Bergmann C, Stroick M, Lutjohann D, Keller P, et al. Simvastatin strongly reduces levels of Alzheimer's disease beta -amyloid peptides A β 42 and A β 40 *in vitro* and *in vivo*. *Proc Natl Acad Sci U S A* 2001; 98: 5856–61.
- Pedrinì S, Carter TL, Prendergast G, Petanceska S, Ehrlich ME, Gandy S. Modulation of statin-activated shedding of Alzheimer APP ectodomain by ROCK. *PLoS Med* 2005; 2: e18.
- Gellermann GP, Ullrich K, Tannert A, Unger C, Habicht G, Sauter SR, et al. Alzheimer-like plaque formation by human macrophages is reduced by fibrillation inhibitors and lovastatin. *J Mol Biol* 2006; 360: 251–7.
- Won JS, Im YB, Khan M, Contreras M, Singh AK, Singh I. Lovastatin inhibits amyloid precursor protein (APP) beta-cleavage through reduction of APP distribution in Lubrol WX extractable low density lipid rafts. *J Neurochem* 2008; 105: 1536–49.
- Fernandez-Hernando C, Suarez Y, Lasuncion MA. Lovastatin-induced PC-12 cell differentiation is associated with RhoA/RhoA kinase pathway inactivation. *Mol Cell Neurosci* 2005; 29: 591–602.
- Pooler AM, Xi SC, Wurtman RJ. The 3-hydroxy-3-methylglutaryl co-enzyme A reductase inhibitor pravastatin enhances neurite outgrowth in hippocampal neurons. *J Neurochem* 2006; 97: 716–23.
- Holmberg E, Nordstrom T, Gross M, Kluge B, Zhang SX, Doolen S. Simvastatin promotes neurite outgrowth in the presence of inhibitory molecules found in central nervous system injury. *J Neurotrauma* 2006; 23: 1366–78.
- Evangelopoulos ME, Weis J, Kruttgen A. Mevastatin-induced neurite outgrowth of neuroblastoma cells via activation of EGFR. *J Neurosci Res* 2009; 87: 2138–44.
- Read DE, Gorman AM. Involvement of Akt in neurite outgrowth. *Cell Mol Life Sci* 2009; 66: 2975–84.
- Chen J, Zhang ZG, Li Y, Wang Y, Wang L, Jiang H, et al. Statins induce angiogenesis, neurogenesis, and synaptogenesis after stroke. *Ann Neurol* 2003; 53: 743–51.
- Kretz A, Schmeer C, Tausch S, Isenmann S. Simvastatin promotes heat shock protein 27 expression and Akt activation in the rat retina and protects axotomized retinal ganglion cells *in vivo*. *Neurobiol Dis*

- 2006; 21: 421–30.
- 18 Skaletz-Rorowski A, Lutchman M, Kureishi Y, Lefer DJ, Faust JR, Walsh K. HMG-CoA reductase inhibitors promote cholesterol-dependent Akt/PKB translocation to membrane domains in endothelial cells. *Cardiovasc Res* 2003; 57: 253–64.
- 19 Alessi DR, Andjelkovic M, Caudwell B, Cron P, Morrice N, Cohen P, *et al*. Mechanism of activation of protein kinase B by insulin and IGF-1. *EMBO J* 1996; 15: 6541–51.
- 20 Burnett PE, Barrow RK, Cohen NA, Snyder SH, Sabatini DM. RAFT1 phosphorylation of the translational regulators p70 S6 kinase and 4E-BP1. *Proc Natl Acad Sci U S A* 1998; 95: 1432–7.
- 21 Brunn GJ, Fadden P, Haystead TA, Lawrence JC Jr. The mammalian target of rapamycin phosphorylates sites having a (Ser/Thr)-Pro motif and is activated by antibodies to a region near its COOH terminus. *J Biol Chem* 1997; 272: 32547–50.
- 22 Jefferies HB, Fumagalli S, Dennis PB, Reinhard C, Pearson RB, Thomas G. Rapamycin suppresses 5'TOP mRNA translation through inhibition of p70s6k. *EMBO J* 1997; 16: 3693–704.
- 23 Scott PH, Brunn GJ, Kohn AD, Roth RA, Lawrence JC Jr. Evidence of insulin-stimulated phosphorylation and activation of the mammalian target of rapamycin mediated by a protein kinase B signaling pathway. *Proc Natl Acad Sci U S A* 1998; 95: 7772–7.
- 24 Jaworski J, Spangler S, Seeburg DP, Hoogenraad CC, Sheng M. Control of dendritic arborization by the phosphoinositide-3'-kinase-Akt-mammalian target of rapamycin pathway. *J Neurosci* 2005; 25: 11300–12.
- 25 Kumar V, Zhang MX, Swank MW, Kunz J, Wu GY. Regulation of dendritic morphogenesis by Ras-PI3K-Akt-mTOR and Ras-MAPK signaling pathways. *J Neurosci* 2005; 25: 11288–99.
- 26 Dufner A, Thomas G. Ribosomal S6 kinase signaling and the control of translation. *Exp Cell Res* 1999; 253: 100–9.
- 27 Gingras AC, Raught B, Gygi SP, Niedzwiecka A, Miron M, Burley SK, *et al*. Hierarchical phosphorylation of the translation inhibitor 4E-BP1. *Genes Dev* 2001; 15: 2852–64.
- 28 Grimes CA, Jope RS. The multifaceted roles of glycogen synthase kinase 3beta in cellular signaling. *Prog Neurobiol* 2001; 65: 391–426.
- 29 Fan QW, Yu W, Gong JS, Zou K, Sawamura N, Senda T, *et al*. Cholesterol-dependent modulation of dendrite outgrowth and microtubule stability in cultured neurons. *J Neurochem* 2002; 80: 178–90.
- 30 Schulz JG, Bosel J, Stoeckel M, Megow D, Dirnagl U, Endres M. HMG-CoA reductase inhibition causes neurite loss by interfering with geranylgeranylpyrophosphate synthesis. *J Neurochem* 2004; 89: 24–32.
- 31 Van Aelst L, Cline HT. Rho GTPases and activity-dependent dendrite development. *Curr Opin Neurobiol* 2004; 14: 297–304.
- 32 Dimmeler S, Aicher A, Vasa M, Mildner-Rihm C, Adler K, Tiemann M, *et al*. HMG-CoA reductase inhibitors (statins) increase endothelial progenitor cells via the PI3-kinase/Akt pathway. *J Clin Invest* 2001; 108: 391–7.
- 33 Kureishi Y, Luo Z, Shiojima I, Bialik A, Fulton D, Lefer DJ, *et al*. The HMG-CoA reductase inhibitor simvastatin activates the protein kinase Akt and promotes angiogenesis in normocholesterolemic animals. *Nat Med* 2000; 6: 1004–10.
- 34 Rodriguez-Viciana P, Warne PH, Dhand R, Vanhaesebroeck B, Gout I, Fry MJ, *et al*. Phosphatidylinositol-3-OH kinase as a direct target of Ras. *Nature* 1994; 370: 527–32.
- 35 Ghosh-Choudhury N, Mandal CC, Choudhury GG. Statin-induced Ras activation integrates the phosphatidylinositol 3-kinase signal to Akt and MAPK for bone morphogenetic protein-2 expression in osteoblast differentiation. *J Biol Chem* 2007; 282: 4983–93.
- 36 Park KK, Liu K, Hu Y, Smith PD, Wang C, Cai B, *et al*. Promoting axon regeneration in the adult CNS by modulation of the PTEN/mTOR pathway. *Science* 2008; 322: 963–6.
- 37 Abe N, Borson SH, Gambello MJ, Wang F, Cavalli V. Mammalian target of rapamycin (mTOR) activation increases axonal growth capacity of injured peripheral nerves. *J Biol Chem* 2010; 285: 28034–43.
- 38 Jaworski J, Sheng M. The growing role of mTOR in neuronal development and plasticity. *Mol Neurobiol* 2006; 34: 205–19.
- 39 Manning BD, Tee AR, Logsdon MN, Blenis J, Cantley LC. Identification of the tuberous sclerosis complex-2 tumor suppressor gene product tuberlin as a target of the phosphoinositide 3-kinase/akt pathway. *Mol Cell* 2002; 10: 151–62.
- 40 Garami A, Zwartkruis FJ, Nobukuni T, Joaquin M, Rocco M, Stocker H, *et al*. Insulin activation of Rheb, a mediator of mTOR/S6K/4E-BP signaling, is inhibited by TSC1 and 2. *Mol Cell* 2003; 11: 1457–66.
- 41 Tee AR, Manning BD, Roux PP, Cantley LC, Blenis J. Tuberous sclerosis complex gene products, Tuberlin and Hamartin, control mTOR signaling by acting as a GTPase-activating protein complex toward Rheb. *Curr Biol* 2003; 13: 1259–68.
- 42 Hresko RC, Mueckler M. mTOR.RICTOR is the Ser473 kinase for Akt/protein kinase B in 3T3-L1 adipocytes. *J Biol Chem* 2005; 280: 40406–16.
- 43 Sarbassov DD, Guertin DA, Ali SM, Sabatini DM. Phosphorylation and regulation of Akt/PKB by the rictor-mTOR complex. *Science* 2005; 307: 1098–101.
- 44 Beretta L, Gingras AC, Svitkin YV, Hall MN, Sonenberg N. Rapamycin blocks the phosphorylation of 4E-BP1 and inhibits cap-dependent initiation of translation. *EMBO J* 1996; 15: 658–64.
- 45 Tang SJ, Reis G, Kang H, Gingras AC, Sonenberg N, Schuman EM. A rapamycin-sensitive signaling pathway contributes to long-term synaptic plasticity in the hippocampus. *Proc Natl Acad Sci U S A* 2002; 99: 467–72.
- 46 Schmelzle T, Hall MN. TOR, a central controller of cell growth. *Cell* 2000; 103: 253–62.
- 47 Herbert TP, Tee AR, Proud CG. The extracellular signal-regulated kinase pathway regulates the phosphorylation of 4E-BP1 at multiple sites. *J Biol Chem* 2002; 277: 11591–6.
- 48 Hay N, Sonenberg N. Upstream and downstream of mTOR. *Genes Dev* 2004; 18: 1926–45.
- 49 Cross DA, Alessi DR, Cohen P, Andjelkovich M, Hemmings BA. Inhibition of glycogen synthase kinase-3 by insulin mediated by protein kinase B. *Nature* 1995; 378: 785–9.
- 50 Kim Y, Seger R, Suresh Babu CV, Hwang SY, Yoo YS. A positive role of the PI3-K/Akt signaling pathway in PC12 cell differentiation. *Mol Cells* 2004; 18: 353–9.
- 51 Ooms LM, Fedele CG, Astle MV, Ivetac I, Cheung V, Pearson RB, *et al*. The inositol polyphosphate 5-phosphatase, PIPP, is a novel regulator of phosphoinositide 3-kinase-dependent neurite elongation. *Mol Biol Cell* 2006; 17: 607–22.
- 52 Segarra J, Balenci L, Drenth T, Maina F, Lamballe F. Combined signaling through ERK, PI3K/AKT, and RAC1/p38 is required for met-triggered cortical neuron migration. *J Biol Chem* 2006; 281: 4771–8.
- 53 Goold RG, Owen R, Gordon-Weeks PR. Glycogen synthase kinase 3beta phosphorylation of microtubule-associated protein 1B regulates the stability of microtubules in growth cones. *J Cell Sci* 1999; 112: 3373–84.

Original Article

The mineralocorticoid receptor-p38MAPK-NFκB or ERK-Sp1 signal pathways mediate aldosterone-stimulated inflammatory and profibrotic responses in rat vascular smooth muscle cells

Chuan-jiang ZHU*, Qing-qing WANG, Jun-lan ZHOU, Han-zhi LIU, Fang HUA, Hong-zheng YANG, Zhuo-wei HU*

State Key Laboratory of Bioactive Substance and Function of Natural Medicines, Institute of Materia Medica, Chinese Academy of Medical Sciences and Peking Union Medical College, Beijing 100050, China

Aim: To explore the signalling pathways involved in aldosterone-induced inflammation and fibrosis in rat vascular smooth muscle cells (VSMCs).

Methods: Using Western blotting and real-time RT-PCR, we investigated the effects of aldosterone on the expression of cyclooxygenase-2 (Cox-2) and IL-6, two important proinflammatory factors, and TGFβ1, a critical profibrotic factor, in VSMCs.

Results: Aldosterone treatment significantly increased the expression of Cox-2 and IL-6 and activation of p38MAPK and NF-κB. The expression of both Cox-2 and IL-6 could be blocked by the mineralocorticoid receptor (MR) antagonist spironolactone and the p38MAPK inhibitor SB203580. Also, the rapid phosphorylation of p38MAPK could be suppressed by SB203580 but not by spironolactone, implicating in nongenomic effects of aldosterone. Similar to SB203580 and spironolactone, the NF-κB inhibitor α-p-tosyl-L-lysine chloromethyl ketone (TLCK) markedly attenuated expression of Cox-2, indicating that MR, p38MAPK and NF-κB are associated with aldosterone-induced inflammatory responses. Furthermore, aldosterone enhanced expression of TGFβ1 in rat VSMCs. This result may be related to activation of the MR/ERK-Sp1 signalling pathway because PD98059, an ERK1/2 inhibitor, significantly blocked the rapid phosphorylation of ERK1/2 and function of Sp1 and led to reduced expression of TGFβ1. Spironolactone was also shown to significantly inhibit TGFβ1 and Sp1 expression but not ERK1/2 phosphorylation.

Conclusion: These results suggest that aldosterone-induced inflammatory responses and fibrotic responses may be mediated by the MR/p38MAPK-NF-κB pathways and the MR/ERK-Sp1 pathways in VSMCs, respectively.

Keywords: aldosterone; inflammation; fibrosis; signal transduction; vascular smooth muscle cells; mineralocorticoid receptor; p38MAPK; NF-κB; ERK1/2; Sp1; nongenomic effect

Acta Pharmacologica Sinica (2012) 33: 873–878; doi: 10.1038/aps.2012.36; published online 4 Jun 2012

Introduction

It has recently been recognized that aldosterone can exert direct effects on the vasculature, a non-epithelial tissue, and lead to vascular inflammation, fibrosis, remodelling, and finally cardiovascular diseases^[1]. In hypertensive rats, there is evidence that aldosterone-salt treatment caused obvious coronary inflammatory lesions that were characterized by monocyte and macrophage infiltration and increased expression of cyclooxygenase-2 (Cox-2) and osteopontin. The administration of eplerenone, a selective aldosterone blocker, attenuated

vascular and myocardial injury and Cox-2 and osteopontin expression^[2, 3]. Meanwhile, eplerenone significantly reduced the aortic expression of IL-β1, IL-6, and tumour necrosis factor alpha (TNF-α), and the mineralocorticoid receptor (MR) antagonist spironolactone prevented aortic collagen accumulation induced by aldosterone in spontaneously hypertensive rats^[4, 5]. A more recent study using aortic tissues from aldosterone-treated hypertensive rats further revealed that aldosterone increased vascular inflammatory changes, angiotensin II content, and the expression of angiotensin-converting enzyme, vascular proinflammatory genes (osteopontin, MMP-2, ICAM-1, VCAM-1, PDGF-A, VEGF, and PAI-1) and oxidative stress genes (4-hydroxy-2-neonenal, p47phox, p22phox, and gp91phox), the expression of which were all abolished by eplerenone^[6]. These findings suggest that aldosterone plays

* To whom correspondence should be addressed.

E-mail zhucj@imm.ac.cn (Chuan-jiang ZHU);

huzhuowei@imm.ac.cn (Zhuo-wei HU)

Received 2012-03-01 Accepted 2012-03-23

an important role in regulating inflammation and fibrosis in the vascular system. But so far, the intracellular signalling mechanisms underlying the aldosterone-induced vascular injury have not been completely elucidated.

Several studies have examined the signalling pathways in vascular cells that regulate the inflammatory/profibrotic effects induced by aldosterone. Jaffe *et al* reported that aldosterone activates the expression of endogenous genes (collagen types I and III, IL-16 and cytotoxic T-lymphocyte-associated protein 4) via functional MRs in human coronary VSMCs^[7]. Callera *et al* observed that aldosterone rapidly increases the phosphorylation of p38 MAP kinase (p38MAPK) and extracellular signal-regulated kinase (ERK) and significantly increases NADPH oxidase activity and collagen synthesis in VSMCs from both Wistar-Kyoto rats and spontaneously hypertensive rats, all of which are mediated through c-Src-dependent pathways^[8,9]. Also, Ishizawa *et al* reported that aldosterone stimulates rat VSMC proliferation via the activation of the big MAP kinase 1 and is not inhibited by cycloheximide^[10]. Recently, two studies demonstrated that in mouse VSMCs, aldosterone-induced activation of ERK1/2, c-Jun NH₂-terminal protein kinase (JNK) and nuclear factor (NF)- κ B depends on the activity of angiotensin type 1a receptors^[11], and that the proinflammatory phenotype promoted by aldosterone in aged rat VSMCs is mediated by ERK1/2 and epidermal growth factor receptor-dependent pathways^[12]. These data suggest that intracellular signalling pathway(s) that regulate aldosterone-stimulated vascular effects could involve receptors, protein kinases, nuclear factors, oxidant factors, and other unknown factors.

In the present study, we provide new evidence that aldosterone induces the expression of inflammatory factors, Cox-2 and IL-6 through the MR-p38 and NF- κ B pathways and induces expression of transforming growth factor- β 1 (TGF β 1), a profibrotic factor, through the MR-ERK1/2 and Sp1 pathways in rat VSMCs.

Materials and methods

Materials

Aldosterone, spironolactone, α -p-tosyl-L-lysine chloromethyl ketone (TLCK), and dimethylsulfoxide (DMSO) were purchased from Sigma-Aldrich Corporation (St Louis, MO, USA); SB203580 (SB) and PD98059 (PD) were from Calbiochem (Darmstadt, Germany). A stock solution of each compound was dissolved in DMSO, aliquoted and stored at -20°C. Mouse anti-Cox-2, mouse anti-phospho-p38MAPK, mouse anti-p38MAPK, mouse anti-NF- κ B p65, rabbit anti-phospho-ERK1/2, rabbit anti-ERK1/2, rabbit anti-Sp1, rabbit anti-actin, biotinylated secondary antibodies, and HRP-conjugated streptavidin, were all obtained from Santa Cruz (Santa Cruz, CA, USA).

Cell culture

Rat VSMCs were maintained in 75-cm² tissue culture flasks in DMEM containing 10% fetal bovine serum, 100 IU/mL peni-

cillin, and 100 IU/mL streptomycin at 37°C with 95% air and 5% carbon dioxide. The cells were grown to 75% confluence and treated with vehicle or aldosterone at serial concentrations from 10⁻⁹ to 10⁻⁶ mol/L for the times indicated. Twenty four hours before the treatment, the medium was replaced with medium containing 0.4% serum. For the inhibitor studies, SB at 2 \times 10⁻⁵ mol/L, PD at 5 \times 10⁻⁵ mol/L, TLCK at 10⁻⁴ mol/L, or spironolactone at 5 \times 10⁻⁵ mol/L was added to the culture medium 1 h prior to the addition of aldosterone.

Western blot analyses of Cox-2, p38MAPK, and ERK1/2 proteins

At the end of the treatment, the cells were washed with ice-cold PBS twice and lysed with 80–100 μ L of the following buffer: Tris-HCl [50 mmol/L (pH 8.0)], NaCl (150 mmol/L), SDS (0.1%), PMSF (100 μ g/mL), aprotinin (1 μ g/mL), Nonidet P-40 (1%). The lysates were frozen with liquid nitrogen and then thawed in water at 37°C three times, and centrifuged at 15000 \times g for 10 min. The protein concentration of the supernatant was determined by the Lowry method using bovine serum albumin as the standard. The proteins (20–40 μ g) were separated by SDS-PAGE on an 8% separating gel and 5% stacking gel for Cox-2 or 10% separating gels for p38 and ERK1/2, blotted onto PDVF membranes, incubated in a blocking buffer (5% non-fat, dried milk and 0.05% Tween-20 in PBS), and then incubated with the primary antibodies (at a 1:1000 dilution), biotinylated secondary antibodies (1:2000 dilution), and HRP-conjugated streptavidin (1:2000 dilution). The protein bands were visualized with enhanced chemiluminescence (ECL, Beijing Pulilai Company, Beijing, China) according to the manufacturer's instructions.

Western blot analysis of NF- κ B and Sp1 proteins

Two steps were taken to extract the NF- κ B and Sp1 proteins from the cytoplasm and nucleoplasm, respectively. After being washed with ice-cold PBS, the cells were lysed with 150 μ L of buffer A, which consists of HEPES [10 mmol/L (pH 7.9)], KCl (10 mmol/L), and EDTA (0.1 mmol/L). Just before use, PMSF (0.5 mmol/L), DTT (1 mmol/L), and 1 μ L of protease inhibitors (including leupeptin, aprotinin, and pepstatin) (10 μ g/mL) were added, incubated for 10 min at room temperature, then scraped and centrifuged at 15000 \times g for 3 min. The supernatant (cytoplasmic fraction) was collected, aliquoted and stored at -86°C. The pellet was resuspended with 150 μ L of buffer B: HEPES [20 mmol/L, (pH 7.9)], NaCl (0.4 mol/L), EDTA (1 mmol/L), and glycerol (10%). Before use, PMSF (0.5 mmol/L), DTT (1 mmol/L), and 1 μ L of each protease inhibitor (leupeptin, aprotinin, and pepstatin, 10 μ g/mL) was added to buffer B. The resuspended solution was shaken vigorously at 4°C for 2 h then centrifuged at 15000 \times g for 5 min. The supernatant (nucleoplasmic fraction) was collected, aliquoted and stored at -86°C.

The protein concentrations of the cytoplasmic and nucleoplasmic extracts were quantitated. The proteins were electrophoresed on 10% separating gels and analysed by the same methods described above.

Densitometric analysis

The density of the bands on the Western blots was quantified by scanning densitometry (LAS-3000 Fujifilm and Kodak Digital Science 1D software) and expressed as the normalized values to actin.

Real-time quantitative reverse-transcription polymerase chain reaction analyses of IL-6 and TGF β 1 mRNA levels

The total RNA from rat VSMCs was extracted according to the TRIzol reagent protocol (Invitrogen). Two micrograms of total RNA was reverse transcribed in a MyCycler (BioRad) in a 25- μ L reaction volume containing 1 μ L Moloney murine leukemia virus reverse transcriptase (5 IU/mL), 0.5 μ L RNA-sin (40 IU/mL), 2.5 μ L deoxynucleotide triphosphate (10 mmol/L), 5 μ L 5 \times PCR buffer, 2.5 μ L Oligo dT (0.5 μ g/ μ L), and diethylpyrocarbonate-water added to the final volume. The resulting cDNA was amplified and quantified by real-time RT-PCR (PRISM-7000, ABI) in a 10- μ L reaction volume containing 1 μ L cDNA (RT product), 5 μ L 2 \times mixture, 0.2 μ L of the sense primer (20 pmol/L), 0.2 μ L of the antisense primer (20 pmol/L), 0.2 μ L 50 \times SYBR Green I (Invitrogen), and 3.4 μ L double distilled water. The primers and reaction conditions were as follows: IL-6, sense 5'-AGGAACGAAAGTCAACTC-CATCTG-3'; antisense 5'-GGCAGTGGCTGTCAACAA-CATC-3, product size 111 bp; β -actin, sense 5'-CAGCGGAAC-CGCTCATTTGCCAATGG-3', antisense 5'-TCACCCACACT-GTGCCATCTACG-3', product size, 360 bp; TGF β 1, sense 5'-GCTAATGGTGGACCGCAACAAC-3', antisense 5'-CACT-GCTTCCCGAATGTCTGAC-3', product size, 122 bp; GAPDH, sense 5'-TGGAGTCTACTGGCGTCTTCAC-3', antisense 5'-ATGAGCCCTCCACGATGC-3', product size, 238 bp; reaction conditions: activation of enzymes at 50 $^{\circ}$ C for 5 min, one cycle of denaturation at 95 $^{\circ}$ C for 5 min; 42 cycles of denaturation at 95 $^{\circ}$ C for 15 s, primer annealing at 60 $^{\circ}$ C for 31 s, primer extension at 72 $^{\circ}$ C for 30 s; then dissociation curves at 95 $^{\circ}$ C for 0 min, 65 $^{\circ}$ C for 15 s, and 4 $^{\circ}$ C for 1 min. The IL-6 and TGF β 1 mRNA levels were normalized to the β -actin and GAPDH mRNA amounts, respectively. The results are expressed as the fold of control.

Statistical analysis

All values are expressed as the mean \pm SD. The data were analysed using the Student's *t* test. A *P*<0.05 was accepted as statistically significant.

Results

Aldosterone induces the expression of Cox-2 protein and IL-6 mRNA in VSMCs

In rat VSMCs, aldosterone induced the expression of Cox-2 protein in a concentration- and time-dependent manner, from 1 to 1000 nmol/L and 30 min to 2 or 4 h, respectively (Figure 1A). Aldosterone treatment also significantly enhanced IL-6 mRNA levels by 10-fold over the control group (Figure 2). These activities were blocked by the MR antagonist spironolactone and the p38MAPK inhibitor SB203580, but not by the ERK1/2 inhibitor PD98059, although PD98059 did reduce

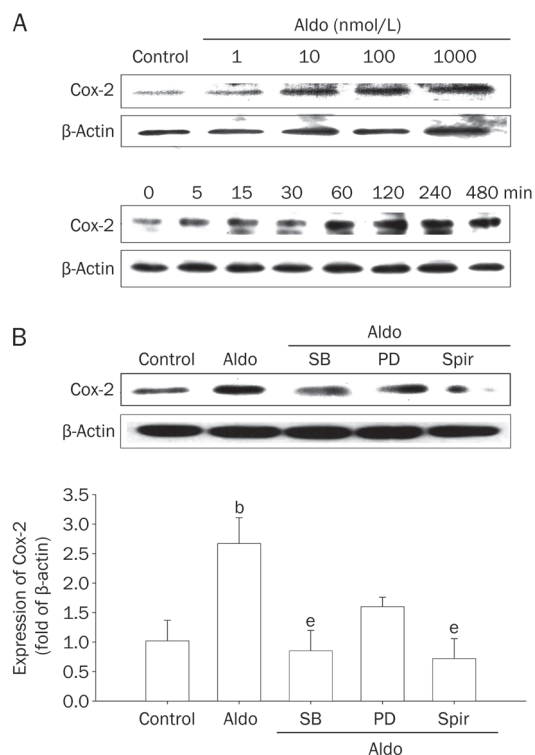


Figure 1. The expression of cyclooxygenase 2 (Cox-2) in rat vascular smooth muscle cells (VSMCs) induced by aldosterone (Aldo). (A) Upper panel, the concentration-dependent increase in Cox-2 expression induced by Aldo for 4 h. Lower panel, the time-related increase in Cox-2 expression induced by Aldo (0.1 μ mol/L) for the indicated times. (B) The effects of different inhibitors on Cox-2 expression induced by Aldo. The cells were pretreated with SB203580 (SB, 20 μ mol/L), PD98059 (PD, 50 μ mol/L), and spironolactone (Spir, 50 μ mol/L) for 1 h, then stimulated by Aldo (0.1 μ mol/L) for 4 h. The cell lysates were analysed by Western blotting with specific antibodies. Mean \pm SD. *n*=3. ^b*P*<0.05 vs control. ^e*P*<0.05 vs Aldo.

the levels to a certain extent (Figure 1B and 2). TLCK had no inhibitory effects on IL-6 mRNA expression. These data suggest that aldosterone potentially elicits vascular inflammatory responses through the MR and protein kinase system.

Aldosterone increases the phosphorylation of p38MAPK

SB203580 could significantly down-regulate the expression of Cox-2 and IL-6, implying that p38MAPK is involved in the inflammatory responses induced by aldosterone. Incubation of cultured VSMCs with aldosterone for 15 or 30 min markedly enhanced the phosphorylation of p38MAPK, which was obviously suppressed by SB203580 but not spironolactone (Figure 3A), suggesting that MAPKs are involved in the signal transduction of direct vascular effects (nongenomic effects) induced by aldosterone.

Aldosterone stimulates NF- κ B p65 expression

The role of the proinflammatory transcription factor NF- κ B in the inflammatory responses induced by aldosterone was investigated. After the administration of aldosterone to VSMCs for

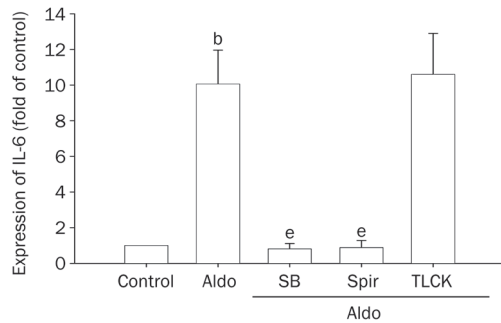


Figure 2. The expression of IL-6 in VSMCs induced by aldosterone (Aldo). The cells were pretreated with SB203580 (SB, 20 $\mu\text{mol/L}$), spironolactone (Spir, 50 $\mu\text{mol/L}$) and TLCK (100 $\mu\text{mol/L}$) for 1 h, then stimulated with Aldo (0.1 $\mu\text{mol/L}$) for 7 h. The cell lysates were analysed by real time RT-PCR. Mean \pm SD. $n=3$. ^b*P*<0.05 vs control. ^e*P*<0.05 vs Aldo.

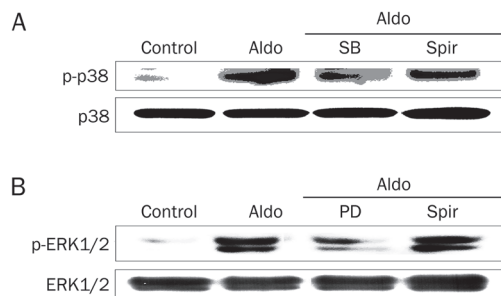


Figure 3. Aldosterone (Aldo) stimulates the phosphorylation of p38MAPK (A) and ERK1/2 (B) in VSMCs. The cells were pretreated with SB203580 (SB, 20 $\mu\text{mol/L}$), PD98059 (PD, 50 $\mu\text{mol/L}$), and spironolactone (Spir, 50 $\mu\text{mol/L}$) for 1 h, then stimulated with Aldo (0.1 $\mu\text{mol/L}$) for 30 min. The cell lysates were analysed by Western blotting with specific antibodies.

4 h, both the cytoplasmic and nucleoplasmic extracts were prepared, and the amount of NF- κ B p65 protein was determined by Western blot analysis. As shown in Figure 4, the expression of p65 was almost undetectable in the cytoplasm but was expressed 6.7-fold over the control in the nucleoplasm, even after aldosterone stimulation, indicating that NF- κ B mediates the inflammatory responses of aldosterone.

Inhibition of NF- κ B and p38MAPK activities stimulated by aldosterone

Further studies revealed that pretreating cells with TLCK, a

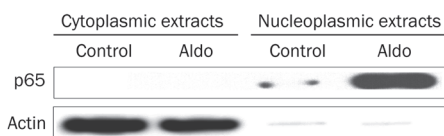


Figure 4. The expression of NF- κ B p65 in the cytoplasmic and nucleoplasmic extracts from rat VSMCs induced by aldosterone (Aldo). The cells were stimulated by Aldo for 4 h. The cytoplasmic and nucleoplasmic extracts were separated by SDS-PAGE and were analysed by Western blotting with specific antibodies.

serine proteinase inhibitor of NF- κ B, could significantly block Cox-2 protein expression induced by aldosterone in cultured VEMCs. Similar results were obtained using the p38MAPK inhibitor SB203580 and the MR receptor blocker spironolactone (Figure 5). The results suggest that aldosterone-induced inflammatory effects could be mediated through a MR-p38MAPK-NF- κ B pathway.

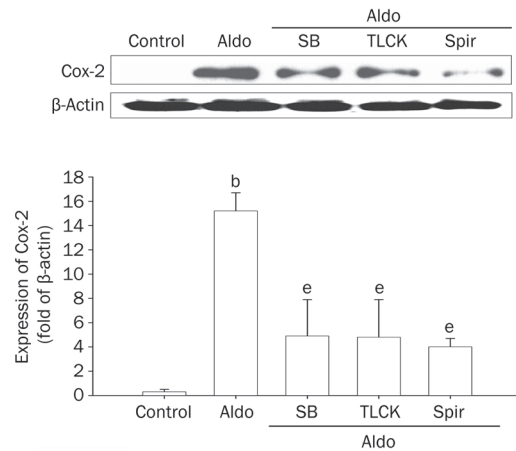


Figure 5. The inhibition of p38MAPK and NF- κ B activities stimulated by aldosterone (Aldo) in rat VSMCs. The cells were pretreated with SB203580 (SB, 20 $\mu\text{mol/L}$), TLCK (100 $\mu\text{mol/L}$), and spironolactone (Spir, 50 $\mu\text{mol/L}$) for 1 h, then stimulated with Aldo (0.1 $\mu\text{mol/L}$) for 4 h. The cell lysates were analysed by Western blotting with specific antibodies. Mean \pm SD. $n=3$. ^b*P*<0.05 vs control. ^e*P*<0.05 vs Aldo.

Aldosterone induces the expression of TGF β 1 mRNA

Aldosterone-stimulated inflammation probably results in fibrosis in vascular tissues. Thus, the mRNA expression of the profibrotic molecule TGF β 1 in rat VSMCs was investigated using quantitative real-time RT-PCR. As shown in Figure 6, aldosterone treatment increased the levels of TGF β 1 mRNA. This effect was significantly reduced by the ERK1/2 inhibitor PD98059 and the MR receptor antagonist spironolactone,

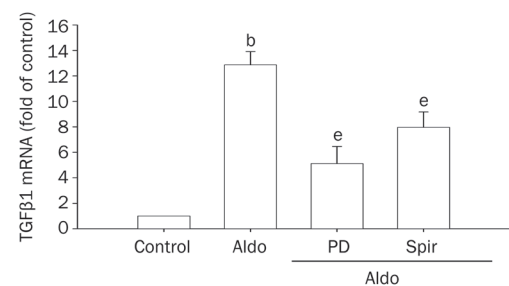


Figure 6. Aldosterone (Aldo) induces the expression of TGF β 1 mRNA in rat VSMCs. The cells were pretreated with PD98059 (PD, 50 $\mu\text{mol/L}$) or spironolactone (Spir, 50 $\mu\text{mol/L}$) for 1 h, then stimulated with Aldo (0.1 $\mu\text{mol/L}$) for 7 h. The cell lysates were analysed by real time RT-PCR. Mean \pm SD. $n=3$. ^b*P*<0.05 vs control. ^e*P*<0.05 vs Aldo.

suggesting that ERKs and MR have a role in the profibrotic effects of aldosterone.

Aldosterone increases the phosphorylation of ERK1/2

Incubation of cultured VSMCs with aldosterone for 15 or 30 min markedly increased not only the phosphorylation of p38MAPK but also ERK1/2. The phosphorylation of ERK1/2 was strongly blocked by PD98059, while spironolactone had no effect (Figure 3B), implying it was rapid, nongenomic effects of aldosterone. These data further demonstrate that MAPKs have a role in the proinflammatory and profibrotic effects of aldosterone.

Aldosterone stimulates Sp1 expression in the nucleoplasm

The role of Sp1, a nuclear transcription factor, in profibrotic responses induced by aldosterone was also studied. As shown in Figure 7, aldosterone significantly increased Sp1 expression in the nucleoplasm, and this effect was blocked by PD98059 and spironolactone, which is similar to their effect on inhibiting TGF β 1 expression (Figure 6). These results indicate that the profibrotic effects of aldosterone could be associated with the MR-ERKs-Sp1 pathway.

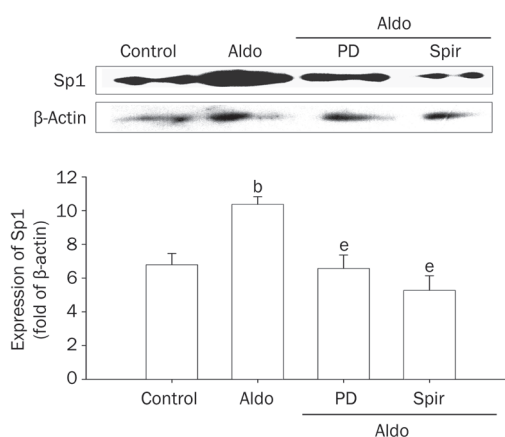


Figure 7. Aldosterone (Aldo) stimulates Sp1 protein expression in rat VSMCs. The cells were pretreated with PD98059 (PD, 50 μ mol/L), and spironolactone (Spir, 50 μ mol/L) for 1 h, then stimulated with Aldo (0.1 μ mol/L) for 30 min. Nucleoplasmic extracts were separated by SDS-PAGE and analysed by Western blotting with specific antibodies. Mean \pm SD. $n=3$. ^b $P<0.05$ vs control. ^e $P<0.05$ vs Aldo.

Discussion

In this study, we showed that aldosterone stimulation caused inflammatory responses in rat VSMCs and resulted in the enhanced expression of the inflammatory factors Cox-2 and IL-6. This effect was attenuated by the MR antagonist spironolactone (Figures 1 and 2). These results are consistent with previous reports demonstrating that aldosterone treatment in uninephrectomized rats elevated the levels of Cox-2 mRNA and coronary inflammatory lesions; these vascular inflammatory responses were reduced by the aldosterone

blocker eplerenone^[2,3]. The results indicated that the MR was part of the signalling pathway involved in the inflammatory responses induced by aldosterone. Further studies in our laboratory have demonstrated that aldosterone has two different effects: (1) phosphorylation of p38MAPK (rapid, nongenomic effect), which was suppressed by SB203580 but not by spironolactone (Figure 3), implying that the MR does not mediate this effect; (2) activation and nuclear translocation of NF- κ B p65 (delayed genomic effect; Figure 4). In VSMCs, the activation of both p38MAPK and NF- κ B might result in the production of chemokines and inflammatory cytokines^[1,13]. Indeed, we observed a significant increase in the expression of Cox-2 and IL-6 (Figure 5). Furthermore, in spontaneously hypertensive rats, aldosterone up-regulated NF- κ B p50 expression and down-regulated I κ B mRNA expression. This effect was accompanied by the enhanced expression of cytokines (such as IL-1 β , IL-6, and TNF- α)^[4]. Similarly, in VSMCs from both Wistar-Kyoto rats and spontaneously hypertensive rats, aldosterone-induced phosphorylation of the protein tyrosine kinase c-Src, results in the amplification of NAD(P)H-mediated generation of reactive oxygen species (ROS) and leads to the activation of ROS-sensitive transcription factors, such as NF- κ B and activation protein-1 (AP-1), recruitment of inflammatory cells and elaboration of inducible NO synthase (iNOS), and, consequently, vascular damage^[8-10]. Therefore, protein kinases (p38MAPK, Src) and transcription factors (NF- κ B, AP-1) are two elements of the signalling pathway that mediate the inflammatory responses of aldosterone. Recent studies using siRNA in mouse VSMCs revealed that the activation of NF- κ B requires not only the MR but also the AT1 receptor^[11]. The data from this study demonstrated that the aldosterone-induced expression of inflammatory factors (Cox-2) could be significantly reduced by the MR blocker spironolactone, the p38 MAPK inhibitor SB203580, and the NF- κ B inhibitor TLCK (Figure 5), indicating that the MR-p38MAPK-NF- κ B signalling pathway mediates the inflammatory responses induced by aldosterone. In this signalling pathway, the activation of p38MAPK may not require the MR because spironolactone did not inhibit phosphorylation of p38 MAPK (Figure 3). This result may be due to the direct, nongenomic effects of aldosterone, which may facilitate classical MR-mediated effects^[1].

It is known that aldosterone induces fibrosis in rat heart and blood vessels^[14], and spironolactone prevents aortic collagen accumulation in spontaneously hypertensive rats^[5,15]. These data imply that the MR is involved in vascular fibrosis, but the underlying, detailed molecular mechanism has not been completely elucidated. In the present study, we observed the effects of aldosterone on the profibrotic molecule TGF β 1 in rat VSMCs. Our data show that the incubation of VSMCs with aldosterone significantly increased the expression of TGF β 1 mRNA, which was then inhibited by spironolactone and PD98059 (Figure 5), implying that ERK1/2 is also involved in vascular fibrosis. Similar results were reported by Kobayashi *et al*^[14] in Dahl salt-sensitive hypertensive rats. In that study, treating the animals with eplerenone significantly decreased the phosphorylation of protein kinase C (PKC) β II, c-Src,

ERK1/2, and p70S6 kinase (p70S6K), as well as the expression of TGF β 1 and type I collagen mRNA and protein, which suggests that aldosterone-induced profibrotic effects could be mediated through the PKC β II-c-Src (upstream regulator)-ERK1/2-p70S6K (downstream effector) pathway. Furthermore, studies by Callera *et al*^[8, 9] in VSMCs from spontaneously hypertensive rats demonstrated that aldosterone stimulation could enhance the phosphorylation of c-Src and MAPKs, and the incorporation of [³H]-proline, a marker of collagen synthesis, and stimulatory effects of aldosterone on collagen synthesis was inhibited by PP2 (c-Src inhibitor) and SB212190 (p38MAPK inhibitor), confirming that the vascular profibrotic actions of aldosterone could be mediated through the c-Src/MAPK signalling pathways. Additionally, it was reported that the epidermal growth factor receptor (EGFR) could be involved in mediating the profibrotic responses of aldosterone because the EGFR is involved in the development of fibrosis and vascular dysfunction^[16, 17], and aldosterone-induced stimulation of ERK1/2 in VSMCs is dependent on the EGFR^[18]. In this study, our data also show that aldosterone could induce rapid phosphorylation of ERK1/2 in rat VSMCs, which was suppressed by PD98059 but not spironolactone, implying that aldosterone has nongenomic effects (Figure 3). Moreover, spironolactone and PD98059 inhibited the enhanced expression of TGF β 1 mRNA and Sp1 protein, suggesting that the MR-ERKs-Sp1 pathway could mediate aldosterone-activated profibrotic responses in rat VSMCs.

Taken together, our studies provide new evidence on the proinflammatory and profibrotic effects of aldosterone (including genomic and nongenomic effects) that are mediated through the MR-MAPKs (ERK1/2, p38MAPK), transcription factors (Sp1, NF- κ B) signalling pathways. Regulating the aldosterone-induced effects through these factors will potentially reduce vascular remodelling and damage. This effect could be beneficial and effective in the treatment of cardiovascular diseases.

Acknowledgements

This work was supported by National Natural Science Foundation of China (No 30472025).

Author contribution

Zhuo-wei HU directed the research; Chuan-jiang ZHU conducted the research and wrote and revised the manuscript; Qing-qing WANG, Jun-lan ZHOU, and Han-zhi LIU assisted with the experiments; Fang HUA and Hong-zheng YANG gave some technical support for the research.

References

- Gilbert KC, Brown NJ. Aldosterone and inflammation. *Curr Opin Endocrinol Diabetes Obes* 2010; 17: 199–204.
- Rocha R, Rudolph AE, Friedrich GE, Nachowiak DA, Kekec BK, Blomme EA, *et al*. Aldosterone induces a vascular inflammatory phenotype in the rat heart. *Am J Physiol Heart Circ Physiol* 2002; 283: H1802–10.
- Rocha R, Martin-Berger CL, Yang P, Scherrer R, Delyani J, McMahon E. Selective aldosterone blockade prevents angiotensin II/salt-induced vascular inflammation in the rat heart. *Endocrinology* 2002; 143: 4828–36.
- Sanz-Rosa D, Cediel E, de las Heras N, Miana M, Balfagon G, Lahera V, *et al*. Participation of aldosterone in the vascular inflammatory response of spontaneously hypertensive rats: role of the NF κ B/I κ B system. *J Hypertens* 2005; 23: 1167–72.
- Benets A, Lacolley P, Safar ME. Prevention of aortic fibrosis by spironolactone in spontaneously hypertension rats. *Arteriosclerosis* 1997; 17: 1152–6.
- Hirono Y, Yoshimoto T, Suzuki N, Sugiyama T, Sakurada M, Takai S, *et al*. Angiotensin II receptor type 1-mediated vascular oxidative stress and proinflammatory gene expression in aldosterone-induced hypertension: the possible role of local rennin-angiotensin system. *Endocrinology* 2007; 148: 1688–96.
- Jaffe IZ, Mendelsohn ME. Angiotensin II and aldosterone regulate gene transcription via functional mineralocorticoid receptors in human coronary artery smooth muscle cells. *Circ Res* 2005; 96: 643–50.
- Callera GE, Touyz RM, Tostes RC, Yogi A, He Y, Malkinson S, *et al*. Aldosterone activates vascular p38MAP kinase and NADPH oxidase via c-Src. *Hypertension* 2005; 45: 773–9.
- Callera GE, Montezano AC, Yogi A, Tostes RC, He Y, Schiffrin EL, *et al*. c-Src-dependent nongenomic signaling responses to aldosterone are increased in vascular myocytes from spontaneously hypertensive rats. *Hypertension* 2005; 46: 1032–8.
- Ishizawa K, Izawa Y, Ito H, Miki C, Miyata K, Fujita Y, *et al*. Aldosterone stimulates vascular smooth muscle cell proliferation via big mitogen-activated protein kinase 1 activation. *Hypertension* 2005; 46: 1046–52.
- Lemarié CA, Simeone SM, Nikonova A, Ebrahimian T, Deschênes ME, Coffman TM, *et al*. Aldosterone-induced activation of signaling pathways requires activity of angiotensin type 1a receptors. *Circ Res* 2009; 105: 852–9.
- Krug AW, Allenhöfer L, Monticone R, Spinetti G, Gekle M, Wang M, *et al*. Elevated mineralocorticoid receptor activity in aged rat vascular smooth muscle cells promotes a proinflammatory phenotype via extracellular signal-regulated kinase 1/2 mitogen-activated protein kinase and epidermal growth factor receptor-dependent pathways. *Hypertension* 2010; 55: 1476–83.
- Mukundan L, Milhorn DM, Matta B, Suttles J. CD40-mediated activation of vascular smooth muscle cell chemokine production through a Src-initiated, MAPK-dependent pathway. *Cell Signal* 2004; 16: 375–84.
- Kobayashi N, Yoshida K, Nakano S, Ohno T, Honda T, Tsubokou Y, *et al*. Cardioprotective mechanisms of eplerenone on cardiac performance and remodeling in failing rat hearts. *Hypertension* 2006; 47: 671–9.
- Park JB, Schiffrin EL. Cardiac and vascular fibrosis and hypertrophy in aldosterone-infused rats: role of endothelin-1. *Am J Hypertens* 2002; 15: 164–9.
- Grossmann C, Krug AW, Freudinger R, Mildenerger S, Voelker K, Gekle M. Aldosterone-induced EGFR expression: interaction between the human mineralocorticoid receptor and the human EGFR promoter. *Am J Physiol Endocrinol Metab* 2007; 292: E1790–800.
- Flamant M, Tharaux PL, Placier S, Henrion D, Coffman T, Chatziantoniou C, *et al*. Epidermal growth factor receptor trans-activation mediates the tonic and fibrogenic effects of endothelin in the aortic wall of transgenic mice. *FASEB J* 2003; 17: 327–9.
- Mazak I, Fiebeler A, Muller DN, Park JK, Shagdarsuren E, Lindschau C, *et al*. Aldosterone potentiates angiotensin II-induced signaling in vascular smooth muscle cells. *Circulation* 2004; 109: 2792–800.

Original Article

Phosphorylation of endothelial NOS contributes to simvastatin protection against myocardial no-reflow and infarction in reperfused swine hearts: partially via the PKA signaling pathway

Xiang-dong LI¹, Yue-jin YANG^{1,*}, Yong-jian GENG², Jing-lin ZHAO¹, Hai-tao ZHANG¹, Yu-tong CHENG³, Yi-ling WU⁴

¹Department of Cardiology, State Key Laboratory of Cardiovascular Disease, Fu Wai Hospital, National Center for Cardiovascular Diseases, Chinese Academy of Medical Sciences and Peking Union Medical College, Beijing 100037, China; ²The Center for Cardiovascular Biology and Atherosclerosis, Department of Internal Medicine, The University of Texas Houston Medical School, Houston, TX 77030, USA; ³Department of Cardiology, Beijing An Zhen Hospital, Capital Medical University, Beijing 100029, China; ⁴The Integration of Traditional and Western Medical Research Academy of Hebei Province, Shijiazhuang 050035, China

Aim: The cholesterol-lowering drugs statins could enhance the activities of endothelial nitric oxide synthase (eNOS) and protect myocardium during ischemia and reperfusion. The aim of this study was to examine whether protein kinase A (PKA) was involved in statin-mediated eNOS phosphorylation and cardioprotection.

Methods: 6-Month-old Chinese minipigs (20–30 kg) underwent a 1.5-h occlusion and 3-h reperfusion of the left anterior descending coronary artery (LAD). In the sham group, the LAD was encircled by a suture but not occluded. Hemodynamic and cardiac function was monitored using a polygraph. Plasma activity of creatine kinase and the tissue activities of PKA and NOS were measured spectrophotometrically. p-CREB, eNOS and p-eNOS levels were detected using Western blotting. Sizes of the area at risk, the area of no-reflow and the area of necrosis were measured morphologically.

Results: Pretreatment of the animals with simvastatin (SIM, 2 mg/kg, po) before reperfusion significantly decreased the plasma activity of creatine kinase, an index of myocardial necrosis, and reduced the no-reflow size (from 50.4%±2.4% to 36.1%±2.1%, $P<0.01$) and the infarct size (from 79.0%±2.7% to 64.1%±4.5%, $P<0.01$). SIM significantly increased the activities of PKA and constitutive NOS, and increased Ser¹³³ p-CREB protein, Ser¹¹⁷⁹ p-eNOS, and Ser⁶³⁵ p-eNOS in ischemic myocardium. Intravenous infusion of the PKA inhibitor H-89 (1 μg·kg⁻¹·min⁻¹) partially abrogated the SIM-induced cardioprotection and eNOS phosphorylation. In contrast, intravenous infusion of the eNOS inhibitor L-NNA (10 mg·kg⁻¹) completely abrogated the SIM-induced cardioprotection and eNOS phosphorylation during ischemia and reperfusion, but did not affect the activity of PKA.

Conclusion: Pretreatment with a single dose of SIM 2.5 h before reperfusion attenuates myocardial no-reflow and infarction through increasing eNOS phosphorylation at Ser¹¹⁷⁹ and Ser⁶³⁵ that was partially mediated via the PKA signaling pathway.

Keywords: heart; ischemia-reperfusion injury; no-reflow; infarction; simvastatin; H-89; L-NNA; protein kinase A; CREB; endothelial NOS

Acta Pharmacologica Sinica (2012) 33: 879–887; doi: 10.1038/aps.2012.27; published online 4 Jun 2012

Introduction

Timely reopening of the occluded coronary artery after acute myocardial infarction rescues the ischemic myocardium and reduces mortality. However, impaired regional perfusion and microvascular or endothelial dysfunction within the previously ischemic myocardium after revascularization therapy also produce the no-reflow phenomenon, which may lead

to increased infarct size, contractile dysfunction, higher incidence of complications, and poor clinical outcome^[1–4]. Prevention and treatment of the no-reflow phenomenon have been a worldwide challenge in this reperfusion times.

Statins are cholesterol-lowering drugs that inhibit 3-hydroxy-3-methylglutaryl coenzyme A reductase, a key enzyme in the cholesterol synthesis pathway. Previous studies have demonstrated that chronic and early pretreatment with statins can improve coronary circulation and reduce the sizes of no-reflow and infarct after ischemia-reperfusion injury by enhancing endothelial (e-)nitric oxide synthase (eNOS) activ-

* To whom correspondence should be addressed.

E-mail yangjfw@yahoo.com.cn

Received 2011-12-28 Accepted 2012-03-05

ity through the phosphatidylinositol 3-kinase (PI3K)/protein kinase B (Akt) signaling cascade^[4-10].

According to the European Society of Cardiology (ESC) guidelines, the optimal revascularization time is within 3 h after the onset of acute myocardial infarction^[11]. In almost all of the existing studies, statins were delivered several days before myocardial reperfusion. It is not clinically practical to pre-treat patients undergoing acute post-infarct percutaneous coronary intervention with high-dose statins several days before the procedure. In addition, recent studies have reported that the cyclic adenosine monophosphate (cAMP)/protein kinase A (PKA) pathway plays a role in cardioprotection during ischemic preconditioning and in the cardioprotection provided by Tongxinluo, a traditional Chinese medicine^[12-14], but it is unclear whether PKA is associated with the cardioprotective effects of statins. Therefore, in this study, we tested the hypothesis that acute pretreatment with single-dose statins before reperfusion exerts a cardioprotective effect against myocardial no-reflow and infarction by enhancing eNOS activity in a PKA-dependent manner.

Materials and methods

Animal experimental protocols

The animal experimental protocols and procedures were approved by the Care of Experimental Animals Committee of Fu Wai Hospital, National Center for Cardiovascular Diseases, Chinese Academy of Medical Sciences and Peking Union Medical College, China. All animals received humane care in compliance with the *Guide for the Care and Use of Laboratory Animals* published by the National Institutes of Health, USA.

As described previously^[4, 14], 6-month-old Chinese Minipigs weighing 20 to 30 kg were anesthetized with a mixture of 700 mg ketamine hydrochloride and 30 mg diazepam administered intramuscularly and were continuously infused with this mixture (2 mg/kg per hour) intravenously to maintain the anesthesia. Minipigs were assigned to 1 of 7 groups ($n=7-8$ in each group): control, simvastatin (SIM), SIM coadministered with H-89 (SIM+H-89), H-89, SIM coadministered with *N*^o-nitro-*L*-arginine (*L*-NNA; SIM+*L*-NNA), *L*-NNA, and sham group. All pigs except for the sham group underwent a 1.5-h occlusion and 3-h reperfusion of the left anterior descending coronary artery (LAD). The LAD of the sham animals was encircled by a suture but not occluded.

The control pigs underwent no intervention either before or after reperfusion. SIM (2 mg/kg, Merck & Co, USA) was gavaged 2.5 h before myocardial reperfusion; the SIM dosage was determined based on the loading dose (80 mg) before acute percutaneous coronary intervention and was converted to the pig dose according to body surface area^[15]. H-89 (1.0 $\mu\text{g}\cdot\text{kg}^{-1}\cdot\text{min}^{-1}$, Alexis, USA), a PKA inhibitor, was intravenously and constantly infused throughout the procedure to inhibit PKA activity^[13]. *L*-NNA (10 mg/kg, Aldrich, USA), an arginine derivative that can nonselectively and competitively inhibit NOS, was intravenously infused and maintained until the end of reperfusion to inhibit eNOS activity^[16]. Although *L*-NNA inhibits both constitutive (cNOS) and inducible

(iNOS), the effect of *L*-NNA inhibition on cNOS is 300 fold greater than that on iNOS, and this effect is rapidly reversible. Furthermore, the predominantly expressed isoform of cNOS in the myocardium is eNOS^[17]. Therefore, we chose to use *L*-NNA as a selective inhibitor of eNOS in the present study.

Hemodynamic and cardiac function studies

Heart rate (HR) was monitored by surface limb lead electrocardiograph. A 6F pigtail catheter was inserted into the right femoral artery through an arterial sheath for real time measurements of mean arterial pressure (MAP), left ventricular end-diastolic pressure (LVEDP), and maximum and minimum rates of left ventricular pressure development (dp/dt_{max} and dp/dt_{min} , respectively). Hemodynamic data were recorded on a polygraph (Biopac Systems, MP-150, USA) at baseline, after 1.5 h of ischemia, and after 3 h of reperfusion and analyzed with Acqknowledge v3.8.1 software.

Analysis of myocardial area at risk (AAR), area of no-reflow (ANR), and area of necrosis (AN)

Myocardial AAR, ANR, and AN were measured according to previous methods^[4, 14]. In brief, the area of impaired perfusion was delineated by a bolus of 4% fluorescent thioflavin S (1 mL/kg, Sigma, USA) into the left atrium. Approximately 30 s later, the LAD was religated at the original site, and AAR was outlined by perfusion with a bolus of 2% Evans blue dye (1 mL/kg, Sigma, USA) into the left atrium. The heart was then excised, and the blood was washed out. In ice-cold saline solution, the extra-left ventricular tissue was removed, and the left ventricular tissue was transversely cut into six or seven slices made parallel to the atrioventricular groove. The AAR, or the area unstained by Evans blue, was traced and pictured in visible light. The ANR, or the area not perfused by thioflavin S, was photographed under ultraviolet light (365 nm). The area between the AAR and ANR was the area of reflow (AR). Then, tissue samples were collected from ANR, AR, and non-ischemic area (NA) on the reverse side of the traced slices and immediately placed in liquid nitrogen for the next examination. Finally, tissue slices were weighed and incubated in 1% triphenyltetrazolium chloride (TTC, pH 7.4) at 37°C for 15 min to identify the AN. AAR was expressed as a percentage of the left ventricular mass (AAR/LV), and ANR and AN were expressed as percentages of the AAR (ANR/AAR and AN/AAR, respectively), with the mass of each area determined gravimetrically.

Determination of plasma creatine kinase (CK) activity

Plasma CK activity, an index of myocardial necrosis, was measured spectrophotometrically at baseline, after 1.5 h of ischemia, and after 3 h of reperfusion according to the manufacturer's instructions (Nanjing JianCheng Bioengineering Institute, China).

Tissue PKA activity assay

PKA activity was measured according to the method described previously using a nonradioactive PKA assay kit

(Promega, USA)^[14, 18]. Tissue samples from NA, AR, and ANR were homogenized on ice in PKA extraction buffer containing 25 mmol/L Tris-HCl (pH 7.4), 0.5 mmol/L EDTA, 0.5 mmol/L EGTA, 10 mmol/L β -mercaptoethanol, 1 μ g/mL leupeptin, and 1 μ g/mL aprotinin. The homogenate was centrifuged at 20000 \times g for 5 min at 4°C, and the supernatant was assayed for PKA activity according to the manufacturer's instructions. The reaction products were separated on a 0.8% agarose gel at 100 V for 15 min. The phosphorylated species migrated toward the positive electrode, whereas the non-phosphorylated substrates migrated toward the negative electrode. The fluorescence intensity of the phosphorylated peptides, which reflects the PKA activity, was quantified by spectrophotometry at 570 nm. One unit of kinase activity is defined as the number of nanomoles of phosphate transferred to a substrate per minute per milliliter.

Western blotting analysis

The expression of Ser¹³³ phosphorylated (p-cAMP) response element-binding protein (CREB), eNOS, Ser¹¹⁷⁹ p-eNOS and Ser⁶³⁵ p-eNOS was detected by Western blotting, as described previously^[19]. Rabbit polyclonal p-CREB (Ser¹³³; 1:100 dilution, Santa Cruz, USA), rabbit polyclonal eNOS (1:250 dilution, Cell Signaling, USA), rabbit monoclonal p-eNOS (Ser¹¹⁷⁹; 1:250 dilution, Invitrogen, USA), rabbit polyclonal p-eNOS (Ser⁶³⁵; 1:200 dilution, Upstate, USA), or mouse monoclonal β -actin (1:10000 dilution, Proteintech, USA) antibodies were applied. The immunoreactive bands were visualized using a chemiluminescence reagent. The intensity ratio of the target band to the β -actin band corresponded to the relative amounts of the target protein.

Analysis of tissue NOS activity

Tissue samples from NA, AR, and ANR were homogenized and centrifuged at 3000 r/min for 10 min. The activity of total (t)-NOS, iNOS, and cNOS (the predominantly expressed isoform of cNOS in myocardium is eNOS^[17]) in the supernatant was measured spectrophotometrically at 530 nm according to the manufacturer's instructions (Nanjing KeyGen, China). The activities were expressed as units per milligram of myocardial protein (IU/mg prot).

Statistical analysis

All data are expressed as the mean \pm SEM. Data from all stages were compared by repeated measures analysis of variance followed by *post-hoc* analysis with the Student-Newman-Keuls multiple comparisons test. Differences in a single variable data, such as the no-reflow and infarct areas, and the activities of PKA and NOS were compared among groups by ANOVA followed by the Duncan's *post hoc* test. $P < 0.05$ was considered statistically significant.

Results

Cardiac performance in SIM-treated and -untreated hearts

Physiological examination revealed that there were no significant differences in cardiac hemodynamics between any of the

groups at baseline ($P > 0.05$). However, under the conditions of ischemia and reperfusion, HR and LVEDP were increased in the untreated, control hearts ($P < 0.05$). The effects of ischemia and reperfusion were partially diminished when the animals received SIM pretreatment, as HR and LVEDP were decreased in the SIM group ($P < 0.05$). The effects of SIM appeared to depend on the activation of PKA and eNOS because combined treatment with SIM and the PKA inhibitor H-89 or the eNOS inhibitor L-NNA did not have the same effect as treatment with SIM alone (Table 1).

Sizes of no-reflow and infarction after ischemia and reperfusion

Pathological studies revealed that the area at risk (AAR) per left ventricle (LV) was comparable in the control, SIM, SIM+H-89, H-89, SIM+L-NNA, and L-NNA groups, averaging between 26.1% and 30.4% ($P > 0.05$) (Figure 1A and 1B). SIM pretreatment significantly attenuated the area of no-reflow (ANR/AAR, 36.1% \pm 2.1%) and the area of necrosis (AN/AAR, 64.1% \pm 4.5%) compared to the control group (50.4% \pm 2.4%; 79.0% \pm 2.7%) ($P < 0.01$). The PKA inhibitor H-89 alone reduced the no-reflow size (29.5% \pm 4.2%) relative to the control group ($P < 0.01$), but it partially abolished the SIM effect on no-reflow size and completely abolished the SIM effect on infarct size, indicated by the increased no-reflow (40.4% \pm 6.1%) and infarct (77.4% \pm 1.2%) sizes, respectively, in the SIM+H-89 group. However, the eNOS inhibitor L-NNA completely counteracted the effects of SIM on myocardial no-reflow and infarction; the no-reflow and infarction sizes in the SIM+L-NNA group reverted to the control levels (52.3% \pm 2.8%; 83.9% \pm 2.5%) ($P < 0.01$). These data indicate that the cardioprotective effects of SIM against no-reflow and infarction are completely eNOS-dependent but partially PKA-dependent.

After 1.5 h of ischemia and 3 h of reperfusion, plasma CK activity, a standard enzymatic marker of cardiac injury, was significantly increased in the control group (2.97 \pm 0.45 IU/mL; 4.73 \pm 0.14 IU/mL) compared to the sham group (1.05 \pm 0.09 IU/mL; 1.59 \pm 0.25 IU/mL) ($P < 0.01$) but was lowered in the SIM group (1.66 \pm 0.13 IU/mL; 3.53 \pm 0.29 IU/mL) compared to the control group ($P < 0.01$). However, the addition of H-89 inhibited the SIM effect after 3 h of reperfusion, and L-NNA inhibited the SIM effect after 1.5 h of ischemia and 3 h of reperfusion (Figure 1C).

Myocardial PKA activity in the reflow and no-reflow areas after ischemia and reperfusion

Figure 2A shows that the PKA activity was dramatically induced in the reflow and no-reflow areas in the control group (9.57 \pm 0.56 IU/mL; 12.18 \pm 0.88 IU/mL) compared with that in the sham group (6.04 \pm 0.62 IU/mL) ($P < 0.01$). Myocardial PKA activity in the reflow and no-reflow areas were further activated in the SIM group (12.24 \pm 0.76 IU/mL; 14.47 \pm 0.44 IU/mL) compared to that in the control group ($P < 0.05$). However, SIM-induced PKA activity was inhibited by H-89 but not by L-NNA.

To evaluate the inhibition effect of H-89 on the PKA signaling pathway, Western blotting analysis was performed to

Table 1. Hemodynamic data at baseline, at the end of ischemia, and after reperfusion. Mean±SEM. *n*=7–8 animals/group. ^b*P*<0.05 vs Sham. ^e*P*<0.05 vs Control. ^h*P*<0.05 vs SIM at the same time point.

	HR (beats/min)	MAP (mmHg)	RPP (mmHgbeats/min)	LVEDP (mmHg)	dp/dt _{max} (mmHg/s)	dp/dt _{min} (mmHg/s)
Baseline						
Sham group	95.4±4.4	87.8±7.5	8411.8±900.6	3.2±0.7	1689.8±220.1	-1309.7±225.5
Control group	102.6±10.3	84.6±10.2	8308.7±1023.1	4.6±1.1	1966.2±168	-1574.1±121.8
SIM group	101.9±8.4	93.5±7.6	9135.5±458.9	4.9±1.1	1857.1±183.4	-1581.8±242.0
SIM+H-89 group	112.7±6.4	89.6±4.5	9973.1±475.9	3.9±0.6	2083.4±186.9	-1434.1±123.9
H-89 group	112.9±6.9	76.1±7.4	8621.4±1028.7	5.1±1.1	1844.9±160.1	-1309.4±192.7
SIM+L-NNA group	95.4±8	99.1±8.5	9371.7±1081.9	6±0.3	1569.3±192.5	-1512.2±205.4
L-NNA group	93.5±5.5	102.2±6.9	9438.9±630.6	5.4±0.5	1928.8±157.2	-1832.2±165.6
Ischemia 90 min						
Sham group	89.4±7.7	74.7±5.2	6619.0±726.2	3.6±0.7	1820.7±198.0	-503.1±397.1
Control group	126.0±6.2 ^b	66.1±7.9	8544.7±1354.0	11.3±3.5 ^b	1549.4±137.7	-876.7±108.2
SIM group	85.6±13.8 ^e	65.0±2.9	6808.0±968.2	6.7±1.5	1737.8±129.0	-1096.7±96.9
SIM+H-89 group	90.3±11.6	61.5±3.2	4220.0±301.5 ^h	9.8±2.8	1164.4±99.8 ^h	-713.9±107.1
H-89 group	89.8±7.3 ^e	70.8±6.1	6585.0±1003.5	7.5±1.3	1389.5±91.2	-805.2±87.0
SIM+L-NNA group	100.3±3.2	97.1±5.4 ^h	9754.1±666.8 ^h	8.3±1.3	1262.6±171.7 ^h	-880.4±193
L-NNA group	103.6±4.4	98.4±7.3 ^e	9208.9±777.8	10±1.7	1733.1±89.5	-844.9±74.1
Reperfusion 180 min						
Sham group	69.4±4.9	75.4±4.3	5215.7±462	4.0±1.0	1650.3±231.7	-846.7±105.5
Control group	80.2±7.8	67.0±9.0	5354.3±966.4	12.8±2.6 ^b	1236.2±139.6	-691.9±70.5
SIM group	80.3±7.1	76.0±4.6	6131.6±774.2	6.8±1.4 ^e	1718.7±250.0	-949.1±112.7
SIM+H-89 group	95.8±11.9	59.0±5.8 ^h	5661.8±859.8	7.7±1.6	1397.7±183.6	-786.7±70.1
H-89 group	84.3±3.4	70.4±3.8	5963.3±442.9	6.9±1.3 ^e	1385.2±245.3	-790.3±192.6
SIM+L-NNA group	79.4±5.3	79.3±6.4	6338.2±660.8	8.8±0.9	1013.6±111.9 ^h	-684.2±57.2
L-NNA group	85.8±5.7	82.1±5.3	6334±834.5	6.2±1.2 ^e	1265.9±146.6	-886.7±205.1

Abbreviations: SIM=simvastatin; L-NNA=N^o-nitro-L-arginine; HR=heart rate; MAP=mean arterial pressure; RPP=rate-pressure product; LVEDP=left ventricular end-diastolic pressure; dp/dt_{max} and dp/dt_{min}=maximum and minimum rates of left ventricular pressure development, respectively.

detect the expression of Ser¹³³ p-CREB, which acts downstream of PKA and is thus an indicator of PKA activity^[13] (Figure 2B, 2C, and 2D). In the non-ischemic area (Figure 2B), the expression of Ser¹³³ p-CREB was reduced in the SIM and H-89 groups compared to the control group (*P*<0.05). In the reflow and no-reflow myocardium (Figure 2C and 2D), Ser¹³³ p-CREB was up-regulated in the control group compared to the sham group (*P*<0.05) and was further activated in the SIM group compared to the control group (*P*<0.05). The induction effect of SIM on Ser¹³³ p-CREB expression was abolished by H-89 but not by L-NNA (*P*<0.05). These data suggest that the PKA pathway was activated during ischemia and reperfusion and was further stimulated by SIM pretreatment.

Myocardial NOS activities in the reflow and no-reflow areas after ischemia and reperfusion

In the non-ischemic area (Figure 3A), cNOS activity was increased in the control group (0.68±0.15 IU/mg prot) relative to the sham group (0.26±0.08 IU/mg prot) (*P*<0.01). In the reflow and no-reflow areas (Figure 3B and 3C), tNOS activity was decreased in the SIM+H-89 (0.63±0.09 IU/mg prot; 0.59±0.05 IU/mg prot) and SIM+L-NNA (0.73±0.06

IU/mg prot; 0.73±0.05 IU/mg prot) groups relative to the SIM group (0.97±0.13 IU/mg prot; 0.94±0.06 IU/mg prot) (*P*<0.05); iNOS activity was decreased in the control group (0.37±0.08 IU/mg prot; 0.32±0.09 IU/mg prot) relative to the sham group (0.76±0.11 IU/mg prot) (*P*<0.01); and cNOS activity was increased in the SIM group (0.67±0.15 IU/mg prot; 0.6±0.08 IU/mg prot) relative to the control group (0.4±0.11 IU/mg prot; 0.41±0.08 IU/mg prot) (*P*<0.05) but decreased in the SIM+H-89 (0.3±0.08 IU/mg prot; 0.31±0.07 IU/mg prot) and SIM+L-NNA (0.28±0.07 IU/mg prot; 0.2±0.04 IU/mg prot) groups compared to the SIM group (*P*<0.01).

To investigate the mechanism by which PKA mediates eNOS activity, the expression of eNOS and p-eNOS (Ser¹¹⁷⁹ and Ser⁶³⁵) was detected by Western blotting analysis (Figure 2B, 2C, and 2D). In the non-ischemic area (Figure 2B), the expression of eNOS and Ser⁶³⁵ p-eNOS was increased in the control group compared to that in the sham group (*P*<0.05); the eNOS expression in the SIM and SIM+H-89 groups was decreased, and the Ser⁶³⁵ p-eNOS expression in the H-89 group was increased, compared to that of the control group (*P*<0.05). In the reflow area (Figure 2C), the expression of eNOS and Ser⁶³⁵ p-eNOS was increased in the control group

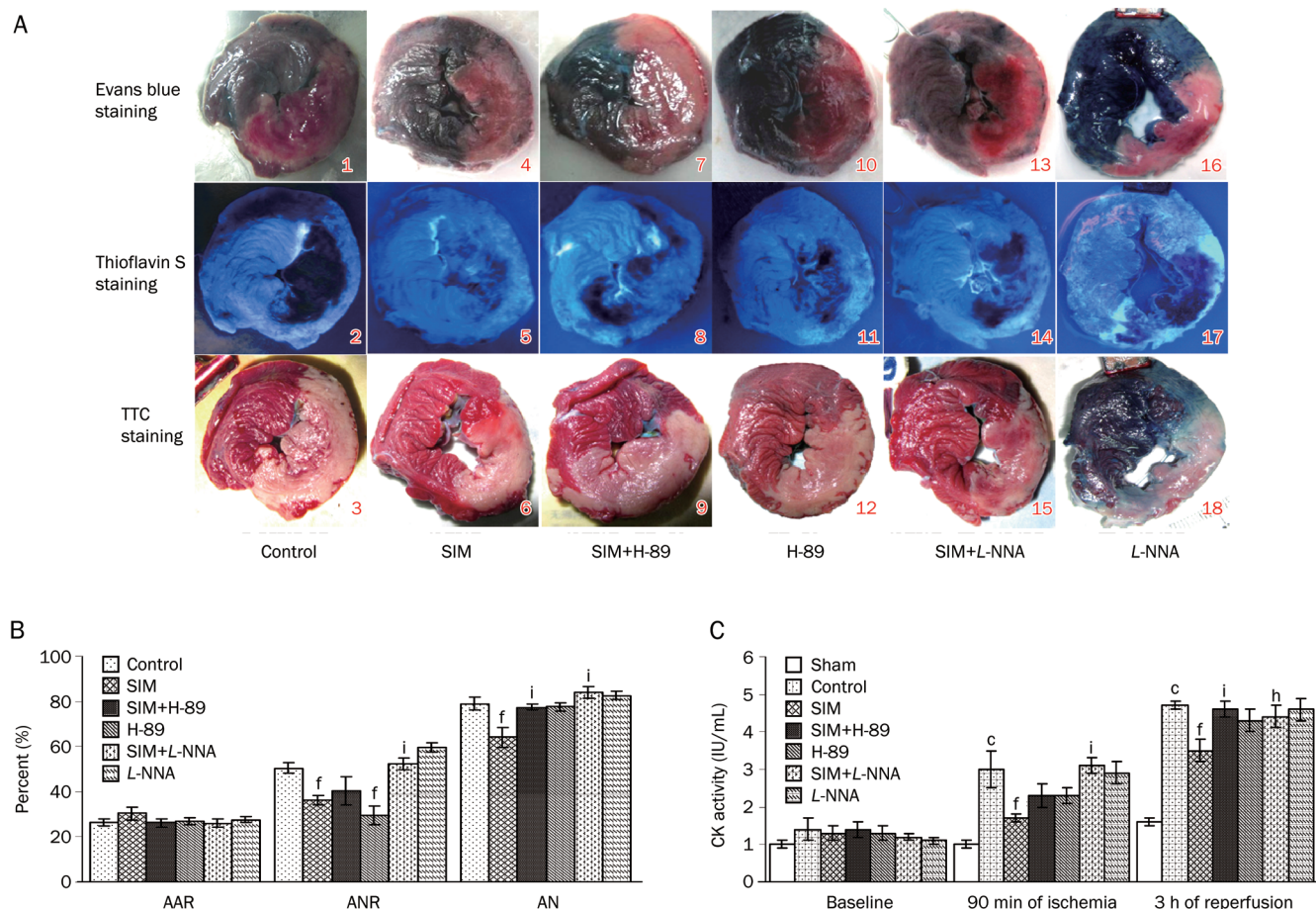


Figure 1. Sizes of area at risk (AAR), area of no-reflow (ANR), and area of necrosis (AN). (A) A representative series of images of the ischemia, no-reflow, and infarction areas at the level of the left ventricle papillary muscle. In the upper panels, the myocardium unstained by Evans blue dye represents AAR. In the middle slices, thioflavin S fluorescent dye negatively stained myocardium indicates the no-reflow area. In the bottom slices, the triphenyltetrazolium chloride (TTC)-unstained white myocardium was identified as the infarct zone. Simvastatin (SIM) pretreatment (4 to 6) decreased the areas of no-reflow and necrosis compared with the control (1 to 3), SIM+H-89 (7 to 9), and SIM+L-NNA (13 to 15) groups. (B) AAR expressed as a percentage of left ventricular mass; ANR and AN expressed as percentages of AAR. SIM significantly reduced the sizes of ANR and AN compared with the control, but these effects disappeared when SIM was coadministered with H-89 or L-NNA. (C) Plasma CK activity assays revealed that SIM eliminated the ischemia-reperfusion-induced elevation of the plasma CK activity after 1.5 h of ischemia and 3 h of reperfusion, while H-89 and L-NNA diminished the effect of SIM treatment. Mean \pm SEM. $n=7-8$ animals/group. ^c $P<0.01$ vs Sham. ^f $P<0.01$ vs Control. ⁱ $P<0.05$, ^h $P<0.01$ vs SIM at the same time point.

compared with that in the sham group ($P<0.05$); the Ser¹¹⁷⁹ p-eNOS and Ser⁶³⁵ p-eNOS phosphorylation was increased in the SIM group compared to that in the control group ($P<0.05$); H-89 suppressed the induction effect of SIM on Ser⁶³⁵ p-eNOS ($P<0.05$), and L-NNA suppressed the induction effect of SIM on both Ser¹¹⁷⁹ p-eNOS and Ser⁶³⁵ p-eNOS ($P<0.05$). In the no-reflow area (Figure 2D), Ser¹¹⁷⁹ p-eNOS phosphorylation was higher in the control group than in the sham group ($P<0.05$). The level of Ser⁶³⁵ p-eNOS was increased in the SIM and H-89 groups compared to that of the control group ($P<0.05$), whereas the levels of Ser¹¹⁷⁹ p-eNOS and Ser⁶³⁵ p-eNOS were decreased in the SIM+L-NNA group ($P<0.05$).

Discussion

The main findings of our study include the following: first, a

single-dose SIM pretreatment just 2.5 hours before reperfusion reduced the sizes of the no-reflow and necrosis areas and activated the PKA pathway and the phosphorylation of eNOS at Ser⁶³⁵ and Ser¹¹⁷⁹ in the reflow and no-reflow myocardium. Second, the PKA inhibitor H-89 blocked the SIM-induced PKA activation and partially abolished the SIM-induced cardioprotection and eNOS phosphorylation, whereas the eNOS inhibitor L-NNA completely blocked the SIM-induced cardioprotection and eNOS phosphorylation without any influence on PKA activity, indicating that the cardioprotection of SIM after ischemia and reperfusion is in part mediated by the PKA/eNOS pathway.

Previous studies have reported that a 3-day pretreatment with atorvastatin or SIM at 10 mg/kg per day decreased the infarct size in rat hearts, but this effect was not observed at

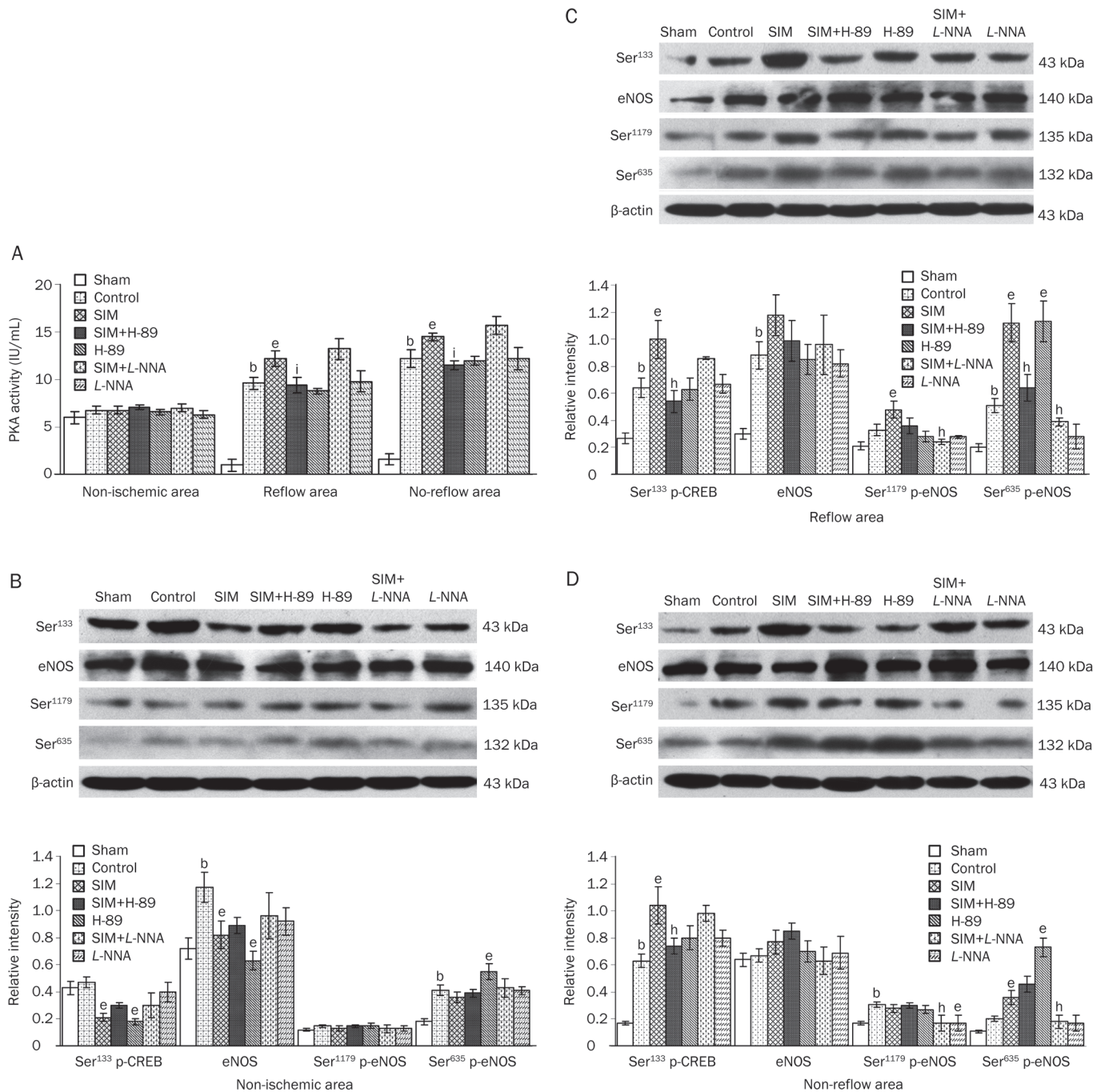


Figure 2. Myocardial PKA activity and the expression of Ser¹³³ p-CREB, eNOS and p-eNOS (Ser¹¹⁷⁹ and Ser⁶³⁵) after ischemia and reperfusion. (A) Myocardial PKA activities in the reflow and no-reflow areas were stimulated by ischemia and reperfusion and were further increased by SIM pretreatment. However, the SIM-induced activation of PKA was silenced by H-89 but not by L-NNA. (B) In the non-ischemic area, the expression of eNOS and Ser⁶³⁵ p-eNOS was increased in the control group, and the expression of Ser¹³³ p-CREB and eNOS was decreased in the SIM and H-89 groups. (C) In the reflow area, the expression of Ser¹³³ p-CREB, eNOS, and Ser⁶³⁵ p-eNOS was stimulated by ischemia and reperfusion. SIM promoted the phosphorylation of Ser¹³³ p-CREB, Ser¹¹⁷⁹ p-eNOS, and Ser⁶³⁵ p-eNOS. However, H-89 counteracted the effects of SIM on Ser¹³³ p-CREB and Ser⁶³⁵ p-eNOS, and L-NNA canceled the effects of SIM on Ser¹¹⁷⁹ p-eNOS and Ser⁶³⁵ p-eNOS. (D) In the no-reflow area, ischemia and reperfusion induced the phosphorylation of Ser¹³³ p-CREB and Ser¹¹⁷⁹ p-eNOS. SIM pretreatment increased the phosphorylation of Ser¹³³ p-CREB and Ser⁶³⁵ p-eNOS. H-89 blocked the effect of SIM on Ser¹³³ p-CREB, and L-NNA inhibited the SIM effects on Ser¹¹⁷⁹ p-eNOS and Ser⁶³⁵ p-eNOS. Mean±SEM. *n*=7–8 animals/group. ^b*P*<0.05 vs Sham. ^e*P*<0.05 vs Control. ^h*P*<0.05, ⁱ*P*<0.01 vs SIM at the same time point.

2 mg/kg^[4, 6, 20, 21]. Similarly, acute pretreatment with high-dose SIM (10 μmol/L) was shown to attenuate the ischemia-

reperfusion injury in isolated rat hearts, but chronic treatment of low-dose SIM did not^[22]. These data suggest that chronic

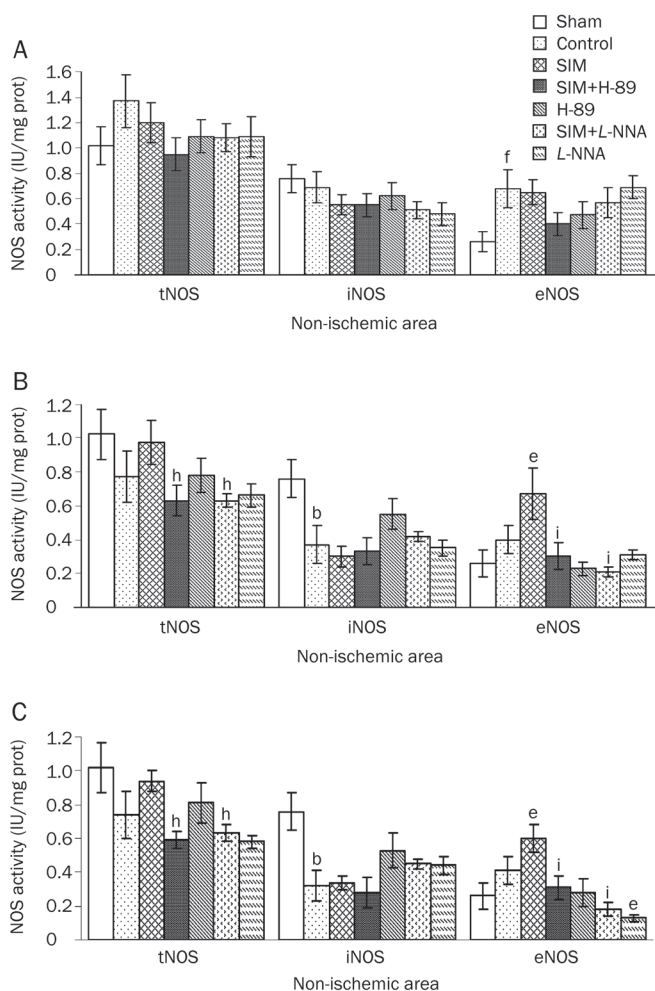


Figure 3. Myocardial NOS activity in the injured and uninjured myocardium after ischemia and reperfusion. (A) After ischemia and reperfusion, myocardial constitutive (cNOS) activities were increased in the non-ischemic area in the control group. (B and C) In the reflow and no-reflow myocardium, inducible (iNOS) activity was suppressed in the control group. SIM pretreatment significantly stimulated cNOS activity, but this effect was abolished by cotreatment with H-89 or L-NNA. Abbreviation: tNOS=total nitric oxide synthase. Mean±SEM. $n=7-8$ animals/group. ^b $P<0.05$ vs Sham. ^e $P<0.05$, ^f $P<0.01$ vs Control. ^h $P<0.05$, ⁱ $P<0.01$ vs SIM at the same time point.

or acute pretreatment with high-dose statins can attenuate infarct size after ischemic reperfusion. The effect of SIM on infarct size in this study is consistent with that found in previous studies because 2 mg/kg of SIM in pigs is approximately equivalent to 10 mg/kg in rats, after correction for body surface area^[15]. The infarct-limitation effect of statins in ischemia-reperfusion is mainly attributed to its pleiotropic effects via the PI3K/Akt/eNOS pathway because the effects of the statins can be abolished by inhibiting PI3K or eNOS^[5-9]. In this study, we further found that acute pretreatment with single-dose SIM not only decreased the infarct size but also attenuated the no-reflow area, and we showed that the PKA pathway was another important mediator in the cardioprotection of SIM

that acts by modulating the phosphorylation of eNOS at Ser¹¹⁷⁹ and Ser⁶³⁵.

PKA seems to be activated by endogenous mechanisms because the PKA inhibitor H89 alone had almost the same effect as SIM on the no-reflow area in the presence of ischemia. The mechanism underlying the idiopathic activation of PKA is considered to be that the decreased level of cyclic guanosine monophosphate (cGMP) inhibits the activity of phosphodiesterase III upon reperfusion, which in turn increases the cAMP concentration, subsequently leading to PKA activation^[23]. The inhibition of PKA activity and Ser¹³³ p-CREB by H-89 indicates that acute SIM treatment actually results in PKA activation. Although it is presently unclear how statins activate PKA in ischemic myocardium, one probable explanation is that statins may stimulate a cell surface receptor that activates small G proteins, which results in the sensitization of adenylate cyclase and the accumulation of myocardial cAMP^[24] and eventually the activation of PKA in the ischemic myocardium. It has been reported that 5'-nucleotidase and the adenosine A₁, A_{2A}, and A_{2B} receptors are involved in atorvastatin-induced eNOS phosphorylation by stimulating phospholipase A₂ and cyclooxygenase (COX) to generate prostacyclin-2 (PGI₂), leading to PKA activation and subsequent eNOS phosphorylation^[5, 25].

Enhancing Ser^{1177/1179} phosphorylation via the PI3K/Akt pathway is considered to be the main mechanism by which statins protect against ischemia-reperfusion injury^[5-9]. However, several lines of evidence have shown that PKA also regulates the phosphorylation of eNOS at Ser¹¹⁷⁹, Ser⁶³⁵, and Ser⁶¹⁷ in bovine eNOS (Ser¹¹⁷⁷, Ser⁶³³, and Ser⁶¹⁵ in humans)^[24, 26-29]. Ser^{633/635} phosphorylation is critical in maintaining NO synthesis after the initial sensitization by Ca²⁺ flux and Ser^{1177/1179} phosphorylation^[30], and it is stimulated via the PKA pathway in response to shear stress and acute statin treatment in aortic endothelial cells^[24, 27], suggesting that PKA-mediated Ser^{633/635} phosphorylation may be another mechanism by which statins protect against myocardial no-reflow and necrosis after ischemia and reperfusion. Our study confirmed this hypothesis in reperfused swine hearts, demonstrating that the inhibition of PKA partially blocked the SIM-induced phosphorylation of eNOS at Ser¹¹⁷⁹ and Ser⁶³⁵ in the reflow and no-reflow myocardium, as well as partially abrogated the effects of SIM against myocardial no-reflow and infarction. Previous studies have reported that statin-induced eNOS activation involves the inhibition of the Rho GTPase and the modulation of Rho A membrane translocation^[31, 32] and that the transient preischemic activation of PKA by ischemic preconditioning reduces infarct size through Rho and Rho-kinase (ROCK) inhibition during sustained ischemia^[13]. Therefore, it is plausible that PKA-Rho pathway is involved in the regulation of eNOS activity by statins, but the specific mechanism should be studied further.

Here, H-89 administered 30 min before ischemia attenuated the no-reflow area, possibly by phosphorylating eNOS at Ser⁶³⁵, but partly inhibited the protective effects of SIM when infused 30 min after SIM administration. This finding

is somewhat contradictory to previous studies. In isolated rat hearts, H-89 (2 $\mu\text{mol/L}$) improved postischemic function and decreased infarct size when injected 3 min before 30 min of global ischemia-reperfusion and further reduced the infarct size when administered 3 min prior to ischemic or forskolin (a cAMP-elevating agents) preconditioning^[33]. However, when delivered at 1.35 $\mu\text{g/kg}$ per minute in dogs or at 10 $\mu\text{mol/L}$ in isolated rat hearts approximately 30 min before preconditioning, H-89 completely blunted the infarct-limitation effect of preconditioning^[12, 34]. Therefore, the partial inhibition of H-89 on SIM cardioprotection in our study most likely occurred because H-89 was delivered later than SIM, and the contradiction between these studies might be explained by the differences in H-89 dosage, experimental protocols, and animal species.

Another mechanism underlying the bidirectional role of H-89 in ischemia and reperfusion may be the cross-talk between the PKA and PI3K/Akt pathways in the regulation of eNOS phosphorylation. It has been reported that H-89 inhibits Akt, ROCK II, and 5'-AMP-activated protein kinase (AMPK)^[35] and that the PKA pathway interacts with the PI3K/Akt pathway in the regulation of gene expression^[36]. Previous studies have shown that the forskolin-induced stimulation of PKA can inhibit Akt activity in human embryonic kidney cells^[37], but epinephrine or forskolin-induced stimulation of PKA enhanced eNOS phosphorylation at Ser¹¹⁷⁷ by activating the Akt pathway in aortic or coronary endothelial cells^[28, 38]. Interestingly, in endothelial cells, PKA is mainly involved in eNOS phosphorylation during the early phase of preconditioning, whereas both PKA and Akt are required for late preconditioning-induced eNOS activation, and Akt is a substrate of PKA^[39]. Therefore, these reports indicate that PKA plays different roles in regulating eNOS phosphorylation in different cells and that cross-talk most likely exists between the PKA and PI3K/Akt pathways in the regulation of eNOS phosphorylation during ischemia and reperfusion. The inhibition of PKA may in turn cause the activation of the PI3K/Akt pathway and the subsequent phosphorylation of Ser⁶³⁵ p-eNOS. This might be another explanation of why H-89 partially inhibited SIM-induced cardioprotection in our study; the exact mechanism may be elucidated in the future when more selective PKA inhibitors are available.

In summary, the present study suggests that acute pretreatment with a single dose of SIM just 2.5 h before reperfusion can attenuate the size of the no-reflow and infarction areas by phosphorylating eNOS at Ser¹¹⁷⁹ and Ser⁶³⁵ in a partially PKA-dependent manner. The observation that H-89 partially abolished the cardioprotective effects of SIM and decreased the no-reflow size when administered alone suggests a bidirectional role for PKA in cardioprotection during ischemia and reperfusion. Our results are helpful for understanding the mechanisms involved in statin-mediated protection against myocardial no-reflow and infarction, and may lead to the development of new criteria for treating patients undergoing acute post-infarct percutaneous coronary intervention.

Acknowledgements

This study was supported by the National Basic Research Program (973 Program) of China (No 2012CB518602 and 2011CB503901).

Author contribution

Yue-jin YANG, Xiang-dong LI, and Yi-ling WU designed research; Xiang-dong LI, Jing-lin ZHAO, Hai-tao ZHANG, and Yu-tong CHENG performed research and analyzed data; Xiang-dong LI and Yong-jian GENG wrote the paper.

References

- 1 Ito H, Maruyama A, Iwakura K, Takiuchi S, Masuyama T, Hori M, *et al*. Clinical implications of the 'no reflow' phenomenon. A predictor of complications and left ventricular remodeling in reperfused anterior wall myocardial infarction. *Circulation* 1996; 93: 223–8.
- 2 Stone GW, Peterson MA, Lansky AJ, Dangas G, Mehran R, Leon MB. Impact of normalized myocardial perfusion after successful angioplasty in acute myocardial infarction. *J Am Coll Cardiol* 2002; 39: 591–7.
- 3 Resnic FS, Wainstein M, Lee MK, Behrendt D, Wainstein RV, Ohno-Machado L, *et al*. No-reflow is an independent predictor of death and myocardial infarction after percutaneous coronary intervention. *Am Heart J* 2003; 145: 42–46.
- 4 Zhao JL, Yang YJ, Cui CJ, You SJ, Gao RL. Pretreatment with simvastatin reduces myocardial no-reflow by opening mitochondrial K(ATP) channel. *Br J Pharmacol* 2006; 149: 243–9.
- 5 Merla R, Ye Y, Lin Y, Manickavasagam S, Huang MH, Perez-Polo RJ, *et al*. The central role of adenosine in statin-induced ERK1/2, Akt, and eNOS phosphorylation. *Am J Physiol Heart Circ Physiol* 2007; 293: H1918–28.
- 6 Manickavasagam S, Ye Y, Lin Y, Perez-Polo RJ, Huang MH, Lui CY, *et al*. The cardioprotective effect of a statin and cilostazol combination: relationship to Akt and endothelial nitric oxide synthase activation. *Cardiovasc Drugs Ther* 2007; 21: 321–30.
- 7 Iwakura K, Ito H, Kawano S, Okamura A, Kurotobi T, Date M, *et al*. Chronic pre-treatment of statins is associated with the reduction of the no-reflow phenomenon in the patients with reperfused acute myocardial infarction. *Eur Heart J* 2006; 27: 534–9.
- 8 Efthymiou CA, Mocanu MM, Yellon DM. Atorvastatin and myocardial reperfusion injury: new pleiotropic effect implicating multiple prosurvival signaling. *J Cardiovasc Pharmacol* 2005; 45: 247–52.
- 9 Birnbaum Y, Ye Y, Rosanio S, Tavackoli S, Hu ZY, Schwarz ER, *et al*. Prostaglandins mediate the cardioprotective effects of atorvastatin against ischemia-reperfusion injury. *Cardiovasc Res* 2005; 65: 345–55.
- 10 Heusch G, Kleinbongard P, Bose D, Levkau B, Haude M, Schulz R, *et al*. Coronary microembolization: from bedside to bench and back to bedside. *Circulation* 2009; 120: 1822–36.
- 11 Van de Werf F, Bax J, Betriu A, Blomstrom-Lundqvist C, Crea F, Falk V, *et al*. Management of acute myocardial infarction in patients presenting with persistent ST-segment elevation: the Task Force on the Management of ST-Segment Elevation Acute Myocardial Infarction of the European Society of Cardiology. *Eur Heart J* 2008; 29: 2909–45.
- 12 Inserte J, Garcia-Dorado D, Ruiz-Meana M, Agullo L, Pina P, Soler-Soler J. Ischemic preconditioning attenuates calpain-mediated degradation of structural proteins through a protein kinase A-dependent mechanism. *Cardiovasc Res* 2004; 64: 105–14.

- 13 Sanada S, Asanuma H, Tsukamoto O, Minamino T, Node K, Takashima S, *et al*. Protein kinase A as another mediator of ischemic preconditioning independent of protein kinase C. *Circulation* 2004; 110: 51–7.
- 14 Li XD, Yang YJ, Geng YJ, Jin C, Hu FH, Zhao JL, *et al*. Tongxinluo reduces myocardial no-reflow and ischemia-reperfusion injury by stimulating the phosphorylation of eNOS via the PKA pathway. *Am J Physiol Heart Circ Physiol* 2010; 299: H1255–61.
- 15 Freireich EJ, Gehan EA, Rall DP, Schmidt LH, Skipper HE. Quantitative comparison of toxicity of anticancer agents in mouse, rat, hamster, dog, monkey, and man. *Cancer Chemother Rep* 1966; 50: 219–44.
- 16 Cheng YT, Yang YJ, Zhang HT, Qian HY, Zhao JL, Meng XM, *et al*. Pretreatment with Tongxinluo protects porcine myocardium from ischaemia/reperfusion injury through a nitric oxide related mechanism. *Chin Med J(Engl)* 2009; 122: 1529–38.
- 17 Brahmajothi MV, Campbell DL. Heterogeneous basal expression of nitric oxide synthase and superoxide dismutase isoforms in mammalian heart: implications for mechanisms governing indirect and direct nitric oxide-related effects. *Circ Res* 1999; 85: 575–87.
- 18 Wu ZQ, Li M, Chen J, Chi ZQ, Liu JG. Involvement of cAMP/cAMP-dependent protein kinase signaling pathway in regulation of Na⁺,K⁺-ATPase upon activation of opioid receptors by morphine. *Mol Pharmacol* 2006; 69: 866–76.
- 19 Robinet A, Hoizey G, Millart H. PI3-kinase, protein kinase C, and protein kinase A are involved in the trigger phase of beta1-adrenergic preconditioning. *Cardiovasc Res* 2005; 66: 530–42.
- 20 Ye Y, Lin Y, Perez-Polo R, Huang MH, Hughes MG, McAdoo DJ, *et al*. Enhanced cardioprotection against ischemia-reperfusion injury with a dipyridamole and low-dose atorvastatin combination. *Am J Physiol Heart Circ Physiol* 2007; 293: H813–8.
- 21 Birnbaum Y, Lin Y, Ye Y, Merla R, Perez-Polo JR, Uretsky BF. Pretreatment with high-dose statin, but not low-dose statin, ezetimibe, or the combination of low-dose statin and ezetimibe, limits infarct size in the rat. *J Cardiovasc Pharmacol Ther* 2008; 13: 72–9.
- 22 Szarszoi O, Maly J, Ostadal P, Netuka I, Besik J, Kolar F, *et al*. Effect of acute and chronic simvastatin treatment on post-ischemic contractile dysfunction in isolated rat heart. *Physiol Res* 2008; 57: 793–6.
- 23 Schulz R, Kelm M, Heusch G. Nitric oxide in myocardial ischemia/reperfusion injury. *Cardiovasc Res* 2004; 61: 402–13.
- 24 Harris MB, Blackstone MA, Sood SG, Li C, Goolsby JM, Venema VJ, *et al*. Acute activation and phosphorylation of endothelial nitric oxide synthase by HMG-CoA reductase inhibitors. *Am J Physiol Heart Circ Physiol* 2004; 287: H560–6.
- 25 Ray CJ, Marshall JM. The cellular mechanisms by which adenosine evokes release of nitric oxide from rat aortic endothelium. *J Physiol* 2006; 570: 85–96.
- 26 Boo YC, Sorescu G, Boyd N, Shiojima I, Walsh K, Du J, *et al*. Shear stress stimulates phosphorylation of endothelial nitric-oxide synthase at Ser1179 by Akt-independent mechanisms: role of protein kinase A. *J Biol Chem* 2002; 277: 3388–96.
- 27 Boo YC, Hwang J, Sykes M, Michell BJ, Kemp BE, Lum H, Jo H. Shear stress stimulates phosphorylation of eNOS at Ser(635) by a protein kinase A-dependent mechanism. *Am J Physiol Heart Circ Physiol* 2002; 283: H1819–28.
- 28 Zhang XP, Hintze TH. cAMP signal transduction induces eNOS activation by promoting PKB phosphorylation. *Am J Physiol Heart Circ Physiol* 2006; 290: H2376–84.
- 29 Michell BJ, Harris MB, Chen ZP, Ju H, Venema VJ, Blackstone MA, *et al*. Identification of regulatory sites of phosphorylation of the bovine endothelial nitric-oxide synthase at serine 617 and serine 635. *J Biol Chem* 2002; 277: 42344–51.
- 30 Mount PF, Kemp BE, Power DA. Regulation of endothelial and myocardial NO synthesis by multi-site eNOS phosphorylation. *J Mol Cell Cardiol* 2007; 42: 271–9.
- 31 Rikitake Y, Liao JK. Rho GTPases, statins, and nitric oxide. *Circ Res* 2005; 97: 1232–5.
- 32 Bulhak A, Roy J, Hedin U, Sjoquist PO, Pernow J. Cardioprotective effect of rosuvastatin *in vivo* is dependent on inhibition of geranylgeranyl pyrophosphate and altered RhoA membrane translocation. *Am J Physiol Heart Circ Physiol* 2007; 292: H3158–63.
- 33 Makaula S, Lochner A, Genade S, Sack MN, Awan MM, Opie LH. H-89, a non-specific inhibitor of protein kinase A, promotes post-ischemic cardiac contractile recovery and reduces infarct size. *J Cardiovasc Pharmacol* 2005; 45: 341–7.
- 34 Sanada S, Kitakaze M, Papst PJ, Asanuma H, Node K, Takashima S, *et al*. Cardioprotective effect afforded by transient exposure to phosphodiesterase III inhibitors: the role of protein kinase A and p38 mitogen-activated protein kinase. *Circulation* 2001; 104: 705–10.
- 35 Davies SP, Reddy H, Caivano M, Cohen P. Specificity and mechanism of action of some commonly used protein kinase inhibitors. *Biochem J* 2000; 351: 95–105.
- 36 Soria LR, Gradilone SA, Larocca MC, Marinelli RA. Glucagon induces the gene expression of aquaporin-8 but not that of aquaporin-9 water channels in the rat hepatocyte. *Am J Physiol Regul Integr Comp Physiol* 2009; 296: R1274–81.
- 37 Mei FC, Qiao J, Tsygankova OM, Meinkoth JL, Quilliam LA, Cheng X. Differential signaling of cyclic AMP: opposing effects of exchange protein directly activated by cyclic AMP and cAMP-dependent protein kinase on protein kinase B activation. *J Biol Chem* 2002; 277: 11497–504.
- 38 Kou R, Michel T. Epinephrine regulation of the endothelial nitric-oxide synthase: roles of RAC1 and beta3-adrenergic receptors in endothelial NO signaling. *J Biol Chem* 2007; 282: 32719–29.
- 39 Bellis A, Castaldo D, Trimarco V, Monti MG, Chivasso P, Sadoshima J, *et al*. Cross-talk between PKA and Akt protects endothelial cells from apoptosis in the late ischemic preconditioning. *Arterioscler Thromb Vasc Biol* 2009; 29: 1207–12.

Original Article

Vam3, a derivative of resveratrol, attenuates cigarette smoke-induced autophagy

Ji SHI^{1,2}, Ning YIN², Ling-ling XUAN¹, Chun-suo YAO³, Ai-min MENG^{2,*}, Qi HOU^{1,*}

¹Institute of Materia Medica, Chinese Academy of Medical Sciences and Peking Union Medical College, Pharmaceutical, National Key Laboratory of Natural Pharmaceutical Active Substance and Function, Beijing 100050, China; ²Institute of Radiation Medicine, Chinese Academy of Medical Sciences and Peking Union Medical College, Key Laboratory of Molecular Nuclear Medicine, Tianjin 300192, China; ³Institute of Materia Medica, Chinese Academy of Medical Sciences and Peking Union Medical College, Department of Natural Medicine Chemistry, Beijing 100050, China

Aim: To appraise the efficacy of Vam3 (Amurensis H), a dimeric derivative of resveratrol, at inhibiting cigarette smoke-induced autophagy.

Methods: Human bronchial epithelial cells were treated with cigarette smoke condensates, and a chronic obstructive pulmonary disease (COPD) model was established by exposing male BALB/c mice to cigarette smoke. The protein levels of the autophagic marker microtubule-associated protein 1A/1B-light chain 3 (LC3), Sirtuin 1 (Sirt1), and foxhead box O 3a (FoxO3a) were examined using Western blotting and Immunohistochemistry. LC3 punctae were detected by immunofluorescence. The levels of FoxO3a acetylation were examined by immunoprecipitation. The level of intracellular oxidation was assessed by detecting ROS and GSH-Px.

Results: Vam3 attenuated cigarette smoke condensate-induced autophagy in human bronchial epithelial cells, and restored the expression levels of Sirt1 and FoxO3a that had been reduced by cigarette smoke condensates. Similar protective effects of Vam3, reducing autophagy and restoring the levels of Sirt1 and FoxO3a, were observed in the COPD animal model. Additionally, Vam3 also diminished the oxidative stress that was induced by the cigarette smoke condensates.

Conclusion: Vam3 decreases cigarette smoke-induced autophagy via up-regulating/restoring the levels of Sirt1 and FoxO3a and inhibiting the induced oxidative stress.

Keywords: COPD; autophagy; Sirt1; FoxO3a; resveratrol; Vam3

Acta Pharmacologica Sinica (2012) 33: 888–896; doi: 10.1038/aps.2012.73; published online 18 Jun 2012

Introduction

Chronic obstructive pulmonary disease (COPD) has become a major global public health problem. The World Health Organization has predicted that by 2020, COPD will be the fifth leading cause of morbidity, and the third leading cause of mortality. Cigarette smoke (CS) contains numerous oxidants, free radical and chemicals, which can induce oxidative stress in lungs, resulting in cell death and senescence. Although the mechanisms responsible for the pathogenesis of COPD remain unclear, there is no doubt that cigarette smoke is a major risk factor.

In the lung, a low level of autophagy eliminates damaged organelles and long-term proteins through the lysosomal deg-

radation pathway, to maintain cellular homeostasis. However, dysregulation or excessive activation of autophagy would lead to cell death and an acceleration of age-related lung abnormalities. Recently, studies have shown that enhanced autophagy occurs in the lungs of patients with COPD and of mice exposed to CS, and may be involved in the pathogenesis of COPD^[1–3]. Thus, protecting cells from autophagic death may be beneficial for the treatment of COPD.

Sirtuin 1 (Sirt1) is an NAD⁺-dependent deacetylase that plays a role in a wide range of biological processes, such as cell differentiation, cell death, cell senescence/aging, metabolism, inflammation, and stress resistance^[4,5]. The function of Sirt1 is mainly achieved by deacetylation of histones and several important transcription factors such as forkhead box O3 (FoxO3), p53, nuclear factor- κ B (NF- κ B), and Ku70^[6–10]. The transcription factor FoxO3a belongs to the FoxO family, which regulates the expression of several genes that are involved in diverse biological processes, such as cell death, the cell cycle,

* To whom correspondence should be addressed.

E-mail qhou77@yahoo.com (Qi HOU);

ai_min_meng@126.com (Ai-min MENG)

Received 2012-01-30 Accepted 2012-05-16

senescence and oxidative stress resistance^[11-13]. An increasing number of studies have shown that both Sirt1 and FoxO3a play important roles in autophagy^[11, 14]. Recently, both *in vitro* and *in vivo* experimental studies have demonstrated that the expression levels of Sirt1 and FoxO3 are decreased in response to CS-induced oxidative stress in the lung^[15-17], but the exact mechanisms have yet to be elucidated.

Resveratrol (3,5,4'-trihydroxystilbene, RES) is a polyphenolic compound found in grapes and wine. Mounting evidence strongly suggests that resveratrol has both anti-inflammatory and anti-oxidative functions that improve the outcomes of COPD^[18, 19]. Recent studies have also shown that resveratrol can inhibit autophagy induced by cigarette smoke^[20]. Vam3 (amurensis H), a resveratrol dimer, was first isolated from ethanol extracts of *Vitis amurensis* Rupr (Figure 1). Our previous *in vivo* and *in vitro* studies have found that Vam3 possesses clear anti-asthmatic^[21-23] and anti-COPD (unpublished) effects, achieved through a reduction in the synthesis of pro-inflammatory cytokines and leukotrienes. However, the molecular basis by which Vam3 protects against COPD is not clear. In this report, we have examined the role of Vam3 in CS-induced autophagy *in vitro* and *in vivo*, in an effort to develop a novel anti-autophagy agent for prevention of COPD progression.

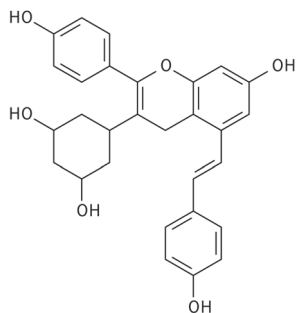


Figure 1. Chemical structure of Vam3.

Materials and methods

Preparation of cigarette smoke condensate

The cigarette smoke condensate (CSC) was prepared from Honghe (15 mg tar, 1.2 mg nicotine), a popular type of cigarette in China, as described previously^[24, 25]. Briefly, a “water-pipe” smoking device was designed and operated to allow a stream of smoke to flow into a 2-L flask submerged in liquid nitrogen. The amount of smoke obtained was determined by the weight increase of the flask. CSC was prepared by dissolving the collected smoke particulates in dimethyl sulfoxide (DMSO) at a concentration of 500 mg/mL. The condensate was then divided into small vials and stored at -80°C. On the day of the experiment, the CSC solution was diluted in M199 medium containing serum (Gibco, Grand Island, NY, USA), to the desired concentration, and used for cell treatment.

Cell culture and treatment

Human bronchial epithelial cells (Beas-2B) were grown in M199 medium (Gibco, Grand Island, NY, USA) containing 10% fetal bovine serum (FBS; HyClone, Logan, UT, USA). The cells were incubated at 37°C in a humidified atmosphere with 5% CO₂ and 95% air. During the logarithmic phase of growth, cells were pretreated with resveratrol (1 μmol/L, 0.1 μmol/L) or Vam3 (1 μmol/L, 0.1 μmol/L) for 2 h before treatment with CSC (300 mg/L) for 12 h. With a final concentration of 0.1 μmol/L, bafilomycin A1 had to be incubated for 2 h before the cells were harvested. All treatments were carried out in complete culture medium to avoid the induction of autophagy through the serum starvation pathway. Bafilomycin A1 and resveratrol were purchased from Fisher Scientific (Pittsburgh, PA, USA) and Sigma-Aldrich (St Louis, MO, USA), respectively, and Vam3 was produced by the Institute of Materia Medica of the Chinese Academy of Medical Sciences (Beijing, China).

Cytoplasmic and nuclear protein extraction

The cytoplasmic and nuclear fractions were prepared from Beas-2B cells (1×10⁶-10×10⁶) using NE-PER nuclear and cytoplasmic extraction reagents, according to the instructions of the manufacturer (Pierce Biotechnology Inc, Rockford, IL, USA). The resulting soluble protein and nuclear protein fractions were then stored at -80°C until use.

Immunofluorescence

Cells were fixed in methanol at room temperature for 15 min, and then in cold-methanol at -20°C for 15 min. After 3 washes with phosphate-buffered saline (PBS), the cells were incubated with blocking buffer [5 μL Tween 20 and 0.3 g bovine serum albumin (BSA), dissolved in 10 mL PBS] at room temperature for 30 min. The cells were then stained with an anti-LC3 antibody (Sigma-Aldrich, St Louis, MO, USA) at 4°C overnight, and this was followed by 30 min incubation with fluorescein isothiocyanate (FITC)-labeled secondary antibody (Zhong Shan Golden Bridge Biotechnology Co, Ltd, Beijing, China). After washing, the cells were visualized with a fluorescence microscope (Olympus Optical, Tokyo, Japan), and images were captured with a digital camera (Kodak, NY, USA).

Western blotting and immunoprecipitation

For Western blot experiments, cells were lysed with a non-denaturing lysis buffer (Applygen Technologies Inc, Beijing, China) supplemented with a protease inhibitor cocktail (Thermo Fisher Scientific, Rockford, IL, USA). Cell extracts (60 μg/lane) were separated on a 10%-15% SDS polyacrylamide gel, and transferred onto PVDF membranes (Millipore, Bedford, MA, USA). The membranes were then blocked for 1 h at room temperature with 5% BSA or non-fat milk. Subsequently, the membranes were probed with specific primary antibodies for LC3, β-actin (Sigma-Aldrich, St Louis, MO, USA), Sirt1, FoxO3a, p53, acetyl-p53 (lysine 382) (Cell Signaling, Beverly, MA, USA), p62, GAPDH, and LaminB

(Santa Cruz, CA, USA) at 4°C overnight. After 3 washes, the membranes were incubated with a goat antibody linked to horseradish peroxidase (Santa Cruz, CA, USA) for 1–2 h, and antibody-antigen reactivity was detected using Western Blotting Substrate (Pierce Biotechnology Inc, Rockford, IL, USA).

For immunoprecipitation experiments, cell extracts were pre-cleared with protein A/G sepharose beads (Santa Cruz, CA, USA) and incubated with FoxO3a antibody for 6 h at 4°C. Then, protein A/G sepharose beads were added, and the samples were incubated at 4°C overnight to capture the immunocomplexes. Western blotting was performed with anti-acetylated-lysine antibody (Cell Signaling, Beverly, MA, USA) and anti-FoxO3a antibody.

Small interfering RNA transfection assay

Pre-validated small interfering RNAs (siRNAs) were purchased from Santa Cruz Biotechnology, and the cells were transfected using Lipofectamine RNAiMAX (Invitrogen, Carlsbad, CA, USA) according to the manufacturer's instructions, with suitable scrambled siRNA controls. After being transfected for about 24 h, the cells were treated as described before.

Measurement of intracellular ROS

Intracellular ROS generation was determined with the fluorescent probe dihydroethidium (DHE) according to the manufacturer's instruction (Vigorous, Beijing, China). Briefly, Beas-2B cells with or without RES and Vam3, after stimulation with CSC for 12 h, were incubated with DHE probe (final concentration 10 μmol/L) at 37°C for 30 min in the dark. Then the cells were washed three times with fresh medium followed by measurement at an emission wavelength of 500 nm and an excitation wavelength of 600 nm using the fluorescent microplate reader (BioTek, Winooski, VT, USA).

Measurement of intracellular glutathione peroxidase (GSH-Px) vitality

Briefly, after stimulation with CSC for 12 h with or without RES and Vam3, cells lysates were measured with the Glutathione Peroxidase Detection Kit (Beyotime Institute of Biotechnology, Beijing, China) closely according to the user's instructions in 96-well plate. Then the plate was measured at 340 nm using the microplate reader (BioTek, Winooski, VT, USA). Finally, the amount of GSH-Px vitality was calculated by the formula $U/mg = [A_{340}/\text{min}(\text{sample}) - A_{340}/\text{min}(\text{blank})] / 0.00622 \times \text{dilution factor} / \text{protein concentration}$.

Animals and cigarette smoke exposure

The type of cigarette was described before. Specific pathogen free (SPF) male BALB/c mice (Beijing HFK Bioscience Co, Ltd, Beijing, China) were exposed to cigarette smoke (CS) or filtered air under identical conditions, beginning at 18–20 g. The cigarette smoke exposure was performed in a 4 L home-made plexiglass container which has a shelf in it according to equipment from Cao^[26]. The container has a rent for each side above and there are many circular gaps in the shelf. Eight

mice were placed on the shelf each time, below which there were 12 cigarettes. It would be taken for about 30 min until the smoke completely disappeared, and then repeated the process again. Mice were exposed for 30 min per exposure, three times a day for a period of 4 weeks. One hour before CS exposure, mice received either resveratrol (30 mg/kg) or Vam3 (50 mg/kg) by intragastric administration. About an hour after the last CS exposure and administration of resveratrol or Vam3, mice were sacrificed for harvesting of tissue. The study was designed to consist of 4 groups, containing 8 mice each: a control group (air-exposed mice), a model group (CS-exposed mice), an RES group (CS-exposed mice with 30 mg/kg resveratrol treatment) and a Vam3 group (CS-exposed mice with 50 mg/kg Vam3 treatment). Procedures followed for care and use of the animals were in accordance with institutional guidelines at the Experimental Animal Center of the Institute of Materia Medica, Beijing, China.

Immunohistochemistry

For hematoxylin and eosin (HE) staining, slices were deparaffinized in xylene and then rehydrated through graded alcohols to PBS, stained with hematoxylin and eosin, and then dehydrated again through graded alcohols. Finally, the slices were mounted with neutral gum and observed using a microscope. For immunohistochemistry staining, mouse lung tissues were fixed in 10% formaldehyde and embedded in paraffin. Lung slices were deparaffinized in xylene, rehydrated through graded alcohols to PBS, treated with 3% H₂O₂ for 10 min, and placed in an EDTA-antigen retrieval buffer in a microwave. The slices were blocked with sheep serum for 10 min, and then incubated with anti-LC3 (Abcam, Cambridge, MA, USA), anti-Sirt1 (Beijing Biosynthesis Biotechnology Co, Ltd, Beijing, China), and anti-FoxO3a (Cell Signaling, Beverly, MA, USA) antibodies; incubation with the primary antibodies was carried out at 4°C overnight. The PV-9000 kit (Zhong Shan Golden Bridge Biotechnology Co, Ltd, Beijing, China) was applied to each section, according to the manufacturer's instructions. The stain was developed using ABC kit (Zhong Shan Golden Bridge Biotechnology Co, Ltd, Beijing, China), and this was followed by dehydration through graded alcohols. Finally, the slices were mounted with neutral gum, and assessment of immunostaining intensity was performed semi-quantitatively, using Image J software^[27].

Statistical analysis

Results are presented as mean ± SD, calculated from at least 3 independent experiments. Differences in measured variables between experimental and control groups were assessed using Student's *t*-test for group comparisons. Statistically significant differences were accepted at *P* < 0.05.

Results

Cigarette smoke condensate (CSC) induces autophagy in a dose- and time-dependent manner

To investigate whether CSC affects the induction of autophagy, a time- and dose-effect analysis of this compound

was carried out in Beas-2B cells. We found that CSC increased the accumulation of LC3-II and the conversion of LC3-I to LC3-II (Figures 2A–2D). At a CSC concentration of 300 mg/L, there was an approximately 6-fold increase in the ratio of LC3-II/LC3-I, compared to controls (Figure 2D). In addition, CSC (300 mg/L) increased the LC3-II/LC3-I ratio at 6 h post treatment, and a peak was reached at 12 h (Figure 2B). The effects of CSC on the formation of LC3 punctae in Beas-2B cells also appeared to be dose-dependent (Figure 2E and 2F), consistent with the immunoblotting analysis. These data clearly suggest that CSC induces autophagy in a dose- and time-dependent manner. Since LC3-II is subject to autophagic protein degradation, it also accumulates when the autophagosome-lysosome fusion is impaired^[28]. In order to exclude this possibility, we observed LC3-II accumulation in the presence of a specific inhibitor of the vacuolar type H (+)-ATPase, bafilomycin A1. We observed that LC3-II accumulation increased in the presence of bafilomycin A1 and increased to an even greater extent when combined with cell exposure to CSC. These data indicate that the autophagic flux is intact in these cells. Additionally, we examined the expression level of p62, also a marker of

autophagy^[29], which was degraded when treatment with CSC (supplementary Figure A). Thus, combining the data showing LC3-II accumulation and p62 degradation with the autophagic flux analysis, we confirm that CSC can induce autophagy in Beas-2B cells.

Vam3 attenuates CSC-induced autophagy and modulates the expression of Sirt1 and FoxO3a

To investigate the involvement of Vam3 in CSC-induced autophagy, Beas-2B cells were pretreated with RES (1 $\mu\text{mol/L}$ or 0.1 $\mu\text{mol/L}$) or Vam3 (1 $\mu\text{mol/L}$ or 0.1 $\mu\text{mol/L}$) for 2 h, and this was followed by treatment with CSC (300 mg/L). The ratio of LC3-II/LC3-I was significantly increased in response to CSC alone, whereas pretreatment with RES or Vam3 prevented the increase in the LC3-II/LC3-I ratio. In addition, Vam3 seemed to be much more effective than RES in attenuating this increase in the LC3-II/LC3-I ratio (Figure 3A and 3B). Pretreatment with RES and Vam3 also reduced the formation of LC3 punctae induced by CSC (Figure 3C and 3D). Furthermore, we found that RES and Vam3 could reverse the CSC-induced decrease of Sirt1 and FoxO3 expression (Figure 3A

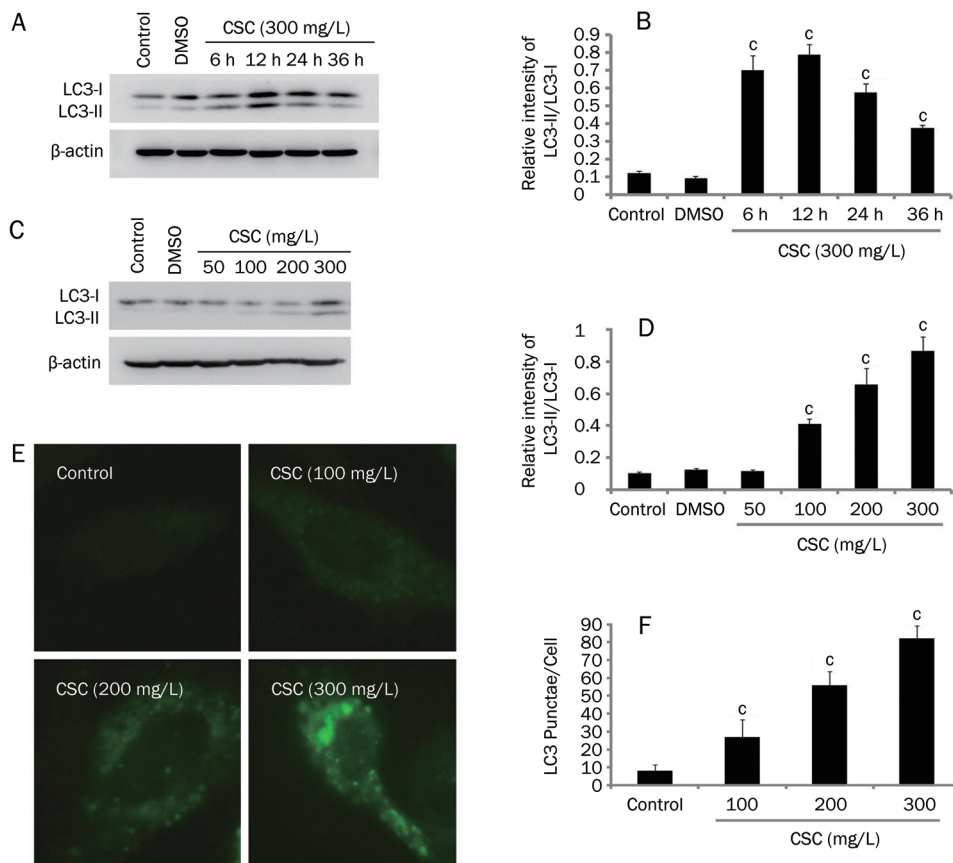


Figure 2. CSC-induced autophagy of Beas-2B cells is dose- and time-dependent. (A) Beas-2B cells were treated with CSC (300 mg/L), and cellular proteins were collected at the indicated time points and analyzed by Western blot. (C) Beas-2B cells were treated with CSC, at the indicated concentrations, for 12 h. Western blot was performed using anti-LC3 antibody. (B and D) The relative intensity of LC3-II/LC3-I was calculated by densitometry. (E) Beas-2B cells were treated with CSC, at the indicated concentrations, for 12 h. LC3 was detected by an immunofluorescence assay and examined using fluorescence microscopy, and representative cells were selected and photographed ($\times 400$). (F) Number of LC3 punctae per cell, for a total of 25 cells in 5 fields of view. Mean \pm SD. $n=3$. $^{\circ}P<0.01$ vs control.

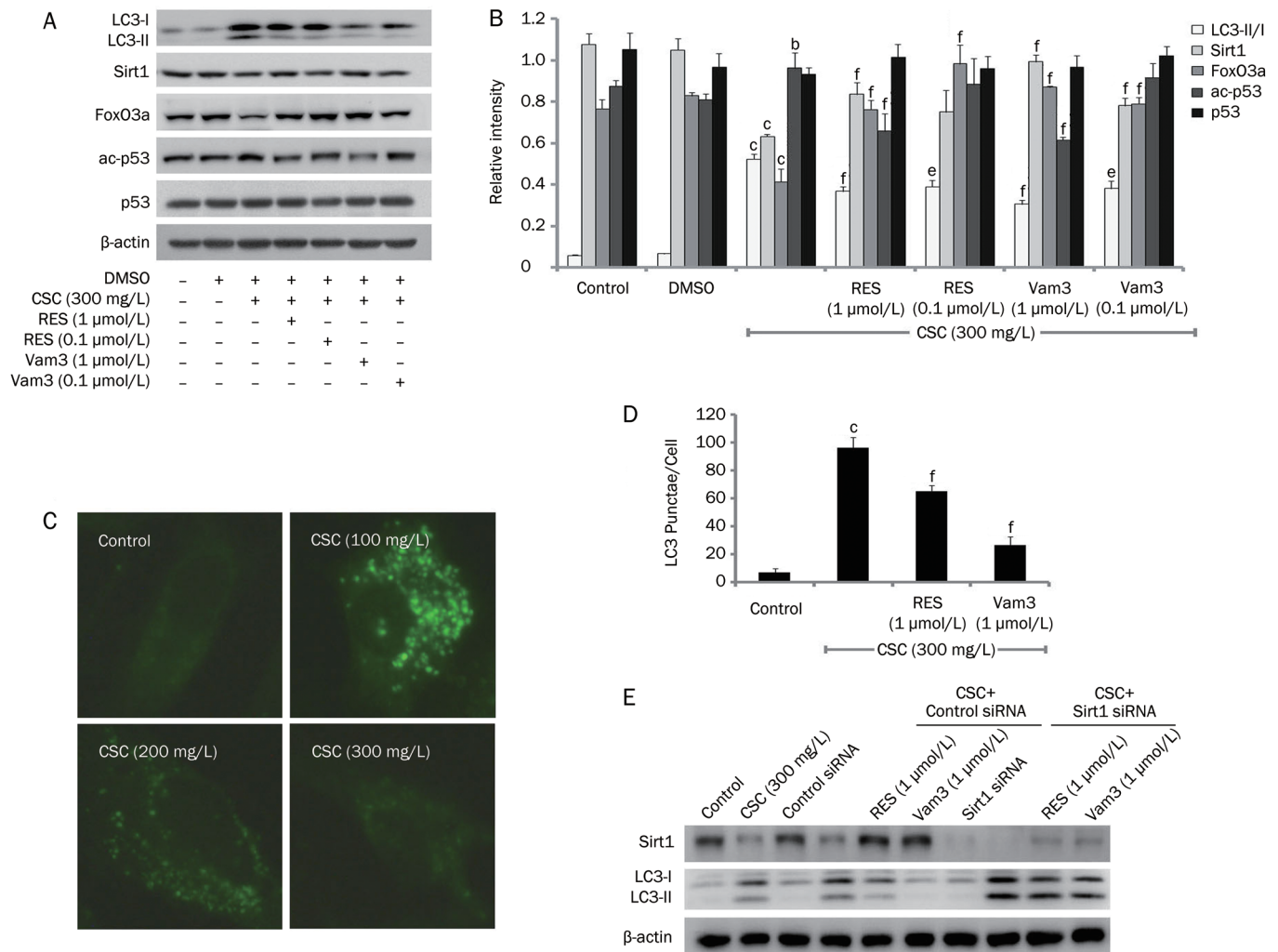


Figure 3. Vam3 attenuates CSC-induced autophagy in Beas-2B cells. Beas-2B cells were treated with CSC (300 mg/L) for 12 h, with or without RES (1 μmol/L, 0.1 μmol/L) or Vam3 (1 μmol/L, 0.1 μmol/L) pretreatment for 2 h. (A) Cell extracts were subjected to immunoblot analysis for detection of LC3, Sirt1, FoxO3a, p53, and acetylated p53 (lysine 382). (B) The relative intensity of LC3-II/LC3-I, Sirt1, FoxO3a, p53, and ac-p53 was calculated by densitometry. (C) LC3 was detected by an immunofluorescence assay and examined using fluorescence microscopy, and representative cells were selected and photographed ($\times 400$). (D) Number of LC3 punctae per cell, for a total of 25 cells in 5 fields of view. (E) After transfected with Sirt1 siRNA or scramble siRNA for 24 h, Beas-2B cells were treated with CSC (300 mg/L) for another 12 h, with or without RES (1 μmol/L, 0.1 μmol/L) or Vam3 (1 μmol/L, 0.1 μmol/L) pretreatment for 2 h. Then Western blot assays were performed with anti-LC3 and anti-Sirt1 antibodies. Mean \pm SD. $n=3$. ^b $P<0.05$, ^c $P<0.01$ vs control; ^e $P<0.05$, ^f $P<0.01$ compared to that in the absence of RES or Vam3. ac-p53, acetylated p53 (lysine 382).

and 3B). Pretreatment with RES and Vam3 reduced acetylation of p53 on lysine 382, indicating that the deacetylase activity of Sirt1 had been restored (Figure 3A and 3B). We also assessed the activation of FoxO3a by detecting its translocation and the level of acetylation of lysine (Figure 4). FoxO3a, which translocated to the nucleus following treatment with CSC, could be retained in the cytoplasm by RES and Vam3 (Figure 4C and 4D). The level of acetylated FoxO3a was increased in response to CSC treatment, and was reduced to some degree by RES or Vam3 pretreatment (Figure 4A and 4B). These data indicate that Vam3 may attenuate the autophagy induced by CSC, through modulating the Sirt1/FoxO3a pathway.

Sirt1 is required in Vam3 effect on autophagy

To observe whether the Sirt1 pathway is required for the effect of Vam3 on autophagy, we knocked down Sirt1 with siRNA and found that RES and Vam3 were not able to inhibit autophagy induced by CSC, which indicated that the inhibitory effect of RES and Vam3 requires Sirt1 (Figure 3E).

Vam3 diminishes CSC-induced oxidative stress

Lots of free radicals and oxidants in CSC can induce oxidative stress in many types of cells and tissues^[30-32], and oxidative stress plays an important role in COPD development. Thus, whether Vam3 affecting oxidative and anti-oxidative balance

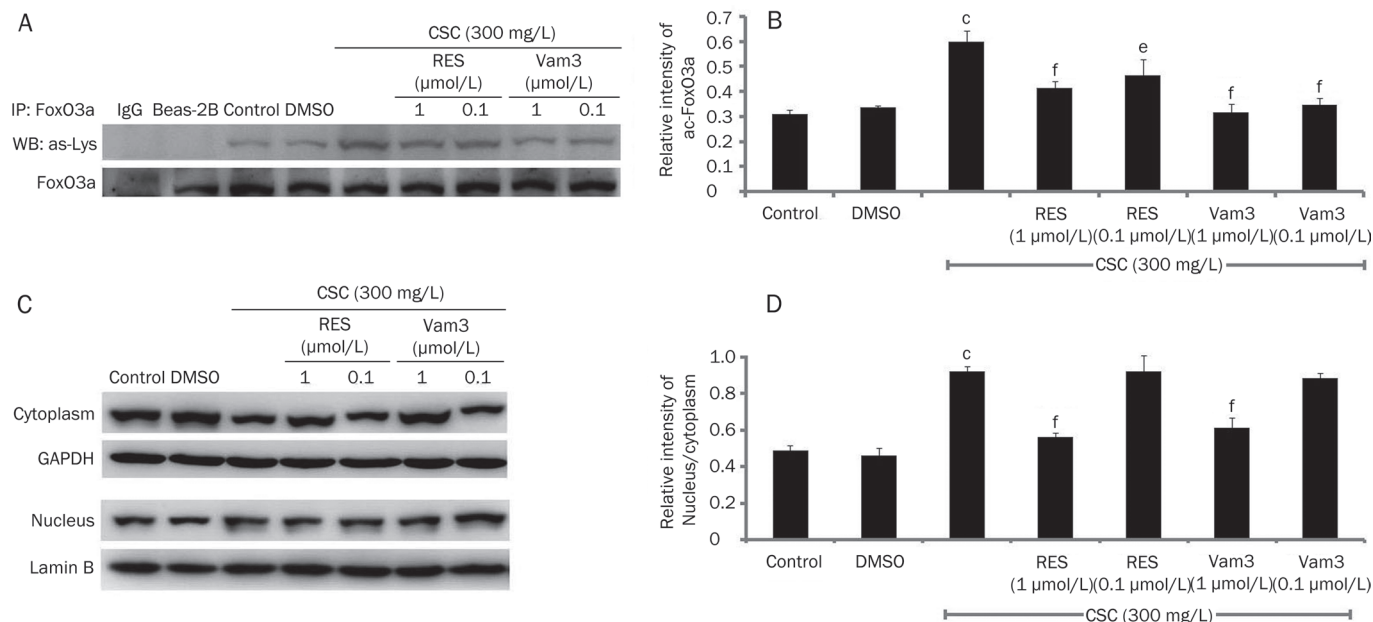


Figure 4. Vam3 inhibits the activation of FoxO3a, which is increased by CSC in Beas-2B cells. Beas-2B cells were treated with CSC (300 mg/L) for 12 h, with or without RES (1 μmol/L, 0.1 μmol/L) or Vam3 (1 μmol/L, 0.1 μmol/L) pretreatment for 2 h. (A) Cell extracts were immunoprecipitated with an anti-FoxO3a antibody, and the immune complexes were subjected to immunoblotting analyses with anti-acetyl-lysine antibody. IgG was used as the negative control. (B) The amounts of acetylated FoxO3a were calculated by densitometry and normalized to corresponding FoxO3a levels. (C) Equal amounts of cytoplasmic (cytoplasm) or nuclear (nucleus) protein extracts (60 μg/lane) were loaded and the membranes were probed with an anti-FoxO3a antibody. GAPDH served as the cytoplasmic control and LaminB was used as the nuclear control. (D) The relative intensity of nucleus/cytoplasm was calculated by densitometry. Mean±SD. $n=3$. ^c $P<0.01$ vs control; ^e $P<0.05$, ^f $P<0.01$ vs that in the absence of RES or Vam3.

or not makes us to detect the oxidative level in Beas-2B cells which were treated by CSC. We found that CSC up-regulated the generation of ROS (supplementary Figure B) and down-regulated the vitality of GSH-Px (supplementary Figure C), an enzyme protecting cells from free radicals damage by removing peroxides, whereas RES and Vam3 could reverse the alteration especially at 1 μmol/L.

Vam3 attenuates autophagy in mouse lungs exposed to CS

In order to examine the efficacy of Vam3 as an inhibitor of autophagy *in vivo*, wild-type (WT) mice were exposed to CS, with or without RES (30 mg/kg) or Vam3 (50 mg/kg) for 4 weeks. We found that both RES and Vam3 inhibited, to varying degrees, the progression of pathology in mouse lungs exposed to CS, with Vam3 being somewhat superior to RES in this regard (Figure 5A). The levels and localizations of LC3, Sirt1, and FoxO3a were also examined. As shown in the immunoblots in Figure 5B and 5C, the conversion of LC3-I to LC3-II was increased in CS-exposed mouse lungs, but was decreased in lungs of mice pretreated with RES or Vam3. RES and Vam3 were also able to restore the expression levels of Sirt1 and FoxO3a that were reduced by CS. Immunohistochemical staining, presented in Figure 5D and 5E, indicated that RES and Vam3 could also reduce CS-induced up-regulation of LC3 and restore the CS-induced decrease in Sirt1 and FoxO3a.

Discussion

To date, there are no effective drugs that inhibit the progressive development of COPD. An increasing number of studies have shown that resveratrol may be superior to other drugs for COPD therapy^[18, 19]. Recently, Hwang *et al* showed that resveratrol could also attenuate autophagy induced by cigarette smoke in a variety of lung cells^[20]. Since excessive autophagy leads to cell death, targeting autophagy may therefore have a beneficial outcome in the treatment of COPD. In this study, using *in vitro* cell culture techniques and *in vivo* animal models, we demonstrated that Vam3, like resveratrol, is able to attenuate CS-induced autophagy. In fact, we found Vam3 to be more effective than resveratrol at inhibiting autophagy induced by CS.

Recently, studies have shown that Sirt1, which acts in a protective role through the deacetylation of target genes, is highly inhibited in COPD patients^[15, 16]. Hwang *et al* reported that resveratrol attenuated CS-induced autophagy through prevention of Sirt1 reduction^[20]. Hence, compounds that maintain or up-regulate Sirt1 levels and activities may be beneficial in attenuating CS-induced autophagy. In this study, we showed that the inhibitory effect of Vam3 on CS-induced autophagy appears to correlate with its ability to maintain Sirt1 expression and deacetylase activity.

FoxO3a has been demonstrated to regulate the expression of several genes that are involved in inflammation, oxida-

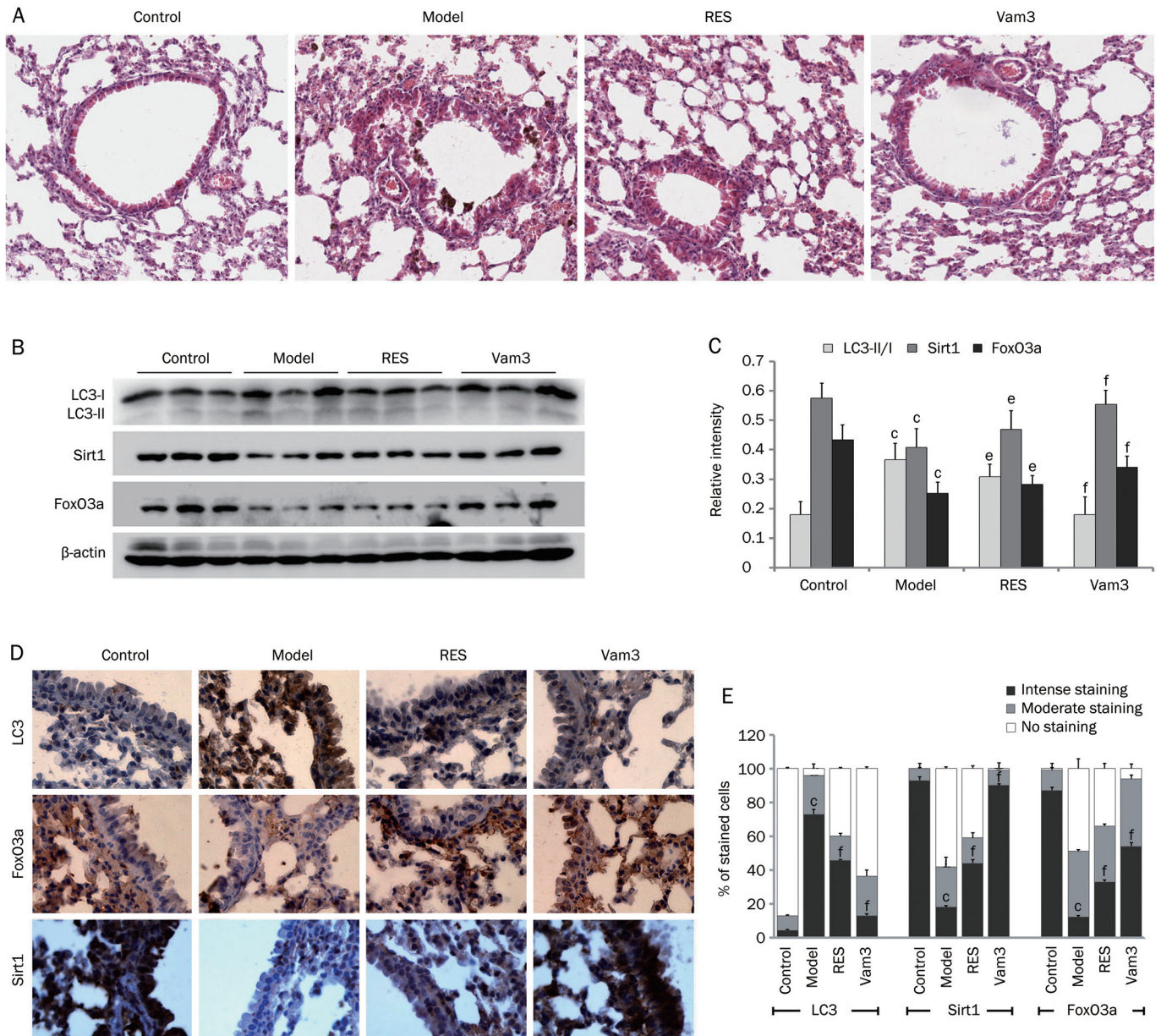


Figure 5. Vam3 attenuates CS-induced autophagy in the lungs of mice. Lung samples from each group (Control group: air-exposed mice; Model group: CS-exposed mice; RES group: CS-exposed mice with 30 mg/kg RES treatment; Vam3 group: CS-exposed mice with 50 mg/kg Vam3 treatment) were used for immunoblotting, HE staining and immunohistochemical analyses. (A) The lung sections were stained with hematoxylin and eosin, and the representative areas were captured by microscopy. (B) Expressions of LC3, FoxO3a, and Sirt1 in lung tissues from each group were determined by Western blotting. (C) The amounts of LC3, Sirt1 and FoxO3a were calculated by densitometry and normalized to corresponding actin levels ($n=8$ per group). (D) Expressions of LC3, FoxO3a, and Sirt1 in lung alveolar/airway epithelial cells from each group were determined using immunohistochemical staining ($\times 400$). (E) The number of stained cells from different levels (Intense staining level, Moderate staining level, No staining level) were calculated by ImageJ and normalized to corresponding total cells ($n=4$ per group). ^c $P<0.01$, compared to control; ^e $P<0.05$, ^f $P<0.01$, compared to the Model group.

tive stress resistance, and cellular senescence, and that are enhanced in the pathogenesis of COPD^[17]. Therefore, FoxO3a may play an important role in the development of COPD. We found that the expression level of FoxO3a was decreased in CS-induced autophagy *in vitro* and *in vivo*, and that Vam3 could reverse this process. Brunet *et al* reported that FoxO3a is localized in the cytoplasm under normal conditions, and trans-

locates to the nucleus in response to oxidative stress^[10]. In our studies, CSC promoted FoxO3a translocation to the nucleus in Beas-2B cells, and Vam3 inhibited this process. Though the mechanism underlying CS-induced reduction and translocation of FoxO3a is unclear, it may be associated with post-translational modifications of FoxO3a, such as acetylation and phosphorylation^[33]. Since the phosphorylation level of FoxO3

is mostly regulated by Akt activity^[34] and CS can induce Akt protein degradation^[35], we examined the Ser256 phosphorylation site in FoxO3a (data not shown). As we expected, the phosphorylation level of FoxO3 is decreased by treatment with CSC and up-regulated or restored by RES and Vam3, indicating that the Akt pathway might be involved in the regulatory role of Vam3 in FoxO3a. Furthermore, FoxO3a acetylation appears to be regulated via CREB-binding protein-mediated acetylation and Sirt1-mediated deacetylation^[10, 36]. Hwang *et al* found that the acetylation of FoxO3a was increased in the lungs of smokers as well as in the lungs of mice exposed to CS^[17]. Consistent with this, our results showed that Sirt1 was reduced in CS-induced stress and that this was accompanied by increased levels of FoxO3a acetylation. Although many studies have shown that post-translational modifications of FoxO3a lead to the suppression of its transcriptional activity, some reports have indicated that FoxO3a acetylation increases target gene transcription^[10, 37]. Since LC3 is a direct target gene regulated by FoxO3a^[38], it is possible that CSC-induced acetylation of FoxO3a and its translocation to the nucleus enhanced the transcription of the LC3 gene to promote autophagy. Meanwhile, Vam3 can maintain Sirt1 level and activity, so it is likely that this would then reduce FoxO3a acetylation and LC3 up-regulation. But the exact mechanism should be further investigated and debated.

CSC contains numerous free radicals and oxidants and induces oxidative stress, resulting in autophagy, apoptosis and cell senescence, all of which are important in the development of COPD^[32]. Sirt1 and FoxO3a are also subjected to the effects of oxidative stress^[39, 40]. So we proposed that Vam3, like resveratrol, might also have an anti-oxidative effect on CSC-induced damage. By detecting the ROS level and GSH-Px vitality, we proved our hypothesis.

Taken together, we demonstrated that Vam3 inhibited autophagy and restored the expression and activity levels of Sirt1, as well as preserved the expression level of FoxO3a in CSC-treated Beas-2B cells and in CS-exposed mouse lungs. We also showed that Vam3 had an anti-oxidative effect. These findings indicate that Vam3 acts as an anti-autophagy agent by affecting Sirt1 and FoxO3a expression and activity, and possibly also through its anti-oxidative effect. Vam3 warrants further studies to investigate potential clinical applications, and it would be interesting to determine the underlying mechanisms by which Vam3 acts on Sirt1 and FoxO3a to inhibit autophagy.

Acknowledgements

This work was supported by grants from the National Natural Science Foundation of China (30772579) & National Drug Research Integrated Platform (2009ZX0 9301-003-13).

Author contribution

Conceived and designed the experiments: Ji SHI, Qi HOU. Performed the experiments: Ji SHI, Ning YIN. Analyzed the data: Ji SHI, Ling-ling XUAN. Contributed reagents/materials/analysis tools: Chun-suo YAO, Ai-min MENG, and Qi HOU. Wrote the paper: Ji SHI.

Supplementary information

supplementary figure is available at the Acta Pharmacologica Sinica website.

References

- 1 Chen ZH, Kim HP, Sciruba FC, Lee SJ, Feghali-Bostwick C, Stolz DB, *et al*. Egr-1 regulates autophagy in cigarette smoke-induced chronic obstructive pulmonary disease. *PLoS One* 2008; 3: e3316.
- 2 Kim HP, Wang X, Chen ZH, Lee SJ, Huang MH, Wang Y, *et al*. Autophagic proteins regulate cigarette smoke-induced apoptosis: protective role of heme oxygenase-1. *Autophagy* 2008; 4: 887–95.
- 3 Ryter SW, Choi AM. Autophagy in the lung. *Proc Am Thorac Soc* 2010; 7: 13–21.
- 4 Chung S, Yao H, Caito S, Hwang JW, Arunachalam G, Rahman I. Regulation of SIRT1 in cellular functions: role of polyphenols. *Arch Biochem Biophys* 2010; 501: 79–90.
- 5 Haigis MC, Sinclair DA. Mammalian sirtuins: Biological insights and disease relevance. *Annu Rev Pathol* 2010; 5: 253–95.
- 6 Vahtola E, Louhelainen M, Forsten H, Merasto S, Raivio J, Kaheinen P, *et al*. Sirtuin1-p53, forkhead box O3a, p38 and post-infarct cardiac remodeling in the spontaneously diabetic Goto-Kakizaki rat. *Cardiovasc Diabetol* 2010; 9: 5.
- 7 Yang SR, Wright J, Bauter M, Seweryniak K, Kode A, Rahman I. Sirtuin regulates cigarette smoke-induced proinflammatory mediator release via RelA/p65 NF-kappaB in macrophages *in vitro* and in rat lungs *in vivo*: implications for chronic inflammation and aging. *Am J Physiol Lung Cell Mol Physiol* 2007; 292: L567–76.
- 8 Nath KA. The role of Sirt1 in renal rejuvenation and resistance to stress. *J Clin Invest* 2010; 120: 1026–8.
- 9 Cohen HY, Lavu S, Bitterman KJ, Hekking B, Imahiyerobo TA, Miller C, *et al*. Acetylation of the C terminus of Ku70 by CBP and PCAF controls Bax-mediated apoptosis. *Mol Cell* 2004; 13: 627–38.
- 10 Brunet A, Sweeney LB, Sturgill JF, Chua KF, Greer PL, Lin Y, *et al*. Stress-dependent regulation of FOXO transcription factors by the SIRT1 deacetylase. *Science* 2004; 303: 2011–5.
- 11 Zhao Y, Wang Y, Zhu WG. Applications of post-translational modifications of FoxO family proteins in biological functions. *J Mol Cell Biol* 2011; 3: 276–82.
- 12 Kitamura T, Kitamura Y. The roles of PPAR, C/EBP and FoxO families in adipocyte differentiation and proliferation. *Nihon Rinsho* 2011; 69: 259–63.
- 13 Maiese K, Chong ZZ, Hou J, Shang YC. Oxidative stress: Biomarkers and novel therapeutic pathways. *Exp Gerontol* 2010; 45: 217–34.
- 14 Salminen A, Kaarniranta K. SIRT1: regulation of longevity via autophagy. *Cell Signal* 2009; 21: 1356–60.
- 15 Rajendrasozhan S, Yang SR, Kinnula VL, Rahman I. SIRT1, an anti-inflammatory and antiaging protein, is decreased in lungs of patients with chronic obstructive pulmonary disease. *Am J Respir Crit Care Med* 2008; 177: 861–70.
- 16 Caito S, Hwang JW, Chung S, Yao H, Sundar IK, Rahman I. PARP-1 inhibition does not restore oxidant-mediated reduction in SIRT1 activity. *Biochem Biophys Res Commun* 2010; 392: 264–70.
- 17 Hwang JW, Rajendrasozhan S, Yao H, Chung S, Sundar IK, Huyck HL, *et al*. FOXO3 deficiency leads to increased susceptibility to cigarette smoke-induced inflammation, airspace enlargement, and chronic obstructive pulmonary disease. *J Immunol* 2011; 187: 987–98.
- 18 Knobloch J, Sibbing B, Jungck D, Lin Y, Urban K, Stoelben E, *et al*. Resveratrol impairs the release of steroid-resistant inflammatory cytokines from human airway smooth muscle cells in chronic obstructive pulmonary disease. *J Pharmacol Exp Ther* 2010; 335: 788–98.

- 19 Wood LG, Wark PA, Garg ML. Antioxidant and anti-inflammatory effects of resveratrol in airway disease. *Antioxid Redox Signal* 2010; 13: 1535–48.
- 20 Hwang JW, Chung S, Sundar IK, Yao H, Arunachalam G, McBurney MW, *et al*. Cigarette smoke-induced autophagy is regulated by SIRT1-PARP-1-dependent mechanism: implication in pathogenesis of COPD. *Arch Biochem Biophys* 2010; 500: 203–9.
- 21 Li YT, Yao CS, Bai JY, Lin M, Cheng GF. Anti-inflammatory effect of amurensin H on asthma-like reaction induced by allergen in sensitized mice. *Acta Pharmacol Sin* 2006; 27: 735–40.
- 22 Yang L, Yao CS, Wu ZY, Xuan LL, Bai JY, Cheng GF, *et al*. Effects of dihydroxy-stilbene compound Vam3 on airway inflammation, expression of ICAM-1, activities of NF-kappaB and MMP-9 in asthmatic mice. *Yao Xue Xue Bao* 2010; 45: 1503–8.
- 23 Huang KS, Lin M, Cheng GF. Anti-inflammatory tetramers of resveratrol from the roots of *Vitis amurensis* and the conformations of the seven-membered ring in some oligostilbenes. *Phytochemistry* 2001; 58: 357–62.
- 24 Yuan J, Ma J, Zheng H, Shi T, Sun W, Zhang Q, *et al*. Overexpression of OLC1, cigarette smoke, and human lung tumorigenesis. *J Natl Cancer Inst* 2008; 100: 1592–605.
- 25 Zhang X, Xiao T, Cheng S, Tong T, Gao Y. Cigarette smoke suppresses the ubiquitin-dependent degradation of OLC1. *Biochem Biophys Res Commun* 2011; 407: 753–7.
- 26 Cao J, Chen P, Yang Y, Ouyang RY, Peng H. Establishment and assessment of a mouse model of cigarette smoke-induced emphysema. *Acta Lab Anim Sci Sin* 2010; 18: 278–82.
- 27 Dunnill MS. Quantitative methods in the study of pulmonary pathology. *Thorax* 1962; 17: 320–8.
- 28 Kliensky DJ, Cuervo AM, Seglen PO. Methods for monitoring autophagy from yeast to human. *Autophagy* 2007; 3: 181–206.
- 29 Bjorkoy G, Lamark T, Pankiv S, Overvatn A, Brech A, Johansen T. Monitoring autophagic degradation of p62/SQSTM1. *Methods Enzymol* 2009; 452: 181–97.
- 30 Barreiro E, Del Puerto-Nevado L, Puig-Vilanova E, Perez-Rial S, Sanchez F, Martinez-Galan L, *et al*. Cigarette smoke-induced oxidative stress in skeletal muscles of mice. *Respir Physiol Neurobiol* 2012; 182: 9–17.
- 31 Valenti VE, de Abreu LC, Sato MA, Ferreira C, Adami F, Fonseca FL, *et al*. Sidestream cigarette smoke effects on cardiovascular responses in conscious rats: involvement of oxidative stress in the fourth cerebral ventricle. *BMC Cardiovasc Disord* 2012; 12: 22.
- 32 Lakhdar R, Denden S, Kassab A, Leban N, Knani J, Lefranc G, *et al*. Update in chronic obstructive pulmonary disease: role of antioxidant and metabolizing gene polymorphisms. *Exp Lung Res* 2011; 37: 364–75.
- 33 Hedrick SM. The cunning little vixen: Foxo and the cycle of life and death. *Nat Immunol* 2009; 10: 1057–63.
- 34 Huang H, Tindall DJ. Regulation of FOXO protein stability via ubiquitination and proteasome degradation. *Biochim Biophys Acta* 2011; 1813: 1961–4.
- 35 Kim SY, Lee JH, Huh JW, Ro JY, Oh YM, Lee SD, *et al*. Cigarette smoke induces Akt protein degradation by the ubiquitin-proteasome system. *J Biol Chem* 2011; 286: 31932–43.
- 36 Dansen TB, Smits LM, van Triest MH, de Keizer PL, van Leenen D, Koerkamp MG, *et al*. Redox-sensitive cysteines bridge p300/CBP-mediated acetylation and FoxO4 activity. *Nat Chem Biol* 2009; 5: 664–72.
- 37 van der Heide LP, Smidt MP. Regulation of FoxO activity by CBP/p300-mediated acetylation. *Trends Biochem Sci* 2005; 30: 81–6.
- 38 Mammucari C, Milan G, Romanello V, Masiero E, Rudolf R, Del Piccolo P, *et al*. FoxO3 controls autophagy in skeletal muscle *in vivo*. *Cell Metab* 2007; 6: 458–71.
- 39 Rajendran R, Garva R, Krstic-Demonacos M, Demonacos C. Sirtuins: molecular traffic lights in the crossroad of oxidative stress, chromatin remodeling, and transcription. *J Biomed Biotechnol* 2011. Published online 2011 September 7. doi: 10.1155/2011/368276.
- 40 Storz P. Forkhead homeobox type O transcription factors in the responses to oxidative stress. *Antioxid Redox Signal* 2011; 14: 593–605.

Original Article

siRNA against plasminogen activator inhibitor-1 ameliorates bleomycin-induced lung fibrosis in rats

Yan-ping ZHANG^{1,2}, Wen-bin LI^{1,4,*}, Wei-li WANG¹, Jian LIU², Shu-xia SONG³, Lin-lin BAI², Yu-yan HU¹, Ya-dong YUAN², Min ZHANG¹

¹Department of Pathophysiology, Hebei Medical University, Shijiazhuang 050017, China; ²Department of Respiration, the Second Hospital of Hebei Medical University, Shijiazhuang 050000, China; ³Department of Immunology, Hebei Medical University, Shijiazhuang 050017, China; ⁴Aging and Cognition Neuroscience Laboratory of Hebei Province, Shijiazhuang 050031, China

Aim: Plasminogen activator inhibitor-1 (PAI-1) is involved in the progression of pulmonary fibrosis. The present study was undertaken to examine the effects on pulmonary fibrosis of silencing PAI-1 expression with small interfering RNA (siRNA) and to assess the possible underlying mechanisms.

Methods: Male Wistar rats were subjected to intratracheal injection of bleomycin (BLM, 5 mg/kg, 0.2 mL) to induce pulmonary fibrosis. Histopathological changes of lung tissue were examined with HE or Masson's trichrome staining. The expression levels of α -smooth muscle actin (α -SMA), collagen type-I and type-III, caspase-3, as well as p-ERK1/2 and PI3K/Akt in the lung tissue were evaluated using immunohistochemistry and Western blot analysis. The fibroblasts isolated from BLM-induced fibrotic lung tissue were cultured and transfected with pcDNA-PAI-1 or PAI-1 siRNA. The expression level of PAI-1 in the fibroblasts was measured using real time RT-PCR and Western blot analysis. The fibroblast proliferation was evaluated using MTT assay.

Results: Intratracheal injection of PAI-1 siRNA (7.5 nmol/0.2 mL) significantly alleviated alveolitis and collagen deposition, reduced the expression of PAI-1, α -SMA, collagen type-I and collagen type-III, and increased the expression of caspase-3 in BLM-induced fibrotic lung tissue. In consistence with the *in vivo* results, the proliferation of the cultured fibroblasts from BLM-induced fibrotic lung tissue was inhibited by transfection with PAI-1 siRNA, and accelerated by overexpression of PAI-1 by transfection with pcDNA-PAI-1. The expression of caspase-3 was increased as a result of PAI-1 siRNA transfection, and decreased after transfection with pcDNA-PAI-1. In addition, the levels of p-ERK1/2 and PI3K/Akt in the fibrogenic lung tissue were reduced after treatment with PAI-1 siRNA.

Conclusion: The data demonstrate that PAI-1 siRNA inhibits alveolitis and pulmonary fibrosis in BLM-treated rats via inhibiting the proliferation and promoting the apoptosis of fibroblasts. Suppression ERK and AKT signalling pathways might have at least partly contributed to this process. Targeting PAI-1 is a promising therapeutic strategy for pulmonary fibrosis.

Keywords: idiopathic pulmonary fibrosis; pulmonary fibroblast; bleomycin; plasminogen activator inhibitor-1; RNA interference; α -smooth muscle actin; collagen; caspase-3; extracellular signal-regulated kinase; phosphatidylinositol 3-phosphate kinase

Acta Pharmacologica Sinica (2012) 33: 897–908; doi: 10.1038/aps.2012.39; published online 4 Jun 2012

Introduction

Idiopathic pulmonary fibrosis (IPF) is characterised by the transformation of fibroblasts into myofibroblasts and by the accumulation of excessive extracellular matrix (ECM)^[1]. Decreasing the deposition of ECM and enhancing its degradation might be particularly valuable in the treatment of lung fibrosis^[2]. However, specific knowledge-based approaches for the prevention and efficacious treatment of lung fibrosis are lacking. Increasing evidence supports the pivotal role of the fibrinolysis system, including urokinase-type plasminogen

activator (uPA) and its receptor, inhibitor of uPA (PAI-1), and plasminogen in regulating the balance between ECM degradation and deposition^[3]. Bueno *et al* observed that transfection with the uPA gene could induce cirrhosis regression and ameliorate hepatic dysfunction^[4]. Hattori *et al* revealed that the plasminogen activation system reduces lung fibrosis through a hepatocyte growth factor-dependent mechanism^[5].

The fibrin deposits persist in patients with IPF because normal fibrinolytic activity is suppressed by an increased expression of PAI-1^[6]. Recent evidence has shown that PAI-1 regulates proliferation and apoptosis in different cell lines by activating the ERK, AKT, JAK-STAT, and NF- κ B signalling pathways. Experimental studies have also revealed the important role of PAI-1 in the pathogenesis of fibrotic disease.

* To whom correspondence should be addressed.

E-mail liwbsjz@yahoo.com.cn

Received 2012-02-27 Accepted 2012-03-23

For example, Eitzman *et al* revealed that overexpression of PAI-1 could lead to more severe bleomycin-induced pulmonary fibrosis^[7], whereas mice with a targeted deletion of the PAI-1 gene (PAI-1^{-/-} mice) developed less fibrosis and survive longer^[8]. Interestingly, silencing PAI-1 expression alleviated hepatic fibrosis induced by CCl₄^[9]. However, it remains unclear whether silencing PAI-1 expression could ameliorate lung fibrosis. In 2010, Senoo *et al* reported that PAI-1 siRNA prevented pulmonary fibrosis by inhibition of the epithelial-to-mesenchymal transition (EMT)^[10]. However, whether PAI-1 siRNA inhibits the proliferation of fibroblasts directly and its effects on the related signalling pathways have not been determined.

Therefore, the present study was undertaken to observe whether silencing PAI-1 expression with siRNA against PAI-1 could inhibit lung fibrosis and whether the mechanisms of ameliorating fibrosis with siRNA against PAI-1 are related to the regulation of (myo)fibroblasts proliferation and apoptosis through the modulation of ERK and AKT signalling molecules, in a rat model of bleomycin (BLM)-induced pulmonary fibrosis.

Materials and methods

Animals and grouping

In accordance with to a report by Hu *et al*^[9], the siRNA against rat PAI-1 mRNA and non-specific siRNA (Ns-siRNA) (designed and synthesised by Guangzhou RiboBio Co, LTD) were selected for evaluating in BLM-induced pulmonary fibrosis in rats. The siRNA sequences mentioned above are shown in Table 1.

Table 1. The sequences of small interfering RNA used for plasminogen activator inhibitor-1 (PAI-1) silencing.

559 siRNA	Sense	5'-GGACUUCUCAGAGGUGGAATT-3'
	Antisense	5'-UUCACCUCUCUGAGAAGUCCTT-3'
Non-specific siRNA	Sense	5'-UUCUCCGAACGUGUCACGUTT-3'
	Antisense	5'-ACGUGACACGUUCGGAGAATT-3'

A total of 72 male Wistar rats weighing 130–140 g were provided by the Experimental Animal Center of Hebei Medical University, China. All rats were housed in the pathogen-free mouse colony and all experiments were performed according to the guidelines for the care and use of medical laboratory animals (Ministry of Health, China, 1998). The rats were divided into 4 treatment groups: sham, BLM, Non-specific siRNA (Ns-siRNA) and siRNA. The tracheas of the rats were exposed, and the rats in the BLM group were subjected to intratracheal injection of BLM (5 mg/kg, 0.2 mL) under chloral hydrate anaesthesia (10%, ip, 350 mg/kg), whereas the rats in the sham group received an equal volume of normal saline. The rats in the siRNA and Non-specific siRNA groups were first treated with BLM according to the protocol described above. From the third day after the administration of BLM,

the rats were treated with tracheal administration of PAI-1-siRNA or non-specific siRNA (7.5 nmol/0.2 mL per rat), respectively, once every three days. For all groups, on d 7, 14, and 28 after the administration of BLM or normal saline, the rats ($n=6$ at each time point) were sacrificed and the lower lobe of the right lung was harvested for histological observation, immunostaining, real time RT-PCR and Western blot analysis. Bronchoalveolar lavage (BAL) was performed to determine the PAI-1 activity using a colorimetric assay (American Diagnostica Inc, USA) according to the manufacturer's instructions.

Histological and immunohistochemical assays

Haematoxylin-Eosin (HE) or Masson's trichrome staining were conducted to examine the histopathological changes of lung tissue. Immunohistochemical examination was carried out to detect the expression of α -SMA, collagen type-I and type-III, and caspase-3 in the lung tissue using the following primary antibodies: rabbit anti- α -SMA (Epitomics, USA), goat anti-collagen type-I and type-III (Santa Cruz), and rabbit anti-caspase-3 (Santa Cruz) antibodies.

Cell isolation and culture

The rat fibroblasts from BLM-induced fibrotic lung tissue were performed to evaluate the effect of expression of the siRNA and pcDNA-PAI-1 on proliferation and apoptosis *in vitro*. Freshly harvested lung tissues were cut into 1×1×1 mm³ strips and maintained in Dulbecco's modified Eagle's medium (DMEM) (Gibco, USA) supplemented with 100 U/mL penicillin, 100 μ g/mL streptomycin, and 15% heat-inactivated foetal calf serum (Gibco, USA). After being cultured for 2–3 passages, purified fibroblasts were obtained and identified by immunohistochemistry staining with antibodies against vimentin and α -SMA proteins. Early-passage cells (2–4 passages) were used in the subsequent experiments.

Determination of fibroblast proliferation and apoptosis

The effects of transfection with pcDNA-PAI-1 (provided by Dr Fang WANG) on the expression levels of PAI-1 were evaluated by Western blot analysis at 48 h and 72 h, and the effects on fibroblast proliferation were evaluated using the 3-(4,5-dimethylthiazol-2-yl)-2,5-diphenyltetrazolium bromide (MTT) assay. The cells were transfected with PAI-1 siRNA or pcDNA-PAI-1 using the Lipofectamine 2000 transfection reagent (Invitrogen, Carlsbad, CA, USA) according to the manufacturer's instructions. Briefly, the cells were trypsinised and diluted in fresh culture medium without antibiotics, plated at a density of 2×10⁴ cells/well in triplicate wells on a 96-well plate and cultured for 24 h. The number of viable cells was determined at 570 nm at 24, 48, and 72 h after transfection with PAI-1 siRNA or pcDNA-PAI-1. Apoptosis was evaluated by detection of caspase-3 expression in the fibroblasts by real time RT-PCR at 24 h after transfection with PAI-1 siRNA or pcDNA-PAI-1.

Real time reverse transcription polymerase chain reaction

Total RNA was extracted from the lung tissues and cultured

Table 2. Primer sequences for real time reverse transcriptase polymerase chain reaction.

PAI-1	Forward	5'-CCTTCCAGAGTCCCATACA-3'
	Reverse	5'-CTGG CTCTTCCACCTCT-3'
Collagen type-I	Forward	5'-GGTGGTTATGACTTCAGCTTCC-3'
	Reverse	5'-CATGTAGGCTACGCTGTTCTTG-3'
Collagen type-III	Forward	5'-GTCTTATCAGCCCTGATGGTTC-3'
	Reverse	5'-GCTCCATTACCAGTGTGTTTA-3'
Caspase-3	Forward	5'-AATCAAGGGACGGGTCATG-3'
	Reverse	5'-GCTTGTGCGCGTACAGTTTC-3'
GAPDH	Forward	5'-CCATGTTTGTGATGGGTGGAACCA-3'
	Reverse	5'-ACCAGTGGATGCAGGATGATGTTCC-3'

fibroblasts using Trizol reagent (TaKaRa, Japan) according to the manufacturer's protocol. The primer sequences are summarised in Table 2. Real time RT-PCR was performed with a SYBR Green PCR Kit (TaKaRa, Japan), and the reactions were conducted on a RotorGene 3000A PCR instrument (Corbett, Australia). The housekeeping gene GAPDH was used as an internal control, and gene-specific mRNA expression was normalised against GAPDH expression.

Western blot analysis

The samples were homogenised in six volumes of lysis buffer containing 50 mmol/L Tris-HCl (pH 7.5), 150 mmol/L NaCl, 12 mmol/L $C_{24}H_{40}O_4 \cdot Na$, 0.1% SDS, 1 mmol/L EDTA, 1 mmol/L $MgCl_2$, 1 mmol/L phenylmethylsulphonyl fluoride (PMSF) and 2 μ g/mL leupeptin. The protein concentration of the supernatant was determined using the Coomassie blue assay. The samples were electrophoresed by SDS-PAGE on 12% gels, transferred to polyvinylidene difluoride (PVDF) filters (Millipore, USA) and incubated with mouse anti-PAI-1 (BD, USA), rabbit anti- α -SMA (Epitomics, USA), rabbit anti-AKT and anti-ERK (Bioworld, USA), rabbit anti-p-AKT and anti-p-ERK (Cell signal, USA), or rabbit anti- β -actin (Santa Cruz) antibodies. The primary antibodies were detected with horseradish peroxidase-conjugated second antibodies against mouse or rabbit IgG and an ECL luminescence system. The integral optical density (IOD) of each band was measured using a gel-image analysis system (Alpha Image 2200, Alpha, USA). The changes in the relative expression levels of PAI-1, α -SMA p-AKT, and p-ERK were represented by the ratio of each band's IOD to that of β -actin.

Assay for the hydroxyproline content of lung tissue

Wet lung samples weighing 30–100 mg were subjected to hydrolysis to determine the content of hydroxyproline according to the protocol of a Hydroxyproline Testing Kit (Jiancheng, Nanjing, China).

Statistical analysis

Statistical analysis of all reported values was performed with SAS8.0 software. The data were presented as the mean \pm SD and tested using one-way ANOVA for 4 groups on d 7, 14,

and 28. *P* values <0.05 were considered significant.

Results

PAI-1 expression increased in BLM-induced rat lung fibrosis and PAI-1 siRNA inhibited PAI-1 expression efficiently

First, we examined whether the PAI-1 expression was increased in BLM-induced rat lung fibrosis. Real time RT-PCR and Western blot analysis (Figure 1A, 1B) showed that the PAI-1 mRNA and protein levels in the lung were significantly increased in the BLM group compared with the sham group, and PAI-1 activity was significantly increased on d 7, 14, and 28 in the BAL fluid (Figure 1C).

Second, the inhibition efficiency of PAI-1 expression was determined by intratracheal injection of PAI-1 siRNA into BLM-induced fibrotic lung tissue. Figure 1A and 1B show that compared with the BLM group, the expression levels of PAI-1 mRNA and protein were reduced significantly after intratracheal injection of the PAI-1 siRNA on d 7, 14, and 28, whereas non-specific siRNA had no significant effect on PAI-1 mRNA and protein expression compared with the BLM group. In addition, the inhibitory effect gradually increased after the administration of the siRNA, corresponding to reductions of 29% \pm 9%, 58% \pm 9%, and 67% \pm 7% in the PAI-1 mRNA level and 46% \pm 11%, 51.9% \pm 5.3%, and 65.5% \pm 4% in the PAI-1 protein level at days 7, 14, and 28, respectively, compared with the BLM group. Figure 1C shows that administration of PAI-1 siRNA significantly decreased the level of PAI-1 in the BAL fluid compared with the BLM group, while the non-specific siRNA had no effect. The results indicated that the PAI-1 siRNA administered by intratracheal injection was delivered to the fibrotic area and silenced the expression of PAI-1 in BLM-induced lung fibrosis.

PAI-1 siRNA ameliorated BLM-induced lung fibrosis in rats

Changes in lung histological structure and collagen deposition

To determine the effect of PAI-1 siRNA on lung fibrosis, we observed the histopathological changes and investigated the expression of pro-fibrogenic molecules. HE staining (Figure 2A) showed that the structure of the alveoli was greatly distorted in the BLM group. There was clear alveolitis represented by the infiltration of the pulmonary mesenchyme by neutrophils, fibroblasts, and macrophages on d 7. The infiltration of the cells gradually decreased on d 14 and 28. Masson's trichrome staining (Figure 2B and 2C) showed that there were small-sized collagen depositions on d 14, and large-scale of collagen accumulations were observed on d 28. In contrast, administration of PAI-1 siRNA alleviated the alveolitis significantly on d 7 and suppressed the collagen deposition on d 14 and 28. The administration of non-specific siRNA had no effect compared with the BLM group.

Changes in hydroxyproline content

The content of hydroxyproline was measured to indicate collagen accumulation within the fibrotic lung tissues. The hydroxyproline content in lungs from rats with BLM-induced

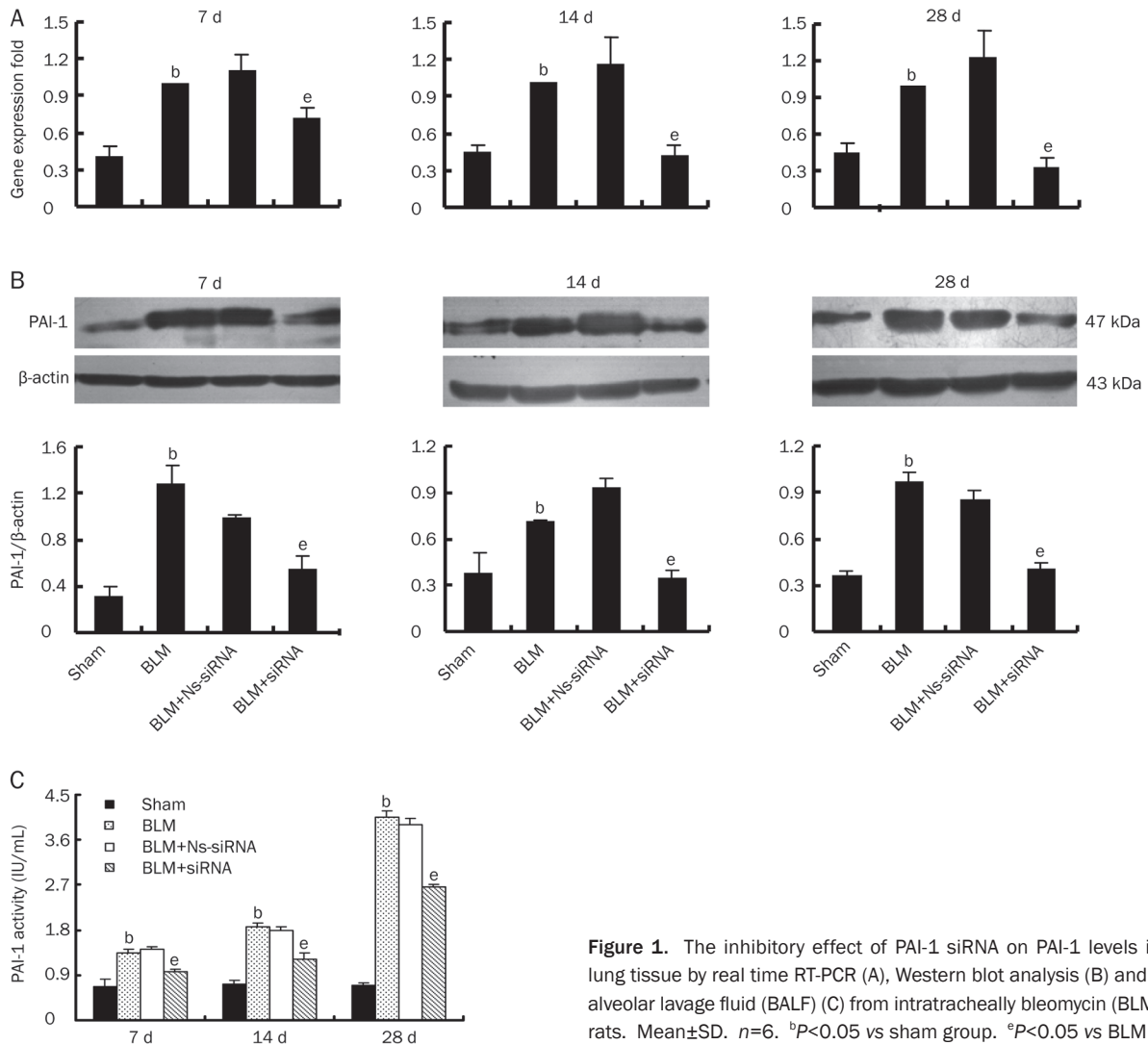


Figure 1. The inhibitory effect of PAI-1 siRNA on PAI-1 levels in fibrotic lung tissue by real time RT-PCR (A), Western blot analysis (B) and bronchoalveolar lavage fluid (BALF) (C) from intratracheally bleomycin (BLM)-treated rats. Mean±SD. $n=6$. ^b $P<0.05$ vs sham group. ^e $P<0.05$ vs BLM group.

lung fibrosis began to increase after 7 d and then increased rapidly thereafter. In the PAI-1 siRNA group, the hydroxyproline content was significantly decreased compared with that in the BLM group on d 14 and 28, while the non-specific siRNA had no effect on the hydroxyproline content compared with the BLM group (Figure 2D).

Changes in α -SMA expression

Immunohistochemistry staining (Figure 3A) showed that pro-fibrogenic molecules in α -SMA-positive cells in the BLM model rats were mainly located in the endochylema and cytomembrane of myofibroblasts around the fibrotic areas, and their levels were significantly increased compared with the sham group. After treatment with the PAI-1 siRNA, the levels were significantly decreased on d 7, 14, and 28. Western blot analysis (Figure 3B) showed that the protein level of α -SMA was significantly upregulated in the group with BLM-induced lung fibrosis compared with the sham group and that the upregulation was significantly inhibited on d 7, 14, and

28 after treatment with PAI-1-targeted siRNA. Non-specific siRNA had no significant effect on the expression of α -SMA compared with the BLM group.

Changes in collagen type-I and type-III

Immunohistochemistry staining revealed that levels of collagen type-I (Figure 4A) and type-III (Figure 5A) were mainly located in the fibroblasts, myofibroblasts and mesenchyma of the fibrotic areas, and their expression levels increased significantly in the BLM group. After administration of siRNA, the levels significantly decreased. Real time RT-PCR analysis showed that the expression of collagen type-I and type-III expression were significantly increased in the lungs of BLM-treated rat, and the upregulation was significantly inhibited by the administration of PAI-1 siRNA on d 7 and 14 for collagen type-I (Figure 4B) and on d 14 and 28 for collagen type-III (Figure 5B) compared with the BLM groups. Non-specific siRNA had no significant effects on the expression of collagen compared with the BLM group.

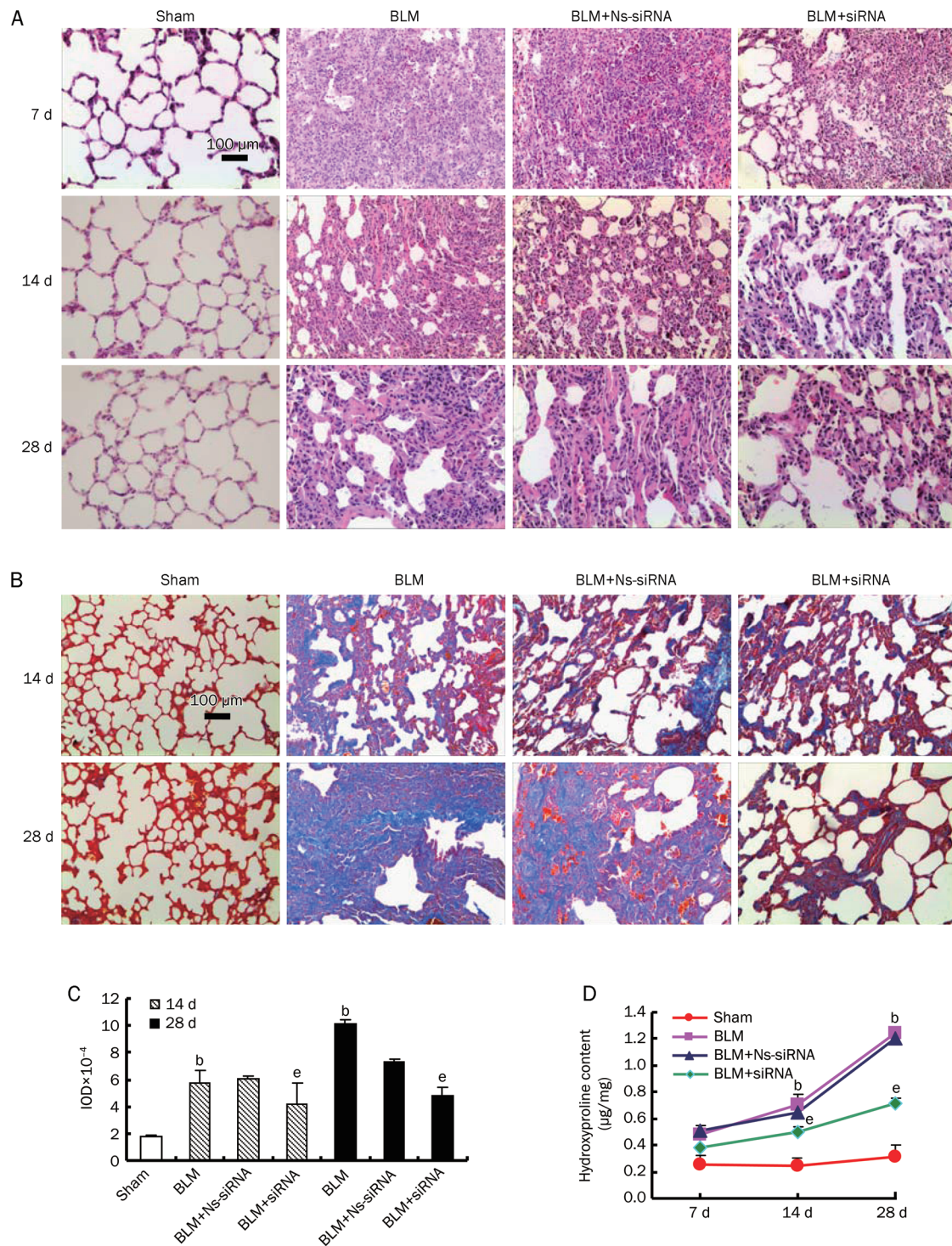


Figure 2. The effect of PAI-1 siRNA on intratracheally BLM-induced lung fibrosis. HE staining (A) and Masson' trichrome staining (B) shows the histological changes after intratracheal administration of PAI-1 siRNA. Scale bar in the upper-left microphotograph represents 100 µm, and this scale was used for all microphotographs. The bar graph in panel C is a quantitative representation of the changes in collagen based on the integral optical density (IOD). Mean±SD. *n*=6. ^b*P*<0.05 vs sham group. ^e*P*<0.05 vs BLM group. The line graph in panel D shows that the administration PAI-1 siRNA significantly inhibited the increase of hydroxyproline content in the fibrotic lung tissue induced by BLM treatment at the observed time points, whereas non-specific siRNA had no effect.

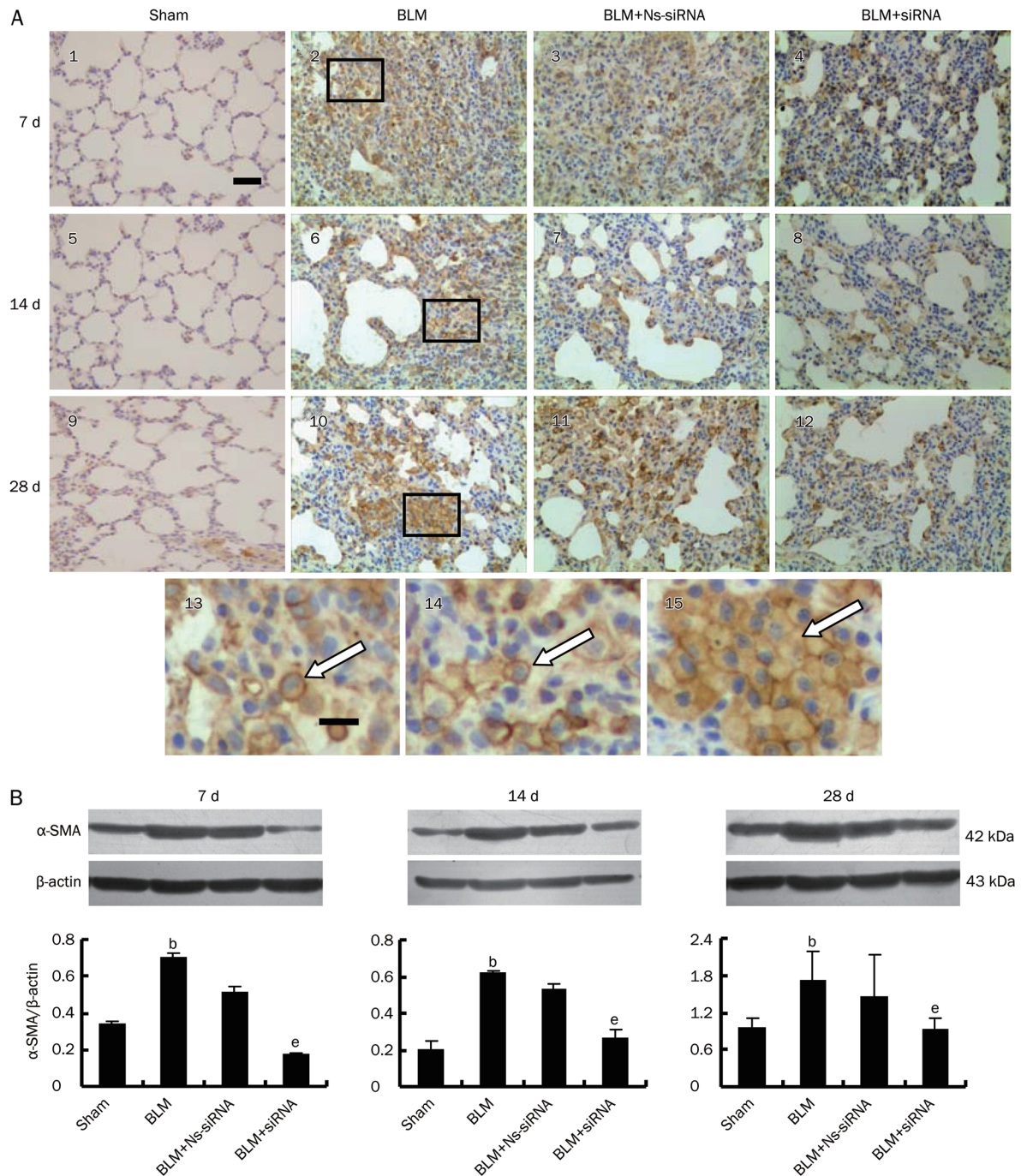


Figure 3. The expression of alpha-smooth muscle actin (α -SMA) in fibrotic lung tissue from intratracheally bleomycin (BLM)-treated rats assayed by immunohistochemical staining (A) and Western blot analysis (B). The scale bar in the first microphotograph represents 100 μ m and applies to microphotographs of 1–12. The scale bar in 13 represents 10 μ m and applies to images 13–15, which are enlargements of the region shown in the black box in microphotographs 2, 6 and 10, respectively. Mean \pm SD. $n=6$. ^b $P<0.05$ vs sham group. ^e $P<0.05$ vs BLM group.

Promoting apoptosis and inhibiting proliferation of pulmonary fibroblasts through the ERK and AKT pathways contributed to the anti-fibrosis effect of PAI-1 siRNA

Changes in apoptosis and proliferation of fibroblasts

To confirm the mechanism by which PAI-1 siRNA prevents lung fibrosis, we investigated whether down- or upregula-

tion PAI-1 expression could affect proliferation and apoptosis in cultured rat fibroblasts. Figure 6A showed that the cells in which vimentin was positively expressed and α -SMA was negatively expressed were verified to be fibroblasts. Figure 6B showed that the plasmid pcDNA-PAI-1 upregulated PAI-1 expression in fibroblasts by 277% and 204% at 48 h and 72 h,

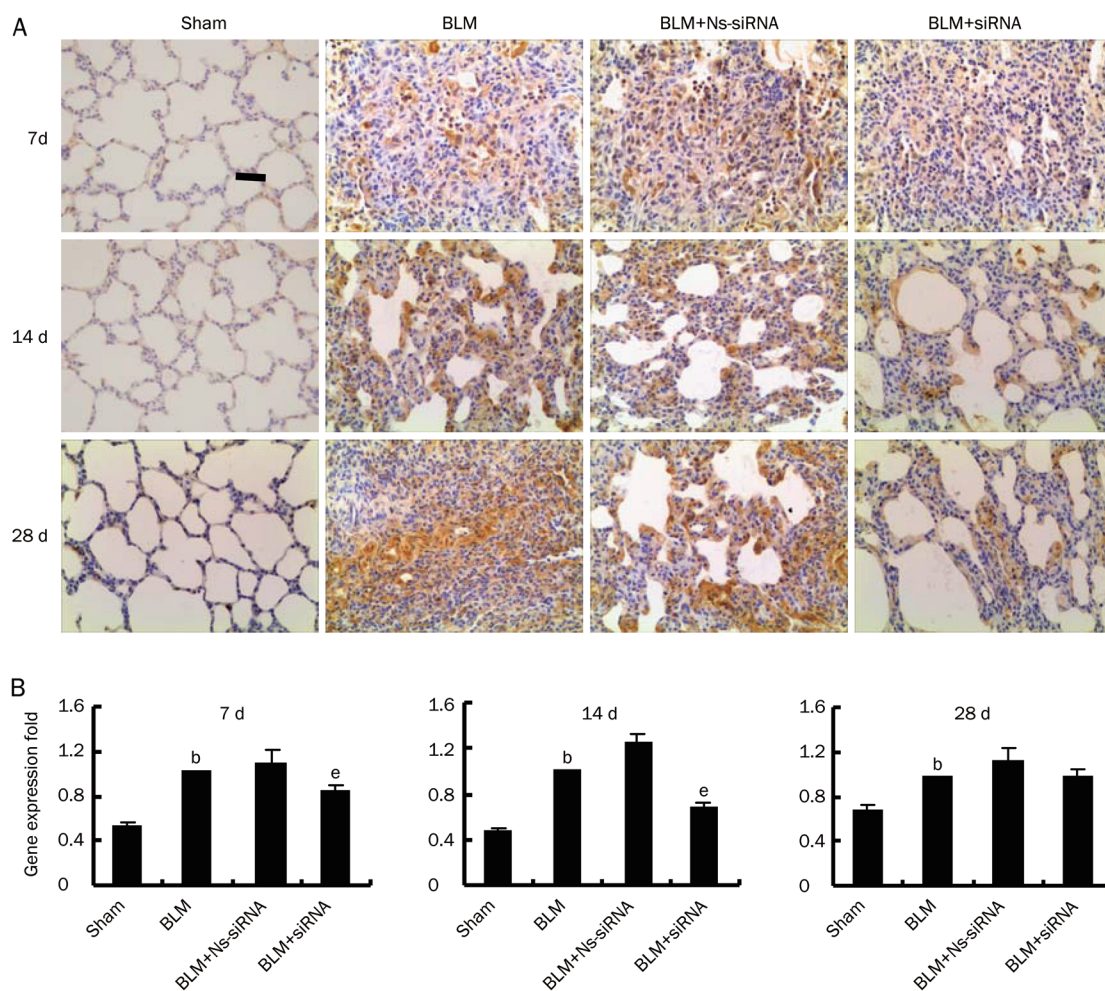


Figure 4. The expression of collagen type-I in the fibrotic lung tissue of the intratracheally bleomycin (BLM)-treated rats as assayed by immunohistochemical staining (A) and real time RT-PCR (B). Scale bar in the upper-left microphotograph represents 100 μ m and applies to all microphotographs. Mean \pm SD. $n=6$. ^b $P<0.05$ vs sham group. ^e $P<0.05$ vs BLM group.

respectively. Figure 6C showed that the proliferation of fibroblasts in the siRNA group was significantly inhibited, and the inhibitory effect peaked at 48 h and descended 72 h after the transfection of PAI-1 siRNA. However, the proliferation of fibroblasts was significantly stimulated until 72 h after transfection of pcDNA-PAI-1, according to the results of the MTT assay.

Apoptosis was evaluated by detecting the levels of caspase-3. Real time RT-PCR analysis (Figure 6D) shows that caspase-3 expression was upregulated after transfection of PAI-1 siRNA, whereas the expression was downregulated after transfection of pcDNA-PAI-1 into fibroblasts. *In vivo* (Figure 6E), immunohistochemistry staining showed that levels of caspase-3 increased after intratracheal treatment of BLM-induced lung tissue with PAI-1 siRNA. These results indicated that PAI-1 siRNA ameliorated lung fibrosis directly by inhibiting the proliferation and promoting the apoptosis of fibroblasts.

Changes in expression of p-ERK1/2 and p-AKT

To investigate the role of the ERK and AKT signaling path-

ways in the amelioration of lung fibrosis by PAI-1 siRNA, we analysed the protein expression of phosphorylated-AKT and phosphorylated-ERK1/2 in fibrotic lung tissue because the level of phosphorylation represents the activation of these signalling pathways. As shown in Figure 7, the expression of p-AKT and p-ERK significantly increased in BLM-treated rat lung tissues on d 7, 14, and 28, and the expression levels were downregulated at the observed time points after intratracheal treatment with PAI-1 siRNA compared with the BLM group. The ERK and AKT signaling pathways contributed to the anti-pulmonary fibrosis effect of PAI-1 siRNA.

Discussion

Local delivery of siRNA to the lungs, for example, through inhalation or intranasal administration, offers a unique opportunity to treat respiratory diseases, including inflammation, cystic fibrosis, infectious diseases, and cancer^[11]. The effectiveness of *in vivo* gene knockdown has been a major question among many investigators^[12]. In the present study, to improve the effectiveness of siRNA, repeat intratracheal injection twice

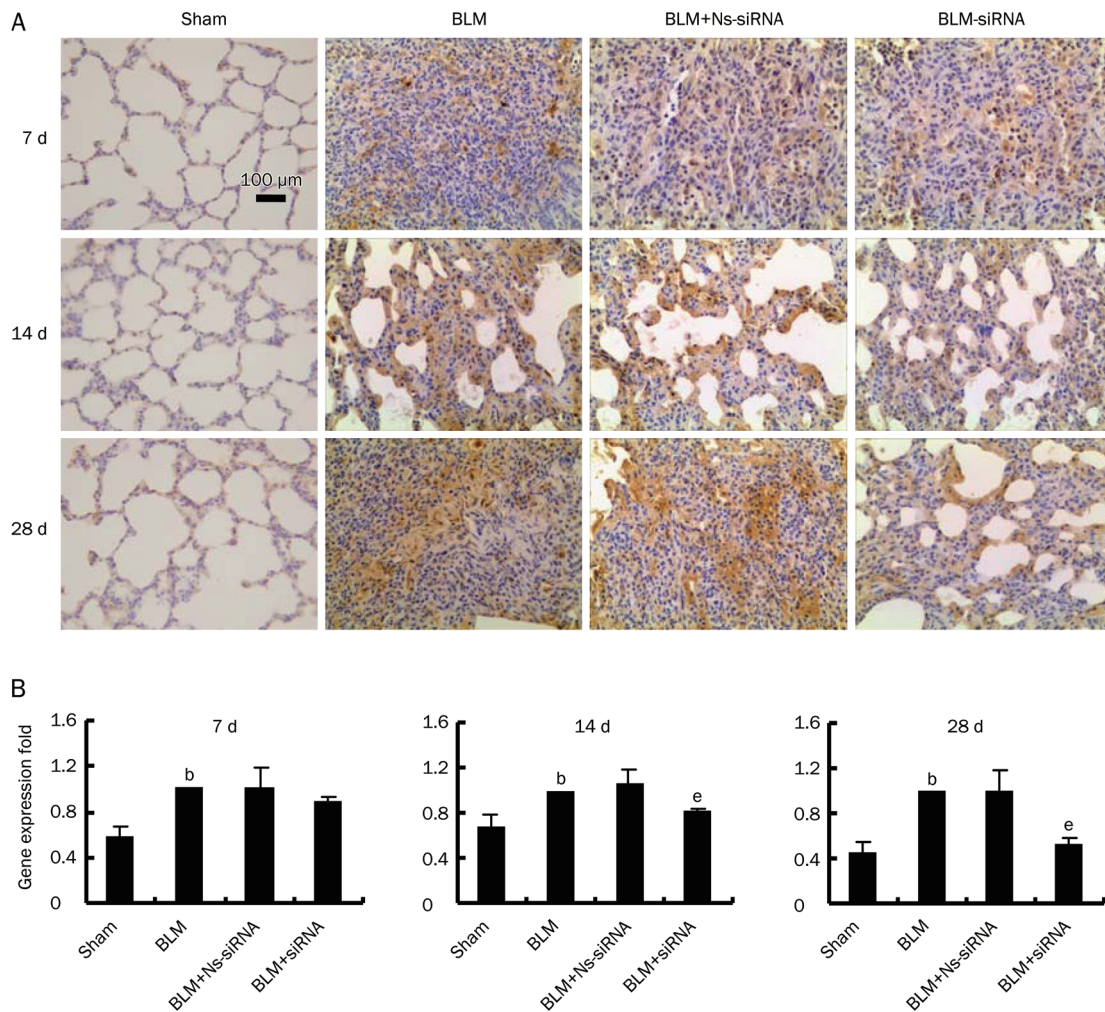


Figure 5. The expression of collagen type-III in the fibrotic lung tissue of the intratracheally bleomycin (BLM)-treated rats as assayed by immunohistochemical staining (A) and real time RT-PCR (B). Mean±SD. $n=6$. ^b $P<0.05$ vs sham group. ^e $P<0.05$ vs BLM group.

a week beginning during the alveolitis phase and extending through the fibrotic phase was performed in a BLM-induced model of rat lung injury. Intriguingly, the repeated administration of PAI-1 siRNA markedly downregulated PAI-1 gene and protein expression as well as the PAI-1 level in the BAL fluid. These findings indicate that repeated intratracheal injection is a highly effective approach for siRNA delivery to reduce PAI-1 levels.

Our study demonstrated that the expression of PAI-1 was increased in rats with BLM-induced lung fibrosis, and the PAI-1 activity in the BAL fluid increased gradually along with the exacerbation of lung fibrosis. Intriguingly, several studies have confirmed that PAI-1 was an important factor during the transformation of fibroblasts to myofibroblasts, which amplified the inflammatory response and resulted in the progression of fibrosis^[13-15]. Offersen *et al* observed that myofibroblasts were the predominant PAI-1-expressing cell in breast carcinomas based on immunohistochemistry double staining^[16]. Another study showed that the crucial step was the cleavage of the uPA receptor to D2D3 after binding of PAI-1 to uPA and

the uPA receptor during fibroblast-to-myofibroblast differentiation^[17]. Hu *et al* observed that hepatic fibrosis in rats could be ameliorated by downregulating the expression of PAI-1^[18]. Furthermore, Senoo *et al* reported that intranasal administration of PAI-1 siRNA attenuated the progression of pulmonary fibrosis^[10] and therefore suggested that PAI-1 might be an important factor capable of accelerating lung fibrosis. The present study provided additional direct evidence to support this assumption by observing the expression of PAI-1 in the fibrotic pulmonary tissue of BLM-treated rats. We found that intratracheal injection of PAI-1 siRNA significantly reduced the level of PAI-1 in the fibrotic pulmonary tissue of BLM-treated rats, and this suppression was accompanied by the amelioration of alveolitis, the inhibition of the transformation of fibroblasts through downregulation of the expression of α -SMA, and a reduction in the synthesis of collagen in fibrotic lung. These findings convincingly indicated that PAI-1 played an important role in the pathogenesis of BLM-induced lung fibrosis and that inhibition of PAI-1 expression with siRNA might be a potential therapeutic target for treatment of lung

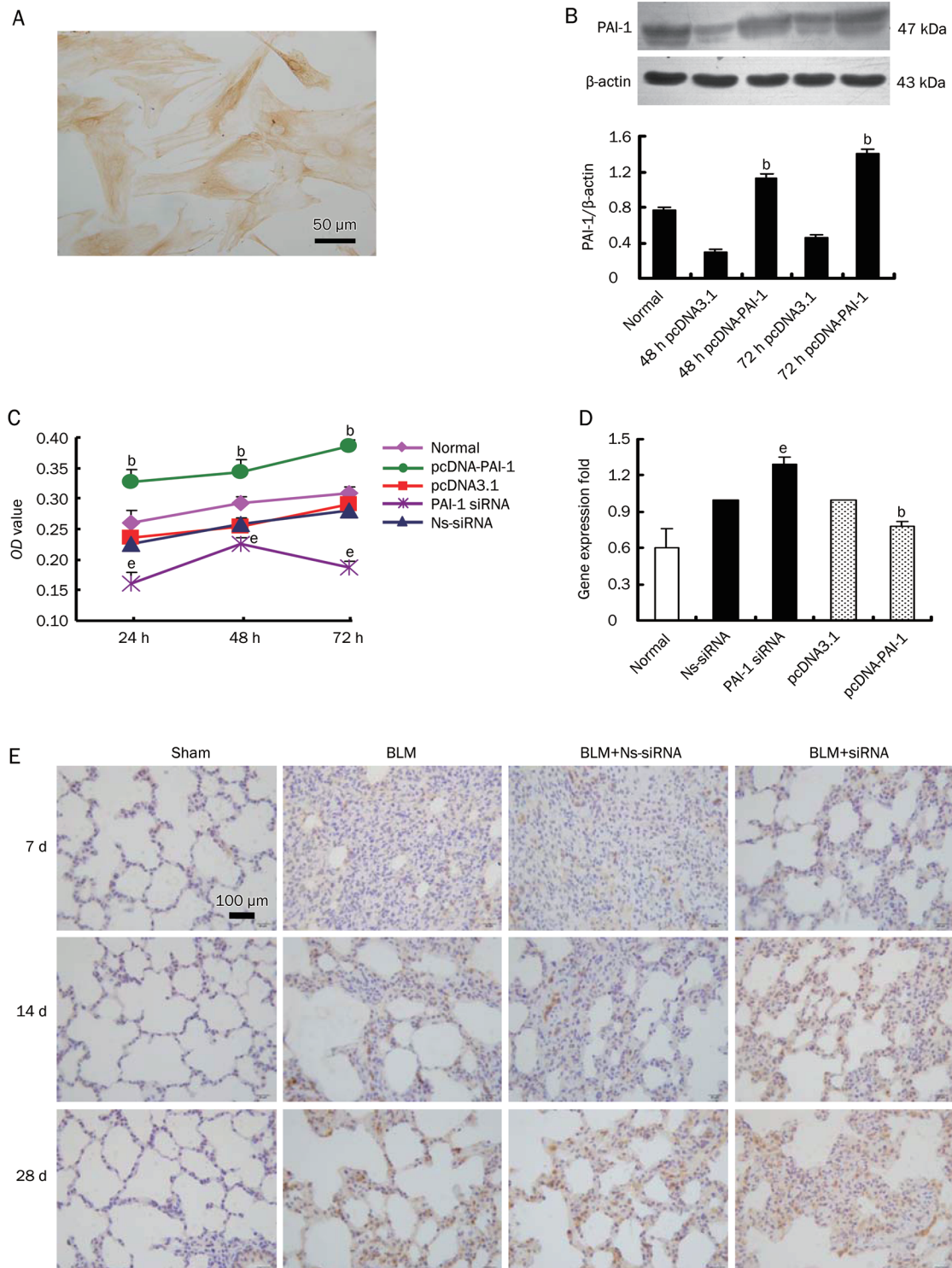


Figure 6. The effects of regulating PAI-1 expression on the proliferation and apoptosis of rat fibroblasts. Immunohistochemistry (A) shows that Vimentin was positively expressed, confirming that these cells are fibroblasts. The scale bar represents 50 μ m. Western blot analysis (B) shows the effect of plasmid pcDNA-PAI-1 on the expression of PAI-1 in fibroblasts. The line graph in panel (C) shows the effect on proliferation after down- or up-regulation of PAI-1 expression based on the MTT assay. Real time RT-PCR analysis (D) shows the caspase-3 expression after transfection with PAI-1 siRNA and pcDNA-PAI-1. Immunohistochemistry (E) shows the caspase-3 expression after intratracheal introduction of PAI-1 siRNA into BLM-induced lung tissue. The scale bar represents 100 μ m. Mean \pm SD. $n=6$. ^a $P<0.05$ vs pcDNA3.1. ^e $P<0.05$ vs Ns-siRNA.

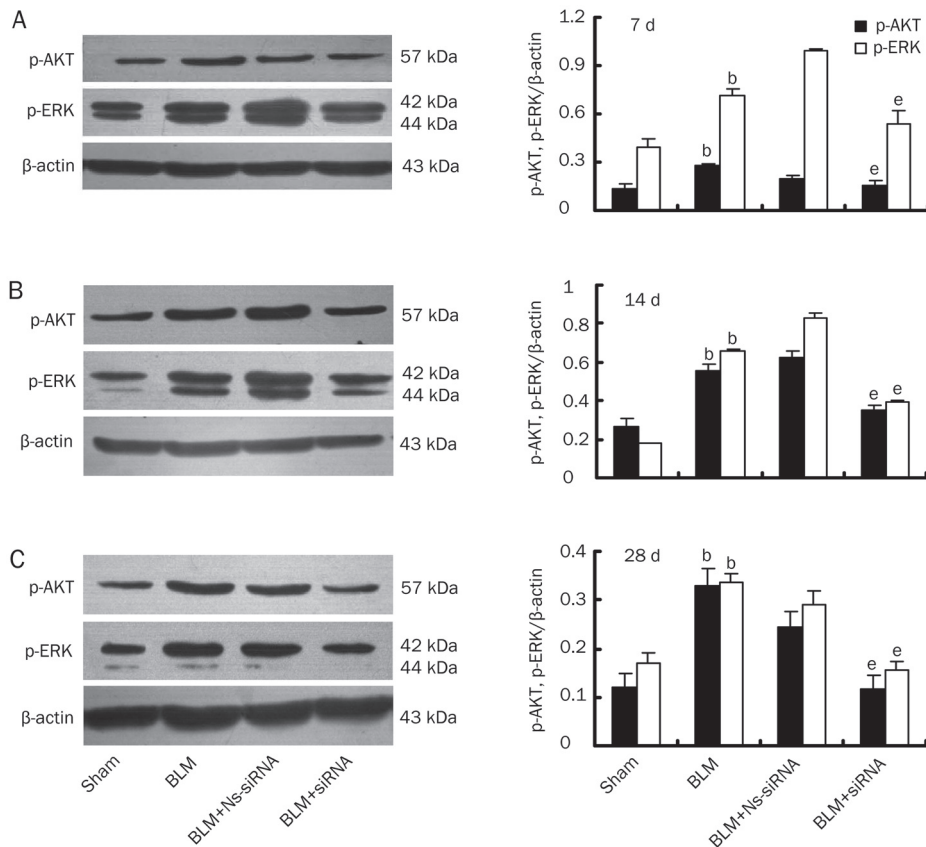


Figure 7. Western blot analysis shows the expression of phosphorylated-extracellular signal-regulated kinase 1/2 (p-ERK1/2) and phosphatidylinositol 3-phosphate kinase (PI3K)/Akt (p-AKT) in fibrotic lung tissue from bleomycin (BLM)-treated rats. The left panels are representative bands from a Western blotting, and the right panels show quantitative representations of the integral optical density (IOD) of the bands. The ratio between the IOD for the band of each target protein and that for β -actin is used for the statistical analysis. ^b $P < 0.05$ vs sham group, and ^e $P < 0.05$ vs BLM group.

fibrosis in a clinical setting.

PAI-1 regulates a variety of cellular processes, including adhesion, migration, detachment, angiogenesis, proliferation and apoptosis, *in vitro* and *in vivo*^[19, 20]. PAI-1 is a paradoxical protein that exerts different effects in various cell lines^[21–24]. Previous studies have shown that PAI-1 could protect fibrosarcoma cells from etoposide-induced apoptosis^[25] and augment the proliferation of vascular smooth muscle cells^[26]. To explore the mechanisms by which PAI-1 siRNA prevents lung fibrosis, we observed the effects of transfection of PAI-1 siRNA and pcDNA-PAI-1 on the proliferation and apoptosis of lung fibroblasts. *In vitro*, we found that downregulation of PAI-1 expression by PAI-1 siRNA could inhibit proliferation and promote the expression of caspase-3 of fibroblasts, whereas upregulation of PAI-1 expression by pcDNA-PAI-1 could promote fibroblast proliferation and inhibit the expression of caspase-3. These results revealed that PAI-1 siRNA inhibited lung fibrosis by promoting apoptosis by determining caspase-3 and suppressing the proliferation of fibroblasts. These findings represent new insights into the mechanisms underlying the anti-fibrotic effects of PAI-1 siRNA in the lungs. In a previous study, Senoo *et al* revealed that PAI-1 siRNA can inhibit lung fibrosis by inhibiting EMT induced by TGF- β in LA-4 cells^[18]. Bauman *et al* observed that plasminogen activation promoted the release of hepatocyte growth factor to promote prostaglandin E₂ (PGE₂) synthesis and fibroblast apoptosis^[27].

It is generally accepted that PAI-1 binding to uPA and the uPA receptor induces internalisation of the complex, thereby facilitating extracellular proteolysis as well as activation of growth factors and anti-apoptosis proteins^[28, 29]. Furthermore, these intermediates activate several signalling pathways. For example, the uPA-uPAR-PAI-1 complex interacts with integrins to induce focal adhesion kinase (FAK) and ERK activation^[30] via low-density lipoprotein receptor-related protein (LRP-1). This complex also regulates ras-related C3 botulinum toxin substrate 1 (Rac1) and ERK activation^[31], the JAK-STAT signalling pathway, the ERK/MAPK and PI3K/AKT pathways^[32], and it modulates the AKT pathway in wild-type and PAI-1-deficient endothelial cells^[33]. Therefore, it is possible that the ERK and AKT signalling pathways play an important role in IPF. Zhong *et al* demonstrated that selective inhibition of ERK1 by AdshERK1 could significantly attenuate the deposition of the extracellular matrix in fibrotic liver models^[34]. In the present study, we report that the expression of p-AKT and p-ERK was significantly increased in a BLM-induced model of lung fibrosis, whereas the expression of p-AKT and p-ERK was significantly decreased after downregulation of the expression of PAI-1 by siRNA. These results suggested that inhibition of the p-AKT and p-ERK protein levels may participate in the inhibition of proliferation and the stimulation of apoptosis observed in fibroblasts treated with PAI-1 siRNA. These results also suggested that the PI3K/AKT signaling pathway and the ERK-signalling pathway were involved in

IPF progression. This is another novel finding of the present study that has not been previously reported. Further investigation should be carried out regarding whether downregulation of the expression of ERK and AKT proteins ameliorates lung fibrosis.

In summary, our results indicate the existence of a significant functional role of PAI-1 in the development of lung fibrosis and suggest that PAI-1 is a potential target that is worth exploiting in the treatment of IPF by using PAI-1-targeted siRNA. In addition, we provide the first strong evidence that suppression of the levels of p-AKT and p-ERK in fibrotic lung tissue by PAI-1-targeted siRNA is associated with the suppression of fibroblast proliferation.

Acknowledgements

We gratefully acknowledge Dr Fang WANG for providing the plasmid pcDNA-PAI-1 and the vector pcDNA3.1; Dr Wenxin WU and Cui-qing MA for their technical assistance; and Madam Li-mei LIU for her assistance with the writing.

This work was funded by the National Natural Science Foundation of China (No. 30770738; No. 31040036; No. 81000477), the Key Base Research Project of Hebei Province (No. 11966121D), and the Natural Science Foundation of Hebei Province (No. C2009001161).

Author contribution

Yan-ping ZHANG and Wen-bin LI were responsible for the conception and design of the research. Yan-ping ZHANG, Wei-li WANG, and Jian LIU performed the experiments; Wei-li WANG and Lin-lin BAI analysed the data; Ya-dong YUAN and Min ZHANG interpreted the results of the experiments; Yu-yan HU prepared the figures; Yan-ping ZHANG drafted the manuscript; Wen-bin LI and Shu-xia SONG revised the manuscript; Yan-ping ZHANG and Wen-bin LI approved the final version of the manuscript;

References

- 1 Doubková M, Skhicková J. Idiopathic pulmonary fibrosis. *Vnitř Lek* 2005; 51: 1375–84.
- 2 Hinz B, Phan SH, Thannickal VJ, Galli A, Bochaton-Piallat ML, Gabbiani G. The myofibroblast: one function, multiple origins. *Am J Pathol* 2007; 170: 1807–16.
- 3 Hildenbrand R, Gandhari M, Stroebel P, Marx A, Allgayer H, Arens N. The urokinase-system-role of cell proliferation and apoptosis. *Histol Histopathol* 2008; 23: 227–36.
- 4 Bueno M, Salgado S, Beas-Zárate C, Armendariz-Borunda J. Urokinase-type plasminogen activator gene therapy in liver cirrhosis is mediated by collagens gene expression down-regulation and up-regulation of MMPs, HGF and VEGF. *J Gene Med* 2006; 8: 1291–9.
- 5 Hattori N, Mizuno S, Yoshida Y, Chin K, Mishima M, Sisson TH, *et al*. The plasminogen activation system reduces fibrosis in the lung by a hepatocyte growth factor-dependent mechanism. *Am J Pathol* 2004; 164: 1091–8.
- 6 Bertozzi P, Astedt B, Zenzius L, Lynch K, LeMaire F, Zapol W, *et al*. Depressed bronchoalveolar urokinase activity in patients with adult respiratory distress syndrome. *N Engl J Med* 1990; 322: 890–7.
- 7 Eitzman DT, McCoy RD, Zheng X, Fay WP, Shen T, Ginsburg D, *et al*. Bleomycin-induced pulmonary fibrosis in transgenic mice that either lack or overexpress the murine plasminogen activator inhibitor-1 gene. *J Clin Invest* 1996; 97: 232–7.
- 8 Chuang-Tsai S, Sisson TH, Hattori N, Tsai CG, Subbotina NM, Hanson KE, *et al*. Reduction in fibrotic tissue formation in mice genetically deficient in plasminogen activator inhibitor-1. *Am J Pathol* 2003; 163: 445–52.
- 9 Hu PF, Zhu YW, Zhong W, Chen YX, Lin Y, Zhang X, *et al*. Inhibition of plasminogen activator inhibitor-1 expression by siRNA in rat hepatic stellate cells. *J Gastroenterol Hepatol* 2008; 23: 1917–25.
- 10 Senoo T, Hattori N, Tanimoto T, Furonaka M, Ishikawa N, Fujitaka K, *et al*. Suppression of plasminogen activator inhibitor-1 by RNA interference attenuates pulmonary fibrosis. *Thorax* 2010; 65: 334–40.
- 11 Durcan N, Murphy C, Cryan SA. Inhalable siRNA: potential as a therapeutic agent in the lungs. *Mol Pharm* 2008; 5: 559–66.
- 12 Castanotto D, Rossi JJ. The promises and pitfalls of RNA-interference-based therapeutics. *Nature* 2009; 457: 426–33.
- 13 Thannickal VJ, Horowitz JC. Evolving concepts of apoptosis in idiopathic pulmonary fibrosis. *Proc Am Thorac Soc* 2006; 3: 350–6.
- 14 Hinz B, Gabbiani G. Cell-matrix and cell-cell contacts of myofibroblasts: role in connective tissue remodeling. *Thromb Haemost* 2003; 90: 993–1002.
- 15 Phan SH. The myofibroblast in pulmonary fibrosis. *Chest* 2002; 122: 286S–9S.
- 16 Offersen BV, Nielsen BS, Høyer-Hansen G, Rank F, Hamilton-Dutoit S, Overgaard J, *et al*. The myofibroblast is the predominant plasminogen activator inhibitor-1-expressing cell type in human breast carcinomas. *Am J Pathol* 2003; 163: 1887–99.
- 17 Bernstein AM, Twining SS, Warejcka DJ, Tall E, Masur SK. Urokinase receptor cleavage: a crucial step in fibroblast-to-myofibroblast differentiation. *Mol Bio Cell* 2007; 18: 2716–27.
- 18 Hu PF, Chen H, Zhong W, Lin Y, Zhang X, Chen YX, *et al*. Adenovirus-mediated transfer of siRNA against PAI-1 mRNA ameliorates hepatic fibrosis in rats. *J Hepatol* 2009; 51: 102–13.
- 19 Dellas C, Loskutoff DJ. Historical analysis of PAI-1 from its discovery to its potential role in cell motility and disease. *Thromb Haemost* 2005; 93: 631–40.
- 20 Binder BR, Mihaly J, Prager GW. UPAR-uPA-PAI-1 interactions and signaling: a vascular biologist's view. *Thromb Haemost* 2007; 97: 336–42.
- 21 Balsara RD, Ploplis VA. Plasminogen activator inhibitor-1: the double-edged sword in apoptosis. *Thromb Haemost* 2008; 100: 1029–36.
- 22 Lademann UA, Rømer MU. Regulation of programmed cell death by plasminogen activator inhibitor type 1 (PAI-1). *Thromb Haemost* 2008; 100: 1041–6.
- 23 Al-Fakhri N, Chavakis T, Schmidt-Wöhl T, Huang B, Cherian SM, Bobryshev YV, *et al*. Induction of apoptosis in vascular cells by plasminogen activator inhibitor-1 and high molecular weight kininogen correlates with their anti-adhesive properties. *Biol Chem* 2003; 384: 423–35.
- 24 Chen SC, Henry DO, Reczek PR, Wong MK. Plasminogen activator inhibitor-1 inhibits prostate tumor growth through endothelial apoptosis. *Mol Cancer Ther* 2008; 7: 1227–36.
- 25 Rømer MU, Larsen L, Offenbergh H, Brünner N, Lademann UA. Plasminogen activator inhibitor 1 protects fibrosarcoma cells from etoposide-induced apoptosis through activation of the PI3K/Akt cell survival pathway. *Neoplasia* 2008; 10: 1083–91.
- 26 Chen Y, Budd RC, Kelm RJ Jr, Sobel BE, Schneider DJ. Augmentation of proliferation of vascular smooth muscle cells by plasminogen activator inhibitor type 1. *Arterioscler Thromb Vasc Biol* 2006; 26:

- 1777–83.
- 27 Bauman KA, Wettlaufer SH, Okunishi K, Vannella KM, Stoolman JS, Huang SK, *et al*. The antifibrotic effects of plasminogen activation occur via prostaglandin E2 synthesis in humans and mice. *J Clin Invest* 2010; 120: 1950–60.
- 28 Huai Q, Mazar AP, Kuo A, Parry GC, Shaw DE, Callahan J, *et al*. Structure of human urokinase plasminogen activator in complex with its receptor. *Science* 2006; 311: 656–9.
- 29 Horowitz JC, Rogers DS, Simon RH, Sisson TH, Thannickal VJ. Plasminogen activation induced pericellular fibronectin proteolysis promotes fibroblast apoptosis. *Am J Respir Cell Mol Biol* 2008; 38: 78–87.
- 30 Aguirre-Ghiso JA, Estrada Y, Liu D, Ossowski L. ERK (MAPK) activity as a determinant of tumor growth and dormancy; regulation by p38 (SAPK). *Cancer Res* 2003; 63: 1684–95.
- 31 Ma Z, Thomas KS, Webb DJ, Moravec R, Salicioni AM, Mars WM, *et al*. Regulation of Rac1 activation by the low density lipoprotein receptor-related protein. *J Cell Biol* 2002; 159: 1061–70.
- 32 Kiian I, Tkachuk N, Haller H, Dumler I. Urokinase-induced migration of human vascular smooth muscle cells requires coupling of the small GTPases RhoA and Rac1 to the Tyk2/PI3-K signalling pathway. *Thromb Haemost* 2003; 89: 904–14.
- 33 Balsara RD, Castellino FJ, Ploplis VA. A novel function of plasminogen activator inhibitor-1 in modulation of the AKT pathway in wild-type and plasminogen activator inhibitor-1-deficient endothelial cells. *J Biol Chem* 2006; 281: 22527–36.
- 34 Zhong W, Shen WF, Ning BF, Hu PF, Lin Y, Yue HY, *et al*. Inhibition of extracellular signal-regulated kinase 1 by adenovirus mediated small interfering RNA attenuates hepatic fibrosis in rats. *Hepatology* 2009; 50: 1524–36.

Original Article

Tissue cholesterol content alterations in streptozotocin-induced diabetic rats

Xin-ting WANG, Jia LI, Li LIU, Nan HU, Shi JIN, Can LIU, Dan MEI, Xiao-dong LIU*

Key Laboratory of Drug Metabolism and Pharmacokinetics, China Pharmaceutical University, Nanjing 210009, China

Aim: Diabetes is associated with elevated serum total cholesterol level and disrupted lipoprotein subfractions. The aim of this study was to examine alterations in the tissue cholesterol contents closely related to diabetic complications.

Methods: Intraperitoneal injection of streptozotocin was used to induce type 1 diabetes in adult male Sprague-Dawley rats. On d 35 after the injection, liver, heart, intestine, kidney, pancreas, cerebral cortex and hippocampus were isolated from the rats. The content of total and free cholesterol in the tissues was determined using HPLC. The ATP-binding cassette protein A1 (ABCA1) protein and ApoE mRNA were measured using Western blot and QT-PCR analyses, respectively.

Results: In diabetic rats, the level of free cholesterol was significantly decreased in the peripheral tissues, but significantly elevated in hippocampus, as compared with those in the control rats. Diabetic rats showed a trend of decreasing the total cholesterol level in the peripheral tissues, but significant change was only found in kidney and liver. In diabetic rats, the level of the ABCA1 protein was significantly increased in the peripheral tissues and cerebral cortex; the expression of ApoE mRNA was slightly decreased in hippocampus and cerebral cortex, but the change had no statistical significance.

Conclusion: Type 1 diabetes decreases the free cholesterol content in the peripheral tissues and increases the free cholesterol content in hippocampus. The decreased free cholesterol level in the peripheral tissues may be partly due to the increased expression of the ABCA1 protein.

Keywords: diabetes; cholesterol; ABCA1; liver X receptor; apolipoprotein E

Acta Pharmacologica Sinica (2012) 33: 909–917; doi: 10.1038/aps.2012.50; published online 18 Jun 2012

Introduction

The maintenance of cellular cholesterol homeostasis is important for normal physiological processes. Type 1 diabetes mellitus (T1DM) is associated with an imbalance of cholesterol homeostasis, which results in an increased risk of death in diabetic patients. It has been estimated that 51% of patients with type 1 diabetes mellitus in the US and Europe showed hypercholesterolemia^[1]. The accumulation of esterified cholesterol in macrophages is an essential step in the progression of atherosclerotic lesions^[2]. Animal experiments showed that an induction of hypercholesterolemia in mice triggered a rapid ingestion of lipid by resident intimal dendritic cells, which led to nascent foam cell lesion formation^[3] and exaggerated atherosclerosis^[4]. Disordered cholesterol homeostasis induced by diabetes also affects other physiological processes. A report showed that the red blood cell membranes from diabetic patients became rigid due to changes in the cholesterol-

to-phospholipid ratio, which resulted in microangiopathic hemolytic anemia^[5]. Accumulating epidemiological evidence shows that there is a clear link between cholesterol levels and neurodegenerative diseases including Alzheimer's disease (AD) and Parkinson's disease^[6,7].

Type 1 diabetes mellitus is a chronic metabolic syndrome characterized by complications including macrovascular and microvascular diseases. Alterations of cholesterol levels in tissues may be a factor contributing to the diabetic complications. However, previous cholesterol disorder studies focused on the serum or macrophages, and information on tissues under diabetic states has not been fully examined. An important way to maintain cellular cholesterol homeostasis is reverse cholesterol transport (RCT) via cholesterol transporters^[8]. ATP-binding cassette protein A1 (ABCA1) is an important rate-controlling protein in reverse cholesterol transport. Several reports showed that the expression of the ABCA1 protein was altered under diabetic states^[9,10].

The aim of this study was to investigate the cholesterol content in tissues related to cholesterol metabolism and diabetic complications using streptozotocin (STZ)-induced diabetic

* To whom correspondence should be addressed.

E-mail xdlu@cpcu.edu.cn

Received 2012-02-10 Accepted 2012-04-11

rats. The expression of the ABCA1 protein, the liver X receptor (LXR) and ApoE mRNA were measured using Western blot and quantitative real-time PCR (QT-PCR) analyses, respectively.

Materials and methods

Materials

Cholesterol was purchased from Aladdin Reagents (Shanghai Jingchun Chemical Co Ltd, Shanghai, China). Streptozotocin was supplied by Sigma-Aldrich (St Louis, MO, USA). The internal standard stigmaterol was supplied by Acros Organics (Geel, Belgium). The 7 α -hydroxycholesterol (7 α -HC) was supplied by Toronto Research Chemicals (TRC; Ontario, Canada). Water was purified using a Milli-Q system (Millipore, Bedford, MA, USA). All other chemicals were of HPLC grade and commercially available.

Animals

Male Sprague-Dawley (SD) rats, which weighed 160–170 g, were supplied by SLAC Laboratory Animals (Shanghai, China). The rats were maintained in an air-conditioned animal facility at a temperature of 22 \pm 2 $^{\circ}$ C and a relative humidity of 50% \pm 10% on a 12-h day/night cycle. A standard commercial rodent diet (Xietong BioTech, Nanjing, China) and water were provided *ad libitum*. The animals were acclimatized to the facilities for 5 d and fasted with free access to water for 8 h prior to experimentation. All animal experiments were approved by the Animal Ethics Committee of China Pharmaceutical University.

Diabetic rats induced by STZ

Diabetes was induced in the rats by an intraperitoneal administration of 65 mg/kg of STZ dissolved in sodium citrate buffer (pH 4.5). The age-matched normal rats only received the vehicle (sodium citrate buffer, pH 4.5). On d 7 post-STZ injection, the fasting blood glucose levels were measured using a commercially available glucose kit (Rongsheng BioTech Co Ltd, Shanghai, China) based on the glucose oxidase method. Rats with fasting blood glucose levels in excess of 11.1 mmol/L were considered to be diabetic and were included in subsequent experiments.

Animal experiments

All the animal experiments were conducted on d 35 after the injection of STZ or vehicle. Rats were euthanized under ether anesthesia after an 8-h fast. Blood and the tissues closely related to diabetic symptoms and cholesterol metabolism, including the heart, liver, intestine, kidney, pancreas, cerebral cortex and hippocampus, were immediately collected. Serum samples were obtained for the analysis of biochemical parameters, including triglycerides, insulin, HDL cholesterol, glucose, total cholesterol (TC), free cholesterol (FC) and its metabolite 7 α -HC. Tissues were used for the determination of TC, FC and insulin levels using Western blot and QT-PCR analyses. The levels of serum triglycerides and HDL cholesterol were measured using colorimetric kits (Beijing BHKT

Clinical Reagent Co, Ltd, Beijing, China). Serum glucose levels were measured using a glucose oxidase method kit. The levels of insulin in the serum and tissues were measured by an insulin radioimmunoassay (RIA) kit (Beijing North Institute of Biological Technology, Beijing, China) according to the manufacturer's protocol. Tissues were weighed and homogenized in equal volumes of 50 mmol/L NaH₂PO₄ and 50 mmol/L Na₂HPO₄ buffer containing 1% bovine serum albumin (pH 7.4). An aliquot of 100 μ L of tissue homogenate or serum was used for the determination of insulin levels.

Determination of TC, FC and 7 α -HC levels in serum and tissues

The levels of cholesterol in the serum and tissues were measured using the HPLC method^[11]. The levels of cholesterol were represented as FC (prior to hydrolysis) and TC (after hydrolysis). The tissues were weighed and homogenized in (1:10) cold saline (*w/v*) under an ice-bath condition. The homogenates were diluted using saline when necessary. For the measurement of TC, 50 μ L of serum or tissue homogenate was hydrolyzed in a 50 $^{\circ}$ C water bath for 2 h in 500 μ L of alcoholic potassium hydroxide solution [33% KOH/ethanol (6/94, *v/v*)]^[12]. A 50- μ L aliquot of the hydrolyzed mixture was extracted with 1 mL of n-hexane by vortexing for 5 min. For the measurement of FC, unhydrolyzed serum or tissue homogenates were subjected to the same extraction method. After centrifugation at 2000 \times g for 5 min, 400 μ L of the upper organic layer was transferred to a tube containing 200 ng of stigmaterol (internal standard) and evaporated to dryness under nitrogen. The residues were reconstituted in 400 μ L of acetone and subjected to Jones oxidation^[11]. Briefly, the samples were treated with a derivative agent (equal volumes of 2 mol/L chromic acid and 2 mol/L sulfuric acid) in acetone for 5 min in a 25 $^{\circ}$ C water bath. At the end of the reaction, 550 μ L of water was added. The derivative of cholesterol was extracted with n-hexane, dried under nitrogen and reconstituted in 200 μ L of methanol. After centrifugation, 20 μ L of the supernatant was injected into a Shimadzu LC-10Avp system (Shimadzu, Japan) consisting of an LC-10Avp liquid chromatographic pump, a Shimadzu VP-ODS column (5.0 μ m; 150 mm \times 4.6 mm id) and an SPD-10Avp ultraviolet detector operating at a wavelength of 250 nm. The mobile phase consisted of methanol/water (98/2, *v/v*). The flow rate was maintained at 1.0 mL/min. The derivative of cholesterol was stable within the analyzing time ranges (24 h), and the recovery was larger than 80%. The linearity of free cholesterol was between 3.9 μ g/mL and 250 μ g/mL while that of total cholesterol was between 15.6 μ g/mL and 1.0 mg/mL.

The levels of 7 α -HC in serum were measured using the liquid chromatography mass spectrometry (LC-MS) method according to a previously described method^[13] with minor modifications. Briefly, 200 μ L of serum was saponified in 0.5 mL of 1 mol/L ethanolic NaOH for 1 h at 37 $^{\circ}$ C in a shaking water bath. The mixture was extracted by adding 1 mL of n-hexane and isopropyl alcohol (9:1, *v/v*) and vortexing for 5 min. After centrifugation at 2000 \times g for 5 min, 0.8 mL of the upper organic layer was transferred to a tube containing 100

ng of stigmasterol as an internal standard and evaporated to dryness under nitrogen. The residues were then reconstituted in 100 μ L of methanol, which was followed by centrifugation at 37000 \times g for 10 min. An aliquot of 10 μ L was injected into the LC-MS system.

LC separation was achieved on a Shimadzu VP-ODS column (5.0 μ m; 150 mm \times 4.6 mm id; Shimadzu, Japan) maintained at 40°C. The mobile phase consisted of methanol and water (98:2), and the flow rate was maintained at 1.0 mL/min. The effluent from the HPLC column was directed into an atomic pressure chemical ionization (APCI) probe. The mass spectrometer conditions were optimized to obtain maximal sensitivity. The optimized APCI conditions employed included a DL temperature of 250°C and an interface temperature of 350°C, and the heating block temperature was maintained at 250°C. The nebulizing and drying gas were maintained at 4 L/min and 10 L/min, respectively. The selected ion monitoring (SIM) including a series of ions with m/z 385.35, and 395.4 [M+H-H₂O]⁺ that corresponded to 7 α -HC and internal standard (IS) was used for the quantitative analysis. The data were acquired, processed and analyzed by Lab Solutions chromatographic software (Shimadzu, Japan). An assay validation was carried out. No matrix effect was observed for either 7 α -HC or the IS. The intra-day relative standard deviation of 7 α -HC was lower than 5%. The linear range of 7 α -HC in the serum was between 31.25 ng/mL and 250 ng/mL. The lowest limit for the quantification of 7 α -HC in the serum was 31.25 ng/mL.

Western blot analysis

Western blot analysis was used for quantification of the ABCA1 protein in the tissues. Briefly, tissues were weighed and homogenized in RIPA (radioimmunoprecipitation) buffer (Applygen Technologies Inc, Beijing, China). The protein concentration was determined by the Bio-Rad Protein Assay (Bio-Rad Labs, Richmond, CA, USA). Different amounts of protein (120, 80, 100, 100, 80, 80, and 160 μ g for the intestine, liver, hippocampus, cerebral cortex, kidney, heart and pancreas, respectively) were separated by SDS-PAGE and transferred to polyvinylidene difluoride (PVDF) membranes. ABCA1 was detected using a rabbit anti-rat monoclonal ABCA1 antibody (Abcam, USA) as the primary antibody and horseradish peroxidase (HRP)-conjugated goat anti-rabbit IgG (GeneScript, Nanjing, China) as the secondary antibody. Anti-GAPDH (GeneScript, Nanjing, China) was used as an internal protein-loading control. Detection of the ABCA1 protein band was performed with an enhanced chemiluminescence (ECL) kit (Haigene, Harbin, China), and the densitometry of the subsequent images were analyzed by ImageJ software (Bio-Rad, Hercules, USA).

QT-PCR analysis

For a quantitative comparison of the LXR- α , LXR- β , and ApoE mRNA levels, QT-PCR was performed using SYBR Green fluorescence. Total RNA was extracted with TRIzol reagent (Sun-ShineBio, Nanjing, China) from frozen tissues according to the

manufacturer's instructions. The primers for the LXR- α , LXR- β , and ApoE sequences are listed in Table 1. The RNA concentration was quantified by spectrophotometry at 260 nm. Total RNA from each original sample was converted into cDNA, and QT-PCR was performed in a PTC-200 Thermo Cycler (MJ Research, Waltham, USA) according to the manufacturer's protocols. The amplification was performed in a 26.5- μ L reaction mixture that consisted of the following: 12.5 μ L of qPCR Master Mix (Promega, Madison, WI, USA), 2.0 μ L of 10 \times cDNA, 2.5 μ L of 2 μ mol/L forward and reverse primers and 9.5 μ L of nuclease-free water. Each assay was performed in triplicate with β -actin mRNA as the endogenous control. The QT-PCR thermal cycling parameters were an initial denaturation for 2 min at 95°C that was followed by 40 cycles at 95°C for 5 s and 60°C for 30 s. Melting curves were performed to investigate the specificity of the PCR reaction. Relative quantification (RQ) of each gene expression was calculated according to the comparative Ct method using the formula: $RQ=2^{-\Delta C_t^{[14]}}$.

Table 1. Primer sequences for QT-PCR.

DNA amplified	Primer sequence 5'→3'	Size (bp)
LXR- α	Sense	AGCAACAGTGTAAACAGGCGCT
	Antisense	GTGCAATGGGCCAAGGC
LXR- β	Sense	CAACCACGAGACAGAGTGCATCA
	Antisense	GCATAGCCCCGAGAGAACTCAAAG
Apo E	Sense	ACCGCTTCTGGGATTACCTGC
	Antisense	ATGCCCTTACTTCCGTCATAGTGTC
β -Actin	Sense	GGGAAATCGTGCGTGACATT
	Antisense	GCGGCAGTGGCCATCTC

Statistical analysis

The data are presented as the mean \pm standard deviation (SD). Statistical comparisons were made using the 2-tailed Student's *t*-test. A *P* value less than 0.05 was considered significant.

Results

Biochemical parameters in STZ-induced diabetic rats

STZ-induced diabetes is a well-documented model of experimental T1DM^[15]. As expected, a single administration of STZ to rats produced diabetic symptoms, including polyphagia, polyuria, polydipsia and a loss of body weight. Biochemical parameters in the serum of the STZ-induced rats and normal rats were obtained (Table 2). It was found that diabetes dramatically increased the serum levels of glucose, FC, TC, and triglycerides, which was accompanied by a low level of insulin. Diabetes also significantly elevated the level of 7 α -HC, which is a metabolite of cholesterol. The levels of HDL cholesterol in the serum of diabetic rats showed a tendency to decrease, but no significance was observed.

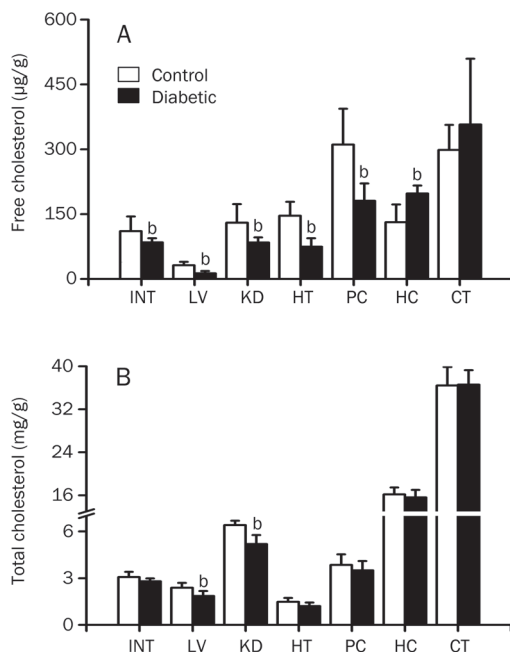
Cholesterol content in tissues of STZ-induced diabetic rats

The cholesterol content in the intestine, heart, kidney, liver,

Table 2. Serum biochemical parameters of rats 5 weeks after injection of STZ. Mean±SD. *n*=6. ^b*P*<0.05 vs control rats.

Parameters	Control	Diabetes
Initial body weight (g)	162.8±2.5	171.4±2.3 ^b
Final body weight (g)	361.0±25.8	210.8±23.0 ^b
Glucose (mmol/L)	6.10±0.52	20.52±3.22 ^b
Triglycerides (mmol/L)	2.50±0.60	3.28±0.37 ^b
HDL cholesterol (mg/mL)	0.40±0.06	0.36±0.04
Insulin (mIU/mL)	0.07±0.01	0.04±0.002 ^b
Free cholesterol (μg/mL)	27.36±8.96	65.83±27.65 ^b
Total cholesterol (mg/mL)	0.81±0.1	1.51±0.51 ^b
7α-hydroxycholesterol (ng/mL)	106.20±43.81	237.23±94.30 ^b

hippocampus, cerebral cortex and pancreas of STZ-induced diabetic rats was measured (Figure 1). The levels of cholesterol are presented as FC and TC. The results showed that the cholesterol in tissues existed mainly as TC. High levels of TC were observed in the hippocampus (16.2 mg/g tissue) and cerebral cortex (36.4 mg/g tissue). Only a small portion of cholesterol existed as FC in most tissues. For example, the free fractions of cholesterol in the hippocampus and cerebral cortex were less than 1%. Interestingly, the pancreas and heart had lower contents of TC (1.5 mg/g in the heart and 3.9 mg/g in the pancreas) but showed high concentrations of FC (146.5 mg/g in the heart and 310.9 mg/g in the pancreas), which resulted in fractions of FC in the two tissues of 9.8% and 7.9%,

**Figure 1.** The levels of free cholesterol (A) and total cholesterol (B) in the intestine (INT), liver (LV), kidney (KD), heart (HT), pancreas (PC), hippocampus (HC) and cerebral cortex (CT) of control rats (white bars) and diabetic rats (black bars). Cholesterol was determined by HPLC analysis. Values are expressed as the mean±SD (*n*=6). ^b*P*<0.05 vs control rats.

respectively.

Diabetes significantly decreased the levels of FC in the peripheral tissues. Diabetes also decreased the TC level in peripheral tissues, but significance was only found for the kidney and liver. The extent of decreased levels of FC was greater than that of TC in the corresponding tissues, which indicated that FC was more sensitive to diabetes. In contrast, diabetes increased the levels of FC in both the hippocampus and cerebral cortex. A significant increase (50.4%) was found in the hippocampi of diabetic rats, but the cerebral cortex (19.8%) only showed a tendency to increase.

Insulin levels in tissues of STZ-induced diabetic rats

Insulin levels in the tissues of diabetic rats were assayed using the RIA method (Table 3). The results showed that the effects of diabetes on the insulin levels in tissues were tissue-dependent. Diabetes significantly reduced the insulin levels in the liver, pancreas and intestine, resulting in a 38.5%, 33.0%, and 63.0% decrease, respectively, compared with the levels in normal rats. However, the insulin levels in the kidney, heart, hippocampus and cerebral cortex of STZ-induced diabetic rats remained unchanged or only slightly decreased.

Table 3. Tissue insulin levels in control and STZ-induced diabetic rats. Insulin was determined by RIA method. Mean±SD. *n*=6. ^b*P*<0.05 vs control rats.

Insulin (mIU/g)	Control	Diabetes
Liver	1.54±0.23	0.94±0.07 ^b
Intestine	4.12±0.92	1.52±0.61 ^b
Kidney	1.28±0.27	1.25±0.24
Heart	0.84±0.24	0.79±0.57
Hippocampus	1.14±0.24	1.25±0.15
Cortex	1.02±0.09	0.94±0.08
Pancreas	645.56±76.74	432.27±104.24 ^b

Expression of ABCA1 protein in tissues of STZ-induced diabetic rats

ABCA1 is the rate-controlling transporter in reverse cholesterol transport, which plays the most important role in the maintenance of cellular cholesterol homeostasis^[16,17]. To investigate whether the alteration in cholesterol in the tissues of diabetic rats came from a change in ABCA1 expression, the levels of the ABCA1 protein in the tissues were measured using Western blot analysis. The results showed that the heart and cerebral cortex exhibited the highest basal expression of the ABCA1 protein (Figure 2). The pancreas showed only a weak basal expression of the ABCA1 protein. The expression of the ABCA1 protein was induced by diabetes. The strongest induction occurred in the pancreas of diabetic rats, which resulted in an 11.7-fold increase compared with normal rats. Diabetes also increased the expression of ABCA1 in the liver, kidney and cerebral cortex to 105.6%, 314.5%, and 53.9%, respectively,

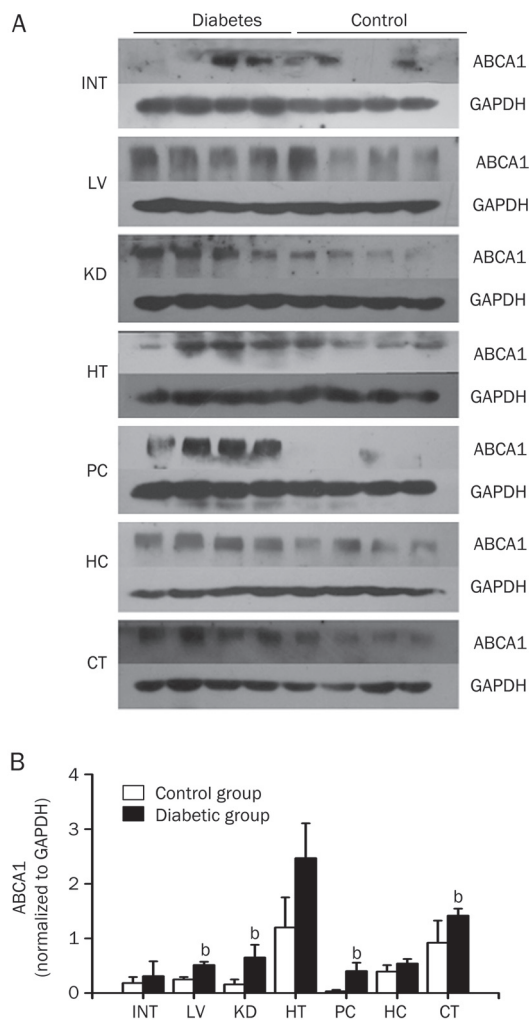


Figure 2. The levels of ABCA1 expression in the intestine (INT), liver (LV), kidney (KD), heart (HT), pancreas (PC), cerebral cortex (CT) and hippocampus (HC) of control rats (white bars) and diabetic rats (black bars). Western blots of ABCA1 (A) and the ratio of relative staining intensity for ABCA1 (B) in the control and STZ-induced diabetic rats are shown. Mean \pm SD ($n=4$). ^b $P<0.05$ vs control rats.

of the expression in the normal rats. The expression of the ABCA1 protein in the heart of diabetic rats also increased by 105.7% compared with normal rats, although no significance was observed. The increased expression of the ABCA1 protein in the peripheral tissues was in agreement with decreases in the concentration of cholesterol in the corresponding tissues.

Expression of LXR- α , LXR- β , and ApoE mRNA in tissues of STZ-induced diabetic rats

It is generally acknowledged that ABCA1 expression in tissues is mainly modulated by the nuclear receptors LXR- α and LXR- β . The mRNA levels of these genes were measured using QT-PCR. The results showed that the expression of LXR mRNA in the tissues of rats was tissue-dependent and LXR subtype-dependent.

For LXR- α mRNA, the highest expression was observed in

the liver, and a modest expression was found in the pancreas, kidney, intestine and heart (Figure 3A). The hippocampus and cerebral cortex showed only a weak expression of LXR- α mRNA. The expression of LXR- α mRNA in the intestine, liver and pancreas tissues was 5–10-fold higher than that of LXR- β mRNA in the corresponding tissues. Diabetes significantly induced the LXR- α mRNA levels in the liver, kidney and heart. The strongest induction of LXR- α mRNA was found in the heart of diabetic rats, which showed a 2.64-fold increase compared with normal rats. However, diabetes only marginally increased or did not alter the expression of LXR- α mRNA in the intestine, pancreas, hippocampus and cerebral cortex.

For LXR- β mRNA, a lower expression of LXR- β mRNA was found in the intestine, liver, heart, kidney and pancreas tissues compared with LXR- α mRNA (Figure 3B). Diabetes signifi-

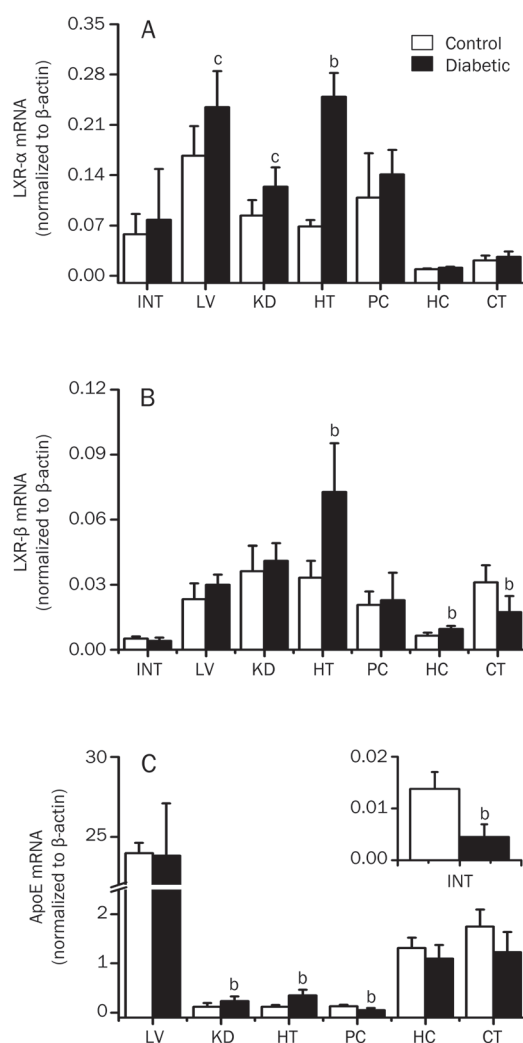


Figure 3. The levels of LXR- α (A), LXR- β (B), and ApoE (C) mRNA in the intestine (INT), liver (LV), kidney (KD), heart (HT), pancreas (PC), cerebral cortex (CT) and hippocampus (HC) of the control rats (white bars) and diabetic rats (black bars). The levels of LXR- α , LXR- β , and ApoE mRNA were determined by QT-PCR analysis, and all values were normalized to the levels of β -actin mRNA. The data are expressed as $2^{-\Delta\Delta Ct}$ values of mean \pm SD ($n=4$). ^b $P<0.05$, ^c $P<0.01$ versus control rats.

cantly elevated the expression of LXR- β mRNA in the heart and hippocampus and decreased the expression of LXR- β mRNA in the cerebral cortex. However, diabetes did not affect the expression of the gene in other tissues. Similar to LXR- α mRNA, the strongest induction of LXR- β mRNA occurred in the heart of diabetic rats, which showed a 1.18-fold increase compared with control rats.

It is generally accepted that ApoE, the main apolipoprotein in the brain, is crucial for brain cholesterol homeostasis^[18-21]. The levels of ApoE mRNA in the indicated tissues were measured, and the results showed a high expression of ApoE mRNA in the liver, hippocampus and cerebral cortex (Figure 3C). Other tissues showed only a low level of ApoE mRNA. Diabetes significantly increased the levels of ApoE mRNA in the kidney and heart and decreased the mRNA levels in the pancreas and intestine. Diabetes also decreased the ApoE mRNA level in the hippocampus (16.3%) and cerebral cortex (29.9%), although no significance was observed.

Discussion

The main findings of this study were that the effects of diabetes on the cholesterol content in the brain and peripheral tissues were different. Diabetes increased the FC levels in the hippocampus and cerebral cortex without altering the TC content but decreased both the FC and TC levels in the liver, kidney, heart, intestine and pancreas. It is noteworthy that the magnitude of tissue TC level changes under diabetic conditions was smaller than that of the serum FC and TC levels. This may derive from the fact that the serum cholesterol existed almost exclusively in a rapidly exchangeable pool, while the tissue cholesterol consisted of both a slowly exchanging pool and a nonexchangeable pool^[22, 23], which made the serum cholesterol more susceptible to diabetes than the tissue cholesterol.

Several reports have shown that diabetes increases the TC levels in the liver, kidney and heart of type 2 diabetic rats^[24, 25], which is in contrast with the present findings. The quantitative method used in these studies may be an important reason for the differences. The method^[24, 25] used in these studies was that the reaction of cholesterol in the presence of an FeCl₃-H₃PO₄-H₂SO₄ mixture forms a colored complex, which was measured using spectrophotometer. A previous study proved that other sterols might interfere with the quantification of cholesterol by this method, thus resulting in large errors^[26]. Another report also showed that the colorimetric method would generate a value roughly 50% higher than other methods^[27]. All the results indicated that the selectivity and accuracy of the colorimetric method was inferior to the HPLC method that was used in the present study. In addition, STZ-induced type 1 diabetes is characterized by an insulin deficiency, suggesting that the lack of insulin may also be one of the reasons for the discrepancies.

It has generally been accepted that ABCA1 is a key transporter of cholesterol efflux. The present study showed that diabetes increased the ABCA1 protein level in peripheral tissues, which suggested that the decreased FC and TC content was partly due to increases in the expression of ABCA1. How-

ever, other reports describing the expression of the ABCA1 protein under diabetic states are often controversial. A study using virus-induced diabetic mice and type 1 non-obese diabetic mice^[10] showed that diabetes slightly increased the expression of ABCA1 in liver, decreased ABCA1 protein levels in peritoneal macrophages and kidney, and did not affect the ABCA1 protein level in the brain. Another study^[28] showed that the expression of ABCA1 mRNA was decreased in the liver and peritoneal macrophages of STZ-induced diabetic mice. There was also a report showing that the expression of ABCA1 mRNA increased in the aorta of insulin-insufficient mice^[9], which was consistent with our findings. All these results infer that the differences in ABCA1 expression under diabetic conditions might derive from the methodology, animal models, type of diabetes and its duration.

Elevated expression of the ABCA1 protein was also found in the hippocampus and cerebral cortex of diabetic rats, but this did not explain the fact that the levels of FC increased. It is not clear what mechanisms are responsible for increasing the FC levels in the hippocampus and cerebral cortex. ApoE is considered to be a major apolipoprotein for cholesterol transport and clearance in the brain^[18-21]. The data from QT-PCR showed that apart from the liver, the peripheral tissues exhibited a low level of ApoE mRNA, which was in accordance with the fact that the liver is the primary organ for ApoE secretion^[29]. Contrary to the low expression of ApoE mRNA in all the studied peripheral tissues except the liver, high levels of ApoE mRNA were found in the hippocampus and cerebral cortex. Further study showed that diabetes decreased ApoE mRNA in the hippocampus and cerebral cortex by 16.3% and 29.9%, respectively, although no significance was found. Similar phenomena were also observed in alloxan-induced diabetic rabbits^[30]. This indicated that the suppression of ApoE mRNA might at least partly contribute to the increased FC content under diabetic states. Other mechanisms may also be involved in the regulation of cholesterol homeostasis in the brain. All cholesterol input into the central nervous system comes from *de novo* synthesis^[31]. A small excess of cholesterol is exported into the circulation to maintain cholesterol homeostasis in the brain. Two mechanisms are involved in this process. One is reverse cholesterol transport, which is mediated by ABC transporters, the class A scavenger receptor and ApoE. The other important pathway is the conversion of cholesterol into oxysterols^[32]. In contrast to cholesterol, oxysterols are able to traverse the blood-brain barrier. These facts suggest that alterations in these factors may contribute to the increased levels of cholesterol in the brain of diabetic rats. In addition, oxidative stress may also be involved in the elevated brain cholesterol levels under diabetic conditions^[33]. Further studies are still needed to elucidate this issue.

This study showed that diabetes increased the expression of the ABCA1 protein in the indicated tissues, but the underlying mechanism is not clear. A report showed that insulin could enhance the degradation of ABCA1 and downregulate its activity by promoting the phosphorylation of the protein^[34], which suggested that an insulin deficiency may be one of the

causes for increased ABCA1 protein levels under diabetic states. LXRs were considered to be the most important nuclear receptors responsible for the regulation of ABCA1. Although LXR- β is indispensable for the expression of ABCA1^[35], some studies indicated a more important role for LXR- α in the regulation of ABCA1^[36,37]. The QT-PCR results showed that diabetes induced LXR- α mRNA, which could be one of the reasons for the increased ABCA1 protein levels.

In addition, other proteins, including sterol regulatory element-binding protein-2 (SREBP-2) and 3-hydroxy-3-methylglutaryl coenzyme A reductase (HMGCR), may also be involved in the regulation of cholesterol homeostasis^[38, 39]. A report showed that diabetes may decrease both SREBP-2 and HMGCR mRNA in the liver of rats, and insulin partially reversed the alterations induced by diabetes^[40]. Insulin is considered to be a potent inducer of HMGCR^[41]. Insulin treatment increased the HMGCR activity in hepatic microsomes of STZ-induced diabetic rats^[42]. Data from Caco-2 cells demonstrated that a high glucose level might also decrease the SREBP-2 protein level and HMGCR activity^[43]. All these results indicate that SREBP-2 and HMGCR may play a role in imbalanced cholesterol levels, although there are contradictory reports^[31, 44]. These discrepancies may be a result of animal model differences and disease duration.

Oxysterols are considered to be the endogenous ligands of LXRs, and we used 7 α -HC, which is formed by cholesterol-7-hydroxylase (CYP7A1), as a marker for oxysterols. It was found that diabetes increased the serum 7 α -HC level by 1.28-fold compared with normal rats. The increased oxysterol levels could further enhance LXR activities, resulting in elevated ABCA1 protein expression in peripheral tissues. In addition, CYP7A1 is the rate-limiting enzyme in the synthesis of bile acids^[45]. Elevated 7 α -HC levels also suggested that enhanced cholesterol metabolism may constitute one of the reasons for the reduced liver cholesterol levels.

Cholesterol is one of the major constituents of the plasma membrane. Intact plasma membrane microdomains are critical for maintaining cell viability and function. The reduction of cholesterol in peripheral tissues, especially in heart and kidney, may be associated with diabetic nephropathy and diabetic cardiomyopathy. A report showed that both cholesterol esterase and cholesterol oxidase caused marked cytotoxicity by perturbing the plasma membrane cholesterol in normal mouse proximal tubular segments. A further study demonstrated that disturbing lipid raft microdomains with cholesterol esterase dramatically increased the tubule susceptibility to Fe-mediated oxidative stress and Ca²⁺ overloading^[46]. Cholesterol depletion using cyclodextrins also resulted in reduced HEK293A cell viability and increased lactate dehydrogenase levels, which were accompanied by membrane damage, apoptosis and necrosis^[47]. A recent study showed that cholesterol depletion using methyl- β -cyclodextrin (M- β -CD) modulated the basal L-type Ca²⁺ current and abolished its adrenergic enhancement in ventricular myocytes^[48]. Ca²⁺-activated Cl⁻ currents were augmented by M- β -CD in murine portal vein myocytes^[49]. Basolateral membrane cholesterol extraction with

M- β -CD also reduced the Na⁺/K⁺ pump activity in A6 renal epithelia^[50]. In addition, some reports showed that cholesterol depletion suppressed insulin secretion^[51-53], and decreased cholesterol levels in the pancreas may contribute to the severity of diabetes.

In summary, type 1 diabetes decreased the levels of both free and total cholesterol in peripheral tissues but increased the FC levels in the hippocampus without altering the TC level. The decreased free cholesterol levels in the peripheral tissues may be partly due to an increased expression of the ABCA1 protein.

Acknowledgements

This work was supported by the National Science Foundation of China (Grants No 30873123 and 39970862) and the Funding for Innovative Research Team in the Institution of Jiangsu Higher Education.

Author contribution

All of the authors guarantee the integrity of the study. Xin-ting WANG, Li LIU, and Xiao-dong LIU designed the study; Xin-ting WANG, Jia LI, Nan HU, and Shi JIN conducted the animal experiments; Jia LI and Can LIU carried out the other detailed research work; Dan MEI interpreted the data; Xin-ting WANG and Xiao-dong LIU wrote the manuscript. The final version was approved by all of the authors.

References

- 1 Wadwa RP, Kinney GL, Maahs DM, Snell-Bergeon J, Hokanson JE, Garg SK, et al. Awareness and treatment of dyslipidemia in young adults with type 1 diabetes. *Diabetes Care* 2005; 28: 1051-6.
- 2 Miyazaki A, Sakashita N, Lee O, Takahashi K, Horiuchi S, Hakamata H, et al. Expression of ACAT-1 protein in human atherosclerotic lesions and cultured human monocytes-macrophages. *Arterioscler Thromb Vasc Biol* 1998; 18: 1568-74.
- 3 Paulson KE, Zhu S-N, Chen M, Nurmohamed S, Jongstra-Bilen J, Cybulsky MI. Resident intimal dendritic cells accumulate lipid and contribute to the initiation of atherosclerosis. *Circ Res* 2010; 106: 383-90.
- 4 Jun JY, Ma Z, Segar L. Spontaneously diabetic Ins2^{+/Akita}: apoE-deficient mice exhibit exaggerated hypercholesterolemia and atherosclerosis. *Am J Physiol Endocrinol Metab* 2011; 301: E145-54.
- 5 James SH, Meyers AM. Microangiopathic hemolytic anemia as a complication of diabetes mellitus. *Am J Med Sci* 1998; 315: 211-5.
- 6 Hu G, Antikainen R, Jousilahti P, Kivipelto M, Tuomilehto J. Total cholesterol and the risk of Parkinson disease. *Neurology* 2008; 70: 1972-9.
- 7 Hartmann T. Cholesterol, A β and Alzheimer's disease. *Trends Neurosci* 2001; 24: S45-8.
- 8 Luo DX, Cao DL, Xiong Y, Peng XH, Liao DF. A novel model of cholesterol efflux from lipid-loaded cells. *Acta Pharmacol Sin* 2010; 31: 1243-57.
- 9 Calkin AC, Forbes JM, Smith CM, Lassila M, Cooper ME, Jandeleit-Dahm KA, et al. Rosiglitazone attenuates atherosclerosis in a model of insulin insufficiency independent of its metabolic effects. *Arterioscler Thromb Vasc Biol* 2005; 25: 1903-9.
- 10 Tang C, Kanter JE, Bornfeldt KE, Leboeuf RC, Oram JF. Diabetes reduces the cholesterol exporter ABCA1 in mouse macrophages and

- kidneys. *J Lipid Res* 2010; 51: 1719–28.
- 11 Dong J, Chen W, Wang S, Zhang J, Li H, Guo H, et al. Jones oxidation and high performance liquid chromatographic analysis of cholesterol in biological samples. *J Chromatogr B* 2007; 858: 239–46.
 - 12 Abell LL, Levy BB, Brodie BB, Kendall FE. A simplified method for the estimation of total cholesterol in serum and demonstration of its specificity. *J Biol Chem* 1952; 195: 357–66.
 - 13 Honda A, Yamashita K, Hara T, Ikegami T, Miyazaki T, Shirai M, et al. Highly sensitive quantification of key regulatory oxysterols in biological samples by LC-ESI-MS/MS. *J Lipid Res* 2009; 50: 350–7.
 - 14 Livak KJ, Schmittgen TD. Analysis of relative gene expression data using real-time quantitative PCR and the $2^{-\Delta\Delta CT}$ method. *Methods* 2001; 25: 402–8.
 - 15 Liu H, Xu X, Yang Z, Deng Y, Liu X, Xie L. Impaired function and expression of P-glycoprotein in blood-brain barrier of streptozotocin-induced diabetic rats. *Brain Res* 2006; 1123: 245–52.
 - 16 Oram JF, Lawn RM, Garvin MR, Wade DP. ABCA1 is the cAMP-inducible apolipoprotein receptor that mediates cholesterol secretion from macrophages. *J Biol Chem* 2000; 275: 34508–11.
 - 17 Li D, Wang D, Wang Y, Ling W, Feng X, Xia M. Adenosine monophosphate activated protein kinase induces cholesterol efflux from macrophage-derived foam cells and alleviates atherosclerosis in Apolipoprotein E-deficient mice. *J Biol Chem* 2010; 285: 33499–509.
 - 18 Rahman SMA, Van Dam AM, Schultzberg M, Crisby M. High cholesterol diet results in increased expression of interleukin-6 and caspase-1 in the brain of apolipoprotein E knockout and wild type mice. *J Neuroimmunol* 2005; 169: 59–67.
 - 19 Vance JE, Hayashi H. Formation and function of apolipoprotein E-containing lipoproteins in the nervous system. *Biochim Biophys Acta* 2010; 1801: 806–18.
 - 20 Hayashi H. Lipid metabolism and glial lipoproteins in the central nervous system. *Biol Pharm Bull* 2011; 34: 453–61.
 - 21 Lane RM, Farlow MR. Lipid homeostasis and apolipoprotein E in the development and progression of Alzheimer's disease. *J Lipid Res* 2005; 46: 949–68.
 - 22 Wilson JD. The measurement of the exchangeable pools of cholesterol in the baboon. *J Clin Invest* 1970; 49: 655–65.
 - 23 Dell RB, Mott GE, Jackson EM, Ramakrishnan R, Carey KD, McGill HC, et al. Whole body and tissue cholesterol turnover in the baboon. *J Lipid Res* 1985; 26: 327–37.
 - 24 Prince PSM, Kannan NK. Protective effect of rutin on lipids, lipoproteins, lipid metabolizing enzymes and glycoproteins in streptozotocin-induced diabetic rats. *J Pharm Pharmacol* 2006; 58: 1373–83.
 - 25 Geethan PK, Prince PS. Antihyperlipidemic effect of D-pinitol on streptozotocin-induced diabetic wistar rats. *J Biochem Mol Toxicol* 2008; 22: 220–4.
 - 26 Sarkar C, Cenedella R. Reactivity of key metabolic sterols in standard colorimetric assays for cholesterol. *Lipids* 1982; 17: 46–9.
 - 27 Morris TG. A comparison of methods for the estimation of serum cholesterol and values in random samples of populations in the 55–64 age group. *J Clin Path* 1959; 12: 518–23.
 - 28 Uehara Y, Engel T, Li Z, Goepfert C, Rust S, Zhou X, et al. Polyunsaturated fatty acids and acetoacetate downregulate the expression of the ATP-binding cassette transporter A1. *Diabetes* 2002; 51: 2922–8.
 - 29 Shen L, Tso P, Woods SC, Clegg DJ, Barber KL, Carey K, et al. Brain Apolipoprotein E: an important regulator of food intake in rats. *Diabetes* 2008; 57: 2092–8.
 - 30 Lenich CM, Chobanian AV, Brecher P, Zannis VI. Effect of dietary cholesterol and alloxan-diabetes on tissue cholesterol and apolipoprotein E mRNA levels in the rabbit. *J Lipid Res* 1991; 32: 431–8.
 - 31 Suzuki R, Lee K, Jing E, Biddinger SB, McDonald JG, Montine TJ, et al. Diabetes and insulin in regulation of brain cholesterol metabolism. *Cell Metab* 2010; 12: 567–79.
 - 32 Russell DW, Halford RW, Ramirez DMO, Shah R, Kotti T. Cholesterol 24-hydroxylase: An enzyme of cholesterol turnover in the brain. *Annu Rev Biochem* 2009; 78: 1017–40.
 - 33 Kamboj SS, Chopra K, Sandhir R. Hyperglycemia-induced alterations in synaptosomal membrane fluidity and activity of membrane bound enzymes: beneficial effect of N-acetylcysteine supplementation. *Neuroscience* 2009; 162: 349–58.
 - 34 Nonomura K, Arai Y, Mitani H, Abe-Dohmae S, Yokoyama S. Insulin down-regulates specific activity of ATP-binding cassette transporter A1 for high density lipoprotein biogenesis through its specific phosphorylation. *Atherosclerosis* 2011; 216: 334–41.
 - 35 Gerin I, Dolinsky VW, Shackman JG, Kennedy RT, Chiang S-H, Burant CF, et al. LXR β is required for adipocyte growth, glucose homeostasis, and β cell function. *J Biol Chem* 2005; 280: 23024–31.
 - 36 Huang TH-W, Razmovski-Naumovski V, Salam NK, Duke RK, Tran VH, Duke CC, et al. A novel LXR- α activator identified from the natural product *Gynostemma pentaphyllum*. *Biochem Pharmacol* 2005; 70: 1298–308.
 - 37 Tamehiro N, Sato Y, Suzuki T, Hashimoto T, Asakawa Y, Yokoyama S, et al. Riccardin C: A natural product that functions as a liver X receptor (LXR) α agonist and an LXR β antagonist. *FEBS Lett* 2005; 579: 5299–304.
 - 38 Shimano H, Yahagi N, Amemiya-Kudo M, Hasty AH, Osuga J, Tamura Y, et al. Sterol regulatory element-binding protein-1 as a key transcription factor for nutritional induction of lipogenic enzyme genes. *J Biol Chem* 1999; 274: 35832–9.
 - 39 Eberlé D, Hegarty B, Bossard P, Ferré P, Foulfelle F. SREBP transcription factors: master regulators of lipid homeostasis. *Biochimie* 2004; 86: 839–48.
 - 40 Shimomura I, Bashmakov Y, Ikemoto S, Horton JD, Brown MS, Goldstein JL. Insulin selectively increases SREBP-1c mRNA in the livers of rats with streptozotocin-induced diabetes. *Proc Natl Acad Sci U S A* 1999; 96: 13656–61.
 - 41 Schiefelbein D, Goren I, Fisslthaler B, Schmidt H, Geisslinger G, Pfeilschifter J, et al. Biphasic regulation of HMG-CoA reductase expression and activity during wound healing and its functional role in the control of keratinocyte angiogenic and proliferative responses. *J Biol Chem* 2008; 283: 15479–90.
 - 42 Easom RA, Zammit VA. Effects of diabetes on the expressed and total activities of 3-hydroxy-3-methylglutaryl-CoA reductase in rat liver *in vivo*. Reversal by insulin treatment. *Biochem J* 1985; 230: 747–52.
 - 43 Ravid Z, Bendayan M, Delvin E, Sane AT, Elchebly M, Lafond J, et al. Modulation of intestinal cholesterol absorption by high glucose levels: impact on cholesterol transporters, regulatory enzymes, and transcription factors. *Am J Physiol Gastrointest Liver Physiol* 2008; 295: G873–85.
 - 44 Proctor G, Jiang T, Iwahashi M, Wang Z, Li J, Levi M. Regulation of renal fatty acid and cholesterol metabolism, inflammation, and fibrosis in Akita and OVE26 mice with type 1 diabetes. *Diabetes* 2006; 55: 2502–9.
 - 45 Zhao C, Dahlman-Wright K. Liver X receptor in cholesterol metabolism. *J Endocrinol* 2010; 204: 233–40.
 - 46 Zager RA. Plasma membrane cholesterol: A critical determinant of cellular energetics and tubular resistance to attack. *Kidney Int* 2000; 58: 193–205.
 - 47 Wang H, Xie X, Zhang F, Zhou Q, Tao Q, Zou Y, et al. Evaluation of cholesterol depletion as a marker of nephrotoxicity *in vitro* for novel β -cyclodextrin derivatives. *Food Chem Toxicol* 2011; 49: 1387–93.

- 48 Tsujikawa H, Song Y, Watanabe M, Masumiya H, Gupte SA, Ochi R, *et al*. Cholesterol depletion modulates basal L-type Ca^{2+} current and abolishes its β -adrenergic enhancement in ventricular myocytes. *Am J Physiol Heart Circ Physiol* 2008; 294: H285–92.
- 49 Sones WR, Davis AJ, Leblanc N, Greenwood IA. Cholesterol depletion alters amplitude and pharmacology of vascular calcium-activated chloride channels. *Cardiovasc Res* 2010; 87: 476–84.
- 50 Balut C, Steels P, Radu M, Ameloot M, Driessche WV, Jans D. Membrane cholesterol extraction decreases Na^+ transport in A6 renal epithelia. *Am J Physiol Cell Physiol* 2006; 290: C87–94.
- 51 Hao M, Head WS, Gunawardana SC, Hasty AH, Piston DW. Direct effect of cholesterol on insulin secretion. *Diabetes* 2007; 56: 2328–38.
- 52 Larsson S, Wierup N, Sundler F, Eliasson L, Holm C. Lack of cholesterol mobilization in islets of hormone-sensitive lipase deficient mice impairs insulin secretion. *Biochem Biophys Res Commun* 2008; 376: 558–62.
- 53 Hao M, Bogan JS. Cholesterol regulates glucose-stimulated insulin secretion through phosphatidylinositol 4,5-bisphosphate. *J Biol Chem* 2009; 284: 29489–98.

Original Article

Excess genistein suppresses the synthesis of extracellular matrix in female rat mandibular condylar cartilage

Shi-bin YU[#], Xiang-hui XING[#], Guang-ying DONG, Xi-li WENG, Mei-qing WANG^{*}

School of Stomatology, Fourth Military Medical University, Xi'an 710032, China

Aim: To investigate the effect of excess genistein on the extracellular matrix in mandibular condylar cartilage of female rats *in vivo*.

Methods: Female SD rats were administered through oral gavage with genistein (50 mg/kg) or placebo daily for 6 weeks. The morphological changes of temporomandibular joints were studied with HE staining. The expression of cartilage matrix compounds (aggrecan and collagen type II), estrogen-related molecules (aromatase, estradiol, ER α and ER β) and proliferating cell nuclear antigen (PCNA) in mandibular condylar cartilage was detected using immunohistochemistry, ELISA and real-time PCR.

Results: The genistein treatment significantly reduced the thickness of the posterior and middle regions of mandibular condylar cartilage, and decreased the expression of collagen type II, aggrecan and PCNA. Compared with the control group, the estradiol content and expression levels of the key estradiol-synthesizing enzyme aromatase in the genistein-treatment group were significantly decreased. The genistein treatment significantly increased the expression of ER β , but decreased the expression of ER α .

Conclusion: Excess genistein suppresses extracellular matrix synthesis and chondrocytes proliferation, resulting in thinner mandibular condylar cartilage. These effects may be detrimental to the ability of mandibular condylar cartilage to adapt to mechanical loads.

Keywords: genistein; osteoarthritis; mandibular condylar cartilage; estrogen; estrogen receptors

Acta Pharmacologica Sinica (2012) 33: 918–923; doi: 10.1038/aps.2012.49; published online 18 Jun 2012

Introduction

Osteoarthritis (OA) is the most common arthropathy in elderly people, and its socio-economic impact has increased as life expectancy has risen. OA is a degenerative disease characterized by the loss of collagens and proteoglycans as the main structural molecules of articular cartilage^[1]. Epidemiological studies have shown that the prevalence and incidence of OA increase after menopause and that OA symptoms are more severe in postmenopausal women than in men^[2–4], which suggests a link between OA and estrogen.

Although estrogen replacement therapy (ERT) has been proven to reduce the risk of OA^[5–7], its application is hampered by an increased risk of breast cancer, myocardial infarction, and stroke^[8, 9]. Therefore, using phytoestrogens, which lack the specific side-effects of estrogens, may provide an alternative therapy^[10, 11]. Phytoestrogens are abundant in soybean products^[12]; genistein, which structurally resembles

17 β -estradiol, is particularly abundant. It has been shown that genistein can bind to estrogen receptors (ERs) with an affinity 100 to 1000-fold less than that of estradiol and that it competes with estradiol and displaces it from its binding sites^[13]. A clinical study has suggested that consuming 88 mg phytoestrogen per day may benefit OA patients^[14]. Hooshmand *et al* have also reported that genistein reduced the *in vitro* production of lipopolysaccharide-induced cyclooxygenase (COX)-2 in chondrocytes, indicating that genistein may be an attractive and viable alternative therapy for treating or preventing OA^[15].

The temporomandibular joint (TMJ) plays an important role in craniofacial growth and function and shows a high incidence of OA^[16]. In the literature, estrogen has been shown to play an important role in the development of TMJ and temporomandibular diseases^[17–19]. These findings have been supported by the existence of estrogen receptors (ERs) in mandibular condylar cartilage^[20, 21].

As an estrogen-targeted tissue^[20, 21], cartilage is usually a solid connective tissue that covers subchondral bone tissue and plays an important role in the development of OA. To the best of our knowledge, however, few studies of the effect of genistein on cartilage have been reported, especially *in vivo* studies. The

[#] These authors contributed equally to this work.

^{*} To whom correspondence should be addressed.

E-mail mqwang@fmmu.edu.cn

Received 2011-11-18 Accepted 2012-04-16

aim of the present study was to investigate the effect of excess genistein on *in vivo* mandibular condylar cartilage.

Materials and methods

Genistein treatment *in vivo*

All the animal experimental procedures were approved by the Animal Research Committee of the Fourth Military Medical University. Thirty 7-week-old female SD rats, weighing 180–190 g, were provided by the animal center of the Fourth Military Medical University. All animals were housed at 22°C and 30%–60% relative humidity with a normal day-night rhythm (a 12:12 h light-dark cycle). The animals were randomly assigned to vehicle control and genistein-treatment groups (15 in each group). They had free access to tap water and a phytoestrogen-free diet in which corn oil was replaced with soybean oil. In the literature, the bone-protective effects of genistein (3–54 mg·kg⁻¹·d⁻¹) have been reported in OVX rats, mice and postmenopausal women^[22]. There have been few studies focusing on the effect of genistein on normal or intact animals. Based on a series of genistein safety studies, the no observed adverse effect level (NOAEL) for genistein in rats has been estimated to be 50 or 100 mg·kg⁻¹·d⁻¹^[13, 23]. Consistent with our previous study^[22], 50 mg·kg⁻¹·d⁻¹ genistein was chosen as excess dose in the present study. The animals were treated once daily with genistein (50 mg/kg body weight, 99.5% pure, Winherb Medical Science Co Ltd, China) or placebo by oral gavage. The genistein was dissolved in a placebo solution (0.9% NaCl, 2% Tween 80, and 0.5% methyl cellulose in water). The application volume was 5 mL/kg body weight. Changes in body weight during the experimental period were considered when calculating the genistein dosage. All the animals were sacrificed 6 weeks after the initiation of treatment.

Tissue preparation

For the morphological and immunohistochemistry analyses 10 rats (5 from each group) received deep anesthesia from an intraperitoneal injection of pentobarbital sodium (50 mg/kg body weight) and were perfused with 200 mL of normal saline and 400 mL of paraformaldehyde (4% in phosphate buffer saline, pH 7.4) through their ascending aortas. The TMJs and the uterus were harvested without fatty tissue. The wet weight of uterus was measured by electron precision balance. A uterine weight index was used to measure the changes in the uterus [uterine weight index=WW (mg)/BW (g), where WW=wet weight and BW=body weight]^[9]. The TMJs were post-fixed overnight at 4°C with the same fixative and decalcified for 1 week in Kristensen's fluid (sodium formate 52.2 g, formic acid 174.2 mL, and 1000 mL distilled water). The TMJ samples were then dehydrated in graded ethanol and embedded in paraffin. Serial 5- μ m mid-sagittal sections were cut parallel to the lateral surface of the condyle. To ensure a reliable comparison between the vehicle control and experimental groups, mid-sagittal sections from each joint were chosen for the morphological and immunohistochemistry analyses.

The other six rats in each group were sacrificed for the real-time PCR analysis. To obtain enough total RNA, four sets of

condylar cartilages from 2 randomly selected rats constituted one sample; hence, 12 sets of condylar cartilages from 6 rats in each group were randomly assigned to 3 samples.

Histological analysis

The hematoxylin and eosin (HE) stained sections were examined under a light microscope (Leica DM2500, Wetzlar, Germany). A true-color computer-assisted image analyzing system with a digital camera (Leica DFC420, Leica, Wetzlar, Germany) and software (Qwin Plus, Leica Microsystem Imaging Solutions Ltd, Cambridge, United Kingdom) were used for image capture and measurement. The thickness of the condylar cartilage was measured in each section. The condylar cartilage was divided approximately into anterior, middle and posterior regions. In every region, the thickness was measured at three quartering points. The means of the three measurements were used for the statistical analysis.

Immunohistochemical staining and analysis

Five commercially available primary antibodies were used for the immunohistochemical staining: anti-human collagen type II goat polyclonal IgG (SC7763, Santa Cruz Biol Inc, USA); anti-rat proliferating cell nuclear antigen (PCNA) mouse monoclonal IgG (MS-106, Labvision Ltd, USA); anti-human aromatase rabbit polyclonal IgG (AB69653, Abcam, UK); anti-human ER α rabbit polyclonal IgG (SC542, Santa Cruz Biol Inc, USA); and anti-human ER β rabbit polyclonal IgG (SC8974, Santa Cruz Biol Inc, USA). The immunohistochemical staining was conducted using a three-step avidin-biotin complex method that has been previously described^[24]. The sections were incubated overnight at 4°C with anti-human collagen type II goat polyclonal IgG (3 μ g/mL), anti-rat PCNA mouse monoclonal IgG (3 μ g/mL), anti-human aromatase rabbit polyclonal IgG (10 μ g/mL), anti-human ER α rabbit polyclonal IgG (4 μ g/mL), and anti-human ER β rabbit polyclonal IgG (3 μ g/mL).

The immunohistochemical staining for aromatase, ER α , ER β , and PCNA was analyzed by the Qwin Plus software. Briefly, the stained sections were observed under a Leica DM2500 light microscope with a \times 10 objective. The measurements were performed in middle and posterior regions of the condylar cartilage, where they regularly appeared among the animals. For the aromatase, ER α and ER β analyses, the measurement area consisted of the complete mature and hypertrophic layers in which immunoreactive signals were obvious. The positively stained region and the complete selected region covering the mature and hypertrophic layers, respectively, were measured. The percentage of the entire region that stained positive was calculated. For the PCNA sections, 4 cubic regions (300 pixels \times 300 pixels) were selected from approximately the middle and posterior regions of the condylar cartilage. The number of PCNA-positive chondrocytes was determined. Finally, the percent of the region that stained positive and the sum of the PCNA-positive cells in all of the cartilage were used for the statistical analysis.

RNA preparation, reverse transcription, and real-time PCR

The mandibular condylar cartilage samples were pulverized in liquid nitrogen. The total RNA was isolated from frozen tissues using a standard TRIzol[®] protocol (Invitrogen, Carlsbad, CA), followed by first-strand cDNA synthesis with the RevertAid[™] First Strand cDNA Synthesis Kit (Fermentas Inc, Maryland, USA). The real-time PCR was performed in an ABI 7500 Fast thermal cycler. The protocol consisted of 40 cycles of 94 °C for 5 s, 62 °C for 34 s, and 72 °C for 1 min each. The specific primers were designed with the primer 3 software (Whitehead Institute for Biomedical Research, Cambridge, MA, USA) based on the cDNA sequences available at the Genebank database. Table 1 shows the sequences of primers used in this study. All the PCRs were run in triplicate for each sample, and the threshold cycles (CT) were measured. A Δ CT value was calculated for each sample by subtracting the CT value of the reference gene (18S) from the CT value of the gene of interest. 18S has been used as internal standard in several studies. All the samples were normalized to the Δ CT value of a control sample ($\Delta\Delta$ CT). The relative expression of the target gene was calculated using the expression $2^{-\Delta\Delta$ CT} and is reported in arbitrary units^[25].

Table 1. Primer sequences for aggrecan, collagen type II, aromatase, ER α , ER β , and 18S.

Gene	Sequence	Fragment length (bp)	Accession number
Aggrecan	F: 5'-CCCTCACCCCAAGAATCAAGT-3' R: 5'-TCATTGGAGCGAAGGTCTGG-3'	178 bp	NM_022190
Collagen II	F: 5'-AGAAGTGGTGGAGCAGCAAGA-3' R: 5'-ATCTGGACGTTAGCGGTGTTG-3'	124 bp	NM_012929
Aromatase	F: 5'-TCATCAGCAAGTCCTCGAGCA-3' R: 5'-CCATTCTCGTCATGCCAAT-3'	106 bp	M33986
ER α	F: 5'-TGCGCAAGTGTACGAAGTGG-3' R: 5'-TTCGGCCTTCCAAGTCATCTC-3'	108 bp	NM_012689
ER β	F: 5'-AAAACTCACCGTCGAGCCTT-3' R: 5'-GCTGAATACTCATGGCGGTTG-3'	124 bp	NM_012754
18S	F: 5'-CGGCTACCACATCCAAGGAA-3' R: 5'-GCTGGAATTACCGCGGCT-3'	187 bp	M11188

Enzyme-linked immunosorbent assay (ELISA) for determination of estradiol

For the ELISA analysis, the remaining 8 rats (4 from each group) were sacrificed under deep anesthesia. Two mandibular condylar cartilage sections from the same rat were used a single sample, giving 4 samples from each group. The cartilage samples were pulverized in liquid nitrogen and then placed RIPA Lysis Buffer (Beyotime Institute of Biotechnology,

Haimen, China) for 2 h at 4 °C for extraction. The insoluble material was removed by centrifugation at 10000 r/min for 10 min. The protein in the supernatant was estimated by the BCA method according to the manufacturer's instructions (Pierce Biotechnology Inc, Rockford, IL, USA). Forty micrograms of total protein from each group was assayed by enzyme-linked immunosorbent assay. The estradiol content was quantified by a goat anti-rat ELISA kit (QRCT-301330012133EIA\UTL, Adlitteram Diagnostic Laboratories, Inc, San Diego, CA, USA) according to the manufacturer's instructions. The minimum detectable estradiol concentration using this assay was less than 1.0 pg/mL.

Statistical analysis

The SPSS 13.0 software package (SPSS Inc, Chicago, IL, USA) was used to analyze and describe the data. Student's *t* test was used to compare values between the groups. *P*-values were considered statistically significant when less than 0.05.

Results

Excess genistein increased the uterus weight index

The uterus weight index of the genistein-treatment group (2.2714±0.18875) increased significantly (*P*<0.01) compared to the control group (1.7884±0.11068).

Excess genistein suppressed the synthesis of extracellular matrix

In the mandibular condylar cartilage of both the control and genistein-treatment groups, the fibrous, proliferating, mature and hypertrophic layers were regularly arranged and had good continuity within the layers (Figure 1A and 1B). The thickness of the posterior and middle regions of the condylar cartilage in genistein-treated group decreased significantly (*P*<0.01) compared to the control group, however (Figure 1C). Consistent with the decreased cartilage thickness, the

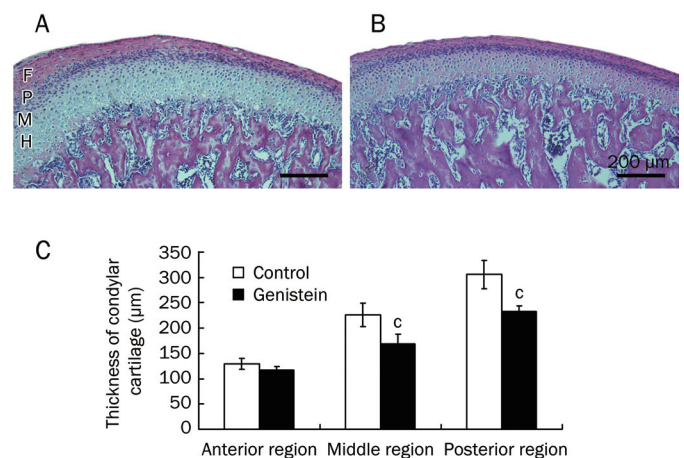


Figure 1. The histological analysis of the mandibular condylar cartilage. (A) and (B) show the histological morphology in middle region of the condylar cartilage from the control and genistein treatment groups. (C) Comparison of the cartilage thickness (mean±SD) between the genistein treatment and control groups (*n*=5). ^c*P*<0.01 vs control. F=fibrous layer, P=proliferating layer, M=mature layer, H=hypertrophic layer. The scale bar is 200 µm.

expression of collagen type II and aggrecan was lower in the genistein-treatment group than in the control group ($P<0.01$) (Figure 2).

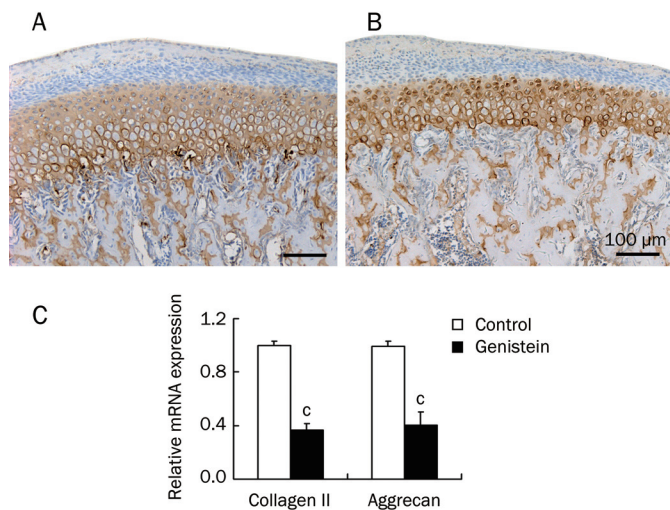


Figure 2. The expression of extracellular matrix in mandibular condylar cartilage. Panels (A) and (B) show the collagen II expression in middle region of the condylar cartilage from the control and genistein treatment groups. Panel (C) shows the comparison of the condylar cartilage collagen II and aggrecan mRNA levels between the control and genistein treatment groups ($n=3$). $^{\circ}P<0.01$ vs control.

Excess genistein suppressed the proliferation of chondrocytes

As shown in Figure 3, the density of PCNA-positive chondrocytes was lower in the genistein-treatment group (90.4 ± 12.7) than in the control group (217.6 ± 28.1) ($P<0.01$).

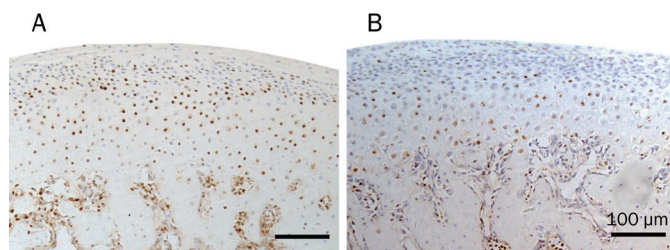


Figure 3. The PCNA expression in mandibular condylar cartilage from (A) the control group and (B) the genistein treatment group.

Excess genistein decreased the level of estradiol in condylar cartilage

The ELISA results showed that the estradiol content was lower in the genistein-treatment group (2.1310 ± 0.20756 ng) than in the vehicle control group (3.4293 ± 0.23953 ng) ($P<0.01$). Additionally, the expression of the key estradiol-synthesizing enzyme aromatase (as measured by both protein and mRNA levels) was lower in the genistein-treatment group ($P<0.01$) (Figure 4) than in the control group.

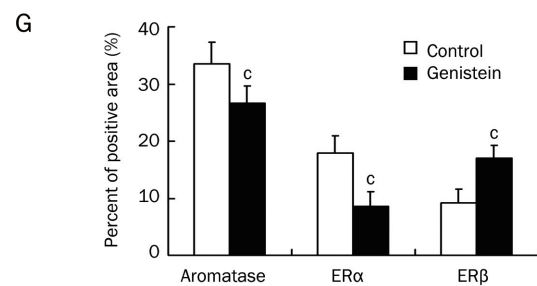
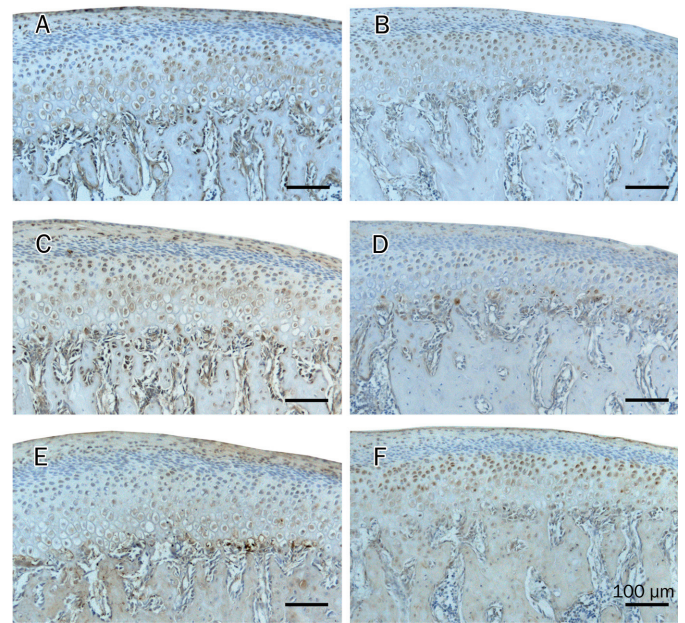


Figure 4. The expression of aromatase (A and B), ER α (C and D) and ER β (E and F) in mandibular condylar cartilage. (A, C, and E) are from the control group; (B, D, and F) are from the genistein-treatment group. (G) shows the comparison of the percent of positive area between the control and genistein treatment groups ($n=5$). $^{\circ}P<0.01$. The scale bar is 100 μ m.

Excess genistein decreased the expression of ER α , but increased that of ER β

As for the ER expression, the ER α mRNA levels and immunohistochemical signals were lower in the genistein-treatment group than in the control group ($P<0.01$). However, both the mRNA levels and immunohistochemical signals for ER β were significantly higher in the genistein-treatment group than in the control group ($P<0.01$) (Figure 4, 5).

Discussion

To the best of our knowledge, our study is the first to investigate the effects of genistein on mandibular condylar cartilage. Although the effect of phytoestrogens, especially genistein, on the extracellular cartilage matrix has been discussed in the literature, the data are not consistent. An *in vitro* study found that articular chondrocyte glycosaminoglycans (GAG) synthesis was significantly diminished following incubation with high doses of genistein (10^{-5} – 10^{-4} mol/L) but that the level of sulfate

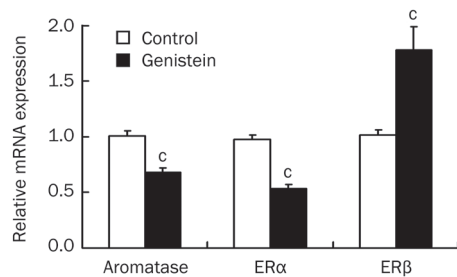


Figure 5. Comparison of the mRNA levels of aromatase, ER α and ER β between the control and genistein treatment groups ($n=3$). $^{\circ}P<0.01$.

incorporation was not affected^[1]. Nevertheless, Hooshmand *et al* found that high doses of genistein (10^{-5} – 10^{-4} mol/L) could suppress the increased levels of YKL-40 (a marker of cartilage glycoprotein degradation) in chondrocyte supernatant that is induced by LPS treatment^[15]. One preclinical study found that long-term soy phytoestrogen treatment (129 mg/day/person) did not have a statistically significant effect on the levels of collagen or proteoglycan in articular cartilage^[26]. Our results showed that compared with the control group, both the expression of the main components of the extracellular matrix cartilage (collagen type II and aggrecan) and chondrocyte proliferation decreased significantly in genistein-treatment group, resulting in thinner mandibular condylar cartilage in the posterior and middle regions. This result is consistent with a previous report that additional estradiol (10^{-8} mol/L) can decrease extracellular matrix synthesis, chondrocyte proliferation and the thickness of mandibular condylar cartilage *in vitro*^[19]. Maintaining articular cartilage throughout the life of an organism plays a crucial role in establishing the biological range of cartilage adaptability^[19]. Modulating cartilage thickness and extracellular matrix properties using excess genistein may create an environment more susceptible to degenerative changes.

It has been shown that chondrocytes in mandibular cartilage can locally synthesize estradiol through the activity of aromatase^[24]. In the present study, both the aromatase expression and estradiol content of mandibular condylar cartilage decreased significantly after the genistein treatment, while the uterus index increased. It is possible that a particular dose of genistein can exert an estrogenic effect in cartilage by competing with local estrogen, although its effect is weak. Therefore, the need for autocrine estrogen in cartilage metabolism decreases when genistein exerts its estrogen-like activity^[13].

The literature has suggested that genistein may be completely agonistic to both ER α and ER β , although it is more potent for ER β than ER α ^[27, 28]. It has been shown that the binding affinity of genistein was seven times greater for ER β than for ER α ^[29]. A recent study found that the increased ER β expression in the genioglossus muscle after genistein treatment was much higher than that of ER α ^[9]. Our previous study also demonstrated that the effect of genistein on mandibular subchondral bone was predominantly mediated through ER β ^[22]. The present study showed that ER β expression increased significantly following treatment with excess genistein, while ER α expression

decreased at both the protein and mRNA levels. These results may indicate that genistein exerts its estrogenic activity in mandibular condylar cartilage mainly through ER β , which is consistent with another recent finding that the effects of genistein on skeletal muscle major histocompatibility complex (MHC) expression was predominantly mediated through ER β ^[30].

In summary, the present study demonstrated that excess genistein can suppress extracellular matrix synthesis and chondrocyte proliferation in rat mandibular condylar cartilage, resulting in thinner mandibular condylar cartilage. This finding may imply decreased adaptivity to mechanical loads in mandibular condylar cartilage. Given the fluctuating differences in estrogen levels between individuals, the proper genistein dose should be studied further if genistein is to be widely used to treat OA or osteoporosis.

Acknowledgements

The authors are grateful to Ms Shu-jing CAI and Ms Cui HUA for technical assistance. This work was financially supported by the National Natural Science Foundation of China (30901699 and 30928028).

Author contribution

Mei-qing WANG and Shi-bin YU designed the study and wrote the manuscript. Shi-bin YU and Xiang-hui XING performed the animal experiments, sample preparation and immunohistochemical staining. Guang-ying DONG performed the ELISA assay and PCR and revised the manuscript. Xi-li WENG performed the HE staining and data analysis and revised the manuscript.

References

- 1 Claassen H, Briese V, Manapov F, Nebe B, Schünke M, Kurz B. The phytoestrogens daidzein and genistein enhance the insulin-stimulated sulfate uptake in articular chondrocytes. *Cell Tissue Res* 2008; 333: 71–9.
- 2 Bergink AP, van Meurs JB, Loughlin J, Arp PP, Fang Y, Hofman A, et al. Estrogen receptor alpha gene haplotype is associated with radiographic osteoarthritis of the knee in elderly men and women. *Arthritis Rheum* 2003; 48: 1913–22.
- 3 Spector TD, Campion GD. Generalised osteoarthritis: a hormonally mediated disease. *Ann Rheum Dis* 1989; 48: 523–7.
- 4 Ushiyama T, Ueyama H, Inoue K, Nishioka J, Ohkubo I, Hukuda S. Estrogen receptor gene polymorphism and generalized osteoarthritis. *J Rheumatol* 1998; 25: 134–7.
- 5 Felson DT, Nevitt MC. Estrogen and osteoarthritis: how do we explain conflicting study results? *Prev Med* 1999; 28: 445–8; discussion 449–50.
- 6 Nevitt MC, Cummings SR, Lane NE, Hochberg MC, Scott JC, Pressman AR, et al. Association of estrogen replacement therapy with the risk of osteoarthritis of the hip in elderly white women. Study of Osteoporotic Fractures Research Group. *Arch Intern Med* 1996; 156: 2073–80.
- 7 Spector TD, Nandra D, Hart DJ, Doyle DV. Is hormone replacement therapy protective for hand and knee osteoarthritis in women? The Chingford Study. *Ann Rheum Dis* 1997; 56: 432–4.
- 8 Azoulay C. Menopause in 2004: “hormone replacement therapy” is not what it used to be anymore. *Rev Med Interne* 2004; 25: 806–15.
- 9 Li W, Liu YH. Effects of phytoestrogen genistein on genioglossus

- function and oestrogen receptors expression in ovariectomized rats. *Arch Oral Biol* 2009; 54: 1029–34.
- 10 Clarkson TB, Anthony MS, Williams JK, Honore EK, Cline JM. The potential of soybean phytoestrogens for postmenopausal hormone replacement therapy. *Proc Soc Exp Biol Med* 1998; 217: 365–8.
- 11 Brzezinski A, Debi A. Phytoestrogens: the “natural” selective estrogen receptor modulators. *Eur J Obstet Gynecol Rep Biol* 1999; 85: 47–51.
- 12 Kapiotis S, Hermann M, Held I, Seelos C, Ehringer H, Gmeiner BM. Genistein, the dietary derived angiogenesis inhibitor, prevents LDL oxidation and protects endothelial cells from damage by atherogenic LDL. *Arterioscler Thromb Vasc Biol* 1997; 17: 2868–74.
- 13 McClain RM, Wolz E, Davidovich A, Edwards J, Bausch J. Reproductive safety studies with genistein in rats. *Food Chem Toxicol* 2007; 45: 1319–32.
- 14 Arjmandi BH, Khalil DA, Lucas EA, Smith BJ, Sinichi N, Hodges SB, *et al*. Soy protein may alleviate osteoarthritis symptoms. *Phytomedicine* 2004; 1: 567–75.
- 15 Hooshmand S, Soung do Y, Lucas EA, Madihally SV, Levenson CW, Arjmandi BH. Genistein reduces the production of proinflammatory molecules in human chondrocytes. *J Nutr Biochem* 2007; 18: 609–14.
- 16 Okeson JP, editors. Management of temporomandibular disorders and occlusion, 5th Edition. St Louis: Mosby Inc; 2003.
- 17 Yamashiro T, Takano-Yamamoto T. Differential responses of mandibular condyle and femur to oestrogen deficiency in young rats. *Arch Oral Biol* 1998; 43: 191–5.
- 18 Yasuoka T, Nakashima M, Okuda T, Tatematsu N. Effect of estrogen replacement on temporomandibular joint remodeling in ovariectomized rats. *J Oral Maxillofac Surg* 2000; 58: 189–96.
- 19 Talwar RM, Wong BS, Svoboda K, Harper RP. Effects of estrogen on chondrocyte proliferation and collagen synthesis in skeletally mature articular cartilage. *J Oral Maxillofac Surg* 2006; 64: 600–9.
- 20 Yamada K, Nozawa-Inoue K, Kawano Y, Kohno S, Amizuka N, Iwanaga T, *et al*. Expression of estrogen receptor alpha (ER alpha) in the rat temporomandibular joint. *Anat Rec A Discov Mol Cell Evol Biol* 2003; 274: 934–41.
- 21 Yu SB, Wang MQ, Li YQ, Lv X, Jiang Y, Dong GY, *et al*. The effects of age and sex on the expression of oestrogen and its receptors in rat mandibular condylar cartilages. *Arch Oral Biol* 2009; 54: 479–85
- 22 Li YQ, Xing XH, Wang H, Weng XL, Yu SB, Dong GY. Dose-dependent effects of genistein on bone homeostasis in rats’ mandibular subchondral bone. *Acta Pharmacol Sin* 2012; 33: 66–74.
- 23 Michael MR, Wolz E, Davidovich A, Pfannkuch F, Edwards JA, Bausch J. Acute, subchronic and chronic safety studies with genistein in rats. *Food Chem Toxicol* 2006; 44: 56–80.
- 24 Yu SB, Wang MQ, Zhao W, Cao HT, Liu YL. The effects of age and sex on the expression of aromatase in the rat temporomandibular joint. *J Orofac Pain* 2006; 20: 156–65.
- 25 Seibel J, Molzberger AF, Hertrampf T, Laudenbach-Leschowski U, Diel P. Oral treatment with genistein reduces the expression of molecular and biochemical markers of inflammation in a rat model of chronic TNBS-induced colitis. *Eur J Nutr* 2009; 48: 213–20.
- 26 Ham KD, Oegema TR, Loeser RF, Carlson CS. Effects of long-term estrogen replacement therapy on articular cartilage IGFBP-2, IGFBP-3, collagen and proteoglycan levels in ovariectomized cynomolgus monkeys. *Osteoarthritis Cartilage* 2004; 12: 160–8.
- 27 Casanova M, Li Y, Gaido KW, Archibeque-Engle S, Janszen DB, Heck HA. Developmental effects of dietary phytoestrogens in Sprague-Dawley rats and interactions of genistein and daidzein with rat estrogen receptors alpha and beta *in vitro*. *Toxicol Sci* 1999; 51: 236–44.
- 28 Kostelac D, Rechkemmer G, Briviba K. Phytoestrogens modulate binding response of estrogen receptors alpha and beta to the estrogen response element. *J Agric Food Chem* 2003; 51: 7632–5.
- 29 Atteritano M, Mazzaferro S, Frisina A, Cannata ML, Bitto A, D’Anna R, *et al*. Genistein effects on quantitative ultrasound parameters and bone mineral density in osteopenic postmenopausal women. *Osteoporos Int* 2009; 20: 1947–54.
- 30 Velders M, Solzbacher M, Schleipen B, Laudenbach U, Fritzscheier KH, Diel P. Estradiol and genistein antagonize the ovariectomy effects on skeletal muscle myosin heavy chain expression via ER-beta mediated pathways. *J Steroid Biochem Mol Biol* 2010; 120: 53–9.

Original Article

Efficacy of zoledronic acid in treatment of teoarthritis is dependent on the disease progression stage in rat medial meniscal tear model

De-gang YU^{1, #}, Bo YU^{2, #}, Yuan-qing MAO^{1, #}, Xin ZHAO¹, Xiao-qing WANG¹, Hui-feng DING¹, Lei CAO¹, Guang-wang LIU¹, Shao-bo NIE³, Shen LIU⁴, Zhen-an ZHU^{1, *}

¹Department of Orthopedics, Shanghai Ninth People's Hospital, Shanghai Jiao Tong University, School of Medicine, Shanghai 200011, China; ²Department of Orthopedics, Affiliated Hospital of Shandong University of Traditional Chinese Medicine, Ji-nan 250014, China; ³Department of Orthopedics, PLA General Hospital, Beijing 100853, China; ⁴Department of Orthopedics, Shanghai Sixth People's Hospital, Shanghai Jiao Tong University, Shanghai 200233, China

Aim: To investigate whether the stage of osteoarthritis (OA) progression influenced the efficacy of the third-generation bisphosphonate zoledronic acid in a rat medial meniscal tear model.

Methods: Medial meniscal tear (MMT) was surgically induced in adult male Sprague Dawley rats. Zoledronic acid (ZOL, 100 µg/kg, sc, twice a week) was administered starting immediately, early (from 4 weeks) or late (from 8 weeks) after OA induction. The degeneration of articular cartilage was evaluated with toluidine blue O staining. Subchondral bone remodeling was evaluated with X-ray micro-CT scanning. Joint pain was measured with respect to weight-bearing asymmetry. Calcitonin gene-related peptide (CGRP) expression in dorsal root ganglia (DRGs) was examined using immunofluorescence analysis. The afferent neurons in DRGs innervating the joint were identified by retrograde labeling with fluorogold.

Results: Progressive cartilage loss was observed during 12 weeks after OA induction. Subchondral bone remodeling manifested as increased bone resorption at early stage (4 weeks), but as increased bone accretion at advanced stages (8 weeks). Immediately and early ZOL administration significantly improved subchondral microstructural parameters, attenuated cartilage degeneration, reduced weight-bearing asymmetry and CGRP expression, whereas the late ZOL administration had no significant effects.

Conclusion: The stage of OA progression influences the efficacy of ZOL in treating joint degeneration and pain. To obtain the maximum efficacy, bisphosphonate treatment should be initiated in rat with early stages of OA pathogenesis.

Keywords: osteoarthritis; zoledronic acid; bisphosphonate; pain; subchondral bone; rat medial meniscal tear model

Acta Pharmacologica Sinica (2012) 33: 924–934; doi: 10.1038/aps.2012.28; published online 21 May 2012

Introduction

Osteoarthritis (OA), a leading cause of disability in the elderly^[1], is characterized by a progressive loss of articular cartilage and abnormalities in subchondral bone and surrounding soft tissue adaptations^[2], with chronic pain being the main clinical symptom^[3]. The search for effective agents that attenuate joint degeneration and relieve joint pain has been challenging.

For decades, articular cartilage has been the focus of major basic research and pharmaceutical therapies, although alterations in the subchondral bone were generally considered to

occur secondary to cartilage degeneration^[4, 5]. However, it is increasingly accepted that subchondral bone plays an important role in the pathogenesis of OA. Accumulating evidence from clinical and animal studies has demonstrated that during OA progression, subchondral bone turnover increases dramatically, with increased bone resorption occurring early, and increased bone accretion occurring later in the disease^[6–8]. Meanwhile, the biochemical composition and biomechanical properties of the subchondral bone are altered^[9, 10]. Therefore, because of an intimate biological and mechanical relationship with articular cartilage, the presence of abnormal subchondral bone influences the integrity of the overlying cartilage^[11–13]. In addition, abnormalities in subchondral bone, such as exposure of the subchondral bone plate, bone attrition, and bone marrow lesions, have been associated with knee pain^[14–17].

Consequently, targeting subchondral bone with bone-mod-

These authors contributed equally to this paper.

* To whom correspondence should be addressed.

E-mail zhuzhenan2006@126.com

Received 2012-02-12 Accepted 2012-03-05

ifying agents would be expected to retard joint degeneration and alleviate pain. Bisphosphonates, the most commonly used agents for osteoporosis treatment, are a promising therapy for OA because of their ability to inhibit osteoclastic bone absorption^[18]. However, the ability of bisphosphonates to preserve the structural integrity of subchondral bone and attenuate cartilage degeneration that has been seen in animal studies has not been consistently confirmed by clinical data^[19–22], which is in part attributed to deficiencies in evaluation criteria or experimental design. Subchondral bone properties are dynamic with disease progression. Therefore, patients with different stages of subchondral bone alterations could have been included in the studies and may have contributed to the inconsistent clinical findings. We hypothesized that the stage of disease progression, especially the stage of subchondral bone remodeling, could influence the efficacy of bisphosphonate therapy.

Many animal models have been developed to experimentally reproduce OA. The most commonly used rat medial meniscal tear (MMT) model demonstrates dynamic subchondral bone changes. Therefore, the cartilage- and bone-preserving activities of therapeutic agents can be evaluated in this model^[23]. Moreover, this model manifests changes in pain behavior, neuron phenotype and neuropeptide expression^[24–26], which, taken together, represent a model of the joint pain associated with OA. Therefore, in the present study, we used the established rat MMT model and initiated zoledronic acid (ZOL, a third-generation bisphosphonate) treatment at different stages after OA induction to evaluate the efficacy of ZOL treatment on joint degeneration and pain. Pain behavior, cartilage histology, subchondral microarchitecture, and the expression of calcitonin gene-related peptide (CGRP), a pain-related neuropeptide, in the dorsal root ganglia (DRG) were evaluated.

Materials and methods

Animals

Adult male Sprague Dawley rats (Sino-British Sippr/BK Lab Animal Ltd, Shanghai) weighing 296±12 g (mean±SD) were used for these experiments. Animals were group-housed on a 12-h light/dark cycle with food and water *ad libitum*. All experimental procedures were approved by the Animal Care and Experiment Committee of Shanghai Jiaotong University School of Medicine and were consistent with the National Institutes of Health Guide for the Care and Use of Laboratory Animals. Every effort was made to minimize the number of animals used and their suffering.

Induction of OA

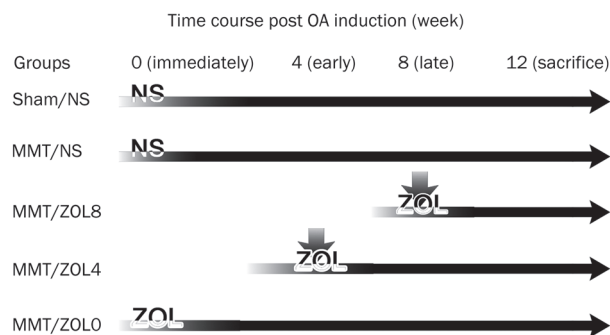
After acclimatization for 1 week, rats were anesthetized with 10% chloral hydrate in phosphate buffered saline (PBS, 0.01 mol/L). The MMT model was induced as previously described^[27]. Briefly, the medial collateral ligament of the right knee was transected, and the medial meniscus was reflected proximally toward the femur and cut through at its narrowest point. For the controls (Sham), the wounds were closed after

exposing the medial collateral ligament.

Experimental design

A total of 154 animals were used for the present study. In the preliminary experiment, of the total number of animals used, 64 animals were used to observe the changes in cartilage and subchondral bone during OA progression. The animals were sacrificed at 2, 4, 8, and 12 weeks after OA induction ($n=8$ at each time point). Another 40 animals were used to confirm the positive effects of ZOL in the MMT model and to choose a dose of ZOL that better preserved subchondral bone. ZOL (Aclasta[®], Novartis Pharma Stein AG) was administered subcutaneously twice a week at low dose 10 µg/kg body weight (MMT/ZoLL) and high dose 100 µg/kg body weight (MMT/ZoLH). The same volume of normal saline was given to the Sham animals (Sham/NS) and MMT control animals (MMT/NS). The animals ($n=10$ per group) were sacrificed at 4 weeks after OA induction.

Based on the above results, ZOL treatment was initiated at three stages following OA induction: immediately (ZOL0), early (4 weeks, ZOL4) and late (8 weeks, ZOL8). ZOL was administered subcutaneously twice a week at 100 µg/kg body weight. The same volume of normal saline was given to the Sham animals (Sham/NS) and MMT control animals (MMT/NS). All five groups of animals ($n=10$ per group) were sacrificed at 12 weeks following the induction of OA. The experimental design is shown as Scheme 1.



Scheme 1. ZOL treatment initiated at three stages following OA induction.

Pain behavior testing

Pain behavior was measured as weight-bearing asymmetry between the OA-induced (right) and contralateral (left) limb using an incapitance meter (IITC Life Sciences, Woodland Hills, CA, USA) as previously described^[24]. Briefly, rats were placed in an angulated Perspex container so that each hind paw rested on a separate transducer pad. The force exerted by each hind limb was averaged over a 5-s period. Each data point is the mean of three 5-s readings. Changes in weight-bearing asymmetry were evaluated one day before and once a week after OA induction. The percentage of weight placed on the right hind limb was determined using the formula below^[28].

$$\frac{\% \text{ of weight on right limb} = \frac{\text{weight on right limb}}{\text{weight on right limb} + \text{weight on left limb}} \times 100$$

Retrograde neuronal labeling

Afferent neurons in DRGs innervating the joint were identified by retrograde labeling with fluorogold (FG). To this end, 5 μ L of 2% FG (Sigma, 39286) in 0.1 mol/L PBS was injected intrarticularly into the right knee of an anesthetized rat using a 33-gauge needle and a Hamilton microsyringe one week prior to the end of the experiment^[25].

Tissue preparation

After anesthesia, rats were transcardially perfused with 250 mL of heparinized saline (10 IU/mL) followed by 300 mL of ice-cold, fresh 4% paraformaldehyde (PFA) in 0.1 mol/L PBS. Lumbar L3, L4, and L5 DRGs were harvested and fixed in 4% PFA for 3 h and then cryoprotected in 30% sucrose in 0.1 mol/L PBS overnight at 4°C. DRGs were then sliced into 12- μ m sections with every sixth section collected on the same glass slide and stored at -80°C. The entire knee joint was also dissected for histological and micro-CT imaging.

Micro-CT imaging and analysis

After fixation in 4% PFA for 48 h, the knee joints were scanned by X-ray microcomputed tomography (micro-CT) (μ CT 80; SCANCO Medical AG) with an isotropic voxel resolution of 10 μ m. A portion (2.0 mm ventrodorsal length) of the load-bearing region at the medial tibial plateau was identified as a region of interest. The following three-dimensional structural parameters were calculated: bone volume fraction (BV/TV), trabecular thickness (Tb.Th), trabecular spacing (Tb.Sp), trabecular number (Tb.N), and connectivity density (CD).

Histological analysis

After being imaged by micro-CT, the knee joints were decalcified in 10% EDTA for 3 weeks. The joints were bisected along the collateral ligament in the frontal plane, and both sections were embedded in the same paraffin block. The samples were cut into 5- μ m sections. On the basis of the OARSI recommendations for the histological assessment of osteoarthritis in the rat^[23], three sections from each knee at 200- μ m steps were stained with toluidine blue O and subsequently evaluated for cartilage degeneration. Three sections at 200- μ m steps were chosen for H&E staining and for evaluation of the synovial reaction. For toluidine blue O staining, the sections were stained with 0.04% *w/v* toluidine blue O (Sigma, T0394) in 0.1 mol/L sodium acetate (pH 4.0) for 10 min, rinsed briefly, air-dried and mounted.

Immunofluorescence analysis

Slides containing every sixth section of L3, L4, and L5 DRGs were chosen for immunofluorescence analysis for CGRP and subsequent Nissl staining to quantify the total number of neurons in each section. The sections were first pre-incubated in 0.1 mol/L PBS containing 1% Triton X-100 and 10% normal

goat serum (NPBST) for 30 min at room temperature (RT) and then incubated with rabbit polyclonal CGRP (1:2000, Sigma, C8198) overnight at 4°C in NPBST. After washing three times with NPBST, the sections were incubated with anti-rabbit-Alexa 488 (1:500, Molecular Probes, A11034) for 1 h at RT. After rinsing 3 times with PBS, the sections were labeled with fluorescent Nissl stain (1:50, Molecular Probes, N-21482). Finally, the sections were mounted with Fluoromount-GTM (SBA, 0100-01) and visualized. All of the images were acquired using a fluorescence microscope (Leica DM 4000B) with BioQuant OSTEO II software (BioQuant Image Analysis Corporation, Nashville, TN). An entire image of every DRG section was acquired at 200 \times magnification with automatic sequential imaging. The immunofluorescent images were analyzed with Image-ProPlus 6.0 (Media Cybernetics). The total numbers of FG-labeled neurons, the percentage of neurons immunolabeled for CGRP, and the total number of Nissl-labeled neurons were determined. The results were averaged for each individual rat.

Statistical analysis

All behavioral testing, micro-CT statistical analysis, cartilage scoring and neuron counting was performed by blinded authors who were unaware of the treatments given. The results are presented as the mean \pm standard deviation (SD). A comparison between groups was performed with one-way analysis of variance using the LSD post-hoc test. *P* values less than 0.05 were considered statistically significant.

Results

Generally, cartilage changes occurred and worsened in a time-dependent manner between 2 and 12 weeks post OA induction (Figure 1). At 2 weeks, matrix and chondrocyte loss affected the superficial and upper middle zone, and at 4 weeks, these changes deepened into the deep zone and extended into more than 1/3 zone of the medial tibial plateau. Severe changes occurred at 8 weeks with full thickness degeneration into the tidemark, which become more widespread at 12 weeks. Subchondral bone structure of the medial tibial plateau showed dynamic alterations following OA induction from increased bone resorption at early stages (2 and 4 weeks) to increased bone accretion at advanced stages (8 and 12 weeks) (Figure 2). Compared with the Sham groups, BV/TV was significantly decreased at 2 and 4 weeks and increased at 8 and 12 weeks post-operation. These changes were accompanied by Tb.Th changing from thinner (2 and 4 weeks) to thicker (8 and 12 weeks), Tb.Sp from broader (2 and 4 weeks) to more narrow (8 and 12 weeks), and Tb.N and CD being reduced at all times.

Compared with MMT/NS animals, cartilage matrix and chondrocyte loss were partly reversed in animals with ZOL administration at both doses, and additional efficacy was observed in the MMT/ZOLH group (Figure 3). Abnormal microarchitecture parameters, such as the noticeably reduced BV/TV, Tb.N, Tb.Th, CD, and increased Tb.Sp seen in the MMT/NS group, were well preserved by high-dose ZOL treatment and partly preserved with low-dose therapy. In

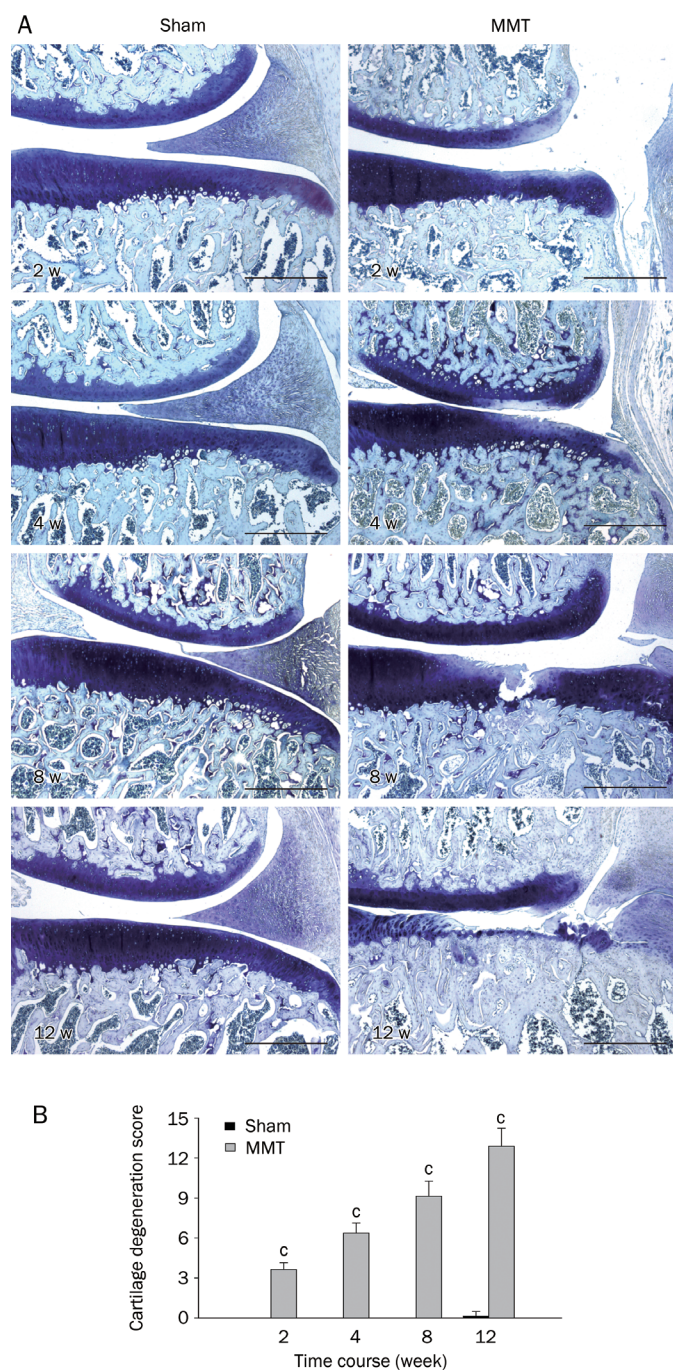


Figure 1. Changes in articular cartilage during OA progression. (A) Representative images with toluidine blue O staining. Bar=400 μ m. (B) Cartilage degeneration score. The comparison between groups was performed with an independent-samples *t*-test. Mean \pm SD. *n*=8. ^c*P*<0.01 vs Sham group.

addition, marked osteosclerosis was observed at the tibial metaphysis in animals treated with ZOL, which was induced by ZOL inhibiting osteoclasts in the growth plate (Figure 4).

Pain behavior

As shown in Figure 5, there was a marked reduction in hind

limb weight-bearing 1 week post-OA induction, which was almost completely resolved by 2 weeks in all of the groups. Subsequently, Sham/NS animals returned to normal weight-bearing, whereas MMT animals (MMT/NS, MMT/ZOL0, MMT/ZOL4, MMT/ZOL8) experienced weight-bearing asymmetry that gradually became worse in a time-dependent manner. Compared with MMT/NS controls at any time point tested, rats that received early ZOL therapy showed less weight-bearing asymmetry (MMT/ZOL0 and MMT/ZOL4) with an increased benefit observed in rats that received therapy immediately after OA induction. However, delayed administration of ZOL (MMT/ZOL8) did not yield a statistically significant difference. Specifically, 12 weeks post-OA induction, the MMT/ZOL0, MMT/ZOL4 and MMT/ZOL8 animals placed 45.21% \pm 1.07% (*P*<0.01), 43.66% \pm 1.39% (*P*<0.05) and 42.15% \pm 1.25% (*P*>0.05), respectively, of their hind limb weight on the right leg compared with 41.97% \pm 0.93% in the MMT/NS animals.

Articular cartilage degeneration

As indicated by toluidine blue O staining and cartilage degeneration scoring (Figure 6), widespread and profound cartilage matrix and chondrocyte loss were observed in MMT/NS animals at 12 weeks; however, this loss was significantly reduced by ZOL administration in MMT/ZOL0 animals and moderately reduced in MMT/ZOL4 animals. No statistically significant improvement was observed in the MMT/ZOL8 animals. Specifically, the cartilage degeneration score was 7.25 \pm 1.28 (*P*<0.01), 10.13 \pm 1.55 (*P*<0.01), and 12.0 \pm 1.69 (*P*>0.05) for the MMT/ZOL0, MMT/ZOL4, and MMT/ZOL8 animals, respectively, compared with 12.13 \pm 1.55 for the MMT/NS animals.

Synovial reaction

The synovial reaction was evaluated based on the OARSI-recommended scoring system. As shown in Figure 7S and 8S, the synovial reaction was similar among all the groups. The synovial lining comprised only 1-2 layers of cells, and no inflammatory cell infiltration was observed.

Subchondral bone remodeling

Representative images of knee joints obtained from micro-CT scanning are shown in Figure 7B. Generally, MMT resulted in increased bone accretion and cyst formation at 12 weeks, whereas ZOL treatment reversed these changes in a stage-dependent manner. The bone cysts observed in the MMT/NS animals were absent in the MMT/ZOL0 and MMT/ZOL4 animals and appeared to be smaller in the MMT/ZOL8 animals, although the size of the cysts was not quantified. In addition, marked osteosclerosis was present at the tibial metaphysis in animals treated with ZOL, which occurred as a result of ZOL treatment inhibiting osteoclasts in active growth plates. The analysis of subchondral bone microstructure indexes is shown in Figure 7C. Compared with the Sham/NS animals, the subchondral bone of the medial tibial plateau in MMT/NS animals was significantly altered. The alterations included increased BV/TV, thickened Tb.Th, narrowed Tb.Sp, and

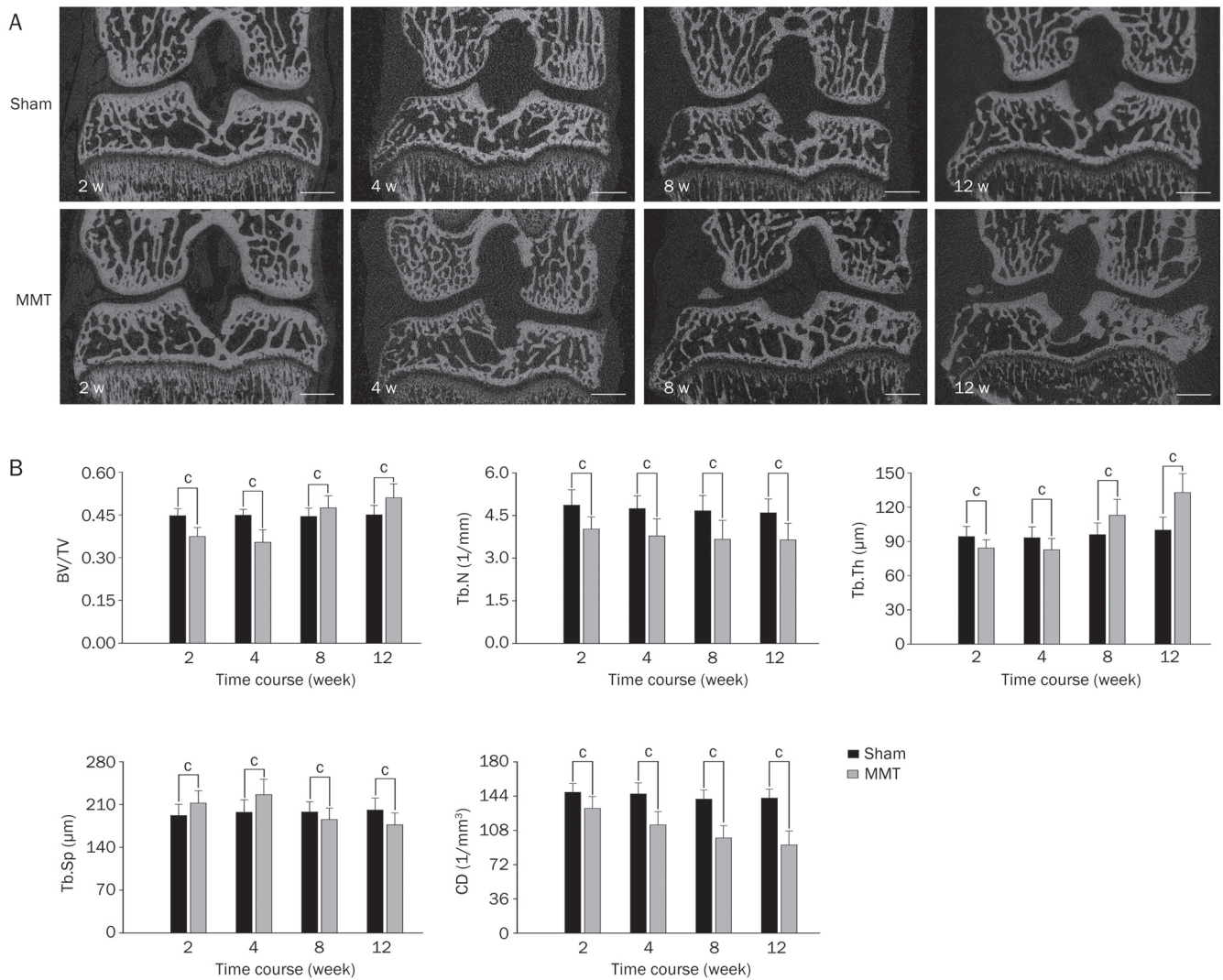


Figure 2. Changes in subchondral bone during OA progression. (A) Representative images of the knee obtained with micro-CT scanning, Bar=1000 μm. (B) Analysis of subchondral bone microstructure parameters. The comparison between groups was performed with an independent-samples t-test. Mean±SD. $n=8$. ^c $P<0.01$ vs Sham group.

reduced Tb.N and CD, which were significantly preserved by immediate ZOL administration (MMT/ZOL0), moderately preserved by early administration (MMT/ZOL4), and not altered by late administration (MMT/ZOL8).

CGRP expression in DRG neurons

As shown in Figure 8, the total neuron number, as determined by fluorescent Nissl staining, was similar among all five groups ($P>0.05$). Retrograde labeling through intra-articular injection of FG allowed the tracing of afferent neurons that innervate the knee joint in L3, L4, and L5 DRGs. The total number of FG-labeled neurons was not significantly different among the groups ($P>0.05$). Among the FG-labeled neurons, the percentage of CGRP-positive neurons in MMT/NS rats ($48.9\% \pm 3\%$) was increased compared with that observed in the Sham/NS rats ($40.7\% \pm 3\%$, $P<0.01$). This ratio was significantly reduced by immediate (MMT/ZOL0, $42.8\% \pm 2.8\%$,

$P<0.01$) and early (MMT/ZOL4, $44.6\% \pm 2.9\%$, $P<0.01$) ZOL administration but not by administration at advanced stages despite a decreasing trend (MMT/ZOL8, $47.5\% \pm 2.4\%$, $P>0.05$).

Discussion

The present study demonstrated that cartilage degeneration and subchondral bone remodeling in the rat MMT model occurred in a time-dependent manner. With disease progression, subchondral bone remodeling shifted from increased bone resorption at an early stage to bone accretion at an advanced stage. These results were consistent with those of earlier published studies^[8, 19]. Similar to previous studies^[19, 29], the current study showed that bisphosphonates demonstrated a protective effect on cartilage and bone changes related to OA in a dose-dependent manner. To better elucidate the time-dependent effects of the therapy, the higher dose was chosen. We found that immediate ZOL administration significantly,

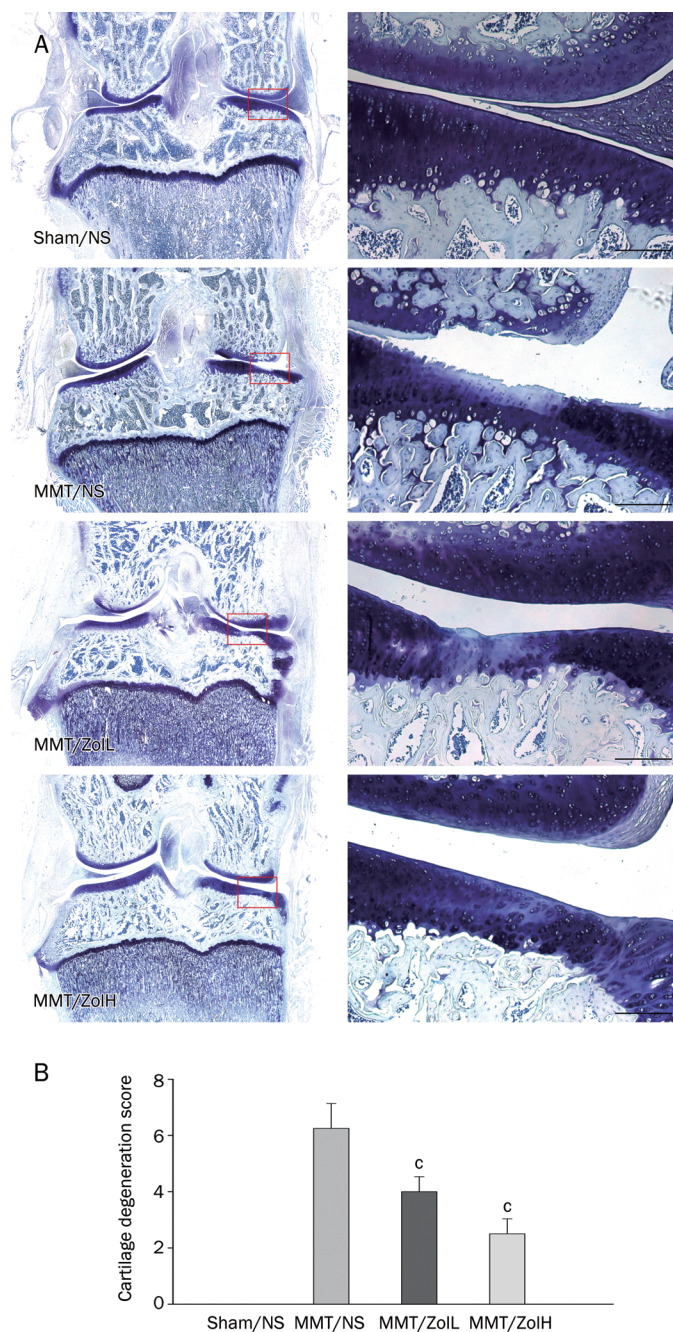


Figure 3. The effects of low dose 10 $\mu\text{g}/\text{kg}$ body weight (MMT/ZoIL) and high dose 100 $\mu\text{g}/\text{kg}$ body weight (MMT/ZoIH) on cartilage degeneration. (A) Representative images with toluidine blue O staining. Bar=200 μm . (B) Cartilage degeneration score. The comparison between groups was performed with one-way analysis of variance using the Tukey *post-hoc* test. Mean \pm SD. $n=10$. ^c $P<0.01$, compared with the MMT/NS group.

and early to some degree, improved subchondral microstructural parameters, decreased the cartilage degeneration score, and reduced weight-bearing asymmetry and CGRP expression. Late administration demonstrated no statistically significant efficacy.

Because of the intimate biological and mechanical relation-

ship of articular cartilage and subchondral bone^[10, 13, 22], the abnormal remodeling of subchondral bone would aggravate the degeneration of overlying articular cartilage; thus, retarded bone remodeling would slow the degeneration of overlying articular cartilage^[9, 11, 12]. However, because subchondral bone properties are dynamic during disease progression, the abnormal subchondral bone cannot always be modified. Our data demonstrated that subchondral bone absorption is increased at an early stage of OA. If ZOL treatment is initiated at this stage, abnormalities in subchondral bone can be reversed to a large extent and then cartilage degeneration would be retarded accordingly. Conversely, at an advanced stage, subchondral bone accretion was increased mainly due to excessive mechanical stress^[30-32]. If ZOL therapy is given at this stage, subchondral bone remodeling would not be reversible, and articular cartilage degeneration would continue.

To better identify the effects of ZOL on joint pain, pain behavior was measured as weight-bearing asymmetry between operated and contralateral hind limbs, and the expression of CGRP in DRG neurons innervating the joint was measured. CGRP is a marker of sensory neurons expressed by C and A δ primary afferent fibers and is mainly involved in pain perception^[33]. It has been shown that nociceptive A δ and C fibers innervate the capsule, ligaments, periosteum and subchondral bone of the joint^[3]. Osteoarthritic conditions activate the nociceptive system, and CGRP is elevated in the DRGs^[25, 34]. A decrease in the number of CGRP-positive DRG neurons was also consistent with improved pain behavior^[25, 35]. In accordance with a previous study, our data show that the percentage of CGRP-positive neurons was markedly increased at advanced stages in the MMT model, whereas ZOL treatment initiated at early stages reduced the expression of CGRP. These findings, combined with the results of pain behavior studies, indicate that ZOL treatment initiated at an early stage could relieve joint pain.

Currently, the origin of pain in osteoarthritis is poorly understood. Synovitis has been found to be associated with knee pain severity^[14, 17]. However, consistent with a previous study^[24], histological analysis of the MMT joint in the present study did not reveal any synovial hyperplasia (Figures 7S and 8S). Hence, the weight-bearing asymmetry and increased CGRP expression after MMT surgery indicate that OA structural changes, rather than synovitis, cause joint pain. ZOL treatment initiated early, but not late, retards cartilage degeneration and subchondral bone remodeling, leading us to believe that ZOL reduces joint pain by inhibiting OA structural changes. Adult articular cartilage is normally an avascular tissue^[3]; therefore, abnormal subchondral bone may be the main source of algogenesis. This hypothesis is supported by findings that knee pain is correlated with abnormalities in subchondral bone^[14-17] and by the following findings. Osteochondral vascular density increased with increasing cartilage deterioration severity and clinical disease activity scores^[36]. Sensory nerves were present within vascular channels at the osteochondral junction in OA^[37]. Therefore subchondral nerves may be exposed to painful stimuli in OA, which would

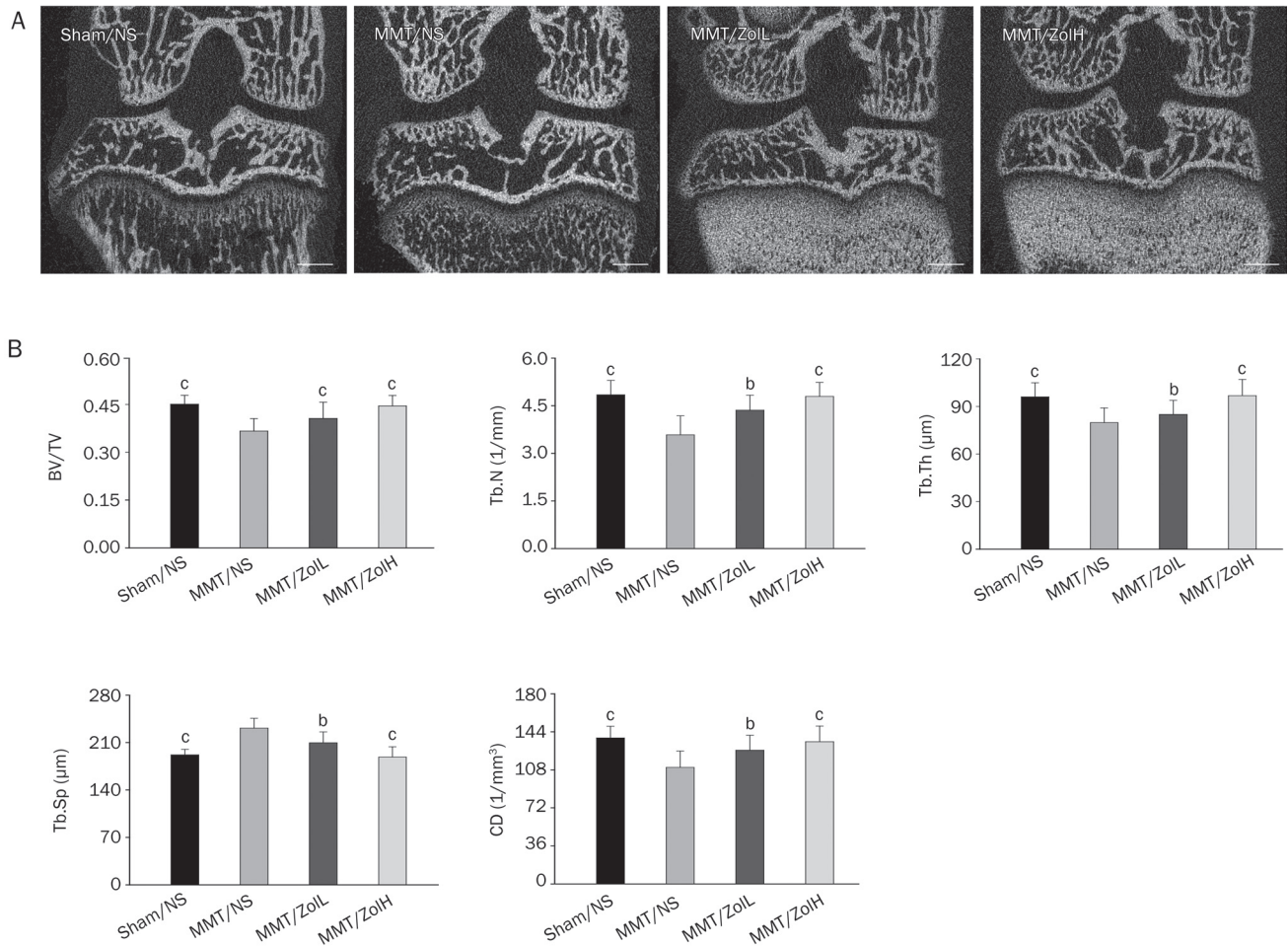


Figure 4. The effects of low dose 10 µg/kg body weight (MMT/ZoIL) and high dose 100 µg/kg body weight (MMT/ZoIH) on subchondral bone remodeling. (A) Representative images of the knee obtained using micro-CT scanning. Bar=1000 µm. (B) Analysis of subchondral bone microstructure parameters. The comparison between groups was performed with one-way analysis of variance using the Tukey *post-hoc* test. Mean±SD. $n=10$. ^b $P<0.05$, ^c $P<0.01$ vs MMT/NS group.

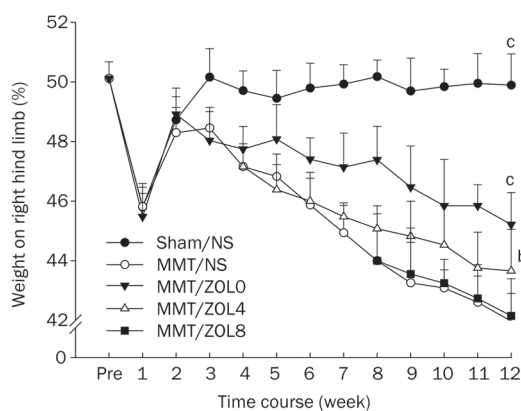


Figure 5. The effect of ZOL 100 µg/kg treatment initiated at different stages on pain behavior, as measured by the percentage of weight borne on the right hind limb. $n=10$ per group. ^b $P<0.05$, ^c $P<0.01$ vs MMT/NS group.

lead to weight-bearing pain, the most common symptom in OA patients^[3]. Immediate pain relief is obtained by total or unicompartmental knee arthroplasty^[38], in which most of the affected subchondral plate is excised. Therefore, we hypothesize that the potential mechanism by which bisphosphonates reduce joint pain mainly lies in improving cartilage and subchondral bone integrity and accordingly inhibiting subchondral neurovascular invasion. However, other potential mechanisms may be involved. For example, the acidic environment created by osteoclasts could cause bone pain during subchondral bone remodeling^[19, 39]. Nevertheless, weight-bearing asymmetry and CGRP expression were similar in MMT/NS rats and MMT/ZoL8 rats. However, subtle differences may be detected with a more sophisticated behavior apparatus, such as a computerized incapacitance meter system and gait analysis system, to measure neuron electrophysiology and detect additional neuropeptides in DRGs and the spinal cord.

In the present study, ZOL was phase-administered based

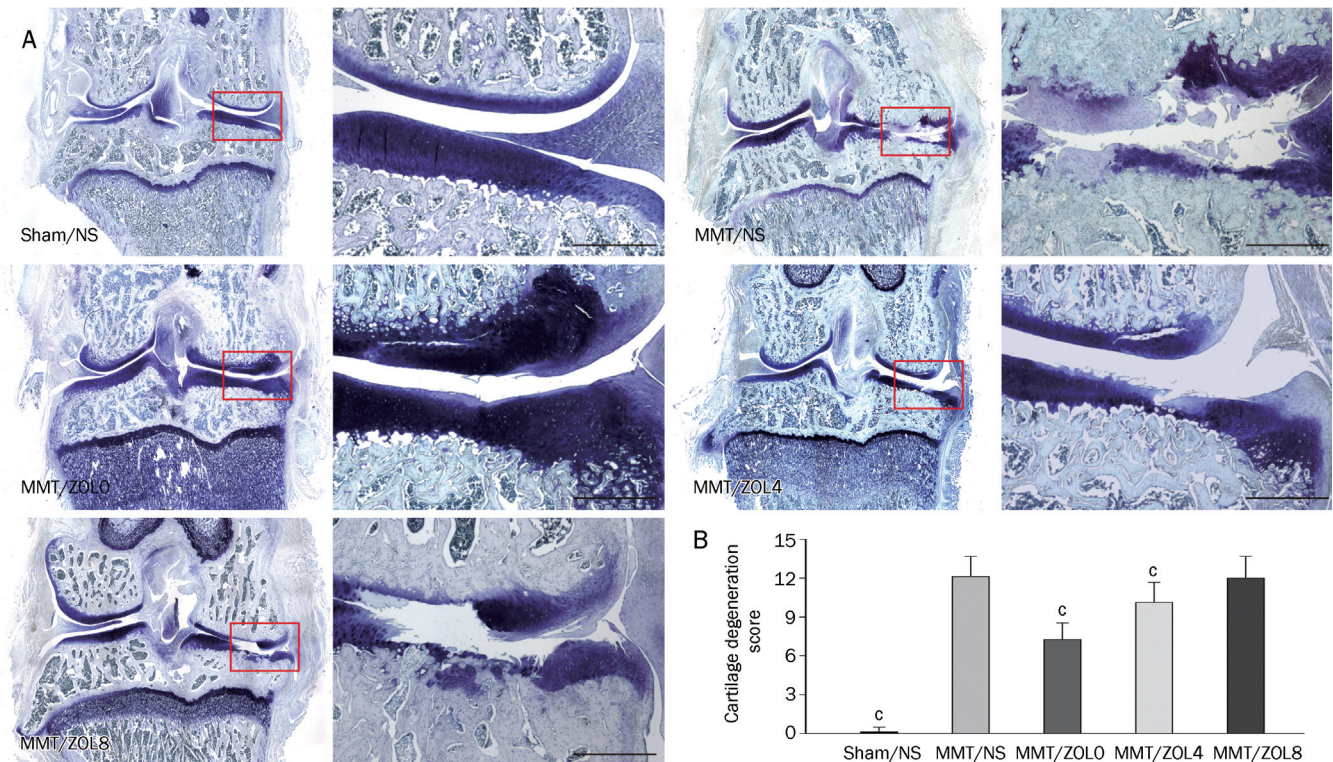


Figure 6. The effect of ZOL 100 µg/kg treatment initiated at different stages on cartilage degeneration. (A) Representative images of toluidine blue O staining. Bar=400 µm. (B) Cartilage degeneration score. $n=10$ per group. $^*P<0.01$ vs MMT/NS group.

on changes in the subchondral bone microarchitecture indices from micro-CT scanning. If combined with changes in bone formation and resorption biomarkers during OA progression, a better understanding of the relationship between the efficacy of ZOL treatment and the stage of disease progression, especially in the situation of subchondral bone remodeling, could be obtained.

In conclusion, our study demonstrated, using an established rat MMT OA model, that the stage of OA progression influences the efficacy of ZOL therapy on joint degeneration and pain. ZOL treatment initiated immediately, and to some degree early, significantly inhibited subchondral bone remodeling, attenuated cartilage degeneration, and alleviated joint pain; no statistically significant efficacy was observed if therapy was initiated at a later stage, when significant cartilage degeneration and subchondral bone accretion were already present. Similarly, to obtain the maximum efficacy, bisphosphonate treatment should be initiated in rat at an early stage of OA, rather than in individuals with advanced stages of OA pathogenesis.

Acknowledgements

This work was supported by grants from the National Natural Science Foundation of China (No 30700852 and 30973038), the Fund for Key Disciplines of Shanghai Municipal Education Commission (J50206) and the Program for the Shanghai Key Laboratory of Orthopedic Implants (Grant No 08DZ2230330). The majority of the research was completed in the Shanghai

Key Laboratory of Orthopedic Implants.

Author contribution

De-gang YU and Bo YU carried out most of the behavioral testing and immunohistochemical experiments. Yuan-qing MAO and Xin ZHAO performed micro-CT imaging experiments. Xiao-qing WANG, Hui-feng DING, Lei CAO, Guang-wang LIU, Shao-bo NIE, Shen LIU, and Zhen-an ZHU conceived the study, designed the experiments, participated in data analysis and helped to draft the manuscript. Xiao-qing Wang and Guang-wang LIU performed H&E staining and synovial reaction evaluation in the supplementary study.

Supplementary Information

Supplementary figures is available at the Acta Pharmacologica Sinica website.

References

- Holman HR, Lorig KR. Overcoming barriers to successful aging. Self-management of osteoarthritis. *West J Med* 1997; 167: 265–8.
- Lane NE, Brandt K, Hawker G, Peeva E, Schreyer E, Tsuji W, et al. OA-RSI-FDA initiative: defining the disease state of osteoarthritis. *Osteoarthritis Cartilage* 2011; 19: 478–82.
- Hunter DJ, McDougall JJ, Keefe FJ. The symptoms of osteoarthritis and the genesis of pain. *Med Clin North Am* 2009; 93: 83–100.
- Felson DT, Neogi T. Osteoarthritis: is it a disease of cartilage or of bone? *Arthritis Rheum* 2004; 50: 341–4.
- Mansell JP, Collins C, Bailey AJ. Bone, not cartilage, should be the major focus in osteoarthritis. *Nat Clin Pract Rheumatol* 2007; 3: 306–7.

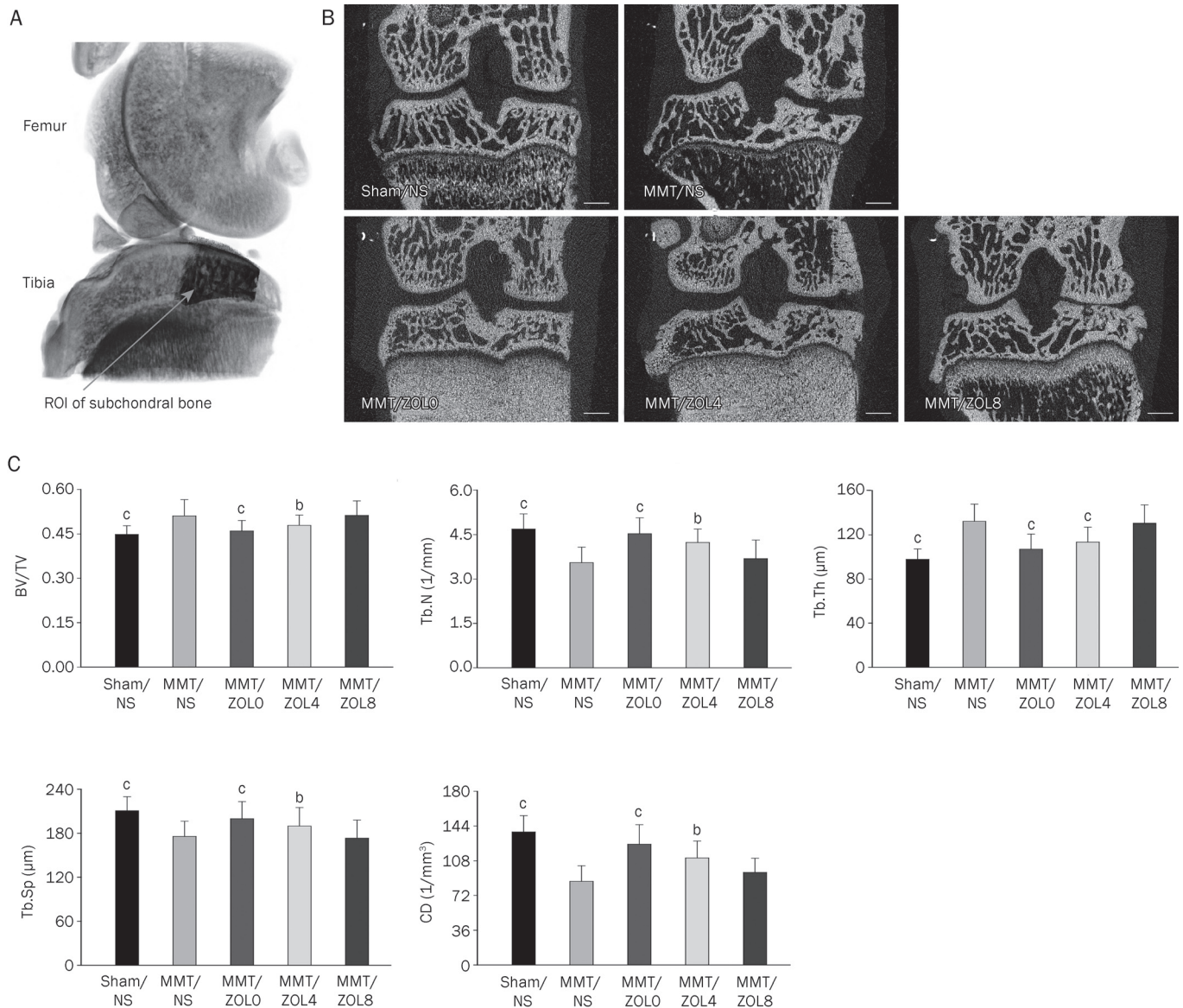


Figure 7. The effect of ZOL 100 $\mu\text{g}/\text{kg}$ treatment initiated at different stages on subchondral bone remodeling. (A) The load-bearing region at the medial tibial plateau was taken as a region of interest (ROI). (B) Representative micro-CT images of the knee. Bar=1000 μm . (C) Analysis of subchondral bone microstructure. $n=10$ per group. ^c $P<0.05$, ^c $P<0.01$ vs MMT/NS group.

- Karsdal MA, Leeming DJ, Dam EB, Henriksen K, Alexandersen P, Pastoureau P, *et al*. Should subchondral bone turnover be targeted when treating osteoarthritis? *Osteoarthritis Cartilage* 2008; 16: 638–46.
- Golding SR. Role of bone in osteoarthritis pathogenesis. *Med Clin North Am* 2009; 93: 25–35.
- Kwan Tat S, Lajeunesse D, Pelletier JP, Martel-Pelletier J. Targeting subchondral bone for treating osteoarthritis: what is the evidence? *Best Pract Res Clin Rheumatol* 2010; 24: 51–70.
- Bailey AJ, Mansell JP, Sims TJ, Banse X. Biochemical and mechanical properties of subchondral bone in osteoarthritis. *Biorheology* 2004; 41: 349–58.
- Burr DB. Anatomy and physiology of the mineralized tissues: role in the pathogenesis of osteoarthritis. *Osteoarthritis Cartilage* 2004; 12: S20–30.
- Calvo E, Castaneda S, Largo R, Fernandez-Valle ME, Rodriguez-Salvanes F, Herrero-Beaumont G. Osteoporosis increases the severity of cartilage damage in an experimental model of osteoarthritis in rabbits. *Osteoarthritis Cartilage* 2007; 15: 69–77.
- Golding MB, Goldring SR. Articular cartilage and subchondral bone in the pathogenesis of osteoarthritis. *Ann N Y Acad Sci* 2010; 1192: 230–7.
- Lories RJ, Luyten FP. The bone-cartilage unit in osteoarthritis. *Nat Rev Rheumatol* 2011; 7: 43–9.
- Felson DT. The sources of pain in knee osteoarthritis. *Curr Opin Rheumatol* 2005; 17: 624–8.
- Neogi T, Felson D, Niu J, Nevitt M, Lewis CE, Aliabadi P, *et al*. Association between radiographic features of knee osteoarthritis and pain: results from two cohort studies. *BMJ* 2009; 339: b2844.
- Moisio K, Eckstein F, Chmiel JS, Guermazi A, Prasad P, Almagor O, *et al*. Denuded subchondral bone and knee pain in persons with knee

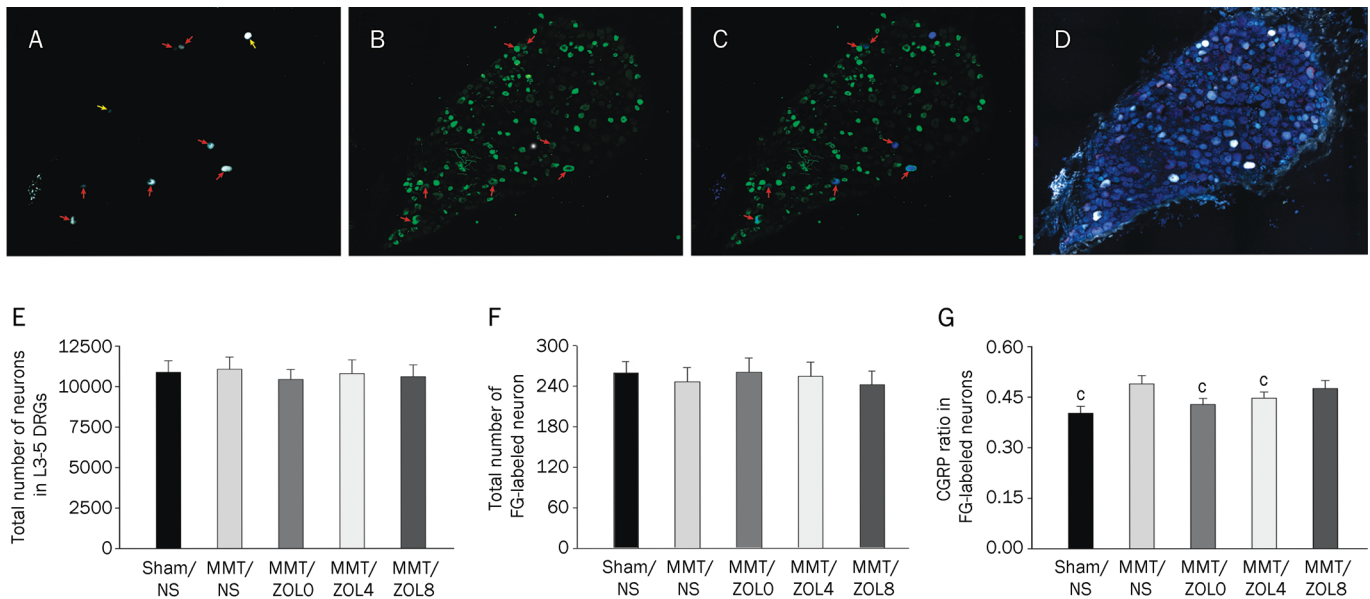


Figure 8. The effects of ZOL 100 µg/kg treatment on the expression of CGRP in DRGs. Representative images of the same DGR section retrograde labeled with FG (A), labeled with CGRP (B), labeled with FG and CGRP (C) and stained with fluorescent nissl (D). The red arrowheads indicate FG-labeled neurons that are CGRP-positive, the yellow arrowheads indicate CGRP-negative. The total number of neurons (E), the total number of FG-labeled neurons (F), and the percentage of CGRP-positive neurons out of the total number of FG-labeled neurons, in L3, L4, and L5 DRGs (G). The results were averaged for each individual rat. $n=10$ per group. $^{\circ}P<0.01$ vs MMT/NS group.

osteoarthritis. *Arthritis Rheum* 2009; 60 : 3703–10.

17 Wenham CY, Conaghan PG. Imaging the painful osteoarthritic knee joint: what have we learned? *Nat Clin Pract Rheumatol* 2009; 5: 149–58.

18 Lash RW, Nicholson JM, Velez L, Van Harrison R, McCort J. Diagnosis and management of osteoporosis. *Prim Care* 2009; 36: 181–98.

19 Hayami T, Pickarski M, Wesolowski GA, McLane J, Bone A, Destefano J, et al. The role of subchondral bone remodeling in osteoarthritis: reduction of cartilage degeneration and prevention of osteophyte formation by alendronate in the rat anterior cruciate ligament transection model. *Arthritis Rheum* 2004; 50: 1193–206.

20 Carbone LD, Nevitt MC, Wildy K, Barrow KD, Harris F, Felson D, et al. The relationship of antiresorptive drug use to structural findings and symptoms of knee osteoarthritis. *Arthritis Rheum* 2004; 50: 3516–25.

21 Saag KG. Bisphosphonates for osteoarthritis prevention: “Holy Grail” or not? *Ann Rheum Dis* 2008; 67: 1358–9.

22 Castaneda S, Roman-Blas JA, Largo R, Herrero-Beaumont G. Subchondral bone as a key target for osteoarthritis treatment. *Biochem Pharmacol* 2012; 83: 315–23.

23 Gerwin N, Bendele AM, Glasson S, Carlson CS. The OARS histopathology initiative-recommendations for histological assessments of osteoarthritis in the rat. *Osteoarthritis Cartilage* 2010; 18: S24–34.

24 Bove SE, Laemont KD, Brooker RM, Osborn MN, Sanchez BM, Guzman RE, et al. Surgically induced osteoarthritis in the rat results in the development of both osteoarthritic-like joint pain and secondary hyperalgesia. *Osteoarthritis Cartilage* 2006; 14: 1041–8.

25 Ochiai N, Ohtori S, Sasho T, Nakagawa K, Takahashi K, Takahashi N, et al. Extracorporeal shock wave therapy improves motor dysfunction and pain originating from knee osteoarthritis in rats. *Osteoarthritis Cartilage* 2007; 15: 1093–6.

26 Im HJ, Kim JS, Li X, Kotwal N, Sumner DR, van Wijnen AJ, et al. Alteration of sensory neurons and spinal response to an experimental osteoarthritis pain model. *Arthritis Rheum* 2010; 62: 2995–3005.

27 Janusz MJ, Bendele AM, Brown KK, Taiwo YO, Hsieh L, Heitmeyer SA. Induction of osteoarthritis in the rat by surgical tear of the meniscus: Inhibition of joint damage by a matrix metalloproteinase inhibitor. *Osteoarthritis Cartilage* 2002; 10: 785–91.

28 Strassle BW, Mark L, Leventhal L, Piesla MJ, Jian Li X, Kennedy JD, et al. Inhibition of osteoclasts prevents cartilage loss and pain in a rat model of degenerative joint disease. *Osteoarthritis Cartilage* 2010; 18: 1319–28.

29 Buckland-Wright JC, Messent EA, Bingham CO, 3rd, Ward RJ, Tonkin C. A 2 yr longitudinal radiographic study examining the effect of a bisphosphonate (risedronate) upon subchondral bone loss in osteoarthritic knee patients. *Rheumatology* 2007; 46: 257–64.

30 Fukuda Y, Takai S, Yoshino N, Murase K, Tsutsumi S, Ikeuchi K, et al. Impact load transmission of the knee joint-influence of leg alignment and the role of meniscus and articular cartilage. *Clin Biomech* 2000; 15: 516–21.

31 Lindsey CT, Narasimhan A, Adolfo JM, Jin H, Steinbach LS, Link T, et al. Magnetic resonance evaluation of the interrelationship between articular cartilage and trabecular bone of the osteoarthritic knee. *Osteoarthritis Cartilage* 2004; 12: 86–96.

32 Cox LG, van Rietbergen B, van Donkelaar CC, Ito K. Bone structural changes in osteoarthritis as a result of mechanoregulated bone adaptation: a modeling approach. *Osteoarthritis Cartilage* 2011; 19: 676–82.

33 Hokfelt T. Neuropeptides in perspective: the last ten years. *Neuron* 1991; 7: 867–79.

34 Hunter DJ, McDougall JJ, Keefe FJ. The symptoms of osteoarthritis and the genesis of pain. *Rheum Dis Clin North Am* 2008; 34: 623–43.

35 Staton PC, Wilson AW, Bountra C, Chessell IP, Day NC. Changes in dorsal root ganglion CGRP expression in a chronic inflammatory model of the rat knee joint: differential modulation by rofecoxib and para-

- cetamol. *Eur J Pain* 2007; 11: 283–9.
- 36 Walsh DA, Bonnet CS, Turner EL, Wilson D, Situ M, McWilliams DF. Angiogenesis in the synovium and at the osteochondral junction in osteoarthritis. *Osteoarthritis Cartilage* 2007; 15: 743–51.
- 37 Suri S, Gill SE, Massena de Camin S, McWilliams DF, Wilson D, Walsh DA. Neurovascular invasion at the osteochondral junction and in osteophytes in osteoarthritis. *Ann Rheum Dis* 2007; 66: 1423–8.
- 38 Ethgen O, Bruyere O, Richy F, Dardennes C, Reginster JY. Health-related quality of life in total hip and total knee arthroplasty. A qualitative and systematic review of the literature. *J Bone Joint Surg Am* 2004; 86: 963–74.
- 39 Yoneda T, Hata K, Nakanishi M, Nagae M, Nagayama T, Wakabayashi H, *et al*. Involvement of acidic microenvironment in the pathophysiology of cancer-associated bone pain. *Bone* 2011; 48: 100–5.

Original Article

Anisomycin induces glioma cell death via down-regulation of PP2A catalytic subunit *in vitro*

Jun-yang LI^{1, #}, Jia-yuan HUANG^{2, #}, Meng LI¹, Han ZHANG¹, Biao XING¹, Gong CHEN¹, Dong WEI¹, Pei-yuan GU¹, Wei-xing HU^{1, *}

¹Department of Neurosurgery, The First Affiliated Hospital of Nanjing Medical University, Nanjing 210029, China; ²Department of Oncology, Jinling Hospital, Nanjing University, Nanjing 210002, China

Aim: To examine the effects of anisomycin on glioma cells and the related mechanisms *in vitro*.

Methods: The U251 and U87 human glioblastoma cell lines were tested. The growth of the cells was analyzed using a CCK-8 cell viability assay. Apoptosis was detected using a flow cytometry assay. The expression of proteins and phosphorylated kinases was detected using Western blotting.

Results: Treatment of U251 and U87 cells with anisomycin (0.01–8 $\mu\text{mol/L}$) inhibited the cell growth in time- and concentration-dependent manners (the IC_{50} values at 48 h were 0.233 ± 0.021 and 0.192 ± 0.018 $\mu\text{mol/L}$, respectively). Anisomycin (4 $\mu\text{mol/L}$) caused $21.5\% \pm 2.2\%$ and $25.3\% \pm 3.1\%$ of apoptosis proportion, respectively, in U251 and U87 cells. In the two cell lines, anisomycin (4 $\mu\text{mol/L}$) activated p38 MAPK and JNK, and inactivated ERK1/2. However, neither the p38 MAPK inhibitor SB203580 (10 $\mu\text{mol/L}$) nor the JNK inhibitor SP600125 (10 $\mu\text{mol/L}$) prevented anisomycin-induced cell death. On the other hand, anisomycin (4 $\mu\text{mol/L}$) reduced the level of PP2A/C subunit (catalytic subunit) in a time-dependent manner in the two cell lines. Treatment of the two cell lines with the PP2A inhibitor okadaic acid (100 nmol/L) caused marked cell death.

Conclusion: Anisomycin induces glioma cell death via down-regulation of PP2A catalytic subunit. The regulation of PP2A/C expression by anisomycin provides a clue to further study on its role in glioma therapy.

Keywords: anisomycin; glioma; apoptosis; p38 MAPK; JNK; protein phosphatase 2A

Acta Pharmacologica Sinica (2012) 33: 935–940; doi: 10.1038/aps.2012.46; published online 11 Jun 2012

Introduction

Anisomycin is an antibiotic that blocks protein synthesis by inhibiting peptidyl transferase activity in ribosomes^[1]. It was reported to induce apoptosis in a variety of cell types, including colon adenocarcinoma cells, leukemia cells, Jurkat cells and ventricular myocytes^[2–5]. Anisomycin was widely used as an agonist for p38 mitogen-activated protein kinase (p38 MAPK) and Jun-NH₂ terminal kinase (JNK) in studies investigating the p38 and JNK signaling pathways. Anisomycin typically induces apoptosis through activation of the p38 MAPK and/or the JNK pathway. A recent novel finding demonstrated that, independent of its ability to activate p38 MAPK and JNK, anisomycin can also decrease FLIP (c-Fas – associated death domain-like interleukin-1 (IL-1) – converting enzyme-like inhibitory protein) protein synthesis in prostate cancer cells.

This decrease in FLIP expression sensitizes cells to anoikis, which is the initiation of apoptosis that is triggered by a loss of contact with the extracellular matrix^[6].

In this study, we found that anisomycin induces U251 and U87 human glioblastoma cell death independent of its ability to activate p38 MAPK and JNK and their downstream kinases and transcription factors. Our data demonstrate that anisomycin suppressed U251 and U87 cell growth in a concentration dependent manner, and at 8 $\mu\text{mol/L}$, the cell viability was reduced to $18.4\% \pm 2.1\%$ for U251 and $14.6\% \pm 1.3\%$ for U87. However, neither p38 MAPK nor JNK inhibitors prevented anisomycin-induced U251 cell death. We also found that anisomycin induced U251 cell death independent of its role as an anoikis sensitizer. Interestingly, our study revealed that anisomycin down-regulates PP2A C subunit protein expression and almost totally inhibits PP2A/C expression after 48 h treatment. C subunit is the catalytic site of PP2A, and its down-regulation can greatly decrease PP2A activity. Our results showed treatment of PP2A inhibitor okadaic acid (OA) causes significant cell death in U251 and U87 cells, indicating that

[#]These authors contributed equally to this paper.

^{*}To whom correspondence should be addressed.

E-mail hwx66@126.com

Received 2012-02-08 Accepted 2012-04-05

anisomycin-induced glioma cell death may be caused by down-regulation of PP2A catalytic subunit. These findings may open new avenues for studying the mechanisms underlying p38 MAPK and JNK pathway-independent anisomycin-induced cell death and further research into the use of anisomycin as a glioma therapeutic agent.

Materials and methods

Agents and antibodies

Anisomycin, SB203580 and SP600125 were purchased from Sigma-Aldrich (St Louis, MO, USA). PP2A inhibitor OA was purchased from Beyotime Institute of Biotechnology (Shanghai, China). For cell treatment, agents were dissolved in dimethyl sulfoxide (DMSO) and then diluted in serum-supplemented media immediately before use. The final concentrations of SB203580 and SP600125 were 10 $\mu\text{mol/L}$, OA was 100 nmol/L. Anisomycin was used at the following concentrations: 0.01, 0.04, 0.1, 0.4, 1, 2, 4, or 8 $\mu\text{mol/L}$.

Antibodies against GAPDH, p38, phospho-p38 (Thr180/Tyr182), JNK, phospho-JNK (Thr183/Tyr185), ERK1/2, phospho-ERK1/2 (Thr202/Tyr204), phospho-ATF-2 (Thr71), phospho-Hsp27 (Ser15), phospho-c-JUN (Ser63 and Ser73), PP2A C subunit, caspase-8 and FLIP were purchased from Cell Signaling Technology (Beverly, MA, USA).

Cell culture

The U251 and U87 human glioblastoma cell lines were gifts from Professor Kun YAO (Department of Microbiology, Nanjing Medical University, Nanjing, China). The cells were maintained in Dulbecco's modified Eagle's medium (DMEM) containing 10% fetal bovine serum, glutamine, nonessential amino acids, and 1% penicillin/streptomycin (complete medium). The cells were grown at 37°C in a humidified atmosphere of 95% air and 5% CO₂.

Cell viability assay

A cell viability assay was performed using the cell counting kit-8 (CCK-8) according to the manufacturer's instructions (Dojindo Laboratories, Kumamoto, Japan). The cells were plated in 96-well plates in 200 μL of culture media with various concentrations of anisomycin. The cells were then cultured at 37°C in a humidified incubator containing 95% air and 5% CO₂. After 48 h, the CCK-8 solution was added to each well and incubated for 1 h in the incubator. The absorbance measurement was performed at 450 nm using an enzyme-linked immunosorbent assay plate reader (Bio-Rad Laboratories, Inc., Berkeley, CA, USA).

Apoptosis assay by flow cytometry

Cells were plated in 10-cm culture dishes, allowed to adhere for 8 h and then exposed to anisomycin for 48 h at 37°C. After 48 h, the cells were collected by trypsinization, centrifuged (3500 r/min for 5 min), and washed twice with PBS. The cells were fixed in 1 mL of 70% ethanol, pelleted by centrifugation (3500 r/min for 5 min), rinsed twice with PBS. Then, cells were incubated for 15 min at room temperature with annexin

V-FITC and propidium iodide before analysis with a FACSAria III flow cytometer (BD Biosciences, San Jose, CA, USA).

Western blotting

The cells were lysed in an appropriate volume of lysis buffer (Cell Signaling Technology, Beverly, MA, USA). Cell lysates were heat denatured for 8 min and separated by SDS-PAGE. After gel electrophoresis, the proteins were transferred to an Immobilon-P Transfer membrane (Millipore Corporation, Bedford, MA, USA). Membranes were blocked for 1.5 h at room temperature in TBST (0.1% Tween-20+TBS) containing 5% (*w/v*) non-fat dry milk. After blocking, the membranes were probed overnight at 4°C with the primary antibodies, followed by a 1-h incubation with the secondary antibodies at room temperature. Antibody detection was performed using the Super Signal West Pico chemiluminescent substrate (Pierce, Chicago, IL, USA) and the ChemiDoc MP Imaging System (Bio-Rad, Hercules, CA, USA).

Statistical analysis

All data were analyzed by the Student-Newman-Keuls test and expressed as the mean \pm standard deviations (SD). The results at $P < 0.05$ were considered to be statistically significant.

Results

Anisomycin inhibits U251 and U87 cell growth and induces apoptosis

To study the effect of anisomycin on U251 and U87 cell growth, cells were treated with anisomycin at the following concentrations: 0.004, 0.01, 0.04, 0.1, 0.4, 1, 2, 4, or 8 $\mu\text{mol/L}$ for 48 h. Cell viability was analyzed using a CCK-8 kit. The data demonstrated that U251 cell growth was suppressed by anisomycin at as low a concentration as 0.01 $\mu\text{mol/L}$ (with cell viability at 75.3% \pm 6.1% for U251 and 74.4% \pm 4.3% for U87). At the high concentration of anisomycin (8 $\mu\text{mol/L}$), cell viability was reduced to 18.4% \pm 2.1% for U251 and 15.6% \pm 1.3% for U87 (Figure 1A). The IC₅₀ at 48 h was measured as 0.233 \pm 0.021 $\mu\text{mol/L}$ for U251 and 0.192 \pm 0.018 $\mu\text{mol/L}$ for U87.

We also detected the presence of apoptosis by flow cytometry. The cells were treated with 0 or 4 $\mu\text{mol/L}$ anisomycin for 72 h, and double stained with annexin V-FITC conjugates and propidium iodide, which was followed by analysis with a flow cytometer. In this assay, the sub-G₁ fraction represents apoptotic cells (indicated by black arrows in Figure 1B). We found that the Q2 plus Q4 proportions indicated apoptosis cells, 4 $\mu\text{mol/L}$ anisomycin caused 21.5% \pm 2.2% of apoptosis proportion in U251 cells and 25.3% \pm 3.1% in U87 cells.

Anisomycin activates p38 MAPK and JNK but inactivates ERK1/2 in U251 and U87 cells

The phosphorylation of p38 MAPK, JNK, and ERK1/2 was detected in U251 and U87 cells either untreated or treated with 4 $\mu\text{mol/L}$ anisomycin for 30 min. As shown in Figure 2, anisomycin-induced phosphorylation of p38 MAPK at Thr180/Tyr182 and JNK at Thr183/Tyr185. To investigate the effect of anisomycin on the downstream substrates of p38 and JNK, we

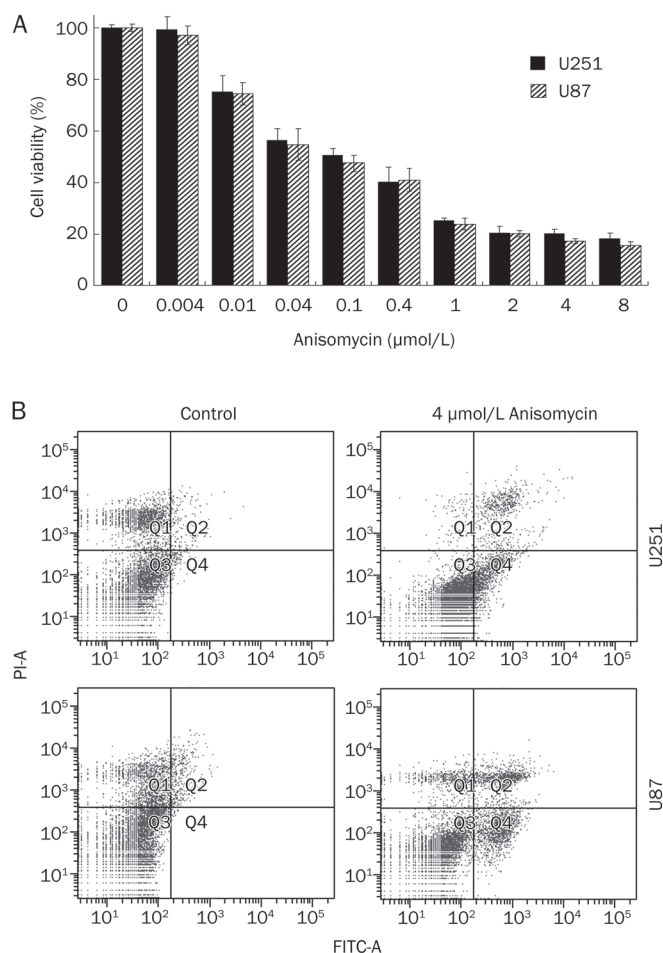


Figure 1. Anisomycin inhibits U251 and U87 cell growth and induces cell apoptosis. (A) U251 and U87 cells were separately treated with anisomycin at concentrations of 0, 0.004, 0.01, 0.04, 0.1, 0.4, 1, 2, 4, or 8 μmol/L for 48 h. Cell viability was analyzed using CCK-8 kit. Anisomycin started to suppress U251 and U87 cell growth at concentration of 0.01 μmol/L (cell viability is 75.3%±6.1% for U251 and 74.4%±4.3% for U87). At 8 μmol/L, the cell viability is only 18.4%±2.1% for U251 and 15.6%±1.3% for U87. Anisomycin inhibits U251 and U87 cell growth in a concentration-dependent manner. (B) U251 or U87 cells were treated with 0 or 4 μmol/L anisomycin for 72 h, and double stained with annexin V-FITC conjugates and propidium iodide followed by analysing in a flow cytometer. The Q2 plus Q4 proportions indicated apoptosis cells, 4 μmol/L anisomycin caused 21.5%±2.2% of apoptosis proportion in U251 cells and 25.3%±3.1% in U87 cells.

detected the phosphorylation of Hsp27, c-JUN, and ATF-2 by Western blotting. We found that anisomycin activated both Hsp27 (Ser15), which is phosphorylated by MAPKAP kinase 2 as a result of the activation of the p38 MAPK pathway, and ATF-2 (Thr71), which can be phosphorylated by both JNK and p38 MAPK. However, c-JUN (Ser63 or Ser73), the substrate of JNK, was not activated in anisomycin treated U251 or U87 cells, compared with control treated cells.

ERK1/2 is another well-studied member of the MAPKs, but its function is usually distinct from the other two mem-

bers, p38, and JNK. Our results demonstrated that activated ERK1/2 expression was high in untreated U251 or U87 cells but very low in anisomycin treated cells (Figure 2).

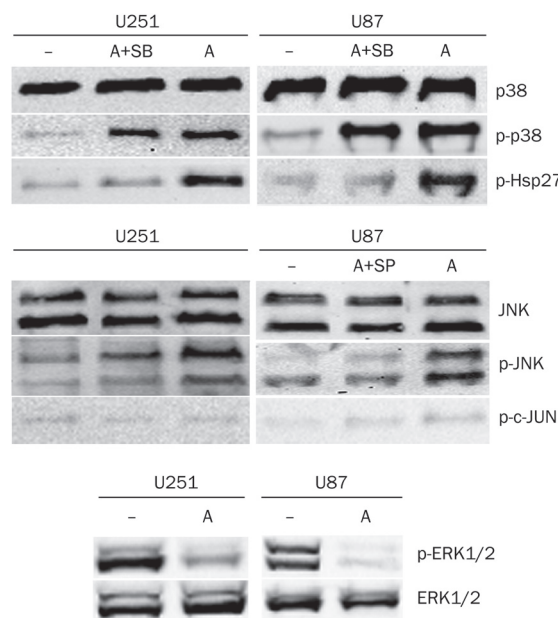


Figure 2. Anisomycin activates p38MAPK and JNK but inactivates ERK1/2 in U251 and U87 cells. Cells were non-treated (-) or treated with 4 μmol/L anisomycin for 30 min, or pre-treated with SB203580 or SP600125 for 1 h and then treated with 4 μmol/L anisomycin for 30 min. The phosphorylated and unphosphorylated p38MAPK, JNK, and ERK1/2 were detected by Western blotting using corresponding antibodies. The activations (phosphorylations) of the downstream substrates of p38 and JNK, Hsp27, and c-JUN were also detected. The unphosphorylated MAPKs served as loading control. A: Anisomycin; SB: SB203580; SP: SP600125.

Neither p38 MAPK nor JNK inhibitors prevented anisomycin-induced U251 cell death

To investigate whether the p38 MAPK or the JNK pathway was mediating anisomycin-induced U251 cell death, the p38 MAPK inhibitor SB203580 and the JNK inhibitor SP600125 were used to pre-treat U251 or U87 cells. First of all, the inhibitory effects of SB203580 and SP600125 on anisomycin treated cells were analyzed (Figure 2). Our results showed SB203580 significantly inhibits activation of Hsp27 which is the downstream substrate of p38MAPK but does not inhibit the phosphorylation of p38MAPK, indicating that SB203580 inhibit p38MAPK activity but not its activation. For SP600125, we demonstrated it significantly inhibits the phosphorylation of JNK (Figure 2). Cells were divided into four groups and pre-treated with either DMSO vehicle control, 10 μmol/L SB203580, 10 μmol/L SP600125 or the combination of 10 μmol/L SB203580 and 10 μmol/L SP600125. After 1 h, the pre-treated cells were treated with with 0 or 4 μmol/L anisomycin for 48 h. A CCK-8 kit was used to detect the quantity of viable cells and determine cell viability. As the results show in Fig-

ure 3, neither SB203580 nor SP600125 prevented anisomycin-induced U251 or U87 cell death ($P>0.05$).

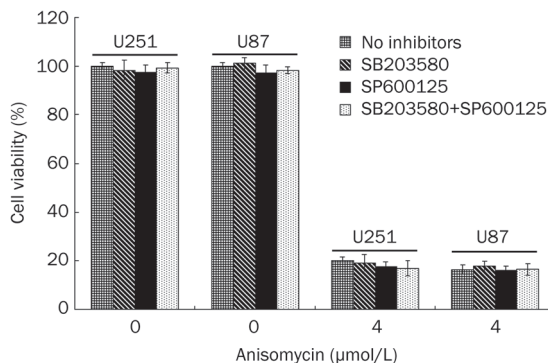


Figure 3. Neither SB203580 nor SP600125 prevents anisomycin-induced U251 or U87 cell death. U251 or U87 cells were divided into four groups and separately pre-treated with DMSO vehicle, 10 μmol/L SB203580, 10 μmol/L SP600125, or 10 μmol/L SB203580 plus 10 μmol/L SP600125. After 1 h, the pre-treated cells were treated with 0 or 4 μmol/L anisomycin for 48 h. Then, cell viability was detected using CCK-8 kit. In groups that pre-treated with 10 μmol/L SB203580, 10 μmol/L SP600125, or 10 μmol/L SB203580 plus 10 μmol/L SP600125, anisomycin-induced cell death was not prevented ($P>0.05$).

Anisomycin induces U251 and U87 cell death independent of its ability to sensitize cells to anoikis

Caspase-8 and the caspase-8 inhibitor FLIP have been reported to participate in anisomycin-induced apoptosis^[6]. Anisomycin can induce apoptosis by decreasing levels of FLIP, resulting in a sensitization of cells to anoikis. We detected the levels of full-length caspase-8, cleaved caspase-8 and FLIP by Western blotting lysates from U251 and U87 cells that were either untreated or treated with anisomycin. We found that full-length caspase-8 and FLIP were both undetectable in untreated U251 and U87 cells. In the cells treated with anisomycin, no activated cleaved caspase-8 was detected (data not shown). Our results suggest that anisomycin-induced U251 and U87 cell death is independent of its role as an anoikis sensitizer.

Anisomycin down-regulates PP2A C subunit expression in U251 and U87 cells

Depletion of the PP2A C subunit has been shown to be lethal in cells. We detected the effect of anisomycin on the expression of the PP2A C subunit in U251 and U87 cells by Western blotting. We found that anisomycin (4 μmol/L) down-regulates PP2A C subunit protein expression in a time-dependent manner and almost completely inhibits its expression after 48 h of treatment (Figure 4). C subunit is the catalytic part of PP2A, and its downregulation can greatly decrease PP2A activity. To investigate whether inhibition of PP2A activity could cause U251 or U87 cell death, we used PP2A inhibitor OA 100 nmol/L to treat U251 and U87 cells for 48 h and detected the cell viability by CCK-8. In OA treated cells, the

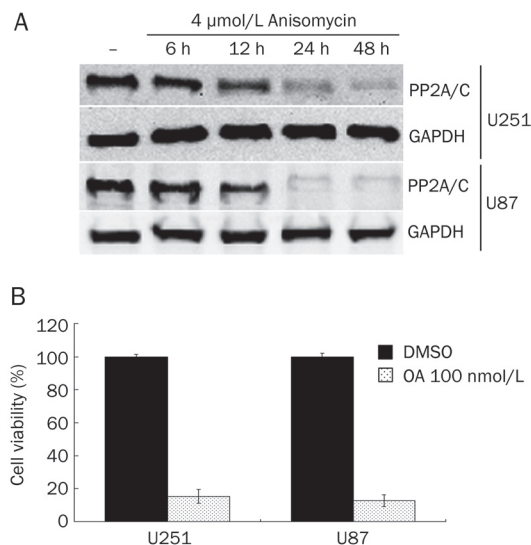


Figure 4. Anisomycin down-regulates PP2A C subunit level in U251 and U87 cells. (A) U251 and U87 cells were non-treated (-) or treated with 4 μmol/L anisomycin for 6, 12, 24, or 48 h. PP2A C subunit level was detected by Western blotting. GAPDH served as loading control. (B) U251 and U87 cells were treated with 0 or 100 nmol/L okadaic acid (OA) for 48 h, then the cell viability were detected by using CCK-8 kit. In OA treated cells, the cell viability was 15.3%±4.2% for U251 and 12.8%±3.5% for U87.

cell viability was 15.3%±4.2% for U251 and 12.8%±3.5% for U87. We demonstrated that PP2A inhibition in glioblastoma cells causes significant cell death (Figure 4B). These results indicate that anisomycin may induce U251 and U87 cell death by downregulation of PP2A catalytic subunit.

Discussion

Anisomycin is an agonist of p38 and JNK and is widely used as a research tool to study these two pathways in various cellular processes. Anisomycin is also well known as a protein synthesis inhibitor that is involved in apoptosis^[7-9]. In this study, we investigated the effects of anisomycin on U251 and U87 human glioblastoma cells. We first detected the effects of anisomycin on U251 and U87 cell growth and found that anisomycin efficiently induced cell death (at 8 μmol/L, cell viability was reduced to 18.4%±2.1%). Previous studies suggest that MAPK plays a major role in anisomycin-induced apoptosis^[10-12]. Stress stimuli, including UV irradiation, anoxia and translation inhibitors like anisomycin, can activate p38 and JNK pathways and induce apoptosis^[13]. ERK1/2 is typically activated by growth factors and phorbol esters and contributes to cell proliferation, differentiation, and survival. These three MAPK pathways interact with each other by cross-talking to influence the cellular outcome^[14, 15]. Thus, we investigated the effects of anisomycin on the phosphorylation of the three major MAPKs: p38, JNK, and ERK1/2. Our results demonstrated that p38 and JNK, as well as their downstream effectors Hsp27 and ATF-2, were activated by anisomycin, whereas ERK1/2 was dephosphorylated after anisomycin treatment.

To confirm whether the p38 and JNK pathways played a role in anisomycin-induced cell death, we introduced their inhibitors, SB203580 and SP600125, into this study. We found that neither of the two inhibitors could prevent anisomycin-induced cell death, even when used in combination. These data indicate that anisomycin induces U251 and U87 cell death independent of its ability to activate p38 MAPK and JNK. These data led to the following important question: through which pathway does anisomycin induce U251 cell death?

A recent study addressed a similar question^[6]. Using a chemical screen, the authors identified a novel mechanism by which anisomycin induces apoptosis. They demonstrated that, independent of the ability to activate p38 MAPK and JNK, anisomycin can also induce apoptosis by decreasing expression of the caspase-8 inhibitor FLIP, resulting in cells being sensitized to anoikis. The term “anoikis” refers to a self-initiated process, during which nonmalignant cells undergo apoptosis upon detachment from the extracellular matrix (ECM)^[16, 17]. More recently, it was found that not only endothelial cells and nonmalignant epithelial cells but also malignant epithelial cells could undergo anoikis through self-initiated activation of the death receptor signaling pathway^[17-20]. The results from these studies suggested that anisomycin initiates anoikis in a caspase-8-dependent manner, due to its inhibition of FLIP protein synthesis, and independent of its ability to activate JNK and p38^[6]. To investigate whether anisomycin initiates anoikis in U251 and U87 cells, we detected the expression of full-length caspase-8, cleaved caspase-8 and FLIP protein by Western blotting. The results showed that full-length caspase-8 and FLIP protein were both undetectable in untreated U251 and U87 cells, and in anisomycin treated cells, active cleaved caspase-8 was also negative. Ashley *et al*^[21] reported similar results in 2005. They demonstrated that caspase-8 is absent or low in many gliomas, and almost no gliomas express significant amounts of cellular FLIP. Taken together, these data suggest that initiation of anoikis cannot be the mechanism by which anisomycin induces U251 or U87 cell death.

In our study, we present a novel finding that may provide a new perspective for investigating anisomycin-induced apoptosis. We detected the protein expression of the PP2A C subunit in anisomycin treated U251 and U87 cells. The results showed that anisomycin down-regulates PP2A/C expression in a time-dependent manner. After 48 h of treatment with anisomycin, almost no PP2A/C protein could be detected. PP2A/C is the catalytic subunit, and its downregulation can greatly decrease PP2A activity. We hypothesize that in anisomycin-induced U251 and U87 cell death, PP2A/C may be a target that initiates apoptosis. To investigate whether inhibition of PP2A activity could cause U251 or U87 cell death, we introduced a PP2A inhibitor Okadaic acid (OA). U251 and U87 cells were treated with 100 nmol/L OA and then the cell viability were evaluated by using CCK-8. Our results demonstrated that PP2A inhibition in U251 and U87 cells causes significant cell death. This indicated that anisomycin-induced U251 and U87 cell death may directly caused by downregulation of PP2A catalytic subunit. Lots of previous studies have proven the

direct effects of PP2A/C on apoptosis, although none of these studies investigated anisomycin-induced apoptosis. Deletion of the PP2A/C α subunit in homozygous null mutant mice is embryonically lethal^[22]. Silencing of the PP2A/C gene was found to greatly decrease PP2A activity and lead to localized death in plant stems and cells^[23]. Knockdown of the PP2A/C led to concurrent loss of nontargeted PP2A subunits, and caused cell death with the morphological and biochemical changes characteristic of apoptosis in cultured S2 cells^[24]. Wong *et al* found that the introduction of siPP2A/C α to cells caused a noticeably accelerated cell death in both the BT474 and the SKBR3 cell lines^[25]. In future studies, PP2A/C would be the focus of our research, not only because of its potential role in mediating anisomycin-induced U251 cell death but also because of its potential role as a target for glioma therapy.

In conclusion, our findings demonstrate that anisomycin can induce U251 cell death independent of its ability to activate p38 MAPK and JNK or its ability to sensitize cells to anoikis. The novel finding that anisomycin sharply down-regulates PP2A/C protein expression may provide new perspectives for anisomycin-induced apoptosis and further studies with anisomycin in glioma therapy.

Acknowledgements

We thank Professor Kun YAO for providing the U251 and U87 human glioblastoma cell line. This work was supported by grants from the Jiangsu Province Natural Science Foundation (No BK2007257).

Author contribution

Jun-yang LI and Wei-xing HU designed the research; Jun-yang LI, Jia-yuan HUANG, Meng LI, Han ZHANG, Biao XING, Gong CHEN, Dong WEI, and Pei-yuan GU performed the research; Jun-yang LI, Jia-yuan HUANG, Meng LI, and Wei-xing HU analyzed the data; Jun-yang LI wrote the paper; and Wei-xing HU revised the paper.

References

- 1 Gold PE. Protein synthesis inhibition and memory: formation vs amnesia. *Neurobiol Learn Mem* 2008; 89: 201-11.
- 2 Yang H, Choi HJ, Park SH, Kim JS, Moon Y. Macrophage inhibitory cytokine-1 (MIC-1) and subsequent urokinase-type plasminogen activator mediate cell death responses by ribotoxic anisomycin in HCT-116 colon cancer cells. *Biochem Pharmacol* 2009; 78: 1205-13.
- 3 Lunghi P, Tabilio A, Pinelli S, Valmadre G, Ridolo E, Albertini R, *et al*. Expression and activation of SHC/MAP kinase pathway in primary acute myeloid leukemia blasts. *Hematol J* 2001; 2: 70-80.
- 4 Caricchio R, D'Adamio L, Cohen PL. Fas, ceramide and serum withdrawal induce apoptosis via a common pathway in a type II Jurkat cell line. *Cell Death Differ* 2002; 9: 574-80.
- 5 Clerk A, Sugden PH. Cell stress-induced phosphorylation of ATF2 and c-Jun transcription factors in rat ventricular myocytes. *Biochem J* 1997; 325: 801-10.
- 6 Mawji IA, Simpson CD, Gronda M, Williams MA, Hurren R, Henderson CJ, *et al*. A chemical screen identifies anisomycin as an anoikis sensitizer that functions by decreasing FLIP protein synthesis. *Cancer Res* 2007; 67: 8307-15.

- 7 Piekarski DJ, Seto T, Zucker I. The protein synthesis inhibitor anisomycin reduces sex behavior during a critical period after testosterone treatment in male Syrian hamsters. *Physiol Behav* 2011; 105: 215–9.
- 8 Sadowski RN, Canal CE, Gold PE. Lidocaine attenuates anisomycin-induced amnesia and release of norepinephrine in the amygdala. *Neurobiol Learn Mem* 2011; 96: 136–42.
- 9 Malysheva MV, Grigoryev AA, Bulycheva TI, Zatsepina OV. Enhanced sensitivity of nucleoli in human proliferating cells to inhibition of protein synthesis with anisomycin. *Bull Exp Biol Med* 2010; 150: 258–62.
- 10 Croons V, Martinet W, Herman AG, Timmermans JP, De Meyer GR. The protein synthesis inhibitor anisomycin induces macrophage apoptosis in rabbit atherosclerotic plaques through p38 mitogen-activated protein kinase. *J Pharmacol Exp Ther* 2009; 329: 856–64.
- 11 Desgranges B, Levy F, Ferreira G. Anisomycin infusion in amygdala impairs consolidation of odor aversion memory. *Brain Res* 2008; 1236: 166–75.
- 12 Wang Q, Zhang JY, Liu SJ, Li HL. Overactivated mitogen-activated protein kinase by anisomycin induces tau hyperphosphorylation. *Sheng Li Xue Bao* 2008; 60: 485–91.
- 13 Qiao S, Murakami K, Zhao Q, Wang B, Seo H, Yamashita H, *et al*. Mimosine-induced apoptosis in C6 glioma cells requires the release of mitochondria-derived reactive oxygen species and p38, JNK activation. *Neurochem Res* 2012; 37: 417–27.
- 14 Junttila MR, Li SP, Westermarck J. Phosphatase-mediated crosstalk between MAPK signaling pathways in the regulation of cell survival. *FASEB J* 2008; 22: 954–65.
- 15 Xia Z, Dickens M, Raingeaud J, Davis RJ, Greenberg ME. Opposing effects of ERK and JNK-p38 MAP kinases on apoptosis. *Science* 1995; 270: 1326–31.
- 16 Frisch SM, Francis H. Disruption of epithelial cell-matrix interactions induces apoptosis. *J Cell Biol* 1994; 124: 619–26.
- 17 Frisch SM, Sreaton RA. Anoikis mechanisms. *Curr Opin Cell Biol* 2001; 13: 555–62.
- 18 Mawji IA, Simpson CD, Hurren R, Gronda M, Williams MA, Filmus J, *et al*. Critical role for Fas-associated death domain-like interleukin-1-converting enzyme-like inhibitory protein in anoikis resistance and distant tumor formation. *J Natl Cancer Inst* 2007; 99: 811–22.
- 19 Frisch SM. Evidence for a function of death-receptor-related, death-domain-containing proteins in anoikis. *Curr Biol* 1999; 9: 1047–9.
- 20 Rosen K, Shi W, Calabretta B, Filmus J. Cell detachment triggers p38 mitogen-activated protein kinase-dependent overexpression of Fas ligand. A novel mechanism of Anoikis of intestinal epithelial cells. *J Biol Chem* 2002; 277: 46123–30.
- 21 Ashley DM, Riffkin CD, Muscat AM, Knight MJ, Kaye AH, Novak U, *et al*. Caspase 8 is absent or low in many *ex vivo* gliomas. *Cancer* 2005; 104: 1487–96.
- 22 Gotz J, Probst A, Ehler E, Hemmings B, Kues W. Delayed embryonic lethality in mice lacking protein phosphatase 2A catalytic subunit Calpha. *Proc Natl Acad Sci U S A* 1998; 95: 12370–5.
- 23 He X, Anderson JC, del Pozo O, Gu YQ, Tang X, Martin GB. Silencing of subfamily I of protein phosphatase 2A catalytic subunits results in activation of plant defense responses and localized cell death. *Plant J* 2004; 38: 563–77.
- 24 Li X, Scuderi A, Letsou A, Virshup DM. B56-associated protein phosphatase 2A is required for survival and protects from apoptosis in *Drosophila melanogaster*. *Mol Cell Biol* 2002; 22: 3674–84.
- 25 Wong LL, Zhang D, Chang CF, Koay ES. Silencing of the PP2A catalytic subunit causes HER-2/neu positive breast cancer cells to undergo apoptosis. *Exp Cell Res* 2010; 316: 3387–96.

Original Article

Arctigenin alleviates ER stress via activating AMPK

Yuan GU¹, Xiao-xiao SUN¹, Ji-ming YE², Li HE¹, Shou-sheng YAN¹, Hao-hao ZHANG¹, Li-hong HU³, Jun-ying YUAN⁴, Qiang YU^{1,*}

¹Department of Tumor Pharmacology, and ³State Key Laboratory of Drug Research, Shanghai Institute of Materia Medica, Chinese Academy of Sciences, Shanghai 201203, China; ²Health Innovations Research Institute and School of Health Sciences, RMIT University, Melbourne, Australia; ⁴Department of Cell Biology, Harvard Medical School, Boston, USA

Aim: To investigate the protective effects of arctigenin (ATG), a phenylpropanoid dibenzylbutyrolactone lignan from *Arctium lappa* L (Compositae), against ER stress *in vitro* and the underlying mechanisms.

Methods: A cell-based screening assay for ER stress regulators was established. Cell viability was measured using MTT assay. PCR and Western blotting were used to analyze gene and protein expression. Silencing of the CaMKK β , LKB1, and AMPK α 1 genes was achieved by RNA interference (RNAi). An ATP bioluminescent assay kit was employed to measure the intracellular ATP levels.

Results: ATG (2.5, 5, and 10 μ mol/L) inhibited cell death and unfolded protein response (UPR) in a concentration-dependent manner in cells treated with the ER stress inducer brefeldin A (100 nmol/L). ATG (1, 5, and 10 μ mol/L) significantly attenuated protein synthesis in cells through inhibiting mTOR-p70S6K signaling and eEF2 activity, which were partially reversed by silencing AMPK α 1 with RNAi. ATG (1–50 μ mol/L) reduced intracellular ATP level and activated AMPK through inhibiting complex I-mediated respiration. Pretreatment of cells with the AMPK inhibitor compound C (25 μ mol/L) rescued the inhibitory effects of ATG on ER stress. Furthermore, ATG (2.5 and 5 μ mol/L) efficiently activated AMPK and reduced the ER stress and cell death induced by palmitate (2 mmol/L) in INS-1 β cells.

Conclusion: ATG is an effective ER stress alleviator, which protects cells against ER stress through activating AMPK, thus attenuating protein translation and reducing ER load.

Keywords: arctigenin; ER stress; human hepatocellular liver carcinoma cell; β -cell death; mTOR-p70S6K; eukaryotic translation elongation factor 2 (eEF2); mitochondrial respiration; AMPK

Acta Pharmacologica Sinica (2012) 33: 941–952; doi: 10.1038/aps.2012.60; published online 18 Jun 2012

Introduction

The endoplasmic reticulum (ER) is a highly dynamic organelle in which proteins and lipids are synthesized, modified, and transported. Under conditions such as glucose starvation, hypoxia, aberrant Ca²⁺ regulation, and virus infection, collectively known as ER stress, proteins fail to be correctly folded and eventually accumulate and aggregate in the ER lumen. In response to the abnormalities in the ER, the ER stress response or the unfolded protein response (UPR) is triggered by three ER-localized transmembrane proteins: PKR-like ER kinase (PERK), activation transcription factor (ATF6), and inositol-requiring kinase (IRE1). During the ER stress response, PERK phosphorylates and inhibits eukaryotic initiation factor 2 α (eIF2 α), leading to translation attenuation^[1]; ATF6 translocates to the Golgi, where it is sequentially cleaved by the S1P

and S2P proteases to form an active 50 kDa transcription factor^[2]; and IRE1 cleaves the mRNA transcript of X box protein 1 (XBP1) by an unconventional splicing mechanism^[3]. The activation of these pathways restricts protein load on the ER through transient attenuation of general protein synthesis, promotes degradation of misfolded proteins and increases protein folding capacity in the ER^[4]. However, severe or prolonged accumulation of unfolded proteins triggers apoptosis of target cells.

Accumulating evidence suggest that ER stress is implicated in a wide range of diseases, including diabetes, neurodegeneration, stroke, cardiac disease, muscle degeneration and others^[5]. Particularly, ER stress has been reported to play a central role in pancreatic β -cell demise in type 2 diabetes and perhaps also in type 1 diabetes^[6]. Elevated ER stress markers have been detected in islet tissues of diet-induced and genetic *db/db* diabetic mice^[7], as well as of type 2 diabetes patients^[8]. Thus, we hypothesize that alleviation of ER stress may represent an attractive therapeutic strategy for the treatment of

* To whom correspondence should be addressed.

E-mail qyu@sibs.ac.cn

Received 2012-02-28 Accepted 2012-05-02

β -cell death in type 2 diabetes.

Arctigenin (ATG) is a phenylpropanoid dibenzylbutyrolactone lignan from *Arctium lappa* L (Compositae)^[9]. *Arctium lappa* L, commonly known as burdock, has been widely used in traditional Chinese medicine (TCM) for treating inflammation^[10]. It has also been used therapeutically in Europe and North America for hundreds of years^[11]. The root of *Arctium lappa* L, a popular edible vegetable in China and Japan, is used to make a general health tonic. Previous studies have shown that ATG exerted protective effects against oxidation^[12], viral infection^[13], and cancer^[14]. Most recently, two research groups have reported that ATG could block the UPR and preferentially inhibit tumor cell viability under glucose-deprived conditions^[15, 16]. The molecular targets and mechanisms of ATG however remain unclear.

In the present study, we established a cell-based screening assay for ER stress regulators and identified ATG as a protective agent against ER stress, which efficiently protected HepG2 cells from the ER stress inducer brefeldin A (BFA)-induced cell death, and investigated its action mechanism. We then explored its therapeutic potential in treating diabetes by examining its effects on palmitate-induced β -cell death.

Materials and methods

Reagents and antibodies

Arctigenin (purity >99%), isolated from dried seeds of *A. lappa* as previously described^[17], was provided by Dr Li-hong HU. Penicillin, streptomycin, Brefeldin A, compound C, 5-aminimidazole-4-carboxamide ribonucleoside (AICAR), *D*-glucose, 3-(4,5-dimethylthiazol-2-yl)-2,5-diphenyltetrazolium bromide (MTT) and propidium iodide (PI) were purchased from Sigma (St Louis, Mo, USA). Palmitate was purchased from Takeda Chemical Industries (TCl, Tokyo, Japan). Fatty acid-free bovine serum albumin (BSA) was purchased from Equitech-Bio (Kerrville, TX, USA). α -MEM medium, RPMI-1640 medium and fetal bovine serum (FBS) were purchased from Invitrogen (Carlsbad, CA, USA). All other chemicals (molecular biology grade) were obtained from standard commercial sources. Anti-PARP antibody, anti-phosphorylated AMPK α (Thr172), anti-phosphorylated acetyl-CoA carboxylase (ACC, Ser79), anti-phosphorylated eIF2 α (Ser51), anti-eIF2 α , anti-phosphorylated mTOR (Ser2448), anti-mTOR, anti-phosphorylated p70S6K (Thr389), anti-p70S6K, anti-phosphorylated eEF2 (Thr56), anti-eEF2, and anti-GAPDH antibodies were purchased from Cell Signaling Technology (Beverly, MA, USA). Anti-AMPK α antibody was purchased from Epitomics (Burlingame, CA, USA).

Cell culture

HepG2 cells, a human hepatocellular liver carcinoma cell line, were grown in α -MEM containing 10% (*v/v*) FBS, 100 U/mL penicillin and 100 μ g/mL streptomycin. INS-1 β -cells, a rat insulinoma cell line, were grown in RPMI-1640 medium supplemented with 10% FBS, 1 mmol/L sodium pyruvate, 2 mmol/L *L*-glutamine, 10 mmol/L HEPES, 0.05 mmol/L 2-mercaptoethanol, 100 units/mL penicillin and 100 mg/mL

streptomycin. All cell lines were cultured at 37°C in a humidified atmosphere of 95% air and 5% CO₂.

MTT assay and PI staining

Cell growth rate was measured by the MTT assay. Briefly, after treatment, 20 μ L MTT (5 mg/mL) was added to the culture medium. After incubating for 3 h at 37°C, the cells were solubilized in dimethyl sulfoxide (DMSO), and the absorbance of each well was measured at 570 nm with a spectrophotometer (Molecular Devices, Silicon Valley, CA, USA). Cell death was examined by PI staining. After treatment, cells were stained with 15 μ g/mL PI for 10 min, and then washed with PBS and photographed using a UV microscope.

Western blot analysis

Cells were lysed with 1 \times Laemmli buffer (Sigma, St Louis, MO, USA) containing 2 mmol/L NaF and 2 mmol/L Na₃VO₄, which are used to prevent the dephosphorylation of serine/threonine and tyrosine residues, respectively. Proteins were separated by sodium dodecyl sulphate (SDS) polyacrylamide gel electrophoresis and transferred to a nitrocellulose membrane (Millipore, Bedford, MA, USA). Membrane was blocked in 5% nonfat milk for 1 h at room temperature and then subjected to immunostaining with primary antibodies at 4°C overnight and peroxidase-conjugated secondary antibodies at room temperature for 1 h. Immunoreactivity was revealed with the Supersignal chemiluminescence detection kit (Pierce, Rockford, IL, USA). Immunoblots were scanned and quantified using the software ImageJ (NIH).

Isolation of total RNA, semiquantitative and quantitative reverse transcription PCR

Total RNA was extracted from cells using TRIzol reagent (Invitrogen, Paisley, UK) following the manufacturer's instructions. 4 μ g total RNA and ReverTra Ace reverse transcriptase (Toyobo, Osaka, Japan) were used in the reverse transcription reaction.

Taq DNA polymerase (Takara, Tokyo, Japan) was used for the subsequent polymerase chain reaction (PCR). The specific primers for semiquantitative PCR were as follows: 5'-CCTTGTAGTTGAGAACCA-3' (forward) and 5'-GGGCTTGGTATATATGTGGG-3' (reverse) for both unspliced and spliced XBP-1 (human); 5'-ACCACAGTCCATGCCATCAC-3' (forward) and 5'-TCCACCACCCTGTTGCTG-3' (reverse) for GAPDH (human); 5'-TTACGAGAGAAAACCATGGGC-3' (forward) and 5'-GGGTCCAACCTTGCCAGAATGC-3' (reverse) for both unspliced and spliced XBP-1 (rat); 5'-CCCCAATGTATCCGTTGTGGA-3' (forward) and 5'-GCCTGCTTACCACCTTCTT-3' (reverse) for GAPDH (rat). RT-PCR for XBP-1 was performed for 30 cycles and GAPDH for 20 cycles. PCR products were separated on 8% polyacrylamide gel and visualized by ethidium bromide staining.

Quantitative PCR was performed and analyzed in ABI-PRISM 7700 Sequence Detection System (Applied Biosystems) with SYBR green real-time PCR kit (Takara).

The specific primer sequences were as follows: 5'-GGC-CAGTTTGGTGTCGGTTT-3' (forward) and 5'-CGTTC-CCCGTCCTAGAGTGTT-3' (reverse) for Grp94 (human); 5'-TGGACTGCAGGTGCTGATAG-3' (forward) and 5'-GGATTCTTGGTTGCCTGGTA-3' (reverse) for EDEM (human); 5'-TCAAACCTCATGGGTTCTCC-3' (forward) and 5'-GTGCATCCAACGTGGTCAG-3' (reverse) for ATF4 (human); 5'-TGTGACCTCTGCTGGTCTG-3' (forward) and 5'-TGGAAAGCCTGGTATGAGGAC-3' (reverse) for CHOP (human); 5'-CACGTCCAACCCGGAGAA-3' (forward) and 5'-ATTCCAAGTGCCTCCGATG-3' (reverse) for Grp78 (Rat); 5'-TACTATGCCAGTCAGAAGAAAACG-3' (forward) and 5'-CATCCTTTCTATCCTGTCTCCATA-3' (reverse) for Grp94 (Rat); 5'-GACATGCCGCCTGGAGAAAC-3' (forward) and 5'-AGCCCAGGATGCCCTTTAGT-3' (reverse) for GAPDH (Rat).

RNA interference and transfection

Small interfering RNAs (siRNAs) against Ca²⁺/calmodulin-dependent protein kinase kinase β (CaMKK β), liver kinase B1 (LKB1) and AMPK α 1 as well as a nonsilencing control siRNA were purchased from GenePharma (Shanghai, China). The siRNA sequences applied to target CaMKK β were: 5'-CGAUCGUCaucucUGGUUAdTdT-3' (sense) and 5'-UAACCAGAGAUGACGAUCGdTdT-3' (antisense); for LKB1, 5'-GGCUCUUACGGCAAGGUGAdTdT-3' (sense) and 5'-UCACCUUGCCGUAAGAGCCdTdT-3' (antisense) and, for AMPK α 1, 5'-UGCCUACCAUCUCAUAUAdTdT-3' (sense) and 5'-UAUUAUGAGAUGGUAGGCAdTdT-3' (antisense) were used. The siRNA sequences employed as a negative control were 5'-UUCUCCGAACGUGUCACGUTT-3' (sense) and 5'-ACGUGACACGUUCGGAGAATT-3' (antisense).

Transfections of HepG2 cells with siRNA or a plasmid encoding green fluorescent protein were performed using Lipofectamine 2000 (Invitrogen) according to the manufacturer's protocol.

Determination of intracellular ATP content

The luciferin-luciferase assay was used to measure intracellular ATP levels. Briefly, after rinsing three times with PBS, cells were solubilized in 200 μ L (for 24-well plate) of somatic cell ATP-releasing agent (Sigma, St Louis, MO, USA). Samples were centrifuged for 5 min in a microcentrifuge. Determination of ATP levels was accomplished by combining equal volumes of supernatant with an ATP assay mix (Sigma, St Louis, MO, USA) and measuring the level of chemiluminescence. Measurements are expressed as a percent of the initial value after subtraction of background countings.

Mitochondrial respiration measurements

Mitochondria were isolated from the muscles of male Wistar rats following standard procedures^[18]. To measure respiration rate, mitochondria were incubated at 37°C in a Clark type oxygen electrode (Strathkelvin Instruments, Motherwell, Scotland) in a buffer (pH 7.0) composed of 225 mmol/L mannitol, 75 mmol/L sucrose, 10 mmol/L Tris-HCl, 10 mmol/L

KH₂PO₄, 10 mmol/L KCl, 0.8 mmol/L MgCl₂, 0.1 mmol/L EDTA, 0.3% fatty acid free BSA. The respiratory control ratio, the ratio of state III to state IV respiration, was approximately 5, indicating that the isolated mitochondria were well coupled. Effects of ATG on mitochondrial respiration were determined in the presence of excess ADP (2.4 mmol/L), using substrate combinations targeting either complex I (5 mmol/L pyruvate plus 2 mmol/L malate) or complex II (10 mmol/L succinate plus 4 μ mol/L rotenone) of the respiratory chain.

Palmitate-BSA solution preparation

Palmitate was dissolved in ethanol: H₂O (1: 1, *v/v*) at 50°C at a concentration of 400 mmol/L. The palmitate solution 150 μ L was then mixed with 3 mL fatty acid-free BSA (20% solution in H₂O) by stirring at 37°C for 1 h. The final molar ratio of palmitate to BSA was 6.7: 1 and the final concentration of palmitate-BSA is 20 mmol/L. All control conditions included a solution of vehicle (ethanol: H₂O) mixed with fatty acid-free BSA at the same concentration as the palmitate-BSA solution.

Statistical analysis

Triplicates were used in each experiment and data were shown only if three independent experiments showed consistent results. All results are expressed as the mean \pm SEM. Statistical differences between groups were determined by using the unpaired Student's *t*-test. *P*<0.05 was considered statistically significant. *P*<0.05, *P*<0.01 *vs* control.

Results

ATG protects HepG2 cells from BFA-induced apoptosis

We identified ATG as a protective agent against ER stress through a cell-based assay, in which ER stress was induced by treating HepG2 cells with BFA, an ER-to-Golgi vesicle transport inhibitor. The MTT assay demonstrated that only 27% of the cells had survived at 72 h after BFA treatment. However, ATG inhibited the BFA-induced cell death in a dose-dependent manner (Figure 1A). Meanwhile, a higher concentration of ATG (> 10 μ mol/L) on its own caused a statistically significant decrease in cell number (Figure 1A), so we chose 5 μ mol/L for further studies of its effects on reducing ER stress.

To determine whether ATG specifically affects the ER stress-induced cell death, we investigated the effects of ATG on cell death induced by non-ER stress stimuli, including protein synthesis inhibitor cycloheximide (CHX), DNA topoisomerase II inhibitor adriamycin (ADM), and the mitochondrial complex I inhibitor berberine (BBR)^[18]. Our data showed that ATG had no protective effect against CHX-, ADM-, or BBR-induced cell death, which indicates that ATG may specifically inhibit ER stress-induced cell death (Figure 1B).

The protective effect of ATG against BFA-induced cell death was further confirmed by PI (propidium iodide) staining and PARP cleavage assay. As shown in Figure 1C, BFA increased the number of round and PI-stained cells, which were obviously inhibited by ATG. As reported, BFA induced apoptosis as indicated by poly (ADP-ribose) polymerase (PARP) cleavage. Co-treatment with ATG significantly prevented the BFA-

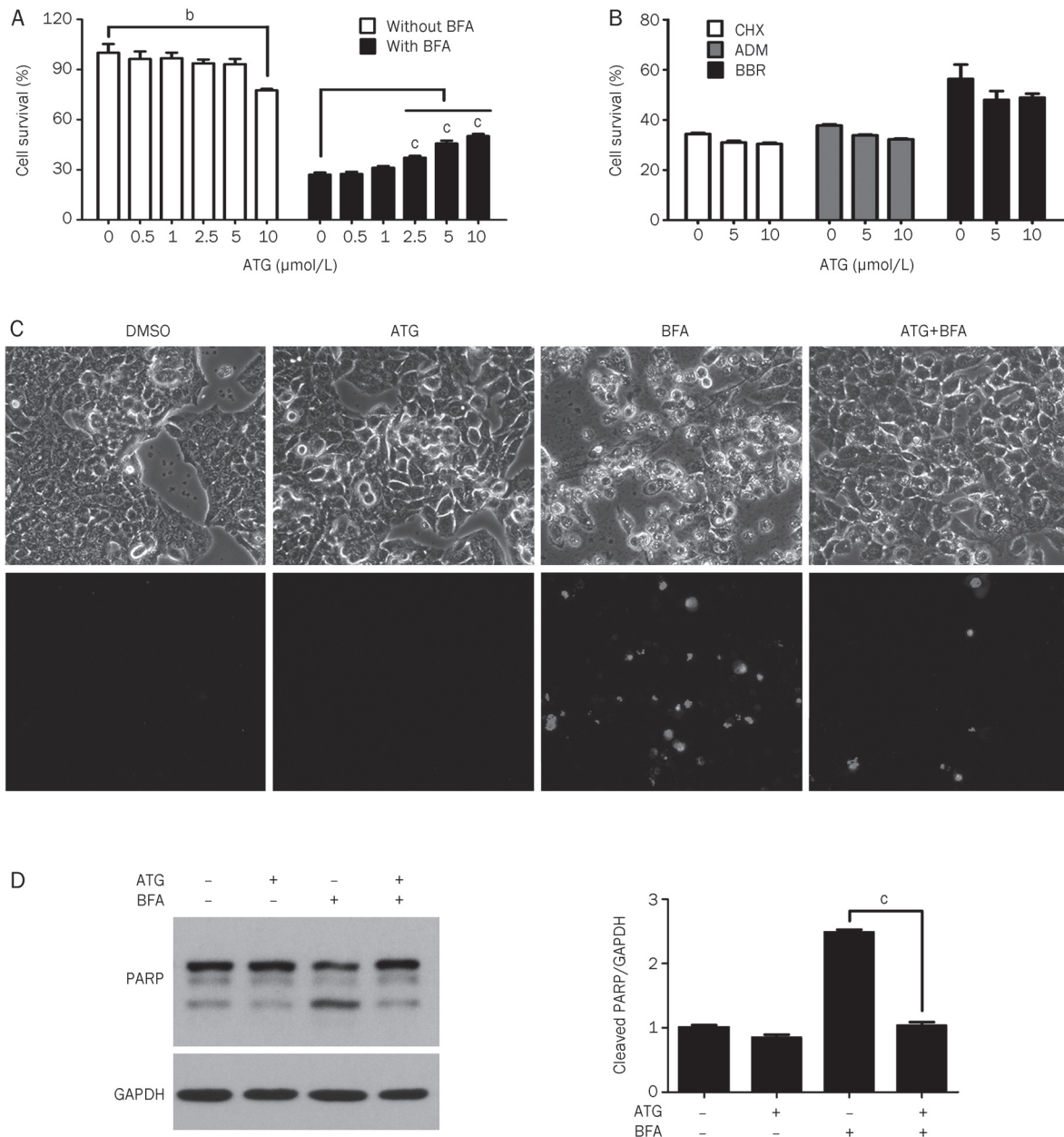


Figure 1. ATG specifically inhibits BFA-induced apoptosis. (A) HepG2 cells were cultured for 72 h with increasing concentrations of ATG alone, or in combination with 100 nmol/L BFA. Viable cell number was measured by MTT assay, and results were reported as a percentage relative to untreated cells. (B) HepG2 cells were cultured for 72 h with the indicated concentrations of ATG in the presence of CHX (50 μmol/L), ADM (500 nmol/L) or BBR (10 μmol/L). Cell growth rate was measured by MTT assay and results were reported as a percentage relative to untreated cells. (C) HepG2 cells were cultured for 48 h in the presence or absence of ATG (5 μmol/L) and/or BFA (100 nmol/L) followed by staining with PI (15 μg/mL) for 15 min. Representative images of cellular morphology (top panel) and PI staining (bottom panel) were shown at 200×magnification. (D) Cells were treated in the same way as in C. PARP cleavage was examined by Western blot analysis. Relative band intensity was normalized for GAPDH and expressed as a percentage compared with the value of untreated control. $n=3$ experiments. Mean±SEM. ^b $P<0.05$, ^c $P<0.01$ vs control.

induced PARP cleavage (Figure 1D). Meanwhile, ATG *per se* did not increase the number of PI-stained cells or induce PARP cleavage (Figure 1C and 1D). These data demonstrate that ATG can effectively protect HepG2 cells from the ER stress inducer (BFA)-induced apoptosis.

ATG down-regulates UPR signaling pathways induced by ER stress

To confirm that ATG protects cells from apoptosis by alleviating ER stress, we investigated the effects of ATG on UPR signaling pathways. Our data showed that BFA increased the

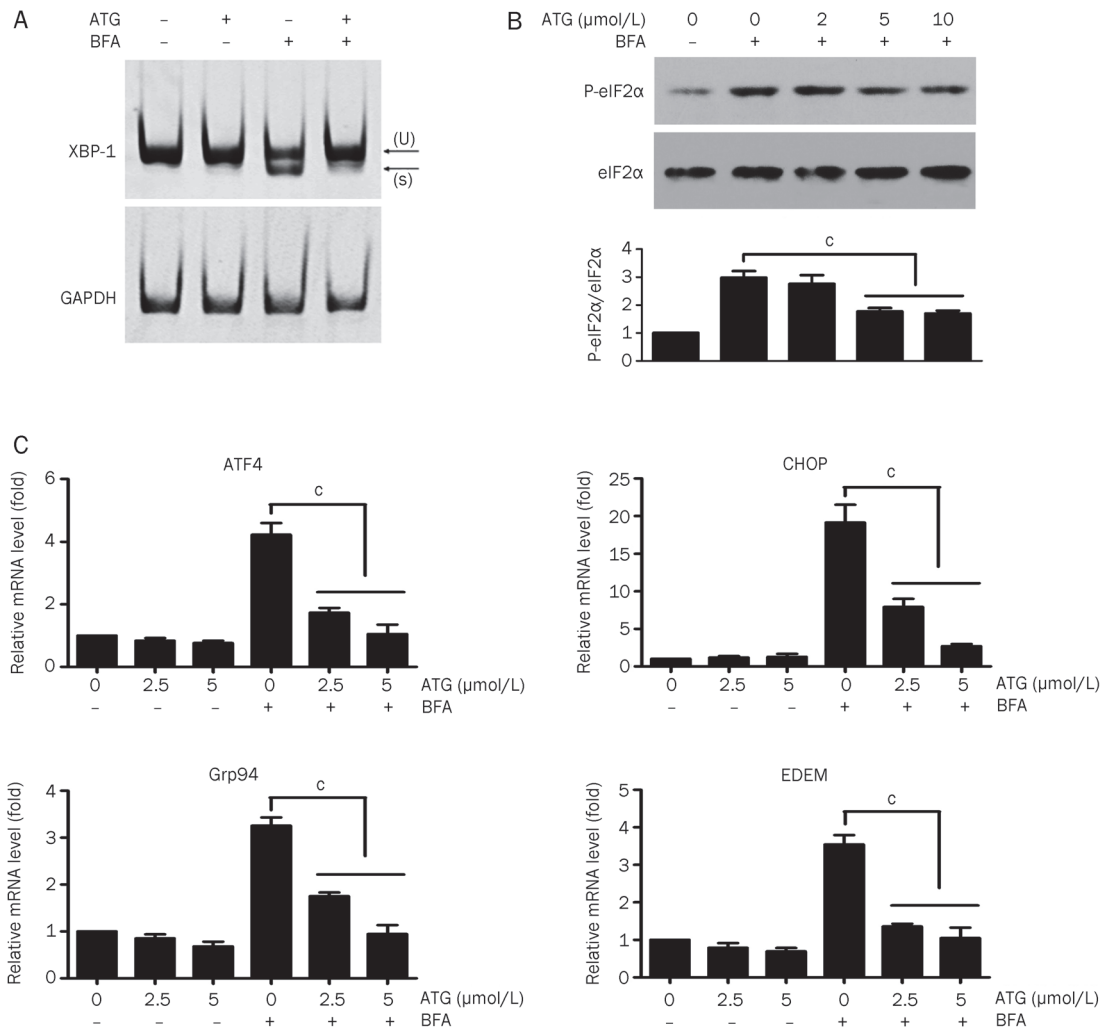


Figure 2. ATG significantly inhibits ER stress-induced UPR. (A) HepG2 cells were cultured for 6 h with or without ATG (5 μmol/L), in the presence or absence of BFA (100 nmol/L), and then lysed for RNA purification. Spliced (S) and unspliced forms of XBP1 mRNA (U) were detected using semi-quantitative RT-PCR. (B) HepG2 cells were cultured with the indicated concentrations of ATG for 3 h in the presence or absence of BFA (100 nmol/L) followed by cell lysis. The phosphorylation level of eIF2α at Ser51 was examined by Western blot analysis. Total eIF2α served as a loading control. The quantification of Western blot images of the ratio between P-eIF2α and eIF2α was shown in the lower panel. (C) HepG2 cells were treated with 0, 2.5, or 5 μmol/L ATG for 6 h, in the presence or absence of BFA (100 nmol/L). The expression levels of UPR downstream genes (Grp94, EDEM, ATF4 and CHOP) were examined by quantitative RT-PCR. *n*=3 experiments. Mean±SEM. ^c*P*<0.01 vs control.

splicing form of XBP-1 mRNA (Figure 2A) as well as phosphorylation of eIF2α on serine (Ser) 51 (Figure 2B), which are two key events in the UPR. And ATG significantly inhibited the BFA-induced splicing of XBP-1 pre-mRNA and phosphorylation of eIF2α (Figure 2A and 2B).

We further used quantitative PCR to evaluate the effects of ATG on the expression of the downstream genes involved in the UPR, which include the activating transcription factor 4 (ATF4), the C/EBP homologous protein (CHOP), the glucose-regulated protein 94 (Grp94), and the ER degradation-enhancing alpha-mannosidase-like protein 1 (EDEM). Our data showed that ATG significantly inhibited BFA-induced expression of all four genes (Figure 2C). In addition, we also investigated the effect of ATG on the UPR induced by tunicamycin (TM), another ER stress inducer that inhibits N-linked

glycosylation in the ER. As shown in supplementary Figure 1, ATG significantly inhibited tunicamycin-induced splicing of XBP-1 pre-mRNA and mRNA expression of four downstream genes involved in the UPR. These results demonstrate that ATG protects cells from BFA-induced apoptosis via alleviating ER stress, and suggest that ATG may act upstream of the UPR, since all downstream signaling pathways were affected.

ATG attenuates protein translation

In mammalian cells, global translation attenuation is the first response to ER stress and is thought to be an important adaptive response that helps cells survive ER stress. Previous studies also reported that protein synthesis inhibitors such as cycloheximide^[19] and salubrinal^[20] displayed potential ER stress-relieving effects. Therefore, inhibition of protein syn-

thesis which reduces the load of substrates presented to the folding machinery in the ER lumen represents an important mechanism to alleviate ER stress^[21]. To explore whether ATG affects protein synthesis, we transfected HepG2 cells with a plasmid encoding green fluorescent protein (GFP), and evaluated the effect of ATG on GFP expression by dividing the IOD (integral optical density) value of green fluorescence by the number of cells that was measured by Hoechst staining. As shown in Figure 3A, 24 h after treatment with ATG, the level of GFP protein was decreased in a dose-dependent manner. Cycloheximide (CHX) served as a positive control. However, neither artigenin nor CHX had effects on the mRNA level of GFP (Figure 3B). These data indicate that ATG can inhibit protein synthesis, which in turn reduces the load on the ER and thereby relieves ER stress.

To investigate how ATG regulates protein translation, we analyzed the effects of ATG on signaling proteins that are responsible for translational control, which include eIF2 α , mTOR (the mammalian target of rapamycin) and p70S6K (p70 ribosomal protein S6 kinase), two components in mTOR signaling, and eEF2 (the eukaryotic translation elongation factor 2). Our data showed that ATG had no effects on the phosphorylation of eIF2 α . However, it significantly inhibited the phosphorylation of mTOR and p70S6K in a dose dependent manner, and increased the phosphorylation/inactivation of eEF2 at threonine (Thr) 56 (Figure 3C).

We also examined the effects of ATG on these proteins in BFA-treated cells. BFA induced an increase in eIF2 α phosphorylation, which was inhibited by ATG (Figure 3D), although ATG alone had no effect on the basal level phosphorylation of eIF2 α . BFA had no effects on the phosphorylation of either p70S6K or eEF2 (Figure 3D), suggesting that the inhibitory effect of ATG on protein translation was unaffected by BFA.

These data suggest that ATG attenuates protein synthesis likely through inhibiting mTOR-p70S6K signaling and eEF2 activity.

ATG reduces the unfolded protein response by activating AMPK

It has been reported that AMPK acts upstream of mTOR signaling and eEF2 in controlling translation. AMPK modulates the activity of mTOR either by direct phosphorylation and inhibition of mTOR^[22], or by phosphorylation and activation of the tuberous sclerosis complex (TSC), an upstream regulator and inhibitor of mTOR activity^[23]. The most characterized downstream effectors of mTOR are p70S6K and the eukaryotic translation initiation factor 4E (eIF4E)-binding protein 1 (4E-BP1), through which mTOR stimulates the initiation step of translation^[24]. AMPK can also activate eEF2 kinase (eEF2K) either by direct phosphorylation of eEF2K at Ser398^[25], or by inhibition of p70S6K, which phosphorylates and inactivates eEF2K at Ser366^[26]. Activated eEF2K in turn phosphorylates and inactivates eEF2 at Thr56^[27]. We therefore investigated the effect of ATG on AMPK phosphorylation/activation. As shown in Figure 4, ATG significantly stimulated the phosphorylation of AMPK at Thr172 of α catalytic subunit in a time- and dose-dependent manner (Figure 4A and 4B). ATG also

increased the phosphorylation of ACC (acetyl-CoA carboxylase) at Ser79, a direct substrate of AMPK^[28], indicating an increase in AMPK activity was induced (Figure 4B).

To determine whether the attenuation of protein translation by ATG is mediated by AMPK activation, we employed RNA interference to knock down AMPK α 1. As shown in Figure 4C, siRNA-mediated AMPK α 1 down-regulation partially reversed the effect of ATG on the phosphorylation of p70S6K and eEF2. These data suggest that AMPK activation at least partially mediates the inhibitory effect of ATG on protein translation.

To further verify that the alleviation of ER stress by ATG is mediated by AMPK activation, we used a selective inhibitor of AMPK, compound C (CC), to block AMPK activity. As shown in Figure 4D and 4E, compound CC significantly reduced the effects of ATG on the BFA-induced XBP-1 splicing and mRNA expression of Grp94, suggesting that the activation of AMPK is necessary for ATG's inhibitory effect on the BFA-induced UPR. Meanwhile, CC itself had no effects on the splicing of XBP-1 pre-mRNA (Figure 4D). The involvement of AMPK in the ATG inhibition of ER stress was further confirmed by using a known AMPK activator AICAR. Similar to artigenin, AICAR significantly prevented BFA-induced cell death in a dose-dependent manner (Figure 4F).

Taken together, our observations demonstrate that ATG alleviates ER stress probably through activating AMPK, which attenuates protein translation and reduces ER load.

ATG inhibits mitochondrial respiration, leading to AMPK activation

There are two main protein kinases involved in phosphorylating AMPK *in vivo*, LKB1 (liver kinase B1) and Ca²⁺/calmodulin-dependent protein kinase kinase, especially the β isoform (CaMKK β)^[29]. To determine whether the two kinases are critically involved in the ATG-induced AMPK phosphorylation, we used RNA interference to down-regulate the expression of LKB1 and CaMKK β . As shown in Figure 5, knockdown of either LKB1 or CaMKK β significantly reduced the phosphorylation of AMPK induced by ATG, suggesting that both kinases are involved in mediating the ATG-induced AMPK activation (Figure 5A).

Phosphorylation of AMPK by the two kinases is regulated by adenosine monophosphate (AMP), which allosterically activates AMPK and makes it a better substrate for the two upstream kinases and a poorer substrate for protein phosphatases^[30]. The intracellular AMP level, however, is regulated by adenosine triphosphate (ATP) content. ATP depletion has been shown to increase AMP production as a consequence of the reaction catalyzed by adenylate kinase^[30]. To investigate whether ATG affects ATP production, we evaluated intracellular ATP levels by a luciferase assay. As shown in Figure 5, intracellular ATP levels were reduced by ATG in a time-dependent and dose-dependent manner (Figure 5B and 5C).

Given the fact that mitochondria are the major ATP production organelles in eukaryotes, we investigated the effects of ATG on mitochondrial respiration in mitochondria isolated from rat muscle. Our data showed that ATG inhibited oxygen

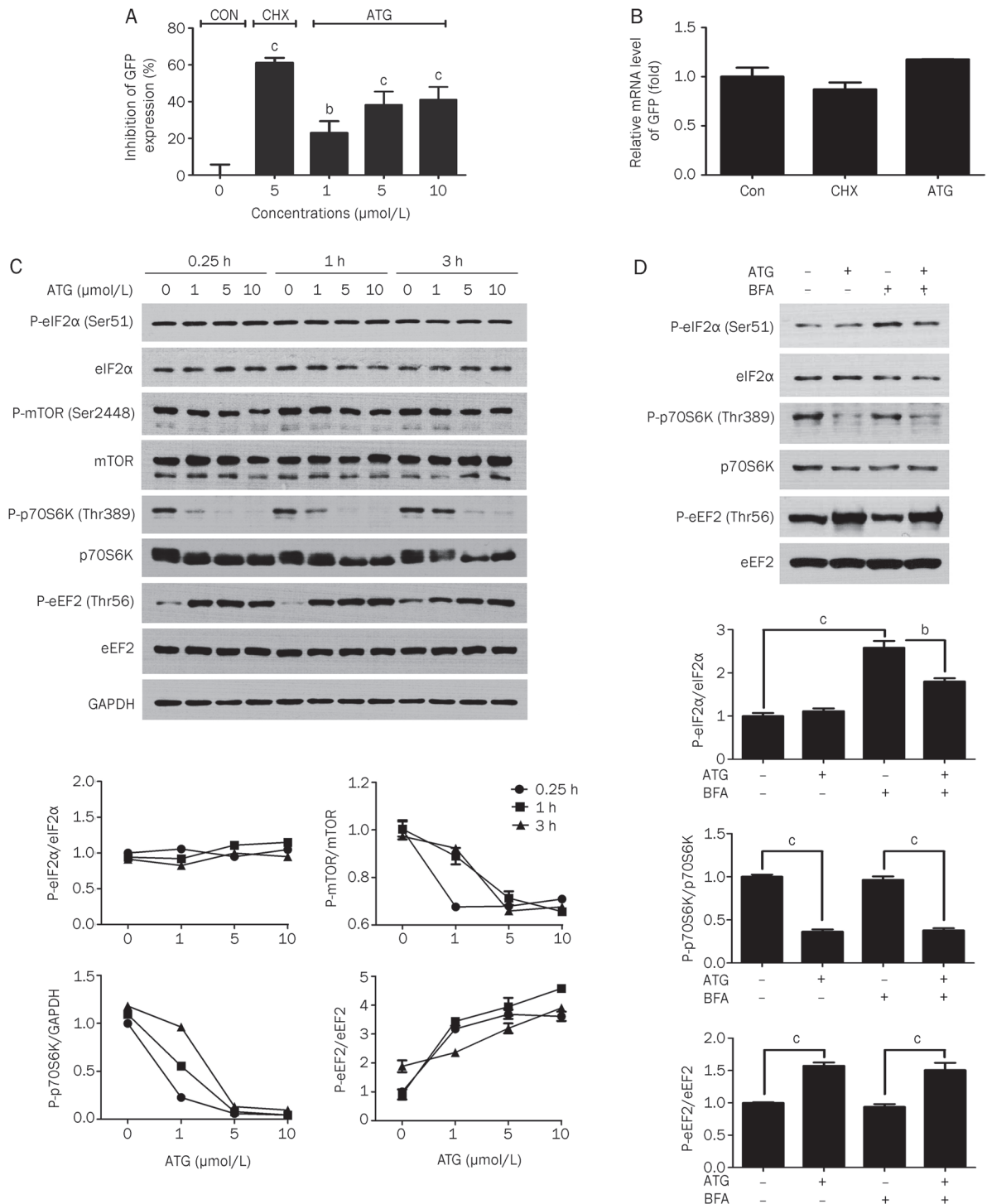


Figure 3. ATG moderately inhibits protein translation. (A) HepG2 cells were transfected with a GFP-expressing plasmid for 16 h, and then treated for another 24 h with DMSO, CHX (5 μmol/L), or the indicated concentrations of ATG followed by staining with Hoechst 33342 (2 μg/mL) for 5 min. At least six photographs per well in different areas of cell cultures were taken by fluorescence microscopy, and GFP expression was evaluated by dividing the IOD of green fluorescence by cell number. The value of GFP expression treated with DMSO was considered as 100%. (B) The expression levels of GFP mRNA were examined by quantitative RT-PCR. (C) HepG2 cells were treated for the indicated times with different concentrations of ATG. The phosphorylation levels of eIF2α, mTOR, p70S6K, and eEF2 were examined by Western blot analysis. Relative band intensity was expressed as a percentage compared with the value of control at 0.25 h. (D) HepG2 cells were cultured for 3 h in the presence or absence of ATG (5 μmol/L) and/or BFA (100 nmol/L) followed by cell lysis. The phosphorylation levels of eIF2α at Ser51, p70S6K at Thr389, and eEF2 at Thr56 were examined by Western blot analysis. Relative band intensity was expressed as a percentage compared with the value of untreated control. *n*=4 experiments. Mean±SEM. ^b*P*<0.05, ^c*P*<0.01 vs control.

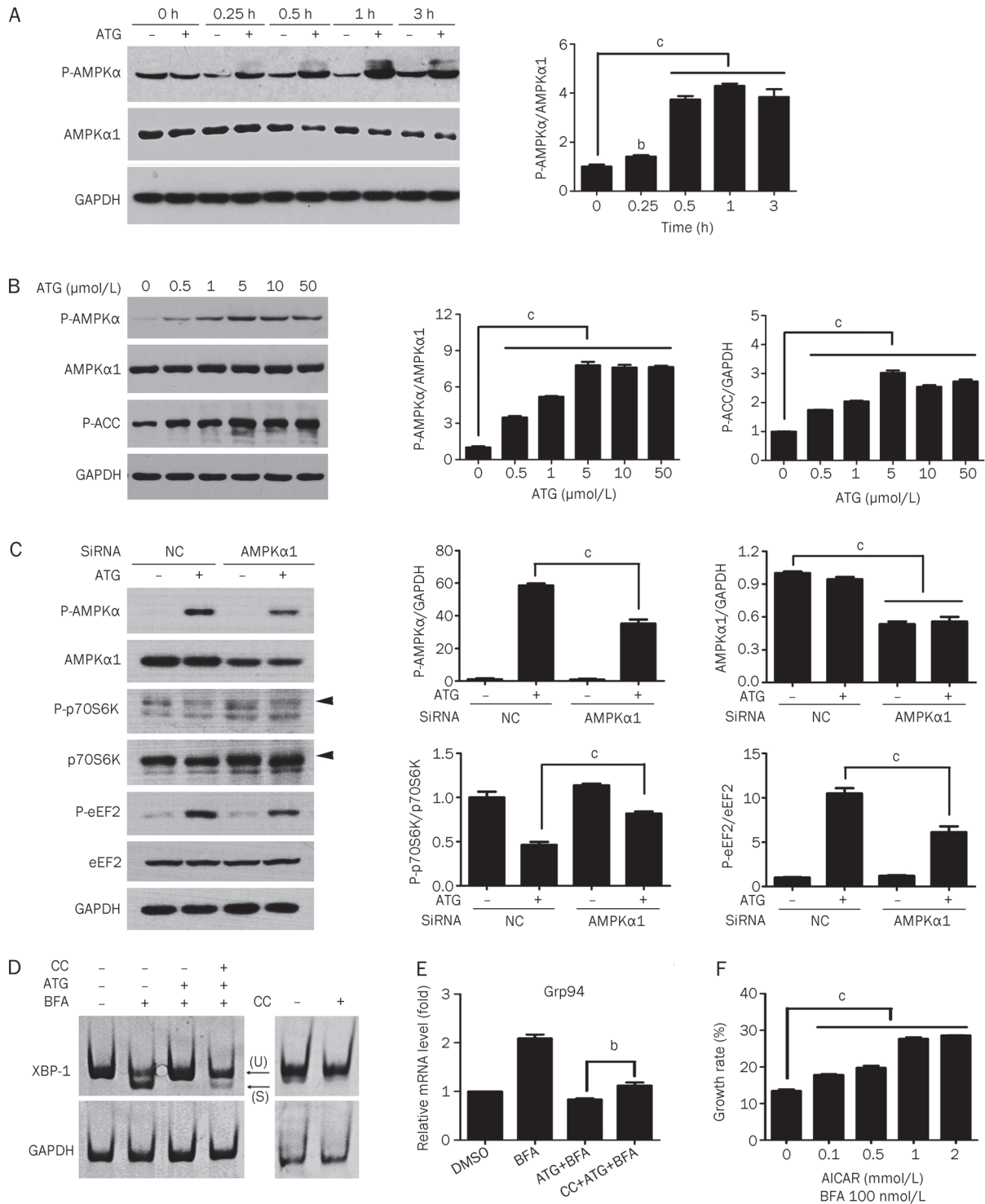


Figure 4. ATG activates AMPK and may lead to ER stress alleviation. (A and B) HepG2 cells were incubated with 5 μ mol/L ATG for the indicated time (A) or with ATG at the indicated concentrations for 1 h (B). Phospho-AMPK α (Thr172), AMPK α 1, and phospho-ACC (Ser79) were analyzed by Western blotting. GAPDH served as a control. Relative band intensity of each protein was expressed as a percentage compared with the value of untreated control. (C) HepG2 cells were transfected with a negative control siRNA (NC) or a siRNA targeting AMPK α 1. At 48 h after transfection, cells were treated with or without ATG (5 μ mol/L) for 1 h. Phospho-AMPK α (Thr172), AMPK α 1, phospho-p70S6K (Thr389, indicated by an arrowhead), p70S6K (indicated by an arrowhead), phospho-eEF2 (Thr56), eEF2, and GAPDH were examined by Western blot analysis. The relative intensity of corresponding protein expression was shown in the right figures. (D and E) Pretreated with DMSO or CC (25 μ mol/L) for 1 h, HepG2 cells were exposed to ATG (5 μ mol/L) and/or BFA (100 nmol/L) for 6 h. Splicing of XBP1 mRNA was detected by semi-quantitative RT-PCR (D). mRNA expression of Grp94 was detected by quantitative RT-PCR (E). (F) HepG2 cells were treated with increasing concentrations of AICAR and 100 nmol/L BFA for 72 h. Cell growth rate was evaluated by MTT assay. $n=4$ experiments. Mean \pm SEM. ^b $P<0.01$, ^c $P<0.01$ vs control.

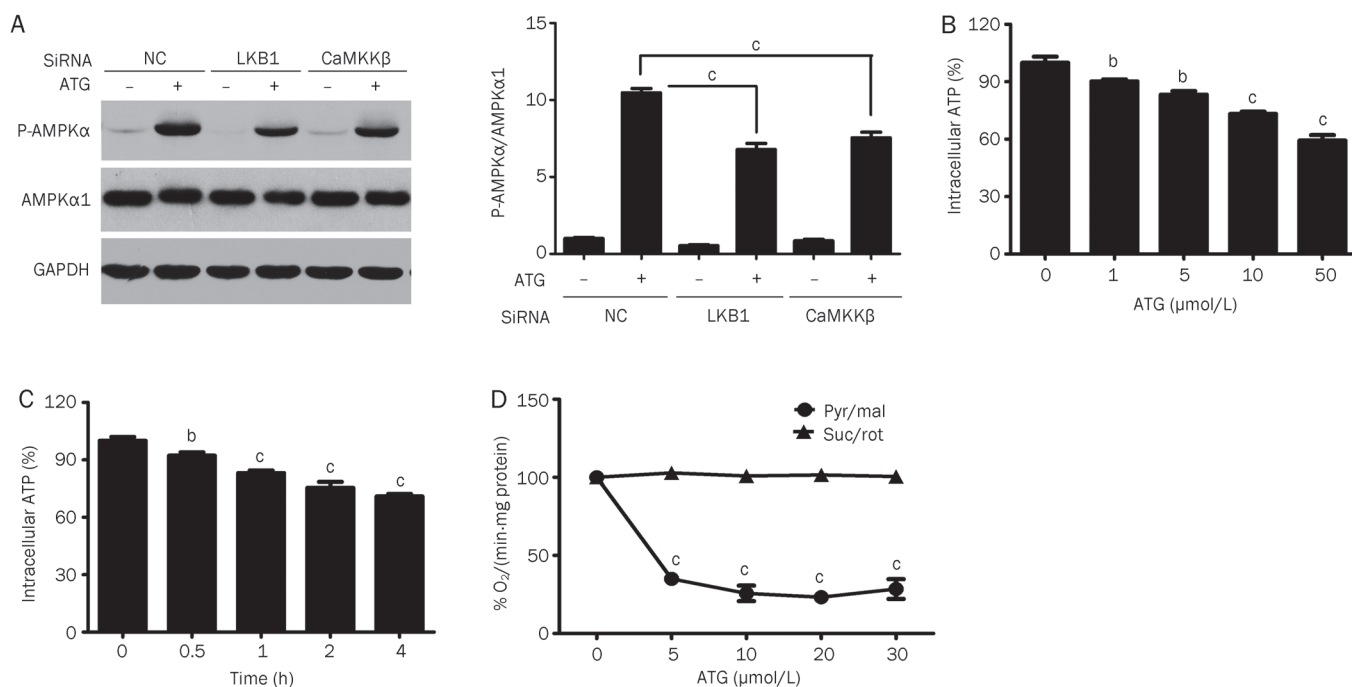


Figure 5. ATG inhibits mitochondrial respiration. (A) HepG2 cells were transfected with a negative control siRNA (NC) or siRNA targeting LKB1 or CaMKK β . After 48 h of transfection, cells were treated with or without ATG (5 μ mol/L) for 1 h. Phospho-AMPK α (Thr172) and AMPK α 1 were examined by Western blot analysis. Relative band intensity was expressed as a percentage compared with the value of untreated control. (B and C) Intracellular ATP levels were measured by the luciferin-luciferase method. HepG2 cells were incubated with various concentrations of ATG for 1 h (B) or with 5 μ mol/L ATG for the indicated periods of time (C). (D) Oxygen consumption rates were measured in mitochondria at 37 °C using substrates combinations targeting respiratory complex I (5 mmol/L pyruvate plus 2 mmol/L malate) or complex II (10 mmol/L succinate plus 4 μ mol/L rotenone). $n=4$ experiments. Mean \pm SEM. ^b $P<0.05$, ^c $P<0.01$ vs control.

consumption in a dose-dependent manner in the presence of substrates for complex I (pyruvate plus malate). In contrast, no effect of ATG on mitochondrial respiration was observed in the presence of substrate for complex II (succinate) and rotenone (Figure 5D).

Taken together, our data demonstrate that ATG selectively inhibits mitochondrial respiration supported by substrates for complex I and decreases ATP production likely leading to AMPK phosphorylation/activation.

ATG protects INS-1 β -cells from palmitate-induced cell death

It has been reported that exposure to high concentrations of free (nonesterified) fatty acid (FFA) induces ER stress and causes β -cell apoptosis^[8, 31], which has been considered as one of the major causes of insufficient insulin production in type 2 diabetes^[32, 33]. We therefore investigated the effects of ATG on palmitate-induced β -cell death. Palmitate severely decreased cell viability of INS-1 β -cells, while treatment with ATG significantly prevented cell death in a dose-dependent manner (Figure 6A). We then investigated whether ATG could activate AMPK in INS-1 cells. Our data showed that ATG significantly increased the phosphorylation of AMPK in the absence or presence of palmitate (Figure 6B). Furthermore, we examined the effects of ATG on palmitate-induced UPR in INS-1 cells. As shown in Figure 6C, 6D, and 6E, palmitate promoted

the splicing of XBP-1 pre-mRNA and the mRNA expression of Grp78 and Grp94, which were significantly inhibited by ATG. These data suggest that ATG protects INS-1 cells from palmitate-induced cell death probably through alleviating ER stress and the protective effects of ATG against ER stress are not specific in HepG2 cells.

Discussion

There has been growing interest in therapeutic strategies to alleviate ER stress, since prolonged ER stress has been associated with a wide range of pathological conditions^[5]. ER stress has been thought to play a central role in the pathogenesis of type 2 diabetes not only because of its role in the induction of insulin resistance but also because of its involvement in β -cell death, a common feature of type 2 diabetes^[34]. Therefore, compounds that alleviate ER stress may act as therapeutic agents for the treatment of β -cell loss in type 2 diabetes. In this study, we have identified ATG, a natural product from *Arctium lappa* L., as a candidate for alleviating ER stress.

Firstly, we presented two lines of evidences to demonstrate that ATG was an ER stress alleviator (Figure 1, 2, and supplementary Figure 1). First, ATG protected HepG2 cells from ER stress inducer BFA-induced apoptosis, but showed no protective effect against non-ER stress stimuli. Our data showed that the lowest effective dose of ATG is 2.5 μ mol/L and ATG at

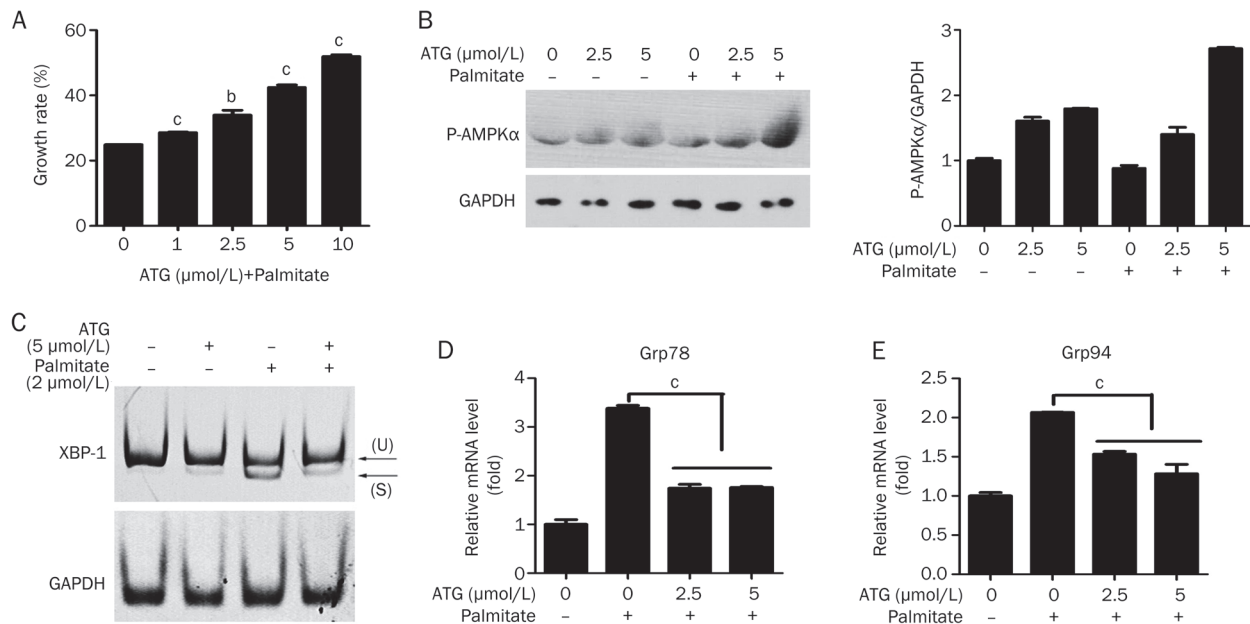


Figure 6. ATG prevents palmitate-induced cell death and ER stress in INS-1 β -cells. (A) INS-1 β -cells were incubated with the indicated concentrations of ATG in the presence of palmitate (2 mmol/L) for 24 h. Cell growth rate was evaluated by MTT assay. (B) INS-1 cells were treated with the indicated concentrations of ATG in the presence and absence of palmitate for 3 h. Phospho-AMPK α (Thr172) and GAPDH were analyzed by Western blotting. The quantification of Western blot images of the ratio between P-AMPK α and GAPDH was shown in the right panel. (C, D, and E) INS-1 cells were incubated with the indicated concentrations of ATG and palmitate for 6 h, followed by RNA purification and reverse transcription. Splicing of XBP1 mRNA in INS-1 β -cell was detected by semi-quantitative RT-PCR (C). mRNA expressions of Grp78 (D) and Grp94 (E) were detected by quantitative RT-PCR. $n=4$. Mean \pm SEM. ^b $P<0.05$, ^c $P<0.01$ vs control.

higher dose (>10 $\mu\text{mol/L}$) displayed cytotoxicity, which might suggest a narrow therapeutic window. However, our data also showed that the protective effect of ATG at 10 $\mu\text{mol/L}$ was quite marked. We therefore assume that ATG may have a wider therapeutic range in clinical settings. Second, ATG inhibited BFA- and tunicamycin-induced UPR, *ie*, the splicing of XBP-1 pre-mRNA, the phosphorylation of eIF2 α and the expression of downstream UPR target genes, including Grp94, EDEM, ATF4, and CHOP. The UPR is involved in both survival and the apoptotic response^[35]. Whether a cell survives or dies upon ER stress will depend on the balance of these opposing signals. In this case, BFA-induced ER stress caused cell apoptosis, which means that the pro-death signal overrides the pro-survival signal. Inhibition of the UPR by ATG promoted cell survival, although ATG inhibited both pro-survival and pro-death signaling downstream of the UPR.

To investigate whether ATG alleviates ER stress through attenuating protein synthesis, we analyzed the effects of ATG on the protein expression level of a transfected GFP gene. Our data demonstrated that ATG decreased the level of GFP protein without influencing its transcription (Figure 3A and 3B). We also examined the effects of ATG on protein degradation and autophagy. Our data showed that ATG had no effects on either protein degradation or autophagy (unpublished data). We therefore conclude that ATG reduced protein expression level by inhibiting protein translation but not transcription or degradation, by which ATG may relieve ER stress.

Unlike some of the ER stress alleviators, such as salubrinal which reduces ER load by inducing the phosphorylation of eIF2 α ^[20], therefore inhibiting the initiation of protein translation, ATG did not seem to affect the initiation factor eIF2 α , but significantly inhibited phosphorylation of mTOR-p70S6K signaling and induced phosphorylation/inactivation of the protein translation elongation factor eEF2 (Figure 3C and 3D), suggesting that ATG attenuates protein synthesis by inhibiting both translation initiation and elongation.

Therefore, inhibition of protein synthesis represents an effective strategy to reduce ER stress. Once the protein synthesis is reduced, inhibition of downstream protein modification and/or folding, as caused by BFA and/or TM, will no longer elicit an UPR. Consistent with this notion, the BFA-induced phosphorylation of eIF2 α is inhibited by ATG, although ATG itself does not directly affect eIF2 α phosphorylation (Figure 3D).

Both mTOR-p70S6K signaling and eEF2 have been reported to be regulated by AMPK^[36]. We therefore investigated whether ATG activated AMPK, and if so, whether AMPK activation mediated ATG action. Our data showed that ATG obviously increased the phosphorylation/activation of AMPK. Encouragingly, knockdown of AMPK α 1 by RNA interference partially reversed the effect of ATG on the phosphorylation of p70S6K and eEF2. Furthermore, an AMPK inhibitor, compound C, could block the inhibitory effect of ATG on BFA-induced XBP-1 splicing, whereas an AMPK activator, AICAR, could mimic ATG to reduce the ER stress-induced cell death.

These data strongly suggest that AMPK plays a central role in mediating all of the ATG effects in alleviating ER stress. Our results, together with an earlier report^[37], also indicate that activating AMPK could be an effective strategy for ER stress reduction.

AMPK is widely recognized as a key regulator of fatty acid and glucose homeostasis^[30], and the activation of AMPK has been considered an attractive strategy for the treatment of type 2 diabetes. The most representative compounds are metformin and berberine, which exert anti-diabetic effects through activating AMPK^[18, 38]. Meanwhile, they are also reported to possess protective effect against ER stress^[39–41]. Given the crucial role of ER stress in the development of pancreatic β -cell loss and insulin resistance in type 2 diabetes^[6], the alleviation of ER stress by AMPK may play an important role in treating type 2 diabetes. Consistent with this notion, our data demonstrated that ATG also protected INS-1 β -cells against palmitate-induced ER stress and cell death (Figure 6). In addition, activating AMPK may also represent a potential therapeutic strategy to relieve ER stress in other ER stress-related diseases, since ER stress is associated with a number of diseases.

AMPK has been reported to be activated by its two main upstream kinases, LKB1 and CaMKK β in response to decreased intracellular levels of ATP^[29]. Our data showed that AMPK phosphorylation induced by ATG was significantly inhibited by either LKB1 or CaMKK β siRNAs, implying that both kinases are involved in ATG-induced AMPK phosphorylation (Figure 5A). This is consistent with a recent study that reported ATG phosphorylated AMPK in H9C2 and C2C12 cells via LKB1 and CaMKK-dependent pathways^[42]. Furthermore, we found the intracellular ATP level was significantly reduced by ATG (Figure 5B and 5C), which might also lead to AMPK activation. Interestingly, ATG at 0.5 μ mol/L and 1 μ mol/L significantly increased AMPK phosphorylation but slightly reduced the intracellular ATP levels, which implies that ATG may also activate AMPK via an ATP depletion-independent manner. Taken together, our data suggest that ATG activates AMPK probably through activating LKB1 and CaMKK β and/or decreasing the ATP level.

Since oxidative phosphorylation and glycolysis are the two main sources of ATP in eukaryotic cells, we then investigated the effects of ATG on mitochondrial respiratory function. Our data demonstrated that ATG inhibited oxygen consumption supported by substrates for complex I but not that supported by complex II substrates (Figure 5D), indicating that the inhibition of mitochondrial respiration by ATG was occurring either at the level of NADH production or at complex I. These results suggest that ATG decreases the intracellular level of ATP and increases the phosphorylation/activity of AMPK through inhibiting mitochondrial respiration.

In conclusion, our findings reveal the molecular mechanism by which ATG alleviates ER stress: the inhibition of mitochondrial respiration by ATG results in reduced ATP production in mitochondria. Under conditions of energy depletion, AMPK is probably activated by LKB1 and CaMKK β , which in turn inhibits mTOR-p70S6K signaling and increases eEF2 phos-

phorylation/inactivation, leading to the attenuation of protein synthesis. As a result, the burden of ER stress is relieved, and cell death is prevented (Figure 7). We also show the protective effect of ATG against palmitate-induced INS-1 β -cell death. These data suggest that ATG may represent a potential therapeutic intervention for treating ER stress-related diseases, such as β -cell loss in type 2 diabetes.

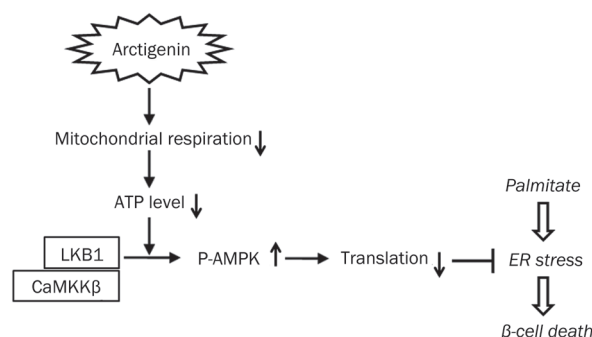


Figure 7. A schematic model of the mechanism of ATG action. ATG inhibits mitochondrial respiration resulting in a reduction in ATP level and an activation of AMPK. Activated AMPK attenuates protein translation, leading to a reduction of the load on the ER and an alleviation of ER stress. As a result, ATG protects INS-1 β -cells from palmitate-induced cell death.

Acknowledgements

This work was supported by the National Science & Technology Major Project “Key New Drug Creation and Manufacturing Program”, China (Number: 2009ZX09301-001 and 2009ZX09103-064); the China Ministry of Science and Technology Research Grant 2008ZX10002-020; and the Shanghai Science and Technology Research Grants 08DZ1971403 and 09JC1416700.

Author contribution

Yuan GU, Jun-ying YUAN, and Qiang YU participated in research design; Yuan GU, Xiao-xiao SUN, Ji-ming YE, and Li HE conducted experiments; Shou-sheng YAN, Hao-hao ZHANG, and Li-hong HU contributed to essential reagents or analytic tools; Yuan GU and Qiang YU performed data analysis; Yuan GU and Qiang YU wrote the manuscript.

Supplementary information

Supplementary figures are available at website of Acta Pharmacologica Sinica on NPG.

References

- 1 Sood R, Porter AC, Ma K, Quilliam LA, Wek RC. Pancreatic eukaryotic initiation factor-2 α kinase (PEK) homologues in humans, *Drosophila melanogaster* and *Caenorhabditis elegans* that mediate translational control in response to endoplasmic reticulum stress. *Biochem J* 2000; 346: 281–93.
- 2 Shen J, Chen X, Hendershot L, Prywes R. ER stress regulation of ATF6 localization by dissociation of BiP/GRP78 binding and unmasking of Golgi localization signals. *Dev Cell* 2002; 3: 99–111.

- 3 Yoshida H, Matsui T, Yamamoto A, Okada T, Mori K. XBP1 mRNA is induced by ATF6 and spliced by IRE1 in response to ER stress to produce a highly active transcription factor. *Cell* 2001; 107: 881–91.
- 4 Ron D, Walter P. Signal integration in the endoplasmic reticulum unfolded protein response. *Nat Rev Mol Cell Biol* 2007; 8: 519–29.
- 5 Kim I, Xu W, Reed JC. Cell death and endoplasmic reticulum stress: disease relevance and therapeutic opportunities. *Nat Rev Drug Discov* 2008; 7: 1013–30.
- 6 Eizirik DL, Cardozo AK, Cnop M. The role for endoplasmic reticulum stress in diabetes mellitus. *Endocr Rev* 2008; 29: 42–61.
- 7 Ozcan U, Cao Q, Yilmaz E, Lee AH, Iwakoshi NN, Ozdelen E, *et al*. Endoplasmic reticulum stress links obesity, insulin action, and type 2 diabetes. *Science* 2004; 306: 457–61.
- 8 Laybutt DR, Preston AM, Akerfeldt MC, Kench JG, Busch AK, Biankin AV, *et al*. Endoplasmic reticulum stress contributes to beta cell apoptosis in type 2 diabetes. *Diabetologia* 2007; 50: 752–63.
- 9 Cho MK, Jang YP, Kim YC, Kim SG. Arctigenin, a phenylpropanoid dibenzylbutyrolactone lignan, inhibits MAP kinases and AP-1 activation via potent MKK inhibition: the role in TNF-alpha inhibition. *Int Immunopharmacol* 2004; 4: 1419–29.
- 10 Zhao F, Wang L, Liu K. *In vitro* anti-inflammatory effects of arctigenin, a lignan from *Arctium lappa* L, through inhibition on iNOS pathway. *J Ethnopharmacol* 2009; 122: 457–62.
- 11 Chan YS, Cheng LN, Wu JH, Chan E, Kwan YW, Lee SM, *et al*. A review of the pharmacological effects of *Arctium lappa* (burdock). *Inflammopharmacology* 2011; 19: 245–54.
- 12 Cervellati R, Speroni E, Govoni P, Guerra MC, Costa S, Arnold UW, *et al*. *Wulfenia carinthiaca* Jacq., antioxidant and pharmacological activities. *Z Naturforsch C* 2004; 59: 255–62.
- 13 Charlton JL. Antiviral activity of lignans. *J Nat Prod* 1998; 61: 1447–51.
- 14 Awale S, Lu J, Kalauni SK, Kurashima Y, Tezuka Y, Kadota S, *et al*. Identification of arctigenin as an antitumor agent having the ability to eliminate the tolerance of cancer cells to nutrient starvation. *Cancer Res* 2006; 66: 1751–7.
- 15 Sun S, Wang X, Wang C, Nawaz A, Wei W, Li J, *et al*. Arctigenin suppresses unfolded protein response and sensitizes glucose deprivation-mediated cytotoxicity of cancer cells. *Planta Med* 2011; 77: 141–5.
- 16 Kim JY, Hwang JH, Cha MR, Yoon MY, Son ES, Tomida A, *et al*. Arctigenin blocks the unfolded protein response and shows therapeutic antitumor activity. *J Cell Physiol* 2010; 224: 33–40.
- 17 Hayashi K, Narutaki K, Nagaoka Y, Hayashi T, Uesato S. Therapeutic effect of arctiin and arctigenin in immunocompetent and immunocompromised mice infected with influenza A virus. *Biol Pharm Bull* 2010; 33: 1199–205.
- 18 Turner N, Li JY, Gosby A, To SW, Cheng Z, Miyoshi H, *et al*. Berberine and its more biologically available derivative, dihydroberberine, inhibit mitochondrial respiratory complex I: a mechanism for the action of berberine to activate AMP-activated protein kinase and improve insulin action. *Diabetes* 2008; 57: 1414–8.
- 19 Bi M, Naczki C, Koritzinsky M, Fels D, Blais J, Hu N, *et al*. ER stress-regulated translation increases tolerance to extreme hypoxia and promotes tumor growth. *EMBO J* 2005; 24: 3470–81.
- 20 Boyce M, Bryant KF, Jousse C, Long K, Harding HP, Scheuner D, *et al*. A selective inhibitor of eIF2alpha dephosphorylation protects cells from ER stress. *Science* 2005; 307: 935–9.
- 21 Ron D. Translational control in the endoplasmic reticulum stress response. *J Clin Invest* 2002; 110: 1383–8.
- 22 Cheng SW, Fryer LG, Carling D, Shepherd PR. Thr2446 is a novel mammalian target of rapamycin (mTOR) phosphorylation site regulated by nutrient status. *J Biol Chem* 2004; 279: 15719–22.
- 23 Inoki K, Zhu T, Guan KL. TSC2 mediates cellular energy response to control cell growth and survival. *Cell* 2003; 115: 577–90.
- 24 Mamane Y, Petroulakis E, LeBacquer O, Sonenberg N. mTOR, translation initiation and cancer. *Oncogene* 2006; 25: 6416–22.
- 25 Browne GJ, Finn SG, Proud CG. Stimulation of the AMP-activated protein kinase leads to activation of eukaryotic elongation factor 2 kinase and to its phosphorylation at a novel site, serine 398. *J Biol Chem* 2004; 279: 12220–31.
- 26 Wang X, Li W, Williams M, Terada N, Alessi DR, Proud CG. Regulation of elongation factor 2 kinase by p90 (RSK1) and p70 S6 kinase. *EMBO J* 2001; 20: 4370–9.
- 27 Redpath NT, Price NT, Severinov KV, Proud CG. Regulation of elongation factor-2 by multisite phosphorylation. *Eur J Biochem* 1993; 213: 689–99.
- 28 Carlson CA, Kim KH. Regulation of hepatic acetyl coenzyme A carboxylase by phosphorylation and dephosphorylation. *J Biol Chem* 1973; 248: 378–80.
- 29 Hardie DG. The AMP-activated protein kinase pathway—new players upstream and downstream. *J Cell Sci* 2004; 117: 5479–87.
- 30 Hardie DG. Minireview: the AMP-activated protein kinase cascade: the key sensor of cellular energy status. *Endocrinology* 2003; 144: 5179–83.
- 31 Elouil H, Bensellam M, Guiot Y, Vander Mierde D, Pascal SM, Schuit FC, *et al*. Acute nutrient regulation of the unfolded protein response and integrated stress response in cultured rat pancreatic islets. *Diabetologia* 2007; 50: 1442–52.
- 32 Pick A, Clark J, Kubstrup C, Levisetti M, Pugh W, Bonner-Weir S, *et al*. Role of apoptosis in failure of beta-cell mass compensation for insulin resistance and beta-cell defects in the male Zucker diabetic fatty rat. *Diabetes* 1998; 47: 358–64.
- 33 Bonner-Weir S. Islet growth and development in the adult. *J Mol Endocrinol* 2000; 24: 297–302.
- 34 Cnop M. Fatty acids and glucolipotoxicity in the pathogenesis of type 2 diabetes. *Biochem Soc Trans* 2008; 36: 348–52.
- 35 Kitamura M. Endoplasmic reticulum stress and unfolded protein response in renal pathophysiology: Janus faces. *Am J Physiol Renal Physiol* 2008; 295: F323–34.
- 36 Chan AY, Dyck JR. Activation of AMP-activated protein kinase (AMPK) inhibits protein synthesis: a potential strategy to prevent the development of cardiac hypertrophy. *Can J Physiol Pharmacol* 2005; 83: 24–8.
- 37 Terai K, Hiramoto Y, Masaki M, Sugiyama S, Kuroda T, Hori M, *et al*. AMP-activated protein kinase protects cardiomyocytes against hypoxic injury through attenuation of endoplasmic reticulum stress. *Mol Cell Biol* 2005; 25: 9554–75.
- 38 Musi N, Hirshman MF, Nygren J, Svanfeldt M, Bavenholm P, Rooyackers O, *et al*. Metformin increases AMP-activated protein kinase activity in skeletal muscle of subjects with type 2 diabetes. *Diabetes* 2002; 51: 2074–81.
- 39 Kim DS, Jeong SK, Kim HR, Chae SW, Chae HJ. Metformin regulates palmitate-induced apoptosis and ER stress response in HepG2 liver cells. *Immunopharmacol Immunotoxicol* 2010; 32: 251–7.
- 40 Hao X, Yao A, Gong J, Zhu W, Li N, Li J. Berberine ameliorates pro-inflammatory cytokine-induced endoplasmic reticulum stress in human intestinal epithelial cells *in vitro*. *Inflammation* 2012; 35: 841–9.
- 41 Wang ZS, Lu FE, Xu LJ, Dong H. Berberine reduces endoplasmic reticulum stress and improves insulin signal transduction in Hep G2 cells. *Acta Pharmacol Sin* 2010; 31: 578–84.
- 42 Tang X, Zhuang J, Chen J, Yu L, Hu L, Jiang H, *et al*. Arctigenin efficiently enhanced sedentary mice treadmill endurance. *PLoS One* 2011; 6: e24224.

Original Article

The biphasic redox sensing of SENP3 accounts for the HIF-1 transcriptional activity shift by oxidative stress

Ying WANG[#], Jie YANG, Kai YANG, Hui CANG, Xin-zhi HUANG, Hui LI, Jing YI^{*}

Department of Biochemistry and Molecular Cell Biology, Key Laboratory of the Shanghai Science and Technology Commission for Cancer Microenvironment and Inflammation, Institutes of Medical Sciences, Shanghai Jiao Tong University School of Medicine, Shanghai 200025, China

Aim: To investigate the mechanisms underlying the biphasic redox regulation of hypoxia-inducible factor-1 (HIF-1) transcriptional activity under different levels of oxidative stress caused by reactive oxidative species (ROS).

Methods: HeLa cells were exposed to different concentrations of H₂O₂ as a simple model for mild and severe oxidative stress. Luciferase reporter assay and/or quantitative real-time PCR were used to investigate the transcriptional activity. Immunoblot was used to detect protein expression. Chromatin immunoprecipitation assay was used to detect HIF-1/DNA binding. The interaction of p300 with HIF-1 α or with SENP3, and the SUMO2/3 conjugation states of p300 were examined by coimmunoprecipitation.

Results: HIF-1 transcriptional activity in HeLa cells was enhanced by low doses (0.05–0.5 mmol/L) of H₂O₂, but suppressed by high doses (0.75–8.0 mmol/L) of H₂O₂. The amount of co-activator p300 bound to HIF-1 α in HeLa cells was increased under mild oxidative stress, but decreased under severe oxidative stress. The ROS levels differentially modified cysteines 243 and 532 in the cysteine protease SENP3, regulating the interaction of SENP3 with p300 to cause different SUMOylation of p300, thus shifting HIF-1 transcriptional activity.

Conclusion: The shift of HIF-1 transactivation by ROS is correlated with and dependent on the biphasic redox sensing of SENP3 that leads to the differential SENP3/p300 interaction and the consequent fluctuation in the p300 SUMOylation status.

Keywords: ROS; redox; SENP3; HIF-1; p300; SUMOylation; HeLa cells

Acta Pharmacologica Sinica (2012) 33: 953–963; doi: 10.1038/aps.2012.40; published online 11 Jun 2012

Introduction

Oxidative stress, a common challenge to cellular homeostasis, is caused predominantly through the excessive production of reactive oxygen species (ROS). Many extracellular insults, such as irradiation, drugs and various disturbances in temperature, pH, osmotic pressure, oxygen tension and sugar concentration, may all increase the production of ROS^[1–5]. The extent of the increase in ROS production usually determines the consequences of cellular adaptive responses to oxidative stress. Mild oxidative stress promotes cell survival or proliferation, while severe oxidative stress causes proliferation arrest, senescence or cell death, during which global alterations of

gene expression and protein post-translational modifications are differentially regulated according to the differences in ROS levels^[1, 2, 6–8].

Hypoxia-inducible factor-1 (HIF-1) is a well-known transcription factor that controls gene expression in response to hypoxia. Interestingly, HIF-1 can also be activated under normoxic conditions. For instance, HIF-1 activation occurs during inflammation^[9–11], growth factor activation^[12, 13] and insulin administration^[14–17]. Notably, ROS generation accompanies these events and is required for normoxic HIF-1 activation. Moreover, it has been demonstrated that ROS production is paradoxically increased during hypoxia and is even required for hypoxic HIF-1 activation^[18, 19]. A correlation of increased ROS and over-expressed/activated HIF-1 has also been suggested in cancer cells^[20–22].

While an increasing body of work has reported that ROS can stabilize HIF-1 α and enhance HIF-1 transactivation^[23–25], we have previously shown that HIF-1 can be suppressed in

[#] Now in Department of Biochemistry and Molecular Cell Biology, Shanghai Jiao Tong University School of Medicine, Shanghai 200025, China.

^{*} To whom correspondence should be addressed.

E-mail yijing@shsmu.edu.cn

Received 2012-03-21 Accepted 2012-03-28

the prostate cancer cell line Du145 by the overwhelming production of ROS induced by a combined administration of the ROS producer emodin and the conventional chemotherapeutic agent cisplatin^[21]. The capacity of HIF-1 to be activated by mild oxidative stress but inhibited by severe oxidative stress, *ie*, the mechanism for the biphasic regulation of HIF-1 transactivation, has thus become an intriguing question.

We have recently found that the SUMO2/3-specific protease SENP3 and its de-SUMOylating catalytic activity are required for the ROS-induced enhancement of HIF-1 transactivation, based on ROS-induced HIF-1 α stabilization^[26]. The SENP3-mediated deconjugation of SUMO2/3 from p300, the co-activator for HIF-1, is beneficial for HIF-1 transcriptional activity under both hypoxic and normoxic conditions. Being different with the other SENPs family members, SENP3 is specifically and sensitively responsive to low oxidative stress^[26, 27]. SENP3 is stabilized upon exposure to hydrogen peroxide (H₂O₂) at very low doses, for instance, 0.05 mmol/L, and redistributes from the nucleolus to the nucleoplasm, which allows it to modulate various nuclear events, including the enhancement of HIF-1 transactivation. However, SENP3, along with all SENP family members, is a cysteine protease^[28–30], meaning that its enzymatic activity relies on cysteine residues in the catalytic site. It has been demonstrated that highly oxidizing conditions (10 mmol/L H₂O₂) inhibit the deconjugation activity of SENP1 and SENP2^[28, 31]. We therefore hypothesize that the oxidation of the catalytic cysteine in SENP3 under severe oxidative stress might inhibit its de-SUMOylating activity that is required for the physiological functions of various substrates, including p300, and HIF-1 transactivation might be thus suppressed.

To test this hypothesis, we used HeLa cells exposed to a series of concentrations of H₂O₂ as a simple model of mild and severe oxidative stress, examined the steps of HIF-1 activation, and analyzed SENP3 activity and the SUMOylation status of p300. Our findings in the present study suggest that the shift of HIF-1 transactivation by ROS is correlated with and dependent on the differential SENP3/p300 interaction and consequent fluctuation in the SUMOylation status of p300. SENP3 protein is induced by mild oxidative stress but its catalytic activity is inactivated by severe oxidative stress, thus leading to opposite SUMOylation status of its substrate p300. This biphasic ROS effect on SENP3 is achieved through a sequential oxidative modification at two cysteine residues.

Materials and methods

Cell culture and treatments

HeLa cells were used for all experiments. Cells were cultured in Dulbecco's modified Eagle's medium (GibcoBRL, Gaithersburg, MD, USA). All media were supplemented with 100 U/mL penicillin, 100 mg/L streptomycin and 10% newborn calf serum (Biochrom AG, Germany). Cells were maintained at 37°C in a humidified atmosphere with 5% CO₂.

To set a cell model of oxidative stress, cells were treated with hydrogen peroxide (H₂O₂, Sigma-Aldrich, St Louis, MO, USA) at increasing doses. When needed, anti-oxidant *N*-ace-

tylcysteine (NAC, Sigma-Aldrich, St Louis, MO, USA) was pre-incubated with cells for 4 h and protein reducing agent dithiothreitol (DTT, Sigma-Aldrich, St Louis, MO, USA) was pre-incubated for 2 h.

Cell viability assay

Cells were seeded at 1.5×10⁴/mL cells per well in 96-microculture-well plates. After exposed to the various concentration of H₂O₂ as indicated for 24 h, cell viability was assayed using the 3-(4,5-dimethylthiazol-2-yl)-2,5-diphenyl-tetrazolium bromide (MTT) (Sigma-Aldrich, St Louis, MO, USA)^[32].

ROS detection

2,7-Dichlorodihydrofluorescein diacetate (DCFH-DA; Sigma-Aldrich, St Louis, MO, USA) was used as ROS capturing reagent with the method described previously^[33, 34].

Luciferase reporter assay

The constructs of the luciferase reporter specific for hypoxia response element (HRE) and the renilla control were transfected and the reporter assay were performed as described previously^[26]. Briefly, cells were transfected with the double reporters, and 40 h post transfection, cells were exposed to H₂O₂ at varied doses once for 6 h before relative luciferase activity was assayed.

Quantitative real-time PCR

Quantitative real-time PCR was carried out on the ABI Prism 7300 system (Applied Biosystems, Foster City, CA, USA) using SYBR Green following the manufacturer's instructions. The primers for the vascular endothelial growth factor (VEGF) gene were 5'-CGGTATAAGTCCTGGAGCGTGT-3' and 5'-TCACCGCCTCGGCTTGTC-3'. The primers for carbonic anhydrase 9 (CA9) were 5'-CTGTCACCTGCTGCTTCTGAT-3' and 5'-TCCTCTCCAGGTAGATCCTC-3'. For real-time PCR, up to 1 μ L of cDNA were used as template. Thermal cycling conditions were 95°C for 60 s, followed by 45 cycles of 95°C for 30 s, 56°C for 30 s and 72°C for 35 s. Primer efficiency of >90% was confirmed with a standard curve spanning four orders of magnitude. Following the reactions, the raw data were exported using the 7300 System Software v1.3.0 (Applied Biosystems, Foster City, CA, USA) and analyzed.

Immunoblotting (IB)

Cells were lysed in sample solution. Proteins were separated on 6%, 8%, or 10% SDS-PAGE gels, transferred to nitrocellulose membranes, and bands were detected using various antibodies as indicated. The membranes were incubated with the primary antibodies at 4°C overnight and horseradish peroxidase-conjugated secondary antibodies (Santa Cruz Biotechnology, Santa Cruz, CA, USA) for 2 h at the room temperature (RT) before detection using an enhanced chemiluminescence (ECL) system (Pierce Biotechnology, Rockford, IL, USA).

Immunofluorescence

Cell monolayers were fixed with 4% paraformaldehyde, per-

meabilized with 0.2% Triton X-100, and were blocked with 5% BSA before incubation with the mouse monoclonal anti-HIF-1 α at 4 °C overnight. Subsequently, the cells were incubated with fluorescent isothiocyanate (FITC)-conjugated anti-mouse antibody (SouthernBiotech, Birmingham, AL, USA) for 1.5 h at RT. Nuclei were stained with 4',6-diamidino-2-phenylindole (DAPI). Cells were then examined under an Axioplan 2 fluorescent microscope (Zeiss, Germany).

Chromatin immunoprecipitation (ChIP) assay

Cells were incubated with 150 μ mol/L CoCl₂ for 20 h to ensure the stabilization of HIF-1 α , and then exposed to various concentration of H₂O₂ for 6 h. Protein-DNA were cross-linked in 1% formaldehyde for 10 min at 37°C before the reaction was quenched by glycine (0.125 mol/L) for 5 min at RT. Cells were then harvested and the ChIP assay was performed using a kit (Upstate Biotechnology Inc, Lake Placid, NY, USA) according to the manufacturer's instructions and as in our previous work^[26]. The sonicated chromatin samples were precipitated with anti-HIF-1 α antibody. The primer sequences for HRE were 5'-CCITTTGGGTTTTGCCAGA-3' and 5'-CCAAGTTTGTGGAGCTGA-3'. The input fractions were used as the internal control.

Co-immunoprecipitation (co-IP)

Cells were washed once with cold PBS and lysed with cold 1 \times IP buffer (1% Triton X-100, 150 mmol/L NaCl, 10 mmol/L Tris, pH 7.4, 1 mmol/L EDTA, 1 mmol/L EGTA, pH 8.0, 0.2 mmol/L sodium ortho-vanadate, 1 mmol/L PMSF, 0.5% protease inhibitor cocktail, 0.5% IGEPAL CA-630) at 4°C for 30 min. N-Ethylmaleimide (NEM 20 mmol/L) was included in the above buffer when SUMOylation of proteins needed to be examined. Cells were transiently co-transfected with various tagged constructs. At 48 h post-transfection, cells were exposed to various reagents as indicated before harvesting using the IP buffer. Cell lysates were passed several times through a 26-gauge needle and centrifuged at 14 000 \times g for 30 min at 4°C. The supernatants were incubated with various antibodies overnight at 4°C, followed by incubation with Protein A/ Protein G-coated agarose beads (Santa Cruz Biotechnology Inc, Santa Cruz, CA, USA) for another 4 h at 4°C. After samples were washed four times with ice-cold IP buffer and supernatants were removed by centrifugation at 2000 \times g for 1 min, proteins were co-precipitated. The proteins were then separated from the beads using IB loading buffer for 15 min at 95°C. The supernatants were collected and subjected to SDS-PAGE analysis and detected using various antibodies as indicated.

Intermolecular cross-linkage assay

HeLa cells were transfected with RGS-SEN3. At 48 h post-transfection, cells were treated with H₂O₂ for 1 h with or without DTT pretreatment for 2 h. Cells were lysed in SDS loading buffers and proteins were separated on 10% SDS-PAGE. IB was performed with anti-RGS antibody to detect the intermolecular SEN3 cross-linkage via disulfide formation^[28].

Antibodies

The mouse monoclonal antibodies against HIF-1 α for IB and immunofluorescence (BD Pharmingen, San Diego, CA, USA), HIF-1 α for IP (ABR Affinity Bioreagents, Golden, CO, USA), RGS (Qiagen, Germany), HA, β -actin (Sigma-Aldrich), p300 for IB, p300 for IP (BD Bioscience, Franklin Lakes, NJ, USA) were purchased. The goat polyclonal anti-SUMO2/3 antibody and mouse monoclonal anti-SEN3 antibody were from Santa Cruz Biotechnology Inc (Santa Cruz, CA, USA).

Constructs and the site-mutagenesis

RGS tagged SEN3, HA tagged SUMO3, SEN3 mutants C243S and C532A were previously used in our work^[35]. The mutant C532S was generated by QuikChange lighting Site-Directed Mutagenesis Kit (Agilent Technology, Santa Clara, CA, USA) with previously used method^[35].

siRNA

siRNA specific for SEN3, SEN3 (3'UTR) and non-specific control (NC) siRNA were synthesized (RIBOBIO, China), and transfected using Lipofectamine 2000. The sequences of siRNA oligonucleotides for endogenous human SEN3 were: 5'-CAAUAAGGAGCUACUGCUAdTdT-3' and 5'-GUUAUCCUCGAUGACGAUdTdT-3'. While those for 3'-UTR of SEN3 were: 5'-GATCCTTTGTTGATACGTAdTdT-3'.

Transfection, co-transfection and rescue

The constructs were transiently transfected or co-transfected into cells using Lipofectamine 2000 (Invitrogen, Carlsbad, CA, USA) according to the manufacturer's instructions.

HeLa cells were first transfected with non-specific siRNA control or siRNA for endogenous SEN3. After 24 h, cells were again transfected with RGS-SEN3 WT, the mutant C243S or the mutant C532S for another 48 h to rescue SEN3 functions.

Statistical analysis

Results were derived from at least three independent experiments and expressed as Mean \pm SD. The difference between groups were compared using Student's *t* test.

Results

HIF-1 transcriptional activity is enhanced by low doses of H₂O₂ but suppressed by high doses of H₂O₂

Varied doses of H₂O₂ were administered to cultured HeLa cells and incubated for 24 h before the cell viability was assayed. The results showed that the cell viability was promoted at doses ranging from 0.05 mmol/L to 0.5 mmol/L with a peak at approximately 0.5 mmol/L, and was suppressed at doses higher than 0.75 mmol/L (Figure 1A). After screening the doses of H₂O₂ that resulted in opposite cellular effects, 0.5 mmol/L and 2 mmol/L were used as the doses to create the low and high oxidative stress conditions respectively. Truly, ROS increased to modest or dramatic levels following treatments with these doses of H₂O₂ (Figure 1B).

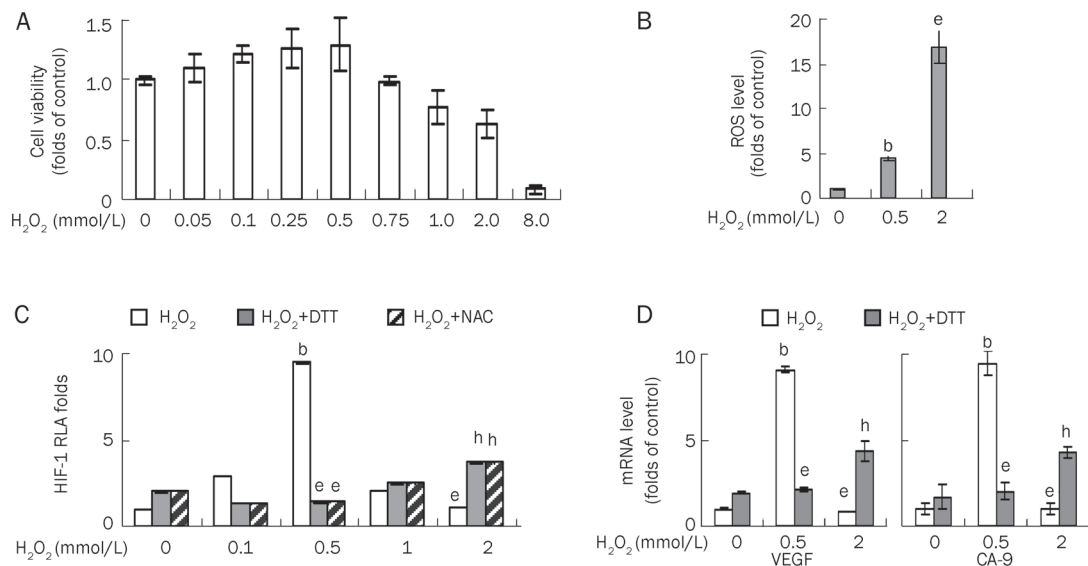


Figure 1. HIF-1 transcriptional activity is enhanced by low doses of H₂O₂, but suppressed by high doses of H₂O₂. (A) HeLa cells were treated once with the indicated concentrations of H₂O₂ for 24 h and then cell viabilities were evaluated by MTT. (B) ROS levels were detected by flow cytometry after HeLa cells were exposed to the indicated concentrations of H₂O₂ for 1 h and incubated with DCFH-DA for 10 min. (C) HeLa cells were co-transfected with the constructs of luciferase reporter for HRE and Renilla. Forty hours posttransfection, HeLa cells were exposed to H₂O₂ as indicated for 6 h. When used, 5 mmol/L NAC was pretreated for 4 h or 10 mmol/L DTT pretreated for 2 h before H₂O₂ exposure. Cells were then lysed, and the relative luciferase activity (RLA) for HIF-1 was assayed as described in “Materials and methods”. (D) HeLa cells were treated with the indicated concentrations of H₂O₂ for 6 h. HIF-1 target gene VEGF and CA-9 mRNA levels were evaluated by quantitative real-time PCR and shown as folds of control. The results were shown as the Mean±SD of three independent experiments, and samples were duplicated in each experiment. Data were represented as Mean±SD. ^b*P*<0.05 vs H₂O₂ 0 mmol/L. ^e*P*<0.05 vs H₂O₂ 0.5 mmol/L. ^h*P*<0.05 vs H₂O₂ 2 mmol/L.

The transcriptional activity of HIF-1 was assessed using luciferase reporters after cells were exposed to H₂O₂ for 6 h. The results showed that the transcriptional activity of HIF-1 was enhanced by 0.5 mmol/L of H₂O₂ but suppressed by 2 mmol/L of H₂O₂ (Figure 1C). The antioxidant NAC and the reducing agent DTT could reverse the alteration of HIF-1 transactivation caused by ROS regardless of whether transactivation was enhanced or suppressed, indicating that this effect was under redox control.

As 2 mmol/L of H₂O₂ led to the repression of viability or mitotic senescence at later time points, it was necessary to distinguish a specific inhibition toward HIF-1 transactivation from a general transcriptional suppression. The luciferase reporter activity for the control (renilla) at this level of oxidative stress was compared with the activity at the lower level, and the result excluded a general transcriptional suppression (data not shown). A reporter assay for p53 showed that the transcriptional activity of p53 was induced while the one for HIF-1 was suppressed by 2 mmol/L of H₂O₂ (Supplementary Figure 1), implying that the inhibition of HIF-1 transactivation by oxidative stress was not a non-specific phenomenon.

The transcriptional activity of HIF-1 was also assessed using real-time PCR for the mRNA levels of the HIF-1 target genes VEGF and CA-9 after the cells were exposed to H₂O₂ for 6 h. The results showed that the transcriptional levels of the HIF-1 target genes were enhanced by 0.5 mmol/L of H₂O₂ and suppressed by 2 mmol/L of H₂O₂ (Figure 1D). The reducing

agent DTT could reverse the alterations in the mRNA levels of HIF-1 target genes caused by ROS, regardless of whether they were enhanced or suppressed (Figure 1D).

Differential HIF-1 transcriptional activity under mild or severe oxidative stress results from altered HIF-1 α /p300 binding

Because HIF-1 activation is a multistep process involving the stabilization of the HIF-1 α protein, the dimerization of the HIF- α and - β subunits, translocation to the nucleus, binding to HIF-1 responsive elements HRE, and the formation of active transcriptional complexes with the co-activators p300/CBP^[36-40], we examined these processes during mild and severe oxidative stress. The result of the immunoblot showed that, although HIF-1 α was stabilized by treatment with a very low dose of H₂O₂, it remained unchanged under increasing doses of H₂O₂ (Figure 2A). In addition, the nuclear accumulation of HIF-1 α remained stable in the presence of increasing doses of H₂O₂, as shown by immunofluorescence (Figure 2B). However, a ChIP assay showed that the amount of HIF-1 α bound to HRE was remarkably increased by 0.5 mmol/L H₂O₂ but was decreased by 2 mmol/L H₂O₂ (Figure 2C). Likewise, a co-IP assay showed that the amount of p300 bound to HIF-1 α increased at low doses of H₂O₂ but decreased at high doses (Figure 2D). These data clearly demonstrated that the biphasic regulation of HIF-1 transactivation by different levels of ROS was not attributable to the altered expression or nuclear accumulation of HIF-1 α but rather to an alteration in HIF-1/p300

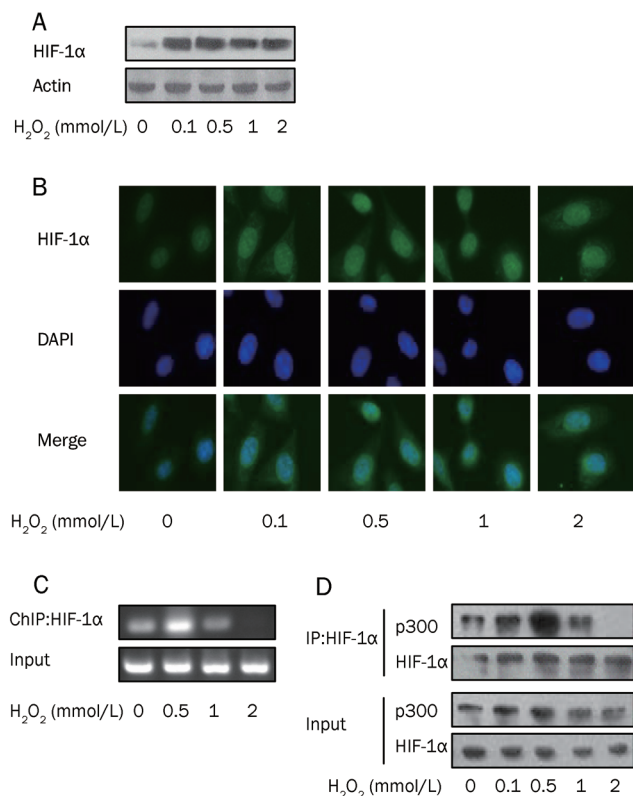


Figure 2. Differential HIF-1 transcriptional activity under mild or severe oxidative stress results from altered HIF-1α/p300 binding (A) HIF-1α protein levels were evaluated by IB after HeLa cells were incubated with cobalt chloride for 20 h and then treated with the indicated H₂O₂ for additional 1 h. β-Actin was shown as a loading control. (B) HIF-1α translocation to nuclei was shown by immunofluorescence. Cells were treated with the indicated H₂O₂ for 1 h. Immunofluorescence was performed with anti-HIF-1α antibody and the FITC-second antibody. DAPI was used for counterstaining the nuclei. (C) Ability of HIF-1 binding with HRE was tested by ChIP assay. HeLa cells were incubated with cobalt chloride for 20 h and then treated with the indicated H₂O₂ for additional 1 h followed by ChIP assay. (D) Interaction of HIF-1 with p300 was detected by co-IP. HeLa cells were incubated with cobalt chloride for 20 h and then treated with the indicated H₂O₂ for additional 1 h. Cells were lysed and endogenous HIF-1α was pulled down using antibody against HIF-1α. The pulled-down HIF-1α and whole cell lysates as input were analyzed by IB as indicated.

binding and a concomitant alteration in HIF/DNA binding.

The ROS level regulates the SENP3-p300 interaction to cause differential SUMOylation of p300

As we had previously found that the SUMO protease SENP3 accumulated in response to a mild increase in ROS and could specifically deconjugate SUMO2/3 from p300 thus promoting p300 binding with HIF-1^[26], the SUMOylation status of p300 at different ROS levels was examined. The results of the co-IP showed that, as predicted, the endogenous SUMO2/3 modification of endogenous p300 obviously decreased after the cells were exposed to a low dose of H₂O₂, while the SUMO2/3 modification of p300 in the cells treated with a high dose of

H₂O₂ remained similar to that in untreated cells. However, the level of the SENP3 protein remained stable in cells undergoing low or high stress (Figure 3A).

We hypothesized that the unchanged SUMOylation status of p300 under high stress might be caused by the inactivation of the enzymatic activity of SENP3, given that the SENP3 protein level was unchanged. To clarify this, RGS-tagged SENP3 was ectopically expressed in cells, and co-IP for RGS-SENP3 was then used to detect the interaction of SENP3 with p300. The results showed that the SENP3 interaction with p300 was enhanced under low stress condition. However, this interaction was markedly blocked under high stress and was even weaker than that under non-stress condition (Figure 3B). This result indicated that the inactivation of SENP3 catalytic capability might occur under severe oxidative stress, and this inactivation could be manifested as the loss of its ability to bind to its substrates.

SENP3 is a cysteine protease, and its enzymatic activity relies on a specific cysteine, C532^[29]. As the mutant that substitutes C532 with alanine, C532A, is typically used as a dominant-negative SENP3^[29], we used this mutant to examine SENP3-p300 binding under low and high stress conditions. The results showed that this mutant could not bind the substrate under any conditions, clearly confirming that C532, which is responsible for enzymatic activity, is required for substrate binding (Figure 3C). Hence, SENP3-p300 binding capacity could be used as a readout for the enzymatic activity of SENP3 in the following experiments.

The ROS level regulates the SENP3-p300 interaction by affecting different cysteines

Our previous studies^[26, 27] have shown that the decrease in the SUMO2/3 modification of p300 during mild stress is due to an accumulation of SENP3. We also found that this accumulation following a blockage of ubiquitination can be attributed to the oxidation of cysteines 243 or 274 within the redox sensing domain of SENP3; the mutants (C243S or C274S) in which these cysteines were replaced by serine, an amino acid residue non-responsive to ROS, failed to accumulate under stress^[35]. Given that the SENP3 protein level was unchanged upon high stress as compared with low stress and that the enzymatic activity of SENP3, as represented by its substrate binding capacity, was lost only under high stress, we hypothesized that, whereas mild stress oxidizes cysteines 243 or 274 to induce SENP3 stabilization, severe stress might oxidize another cysteine and inactivate the enzymatic activity of SENP3, *ie*, its capacity to bind with its substrates. We then generated another mutant in which C532 was replaced with serine. The SENP3-p300 binding was then analyzed by co-IP in cells transfected with the wild-type SENP3 or the mutants C243S or C532S.

The results showed that the C243S mutant could not be stabilized in response to either high or low oxidative stress conditions (Figure 4B, compare the blot of the input RGS of C243S with the wild-type). However, this mutant failed to bind to p300 when exposed to high stress conditions, show-

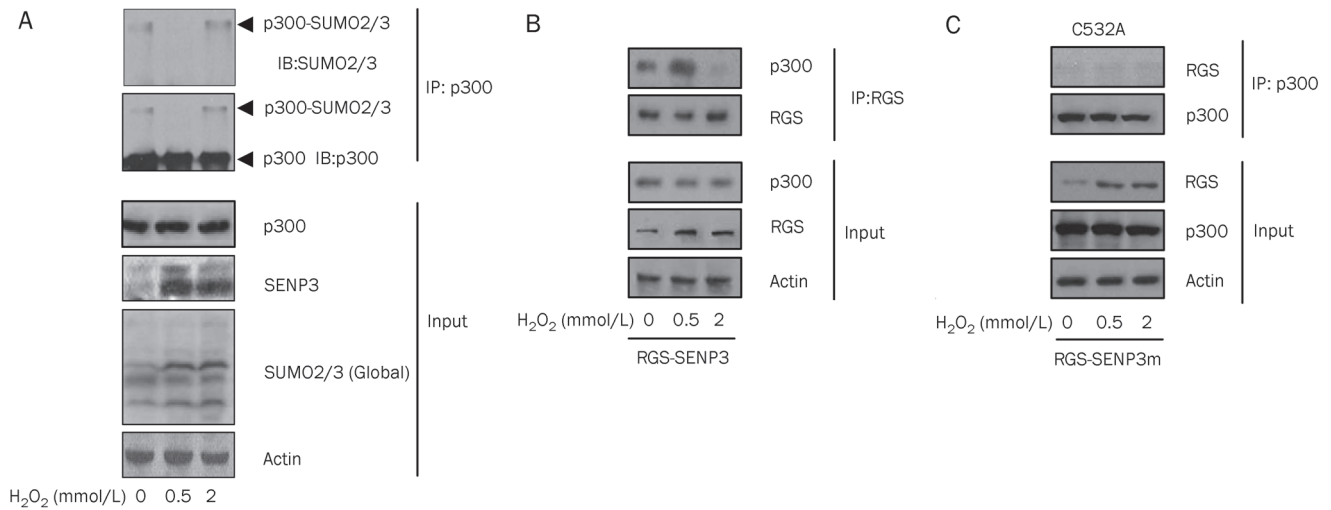


Figure 3. The ROS level regulates the SENP3-p300 interaction to cause differential SUMOylation of p300. (A) The SUMOylation of endogenous p300 was detected by co-IP. HeLa cells were treated with different concentrations of H_2O_2 for 1 h as indicated. Co-IP was carried out with p300 antibody and IB was carried out using the antibodies as indicated. The binding of SENP3 with its substrate p300 was detected by co-IP. HeLa cells were transfected with RGS-SENTP3 for 48 h, then were incubated with different concentrations of H_2O_2 for 1 h. (B) Co-IP was carried out with the antibody against RGS tag and IB was carried out using the antibodies against RGS and endogenous p300. The accumulation of SENP3 (RGS) was shown in the input. β -actin was used as a loading control. (C) The binding of the SENP3 mutant with its substrate p300 was detected by co-IP. HeLa cells were transfected with RGS-SENTP3-C532A for 40 h. Co-IP and IB procedures were the same to above in B. The accumulation of SENP3 (RGS) was shown in the input. β -Actin was used as a loading control.

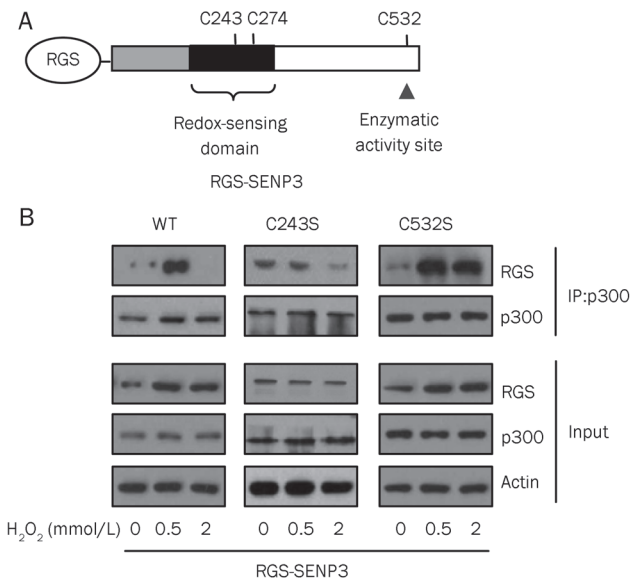


Figure 4. The ROS level regulates the SENP3-p300 interaction by affecting different cysteines. The identified domains and important cysteine residues of SENP3. (A) The plasmid RGS-SENTP3 was constructed and the site mutagenesis was conducted with serines to replace cysteines at 243 and 532 sites. (B) The accumulation of the SENP3 wild-type (WT) or mutants in response to stress conditions and the binding with its substrate p300 was detected by co-IP. HeLa cells were transfected with RGS-SENTP3 WT, C243S, or C532S for 40 h before treated with H_2O_2 for 1 h. The proteins were co-immunoprecipitated using anti-p300 and detected by IB using the indicated antibodies. The accumulation of SENP3 (RGS) was shown in the input. β -Actin was used as a loading control.

ing a similar response as the wild-type SENP3. Interestingly, the C532S mutant was sensitively responsive to ROS-induced accumulation, regardless the degree of stress (Figure 4B, compare the blot of the input RGS of C532S with the wild-type). Furthermore, the co-IP results showed that it retained the capacity to bind with p300 under both low and high stress, being not responsive to ROS-induced inactivation (Figure 4B). These data indicate that the oxidation of C243 is responsible for SENP3 accumulation under both low and high stress conditions, while the oxidation of C532 is responsible for the blockage of the SENP3-substrate interaction under high stress condition.

Oxidative modification of the individual cysteines in SENP3 regulates p300 SUMOylation and HIF-1 transactivation

To elucidate the biochemical consequences of SENP3 regulation by ROS in a biphasic manner, we investigated whether C243S and C532S truly affected p300 SUMOylation. Endogenous SENP3 was knocked down by siRNA that did not target exogenous SENP3, and the SENP3 functions were then rescued by transfection with the wild-type or the C243S or C532S mutants before the co-IP experiments were conducted. The results showed that siRNA effectively abolished basal and the ROS-enhanced SENP3 accumulation and that the conjugation of p300 with SUMO2/3 was unchanged upon stress conditions. The wild-type SENP3 could rescue the ROS-enhanced SENP3 accumulation and p300 de-SUMOylation under low stress, but SENP3 accumulation could not mediate p300 de-SUMOylation under high stress. The mutant C243S could not rescue SENP3 accumulation or p300 de-SUMOylation under

both stress conditions. Remarkably, the mutant C532S could de-SUMOylate p300 under both mild and severe stress conditions, because SENP3 could accumulate under both stress conditions, and the enzyme remained catalytically active under severe stress (Figure 5A).

Taken together, these data suggested that the two redox-sensing cysteines have different functions. C243 is responsible for sensing the increase in ROS production and in turn blocking ubiquitination. After SENP3 becomes stabilized upon mild stress, C532 is responsible for the interaction of SENP3 with its substrates, but this site is inactivated during a further increased ROS generation. The sequential oxidation of these two cysteines leads to changes in SENP3 protein abundance and its catalytic activity during the increase in ROS level,

which eventually results in a fluctuation in the SUMOylation status of p300.

We then examined the HIF-1 transcriptional activity by measuring the mRNA level of the HIF-1 specific target gene VEGF in cells with SENP3 knockdown and rescue. The results showed that the HIF-1 target gene expression was also differently affected by the two SENP3 mutants, which was consistent with the SUMOylation statuses of p300 (Figure 5B).

To exclude the possibility that 2 mmol/L H₂O₂ might cause oxidative damage to SENP3, we finally performed an intermolecular cross-linkage assay. This experiment showed that SENP3 cross-linking only occurred after treatment with 10 mmol/L of H₂O₂ (supplementary Figure 2). This result suggested that SENP3 underwent a selective oxidative modifica-

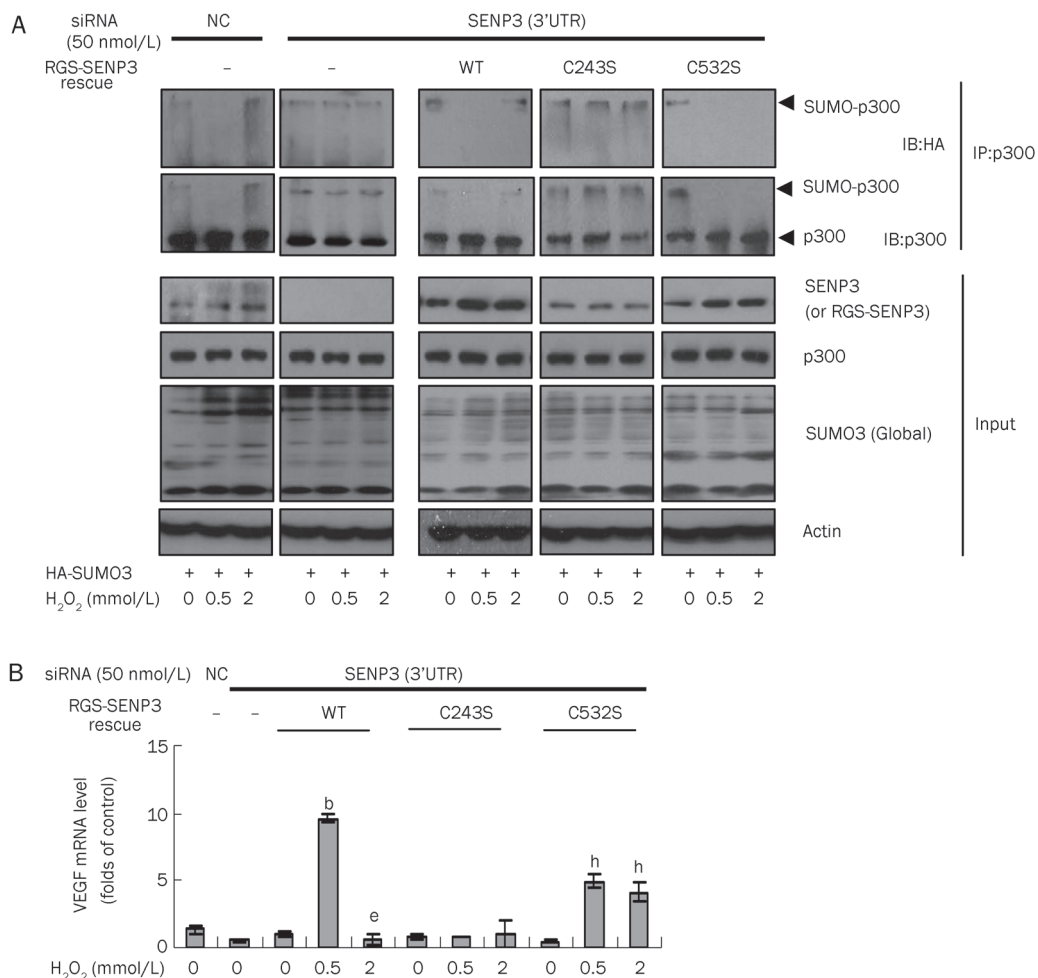


Figure 5. Oxidative modification of the individual cysteines in SENP3 regulates p300 SUMOylation and HIF-1 transactivation. (A) The SUMOylation of p300 was detected by co-IP. HeLa cells were transfected with non-specific siRNA control or siRNA for endogenous SENP3 for 24 h, and then transfected with RGS-SENP3 WT or the mutants C243S or C532S to rescue for another 48 h. HA-SUMO3 was simultaneously co-transfected. Cells were treated with H₂O₂ for 1 h. The proteins were co-immunoprecipitated using anti-p300 and detected by IB using the antibodies against p300 and HA. β -Actin as a control. (B) HeLa cells were transfected with non-specific siRNA control or SENP3 siRNA for 24 h, and then transfected with RGS-SENP3 WT, the mutants C243S or C532S to rescue for another 48 h. Cells were treated with H₂O₂ for 6 h. The VEGF mRNA levels were evaluated by real-time PCR and shown as folds of control. The results were shown as the Mean \pm SD of three independent experiments, and samples were duplicated in each experiment. Data were represented as Mean \pm SD. ^b*P*<0.05 vs siRNA SENP3 rescue WT H₂O₂ 0 mmol/L. ^e*P*<0.05 vs siRNA SENP3 rescue WT H₂O₂ 0.5 mmol/L. ^h*P*<0.05 vs siRNA SENP3 rescue C532S H₂O₂ 0 mmol/L.

tion upon treatment with 2 mmol/L H₂O₂.

Discussion

The dual or biphasic regulatory effects of ROS have been reported for many years^[2, 6, 41–43]. For instance, ROS can mediate phenotypes ranging from survival and growth to apoptosis in vascular endothelial and smooth muscle cells, which may be considered both physiological and pathophysiological^[41]. It has been concluded that the specific response elicited by ROS is determined by their specific intracellular target(s), which, in turn, depends on the species of oxidant(s), the source and subcellular localization of the oxidant(s), the kinetics of production, and the quantities produced^[41]. For example, in some cell types, low levels of ROS (usually submicromolar concentrations) induce growth, but higher concentrations (usually >10 micromolar) induce apoptosis or necrosis^[44]. These studies, although using the words dual or biphasic, actually intended to highlight the fact that ROS may cause opposing effects at different doses.

It has been observed that cellular signaling pathways are generally subjected to dual redox regulation in which ROS have opposing effects on upstream signaling systems and downstream transcription factors^[21, 26, 32, 45, 46]. Our previous research has shown that, when increased by chemical compounds or genetic manipulation, ROS may enhance the transcriptional activities of NF- κ B, AP-1 and HIF-1 at lower doses but suppress them at higher doses^[21, 26, 32, 45, 47, 48]. For instance, when ROS increase modestly, they activate NF- κ B by triggering the degradation of I κ B α and other events in the cytoplasm, which usually lead to prosurvival signaling events. However, as the ROS levels become further excessive, the nuclear environment is shifted from reductive to oxidative, which inhibits the activation of NF- κ B and other transcription factors by preventing them from binding to DNA. As a consequence, the prosurvival transcriptional activity is abolished. This finding shows how ROS can shift the activation/inactivation control of the NF- κ B pathway^[45].

Based on findings in the literature and our own observations, we propose that the opposing effects caused by low *vs* high levels of ROS may be mediated by the biphasic redox sensing of proteins, *ie*, the ability of proteins to sense redox changes through the oxidation of their cysteine residues by different levels of ROS. Oxidative modification of protein thiols is now considered as an emerging role in cell signaling. It has been well recognized that the thiol oxidation state of reactive cysteine residues in proteins controls the function of the proteins and the pathways that they are part of^[49–54]. We hypothesize that, during the biphasic redox sensing, the different cysteines of a given protein molecule might be sequentially oxidized by different levels of ROS, thus leading to different conformational characteristics and functional statuses of the protein.

HIF-1 is one of the most well known redox-sensitive transcription factors. An increasing body of evidence shows that ROS induce the stabilization of HIF-1 α under hypoxic or normoxic conditions^[14, 26, 55, 56]. Our previous study proposed an

additional mechanism in which mild oxidative stress induced by low doses of H₂O₂ can rapidly stabilize SENP3, in turn promoting the transcriptional activity of HIF-1 through the deconjugation of SUMO2/3 from the co-activator p300. This activating mechanism functions independently of HIF-1 α stabilization, and is required for ROS-mediated HIF-1 transcriptional activity under both hypoxia and normoxia^[13]. To establish why the transcriptional activity of HIF-1 can be suppressed by a further dramatic increase of ROS, we hypothesized that SENP3 is a biphasic redox sensor that mediates the biphasic redox regulation of HIF-1. We used a variety of SENP3 mutants to study the responsiveness of SENP3 to increasing levels of ROS. The results of the present study demonstrated that the oxidation of C243 is required for ROS-induced SENP3 accumulation and consequent HIF-1 transactivation, while in contrast, the oxidation of C532 is responsible for ROS-induced SENP3 inactivation and the consequent suppression of the transcriptional activity of HIF-1. Therefore, we suggest that the biphasic redox sensing of SENP3 mediates, at least in part, the bidirectional ROS regulation of HIF-1. To our knowledge, the present study has demonstrated for the first time that the different cysteines in a redox-sensitive protein can sense different ROS levels, and thus mediate a shift in protein function and the related signaling activity.

The cell model of the biphasic redox effects in this study is produced by treating HeLa cells with 0.5 and 2 mmol/L of H₂O₂. This dose range of H₂O₂ used in cancerous or transformed cells is considered to be appropriate in mimicking oxidative stress conditions^[28, 31, 57–59]. Bossis *et al* reported that ROS at low concentrations, 1 mmol/L, result in the rapid disappearance of most SUMO conjugates, which is due to direct and reversible inhibition of SUMO conjugating enzymes through the formation of (a) disulfide bond(s) involving the catalytic cysteines of the SUMO E1 subunit Uba2 and the E2-conjugating enzyme Ubc9. And they also observed the same phenomenon in a physiological scenario of endogenous ROS production, the respiratory burst in macrophages^[31]. Xu *et al* showed a reversible oxidative modification of SUMO protease SENP1 by 10 mmol/L of H₂O₂ that serves as a protective mechanism for the enzyme^[28]. Thus, the cell model of low *vs* high stress in this study may represent ROS fluctuation that is correlated with protein oxidation.

The findings in the present study will shed light on biphasic redox effects in cells and increase our understanding of how the generation of ROS may be relevant to both cancer therapy and to cancer genesis and progression. A typical example of this rationale is arsenic, which is classically recognized as a ROS-dependent environmental carcinogen but becomes an anticancer agent by inducing the apoptosis of leukemic cells^[60, 61].

In summary, SENP3 is a biphasic redox sensor. The increase in intracellular ROS generation could induce SENP3 stabilization through the oxidation of the cysteines 243 or 274 that in turn blocks its ubiquitin-mediated degradation. But, when an overwhelming ROS are generated, the cysteine 532 that is required for the substrate interaction undergoes oxidation

and consequent inactivation. This biphasic redox sensing of SENP3 leads to a fluctuation in the SUMOylation status of its substrate p300, a co-activator of HIF-1, thus making a shift of HIF-1 transcriptional activity from activation to inactivation (Figure 6).

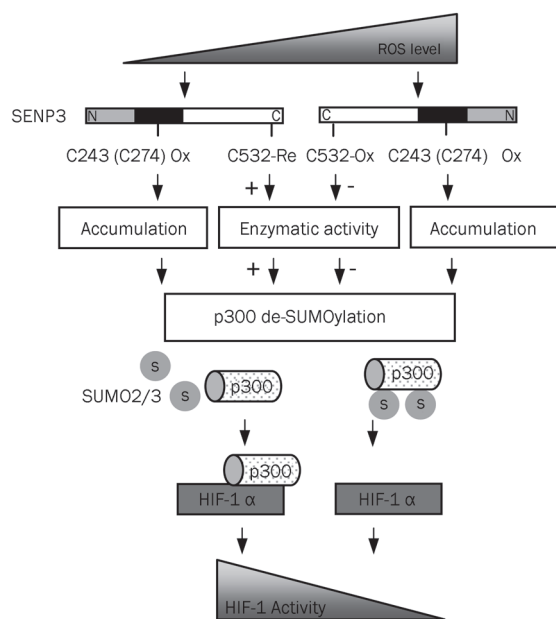


Figure 6. The schematic illustration for the biphasic redox sensing of SENP3 and its role in mediating the shift of HIF-1 transcriptional activity by ROS

Notes: “↓”, to lead to a result; “+ ↓”, to enhance; “↓ -”, to suppress;

▴, from low to high; ▾, from high to low.

Abbreviation

ROS, reactive oxygen species; SUMO, small ubiquitin-like modifier; NAC, *N*-acetylcysteine; DTT, dithiothreitol; RT-PCR, real-time polymerase chain reaction; DCFH-DA, 2, 7-dichlorodihydrofluorescein diacetate; HRE, hypoxia response element; IB, immunoblotting; co-IP, co-immunoprecipitation; CHIP, chromatin immunoprecipitation; siRNA, small interfering RNA; RT, room temperature.

Acknowledgements

This study was supported by grants from the National Natural Science Foundation of China (91013012, 30971437 to Jing YI, 31000613 to Xin-zhi HUANG), Shanghai Municipal Science and Technology Commission (11ZR1419100 to Ying WANG, 11DZ2260200 to Jing YI), and Shanghai Municipal Education Commission (J50201, to Jing YI).

Author contribution

Ying WANG, Jie YANG, Xin-zhi HUANG, and Jing YI designed the experiments and analyzed the data; Ying WANG, Kai YANG, Hui CANG, and Hui LI performed the experiments; Ying WANG, Jie YANG, and Jing YI prepared the manuscript.

Supplementary information

Supplementary figures are available at website of Acta Pharmacologica Sinica on NPG.

References

- Finkel T. Signal transduction by reactive oxygen species. *J Cell Biol* 2011; 194: 7–15.
- Ramsey MR, Sharpless NE. ROS as a tumour suppressor? *Nat Cell Biol* 2006; 8: 1213–15.
- Schulz TJ, Zarse K, Voigt A, Urban N, Birringer M, Ristow M. Glucose restriction extends *Caenorhabditis elegans* life span by inducing mitochondrial respiration and increasing oxidative stress. *Cell Metab* 2007; 6: 280–93.
- Gough DR, Cotter TG. Hydrogen peroxide: a Jekyll and Hyde signalling molecule. *Cell Death Dis* 2011; 2: e213. doi: 10.1038/cddis.96.
- Mesquita A, Weinberger M, Silva A, Sampaio-Marques B, Almeida B, Leão C, et al. Caloric restriction or catalase inactivation extends yeast chronological lifespan by inducing H₂O₂ and superoxide dismutase activity. *Proc Natl Acad Sci U S A* 2010; 107: 15123–8.
- Martindale JL, Holbrook NJ. Cellular response to oxidative stress: signaling for suicide and survival. *J Cell Physiol* 2002; 192: 1–15.
- Gao L, Mann GE. Vascular NAD(P)H oxidase activation in diabetes: a double-edged sword in redox signalling. *Cardiovasc Res* 2009; 82: 9–20.
- Ray PD, Huang BW, Tsuji Y. Reactive oxygen species (ROS) homeostasis and redox regulation in cellular signaling. *Cell Signal* 2012; 24: 981–90.
- Cramer T, Yamnishi Y, Clausen BE, Förster I, Pawlinski R, Mackman N, et al. HIF-1alpha is essential for myeloid cell-mediated inflammation. *Cell* 2003; 112: 645–57.
- Jung YJ, Isaacs JS, Lee S, Trepel J, Neckers L. IL-1beta-mediated up-regulation of HIF-1alpha via an NFkappaB/COX-2 pathway identifies HIF-1 as a critical link between inflammation and oncogenesis. *FASEB J* 2003; 17: 2115–7.
- Walmsley SR, Cadwallader KA, Chilvers ER. The role of HIF-1alpha in myeloid cell inflammation. *Trends Immunol* 2005; 26: 434–9.
- Tacchini L, Dansi P, Matteucci E, Desiderio MA. Hepatocyte growth factor signalling stimulates hypoxia inducible factor-1 (HIF-1) activity in HepG2 hepatoma cells. *Carcinogenesis* 2001; 22: 1363–71.
- Patten DA, Lafleur VN, Robitaille GA, Chan DA, Giaccia AJ, Richard DE. Hypoxia-inducible factor-1 activation in nonhypoxic conditions: the essential role of mitochondrial-derived reactive oxygen species. *Mol Biol Cell* 2010; 21: 3247–57.
- Zelzer E, Levy Y, Kahana C, Shilo BZ, Rubinstein M, Cohen B. Insulin induces transcription of target genes through the hypoxia-inducible factor HIF-1alpha/ARNT. *EMBO J* 1998; 17: 5085–94.
- Carroll VA, Ashcroft M. Role of hypoxia-inducible factor (HIF)-1alpha versus HIF-2alpha in the regulation of HIF target genes in response to hypoxia, insulin-like growth factor-I, or loss of von Hippel-Lindau function: implications for targeting the HIF pathway. *Cancer Res* 2006; 66: 6264–70.
- Roth U, Curth K, Unterman TG, Kietzmann T. The transcription factors HIF-1 and HNF-4 and the coactivator p300 are involved in insulin-regulated glucokinase gene expression via the phosphatidylinositol 3-kinase/protein kinase B pathway. *J Biol Chem* 2004; 279: 2623–31.
- Treins C, Murdaca J, Van Obberghen E, Giorgetti-Peraldi S. AMPK activation inhibits the expression of HIF-1alpha induced by insulin and IGF-1. *Biochem Biophys Res Commun* 2006; 342: 1197–202.
- Chandel NS, Maltepe E, Goldwasser E, Mathieu CE, Simon MC, Schumacker PT. Mitochondrial reactive oxygen species trigger hypoxia-

- induced transcription. *Proc Natl Acad Sci U S A* 1998; 95: 11715–20.
- 19 Chandel NS, Budinger G. The cellular basis for diverse responses to oxygen. *Free Radic Biol Med* 2007; 42: 165–74.
 - 20 Jung SN, Yang W, Kim J, Kim HS, Kim EJ, Yun H, *et al*. Reactive oxygen species stabilize hypoxia-inducible factor-1 alpha protein and stimulate transcriptional activity via AMP-activated protein kinase in DU145 human prostate cancer cells. *Carcinogenesis* 2008; 29: 713–21.
 - 21 Huang XZ, Wang J, Huang C, Chen YY, Shi GY, Hu QS, *et al*. Emodin enhances cytotoxicity of chemotherapeutic drugs in prostate cancer cells: the mechanisms involve ROS-mediated suppression of multidrug resistance and hypoxia inducible factor-1. *Cancer Biol Ther* 2008; 7: 468–75.
 - 22 Galanis A, Pappa A, Giannakakis A, Lanitis E, Dangaj D, Sandaltzopoulos R. Reactive oxygen species and HIF-1 signalling in cancer. *Cancer Lett* 2008; 266: 12–20.
 - 23 Tuttle SW, Maity A, Oprysko PR, Kachur AV, Ayene IS, Biaglow JE, *et al*. Detection of reactive oxygen species via endogenous oxidative pentose phosphate cycle activity in response to oxygen concentration: implications for the mechanism of HIF-1alpha stabilization under moderate hypoxia. *J Biol Chem* 2007; 282: 36790–6.
 - 24 Comito G, Calvani M, Giannoni E, Bianchini F, Calorini L, Torre E, *et al*. HIF-1 α stabilization by mitochondrial ROS promotes Met-dependent invasive growth and vasculogenic mimicry in melanoma cells. *Free Radic Biol Med* 2011; 51: 893–904.
 - 25 Schumacker PT. SIRT3 controls cancer metabolic reprogramming by regulating ROS and HIF. *Cancer Cell* 2011; 19: 299–300.
 - 26 Huang C, Han Y, Wang YM, Sun XX, Yan S, Yeh ET, *et al*. SENP3 is responsible for HIF-1 transactivation under mild oxidative stress via p300 de-SUMOylation. *EMBO J* 2009; 28: 2748–62.
 - 27 Han Y, Huang C, Sun X, Xiang B, Wang M, Yeh ET, *et al*. SENP3-mediated de-conjugation of SUMO2/3 from promyelocytic leukemia is correlated with accelerated cell proliferation under mild oxidative stress. *J Biol Chem* 2010; 285: 12906–15.
 - 28 Xu Z, Lam LS, Lam LH, Chau SF, Ng TB, Au SW. Molecular basis of the redox regulation of SUMO proteases. *FASEB J* 2008; 22: 127–37.
 - 29 Gong L, Yeh ET. Characterization of a family of nucleolar SUMO-specific proteases with preference for SUMO-2 or SUMO-3. *J Biol Chem* 2006; 281: 15869–77.
 - 30 Wang Y, Mukhopadhyay D, Mathew S, Hasebe T, Heimeier RA, Azuma Y, *et al*. Identification and developmental expression of *Xenopus laevis* SUMO proteases. *PLoS One* 2009; 4: e8462.
 - 31 Bossis G, Melchior F. Regulation of SUMOylation by reversible oxidation of SUMO conjugating enzymes. *Mol Cell* 2006; 21: 349–57.
 - 32 Yi J, Yang J, He R, Gao F, Sang H, Tang XM, *et al*. Emodin enhances arsenic trioxide induced apoptosis via generation of reactive oxygen species and inhibition of survival signaling. *Cancer Res* 2004; 64: 108–16.
 - 33 Zuo Y, Xiang BG, Yang J, Sun XX, Wang YM, Cang H, *et al*. Oxidative modification of caspase-9 facilitates its activation via disulfide-mediated interaction with Apaf-1. *Cell Res* 2009; 19: 449–57.
 - 34 Sang J, Yang K, Sun YP, Han Y, Cang H, Chen YY, *et al*. SUMO2 and SUMO3 transcription is differentially regulated by oxidative stress in an Sp1-dependent manner. *Biochem J* 2011; 435: 489–98.
 - 35 Yan S, Sun XX, Xiang BG, Cang H, Kang XL, Chen YY, *et al*. Redox regulation of the stability of the SUMO protease SENP3 via interactions with CHIP and Hsp90. *EMBO J* 2010; 29: 3773–86.
 - 36 Lando D, Peet D, Whelan DA, Gorman JJ, Whitelaw ML. Asparagine hydroxylation of the HIF transactivation domain a hypoxic switch. *Science* 2002; 295: 858–61.
 - 37 Kallio PJ, Okamoto K, O'Brien S, Carrero P, Makino Y, Tanaka H, *et al*. Signal transduction in hypoxic cells: inducible nuclear translocation and recruitment of the CBP/p300 coactivator by the hypoxia-inducible factor-1alpha. *EMBO J* 1998; 17: 6573–86.
 - 38 Freedman SJ, Sun ZY, Poy F, Kung AL, Livingston DM, Wagner G, *et al*. Structural basis for recruitment of CBP/p300 by hypoxia-inducible factor-1 alpha. *Proc Natl Acad Sci U S A* 2002; 99: 5367–72.
 - 39 Ebert BL, Bunn HF. Regulation of transcription by hypoxia requires a multiprotein complex that includes hypoxia-inducible factor 1, an adjacent transcription factor, and p300/CREB binding protein. *Mol Cell Biol* 1998; 18: 4089–96.
 - 40 Huang LE, Arany Z, Livingston DM, Bunn HF. Activation of hypoxia-inducible transcription factor depends primarily upon redox-sensitive stabilization of its alpha subunit. *J Biol Chem* 1996; 271: 32253–9.
 - 41 Irani K. Oxidant signaling in vascular cell growth, death, and survival: a review of the roles of reactive oxygen species in smooth muscle and endothelial cell mitogenic and apoptotic signaling. *Circ Res* 2000; 87: 179–83.
 - 42 Deshpande SS, Angkeow P, Huang J, Ozaki M, Irani K. Rac1 inhibits TNF-alpha-induced endothelial cell apoptosis: dual regulation by reactive oxygen species. *FASEB J* 2000; 14: 1705–14.
 - 43 Lopes N, Gregg D, Vasudevan S, Hassanain H, Goldschmidt-Clermont P, Kovacic H. Thrombospondin 2 regulates cell proliferation induced by Rac1 redox-dependent signaling. *Mol Cell Biol* 2003; 23: 5401–8.
 - 44 Day RM, Suzuki YJ. Cell proliferation, reactive oxygen and cellular glutathione. *Dose Response* 2006; 3: 425–42.
 - 45 Jing YW, Yang J, Wang YM, Li H, Chen YY, Hu QS, *et al*. Alteration of subcellular redox equilibrium and the consequent oxidative modification of nuclear factor kappaB are critical for anticancer cytotoxicity by emodin, a reactive oxygen species-producing agent. *Free Radic Biol Med* 2006; 40: 2183–97.
 - 46 Wang YM, Huang XZ, Cang H, Gao F, Yamamoto T, Osaki T, *et al*. The endogenous reactive oxygen species promote NF-kappaB activation by targeting on activation of NF-kappaB-inducing kinase in oral squamous carcinoma cells. *Free Radic Res* 2007; 41: 963–71.
 - 47 Yi J, Yang J, He R, Gao F, Sang H, Tang XM, *et al*. Emodin enhances arsenic trioxide-induced apoptosis via generation of reactive oxygen species and inhibition of survival signaling. *Cancer Res* 2004; 64: 108–16.
 - 48 Wang J, Yi J. Cancer cell killing via ROS: to increase or decrease, that is the question. *Cancer Biol Ther* 2008; 7: 1875–84.
 - 49 Thamsen M, Jakob U. The redoxome: proteomic analysis of cellular redox networks. *Curr Opin Chem Biol* 2011; 15: 113–9.
 - 50 Winter J, Linke K, Jatzek A, Jakob U. Severe oxidative stress causes inactivation of DnaK and activation of the redox-regulated chaperone Hsp33. *Mol Cell* 2005; 17: 381–92.
 - 51 Leichert LI, Gehrke F, Gudiseva HV, Blackwell T, Ilbert M, Walker AK, *et al*. Quantifying changes in the thiol redox proteome upon oxidative stress *in vivo*. *Proc Natl Acad Sci U S A* 2008; 105: 8197–202.
 - 52 Biswas S, Chida AS, Rahman I. Redox modifications of protein-thiols: emerging roles in cell signaling. *Biochem Pharmacol* 2006; 71: 551–64.
 - 53 Eaton P. Protein thiol oxidation in health and disease: techniques for measuring disulfides and related modifications in complex protein mixtures. *Free Radic Biol Med* 2006; 40: 1889–99.
 - 54 Wang Y, Yang J, Yi J. Redox sensing by proteins: oxidative modifications on cysteines and the consequent events. *Antioxid Redox Signal* 2012; 16: 649–57.
 - 55 Liu XH, Kirschenbaum A, Lu M, Yao S, Dosoretz A, Holland JF, *et al*. Prostaglandin E₂ induces hypoxia-inducible factor-1alpha stabilization and nuclear localization in a human prostate cancer cell line. *J Biol Chem* 2002; 277: 50081–6.
 - 56 Sun W, Chang SS, Fu Y, Liu Y, Califano JA. Chronic CSE treatment

- induces the growth of normal oral keratinocytes via PDK2 upregulation, increased glycolysis and HIF1 α stabilization. *PLoS One* 2011; 6: e16207.
- 57 Mao Y, Song G, Cai Q, Liu M, Luo H, Shi M, et al. Hydrogen peroxide-induced apoptosis in human gastric carcinoma MGC803 cells. *Cell Biol Int* 2006; 30: 332–7.
- 58 Hardwick JS, Sefton BM. Activation of the Lck tyrosine protein kinase by hydrogen peroxide requires the phosphorylation of Tyr-394. *Proc Natl Acad Sci U S A* 1995; 92: 4527–31.
- 59 Sullivan SG, Chiu DT, Errasfa M, Wang JM, Qi JS, Stern A. Effects of H₂O₂ on protein tyrosine phosphatase activity in HER14 cells. *Free Radic Biol Med* 1994; 16: 399–403.
- 60 Chou WC, Dang CV. Acute promyelocytic leukemia: recent advances in therapy and molecular basis of response to arsenic therapies. *Curr Opin Hematol* 2005; 12: 1–6.
- 61 Lallemand-Breitenbach V, Jeanne M, Benhenda S, Nasr R, Lei M, Peres L, et al. Arsenic degrades PML or PML-RARalpha through a SUMO-triggered RNF4/ubiquitin-mediated pathway. *Nat Cell Biol* 2008; 10: 547–55.

Original Article

Pharmacophore-based virtual screening and density functional theory approach to identifying novel butyrylcholinesterase inhibitors

Sugunadevi SAKKIAH, Keun Woo LEE*

Division of Applied Life Science (BK21 Program), Systems and Synthetic Agrobiotech Center (SSAC), Plant Molecular Biology and Biotechnology Research Center (PMBBRC), Research Institute of Natural Science (RINS), Gyeongsang National University (GNU), Jinju 660–701, Korea

Aim: To identify the critical chemical features, with reliable geometric constraints, that contributes to the inhibition of butyrylcholinesterase (BChE) function.

Methods: Ligand-based pharmacophore modeling was used to identify the critical chemical features of BChE inhibitors. The generated pharmacophore model was validated using various techniques, such as Fischer's randomization method, test set, and decoy set. The best pharmacophore model was used as a query in virtual screening to identify novel scaffolds that inhibit BChE. Compounds selected by the best hypothesis in the virtual screening were tested for drug-like properties, and molecular docking study was applied to determine the optimal orientation of the hit compounds in the BChE active site. To find the reactivity of the hit compounds, frontier orbital analysis was carried out using density functional theory.

Results: Based on its correlation coefficient (0.96), root mean square (RMS) deviation (1.01), and total cost (105.72), the quantitative hypothesis Hypo1 consisting of 2 HBA, 1 Hy-Ali, and 1 Hy-Ar was selected as the best hypothesis. Thus, Hypo1 was used as a 3D query in virtual screening of the Maybridge and Chembridge databases. The hit compounds were filtered using ADMET, Lipinski's Rule of Five, and molecular docking to reduce the number of false positive results. Finally, 33 compounds were selected based on their critical interactions with the significant amino acids in BChE's active site. To confirm the inhibitors' potencies, the orbital energies, such as HOMO and LUMO, of the hit compounds and 7 training set compounds were calculated. Among the 33 hit compounds, 10 compounds with the highest HOMO values were selected, and this set was further culled to 5 compounds based on their energy gaps important for stability and energy transfer. From the overall results, 5 hit compounds were confirmed to be potential BChE inhibitors that satisfied all the pharmacophoric features in Hypo1.

Conclusion: This study pinpoints important chemical features with geometric constraints that contribute to the inhibition of BChE activity. Five compounds are selected as the best hit BChE-inhibitory compounds.

Keywords: cholinesterase; butyrylcholinesterase; Alzheimer's disease; virtual screening; density functional theory; molecular docking; ligand-based pharmacophore modeling theory

Acta Pharmacologica Sinica (2012) 33: 964–978; doi: 10.1038/aps.2012.21; published online 11 Jun 2012

Introduction

Cholinesterases (ChEs) are involved in the degradation of choline and show similarity in protein sequence but differences in their kinetic properties. On the basis of their substrate and inhibitor specificities, cholinesterases are divided into two subfamilies: acetylcholinesterases (AChEs; EC 3.1.1.7) and butyrylcholinesterases (BChEs; EC 3.1.1.8). AChE is predominantly present in the central and peripheral nervous system,

as well as in muscles. In muscles, AChE terminates impulse transmission by the rapid hydrolysis of acetylcholine to acetic acid and choline^[1]. BChE is primarily synthesized in the liver and secreted into plasma, and it is responsible for the hydrolysis of a variety of choline (hydrophilic and hydrophobic) and non-choline esters^[2]. BChE plays a key role in cholinergic synapses by terminating acetylcholine action, although the complete physiological function of BChE remains unclear^[3]. Both cholinesterase enzymes belong to the super family of α/β -hydrolase fold proteins^[4]. Both AChE and BChE exist as multimers of catalytic subunits in globular forms such as G1, G2, and G4 that contain one, two, or four subunits, respec-

* To whom correspondence should be addressed.

E-mail kwlee@gnu.ac.kr

Received 2012-01-03 Accepted 2012-02-22

tively. The hydrolysis of substrates by both enzymes proceeds through a transacylation step involving nucleophilic and general acid-base elements^[5]. BChE acts as a scavenger protein that protects the cholinergic system against anticholinesterase poisons. BChE is the sole carboxylesterase^[6,7] with recognized toxicological and pharmacological importance in scavenging and detoxification of numerous ester-containing drugs, pro-drugs^[8,9], and poisonous carbamyl- and phosphoryl-esters, including nerve agents^[10,11].

Currently, BChE is emerging as an important pharmacological target in Alzheimer's disease (AD) therapy^[12]. A 40%–90% increase in BChE expression and activity have been found in AD brain neuronal plaques^[13]. BChE is capable of compensating for reduced AChE catalytic functions in the synaptic cleft^[14,15] and shows significantly increased activity (30%–60%) during the time course of AD^[16,17]. Hence, in recent years, many scientists and researchers have shown keen interest in designing small molecules that can inhibit BChE activity^[18–23]. However, there is also increasing evidence of BChE's involvement in non-cholinergic functions such as cell differentiation^[24], neurogenesis, and the formation of amyloid plaques in AD^[25–27].

In this work, we used computer-aided drug design approaches to identify novel and potent inhibitors of BChE. Pharmacophore studies are more cost-effective than experimental chemical screening of large databases. A 3D pharmacophore model was generated for BChE based on a series of well-known inhibitors. The best quantitative model was used as a 3D query for virtual screening of chemical databases to discover novel hit compounds. The virtual screening results revealed a small subset of database compounds that were promising potential hit compounds for BChE inhibition. The hits were subsequently filtered by Lipinski's Rule of Five, ADME (absorption, distribution, metabolism, and excretion) properties, and molecular docking. Finally, density functional theory (DFT) was used to calculate the orbital energy value and energy gap for the molecules screened by docking.

Computational methods

Pharmacophore modeling is one of the most frequently used and valuable methods to discover novel scaffolds for various targets.

Selection of compounds

To construct the BChE data set, 71 compounds were collected with their corresponding reported inhibitory activity values (IC_{50}) which were tested using the same bioassay technique from various publications^[28–32]. The BChE data set was divided into two sets: training and test sets that contained 26 and 45 compounds, respectively. The training set was prepared based on the following criteria: (i) a minimum of 16 diverse compounds were selected to avoid any chance correlation; (ii) the activity data should have a range of 4–5 orders of magnitude; (iii) the compounds should be selected to provide clear, concise information to avoid redundancy or bias in terms of

both structural features and activity range; (iv) the most active compounds should be included so that they provide information on the most critical features required for a reliable/rational pharmacophore model; and (v) the inclusion of any compound known to be inactive due to steric hindrance must be avoided. The training set was used to build the quantitative hypothesis based on principles of structural diversity and IC_{50} values that spanned a wide activity range, from 3.6 nmol/L to 11 000 nmol/L (Figure 1). The test set was used to evaluate the predictive ability of the generated pharmacophore model. Both the training and test set compounds were classified into three categories based on their activity values. The compounds with IC_{50} values less than or equal to 100 nmol/L were considered to be highly active (+++), compounds with an activity range between 100 nmol/L and 10 000 nmol/L were considered to be moderately active (++) and compounds with IC_{50} values greater than or equal to 10 000 nmol/L were set as low activity compounds (+). The 2D structures of the training and test set molecules were drawn using ChemSketch^[24], and the structures were converted into their corresponding 3D form using DS.

Pharmacophore modeling

Quantitative hypotheses were generated, and the best hypothesis was selected based on the models' ability to predict the biological activity of novel compounds from various chemical databases using Discovery Studio v2.5.5 (DS, www.accelrys.com, San Diego, CA, USA). There are generally two methods to generate molecular conformation: FAST and BEST. The FAST algorithm only considers existing conformers and interrupts a search as soon as a pharmacophore matching conformation is found, whereas the BEST algorithm additionally "tweaks" bond distances, angles, and dihedral angles of pre-generated conformers on the fly to achieve the best matches. Herein, we used the BEST conformation method to generate multiple acceptable conformations for each compound present in the training and test sets with 20 kcal/mol as the energy cutoff^[33]. All default parameters were used to generate the pharmacophore, except the uncertainty default value (3.0) was changed to 2.0^[34]. The uncertainty is the ratio of the reported activity value relative to the minimum, and the maximum values must be greater than 1.0. The uncertainty value affects the categorization of ligands in the data set as either active or inactive compounds and is used during the constructive and subtractive phases. Here, an uncertainty value of 2.0 was more suitable for our data set because the compound activities spanned the requisite 4 orders of magnitude; this choice has been confirmed by evidence in the literature^[35,36]. The feature mapping/DS protocol was used to identify common features present in the active inhibitors of BChE. This protocol computes a maximum of 1000 possible pharmacophore features mappings for the selected ligands. The selected features from the feature mapping were used as one of the key inputs for the 3D-QSAR pharmacophore generation module using a HypoGen algorithm. The HypoGen algorithm further estimates the activity of each training set compound by computing regres-

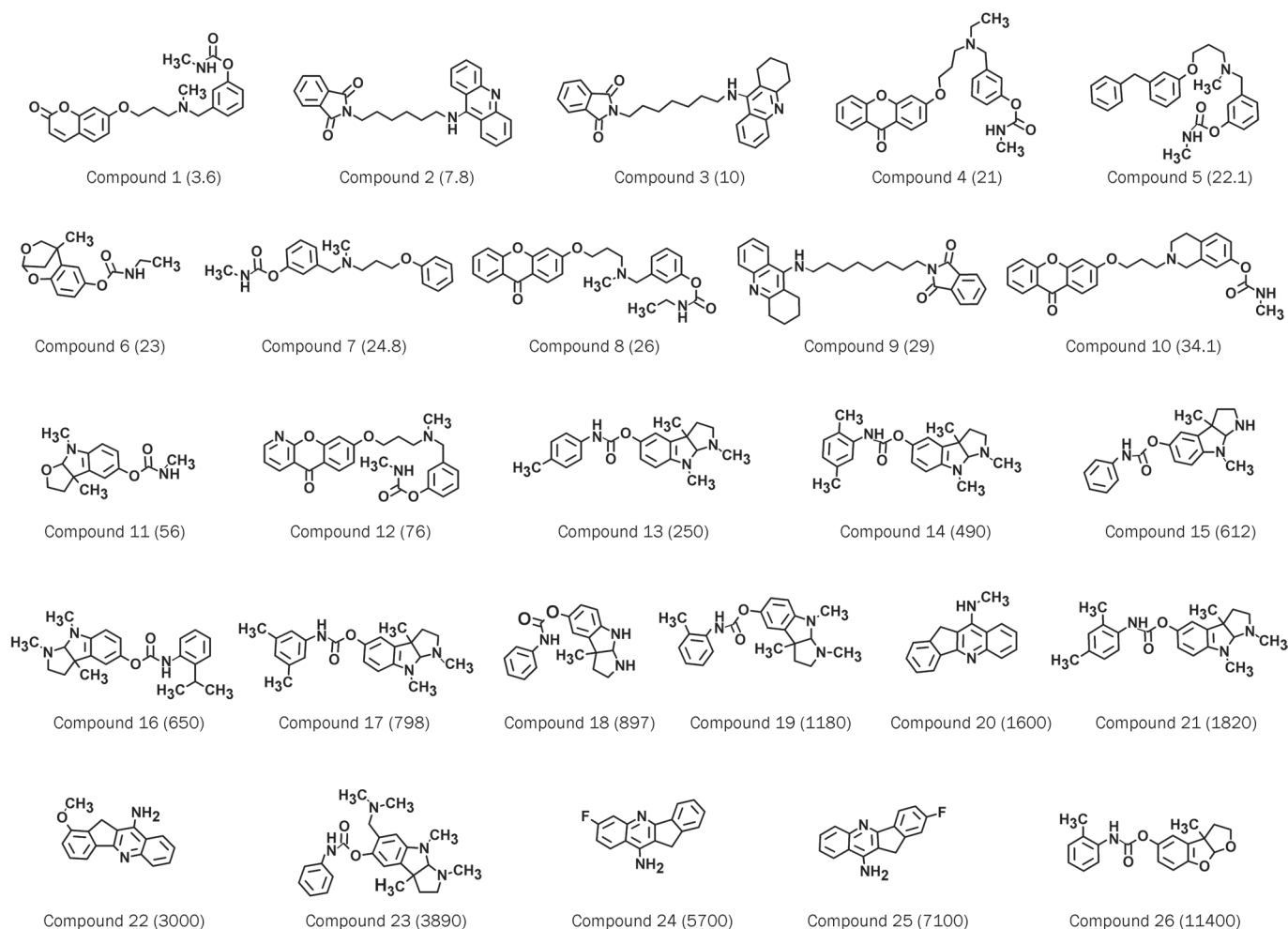


Figure 1. Set of 26 chemically diverse compounds used as the training set in 3D-QSAR discovery studio/pharmacophore generation. IC_{50} values, in nmol/L, are indicated in parentheses for each compound.

sion analysis using parameters such as the relationship of geometric fit value versus the negative logarithm of the activity. While generating the quantitative model, a minimum of 0 to a maximum of 5 features were selected to build a series of hypotheses. Ten quantitative pharmacophore models were generated with corresponding statistical parameters such as cost values, root mean square (RMS), and fit values. The best quality hypothesis was selected based on cost values as defined by Debnath's methods^[34].

Hypothesis validation

In general, pharmacophore models should be statistically significant, accurately predict the activity of molecules, and retrieve active compounds from databases. The best pharmacophore model was validated using various potent approaches such as Fischer's randomization, test set, and decoy set^[33]. The main purpose of validating a quantitative pharmacophore model is to determine its capacity to identify active compounds, as well as its predictive ability for corresponding molecules. Fischer's randomization test was performed

simultaneously during the original hypotheses generation and produced a number of random spreadsheets depending on the selected significance level (90%, 95%, 98%, and 99%) by shuffling the activity values present in the training set. Here, a 95% significance level was selected. Nineteen random spreadsheets were produced by randomly shuffling the activity value of the training set compounds, and the test generated hypotheses using the same chemical features and parameters used to develop the original hypothesis. Test and decoy sets were used to check whether the best hypothesis was able to select molecules with orders of magnitude of activity similar to that of the active training set and to determine how well the model hypothesis could differentiate potential BChE inhibitors from other compounds, respectively. The test set consisted of structurally diverse chemical compounds from the training set to ascertain the broadness of pharmacophore predictability. The decoy set was prepared by calculating the 1D property of 25 active inhibitors of BChE and 2075 inactive or unknown molecules. EF and GF were calculated using the following equations:

$$EF=(H_a/H_t)/(A/D)$$

$$GF=(H_a/4H_tA)(3A+Ht)*\{1-[(H_t-H_a)/(D-A)]\}$$

where H_a is the total number of active compounds in the hit list, H_t is the number of hits retrieved from the database, A is the total number of active compounds in the database, and D is the total number of molecules in the database.

Virtual screening

Pharmacophore-based database searching was used to find potential hit compounds that could repress or trigger BChE activity. The generated, well-validated hypothesis was used as a 3D structural query in the virtual screening of databases such as Maybridge and Chembridge to retrieve novel scaffolds for BChE inhibition. The *Fast Flexible* search method from *Ligand Pharmacophore Mapping/DS* was applied to retrieve hits that satisfy the chemical moiety requirements and spatially map with corresponding features in the pharmacophoric query^[37].

Drug likeness filtration

Poor pharmacokinetic properties are one of the main causes for the termination of a compound's entry or progression along the drug development pipeline. The medicinal chemist needs compounds with good pharmacokinetic properties; thus, all of the hit compounds obtained from database searching were filtered by applying ADME and the Rule of Five developed by Lipinski^[38]. To obtain compounds with good pharmacokinetic properties, ADMET descriptors were calculated. ADMET was applied to check whether the compounds are able to cross the blood-brain barrier (BBB) and have good solubility, human intestinal absorption (HIA), and low toxicity. Here, we mainly focused on oral bioavailability, low or no hepatotoxicity, and the capacity to penetrate the BBB, which is a key decision filter for central nervous system drug discovery. The compounds that satisfied the abovementioned properties were selected for molecular docking studies. Lipinski's rule of 5 states that $\text{clogP} \leq 5$, molecular weight ≤ 500 , and number of hydrogen bond acceptors ≤ 10 and donors ≤ 5 . Compounds violating more than one of these rules may have problems with bioavailability, therefore these parameters were calculated by DS to eliminate compounds that did not pass the above criterias.

Molecular docking

Molecular docking generates a score for each compound based on the binding affinities of protein-ligand complexes. Molecular docking was used to identify the small molecules that were able to fit well into the binding site of BChE proteins. *Ligand-Fit*^[39] was used to execute the molecular docking studies and to determine the accurate orientation of ligands in protein active sites. The *LigandFit* module was classified into three stages: (i) docking, when an attempt was made to dock a ligand into a user defined binding site; (ii) *in situ* ligand minimization; and (iii) scoring, when various scoring functions were calculated for each pose of the ligands. The 3D crystal structure of BChE (PDB code: 1P0I) was downloaded from Protein Data Bank

(PDB, www.rcsb.org) with good resolution (2 Å). The protein was prepared by adding the hydrogen atoms by applying CHARMM force field^[40] using the *Molecular simulation* module. After protein preparation, the active site of the protein must be identified before docking the small molecules. The active site of the protein can be represented as a binding site, essentially as a set of points on a grid that lie in a cavity. Two methods were applied to define the binding site for the protein: (i) based on the receptor shape using "eraser" algorithm and (ii) volume occupied by the known ligand position already in an active site. For this study, we preferred the second method to find the active cavity of BChE. Initially, the docking parameters were validated by docking the co-crystal molecule into the active site of BChE. The hit molecules from the virtual screening process and 5 active inhibitors were docked in the active site of BChE to find the most suitable orientation and compound binding ability. During the docking process, the top 10 conformations were generated for each ligand based on the docking score after energy minimization using the smart minimizer method, which begins with the steepest descent method followed by the conjugate gradient method. The docked poses were validated by the hydrogen bond interactions between the candidate molecules and active site residues.

Density functional theory

The main aim of the orbital energies calculation was to provide valuable information about the electrostatic properties of the BChE inhibitors. DFT is a successful and promising approach adopted by quantum chemists in the quantum mechanical simulation of periodic systems^[41]. There is substantial evidence that DFT provides an accurate description of the electronic and structural properties of small molecules by computing the electronic structure of matter. The selected docked poses of the hit compounds from the molecular docking studies were used as input for the DFT instead of the compounds' bioactive conformations. Because the docking results showed the suitable binding orientation of hit compounds, it was suitable for calculating the orbital energies such as HOMO and LUMO using DS. Calculating the orbital energy using B3LYP provided information regarding the capacity of the molecules to transfer their energies from a HOMO, which can act as an electron donor, to a LUMO, which can act as an electron acceptor. These electrostatic property calculations could provide useful information for designing novel BChE inhibitors.

Results and discussion

A ligand-based pharmacophore method was used to elucidate the spatial arrangement of chemical features that were crucial for the interaction of structurally diverse and potent BChE inhibitors with their target protein. Ligand-based approaches reveal the important and common chemical features of diverse ligands, and these features can then be used as 3D query in virtual screenings of large chemical databases to identify novel hit compounds.

Pharmacophore model

The HypoGen algorithm was used to construct quantitative hypotheses that correlated the experimental and the predicted activity values of the inhibitors. At the end of each run, the top ten hypotheses were generated based on a set of 26 chemically diverse inhibitors of BChE (Figure 1), and the statistical parameters values such as cost, correlation (r), and RMS for each hypothesis are shown in Table 1.

Among the ten hypotheses, nine hypotheses contained 1 hydrogen bond acceptor (HBA) and 1 hydrophobic aliphatic (Hy-Ali) group, which indicates that these chemical features are necessary for BChE inhibition. Out of the 10 hypotheses, only 3 hypotheses were selected for further processing based on the maximum fit value (greater than 9). Debnath's analysis^[42], used to select the best hypothesis, states that the best pharmacophore model should have the highest cost difference, good correlation coefficient, least RMS, and lowest total cost values. Cost differences represent the difference between the null and total cost of hypothesis. A 40–60 bit difference leads to a predictive correlation probability of 75%–90%, and if the difference is greater than 60 bits, the hypothesis is assumed to have a correlation probability of greater than 90%^[31]. Hypo1 showed the highest cost difference of 120.12 bits, compared with Hypo4 and Hypo5, indicating its significance. The correlation coefficient is based on linear regression derived from the geometric fit index; Hypo1 showed the highest correlation coefficient (0.96), demonstrating its high predictive ability. The RMS factor represents the deviation of the predicted activity value from the experimental value, and the RMS values were 1.02, 1.23, and 1.24 for Hypo1, Hypo4, and Hypo5, respectively. This result also supports the conclusion that Hypo1 was significant when compared with the two other hypotheses. The reliability of a pharmacophore model also depends on whether the total cost value is distant from the null cost and close to the fixed cost. The fixed cost represents a simple model that fits all data perfectly, while the null cost presumes that there is no relationship in the data and that the

experimental activities are normally distributed around their average value. The fixed and total cost values of Hypo1 were 94.82 and 108.57, respectively. Thus, Hypo1, which consisted of 2 HBA, 1 Hy-Ali, and 1 hydrophobic aromatic (Hy-Ar), was selected as the best hypothesis and was employed for further analyses. The chemical features and 3D spatial arrangement of Hypo1 are depicted in Figure 2.

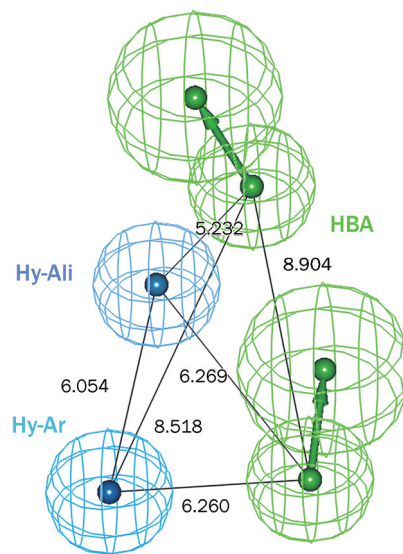


Figure 2. The Hypo1 pharmacophore model and its geometric parameters, where HBA: hydrogen bond acceptor; Hy-Ali: hydrophobic aliphatic; and Hy-Ar: hydrophobic aromatic.

Hypo1 was used to estimate the inhibitory activities of 26 training set compounds to elucidate its predictive accuracy. Hypo1 was able to predict the inhibitory activity value of the 26 training set compounds in the same order of magnitude (Table 2). One moderately active and two inactive compounds

Table 1. Information of statistical significance and predictive power presented in cost values measured in bits for the top 10 hypotheses as a result of automated 3D QSAR pharmacophore generation.

Hypo No	Total cost	Cost difference ^a	RMS ^b	Correlation	Features ^b	Max fit
Hypo1	105.72	120.12	1.01	0.96	2 HBA, 1 Hy-Ali, 1 Hy-Ar	8.58
Hypo2	103.93	116.91	1.10	0.95	2 HBA, 1 Hy-Ali, 1 RA	9.54
Hypo3	109.97	115.87	1.15	0.94	2 HBA, 1 Hy-Ali, 1 Hy-Ar	8.85
Hypo4	112.57	113.27	1.23	0.93	2 HBA, 1 Hy-Ali, 1 RA	9.18
Hypo5	112.98	112.86	1.24	0.93	2 HBA, 1 Hy-Ali, 1 RA	9.48
Hypo6	116.06	109.78	1.34	0.92	2 HBA, 1 Hy-Ali, 1 RA	7.25
Hypo7	117.41	108.43	1.38	0.91	2 HBA, 1 Hy-Ali, 1 RA	7.28
Hypo8	117.43	108.41	1.39	0.91	2 HBA, 1 Hy-Ali, 1 Hy-Ar	7.86
Hypo9	118.78	107.06	1.42	0.91	2 HBA, 1 Hy-Ali, 1 RA	7.50
Hypo10	118.82	107.02	1.43	0.91	2 HBA, 2 Hy-Ar	7.86

^a Cost difference between the null and the total cost. The null cost, the fixed cost and the configuration cost are 225.84, 92.399 and 15.79, respectively.

^b Abbreviation used for features: RMS, root mean square deviation; HBA, hydrogen bond acceptor; Hy-Ali, hydrophobic aliphatic, Hy-Ar, hydrophobic aromatic and RA, ring aromatic.

Table 2. Actual and estimated activity of the training set molecules based on the pharmacophore model Hypo1.

Compound No	Fit value ^a	Exp IC ₅₀ nmol/L	Pred IC ₅₀ nmol/L	Error ^b	Exp scale ^c	Pred scale ^c
1	6.89	3.6	5.5	+1.5	+++	+++
2	6.38	7.8	18	+2.3	+++	+++
3	6.28	10	22	+2.2	+++	+++
4	6.36	21	19	-1.1	+++	+++
5	6.22	22	26	+1.2	+++	+++
6	6.08	23	36	+1.6	+++	+++
7	6.11	25	33	+1.3	+++	+++
8	6.31	26	21	-1.2	+++	+++
9	6.39	29	18	-1.7	+++	+++
10	6.12	34	33	-1.0	+++	+++
11	6.16	56	30	-1.9	+++	+++
12	6.3	76	21	-3.5	+++	+++
13	4.85	250	600	+2.4	++	++
14	4.75	490	760	+1.5	++	++
15	4.25	610	2400	+3.9	++	+
16	4.85	650	600	-1.1	++	++
17	4.62	800	1000	+1.3	++	++
18	4.9	900	540	-1.7	++	++
19	4.55	1200	1200	+1.0	+	+
20	4.01	1600	4200	+2.6	+	+
21	4.72	1800	810	-2.2	+	++
22	3.94	1800	810	-2.2	+	++
22	3.94	3000	5000	+1.7	+	+
23	4.29	3900	2200	-1.8	+	+
24	4.01	5700	4200	-1.3	+	+
25	4.09	7100	3500	-2.1	+	+
26	4.28	11000	2200	-5.1	+	+

^a Fit value indicates how well the features in the pharmacophore overlap the chemical features in the molecule.

^b Division of higher value of experimental or predicted IC₅₀ by lower predicted or experimental IC₅₀ value. '+' indicates that the predicted IC₅₀ is higher than the experimental IC₅₀; '-' indicates that the predicted IC₅₀ is lower than the experimental IC₅₀; a value of 1 indicates that the predicted IC₅₀ is equal to the experimental IC₅₀.

^c Activity scale: IC₅₀<100 nmol/L=+++ (highly active); 100 nmol/L≤IC₅₀<1000 nmol/L=++ (moderately active); IC₅₀≥10000 nmol/L=+ (low active).

were underestimated and overestimated as inactive and moderately active, respectively. All of the active compounds were predicted in their own activity ranges, indicating the predictive ability of Hypo1. Hypo1 aligned with the most active compound 1 (IC₅₀: 3.6 nmol/L) and least active compound 26 (IC₅₀: 11400 nmol/L) in the training set (Figure 3). From this analysis, we suggest that Hypo1 was able to estimate the activity of compounds to a high degree of accuracy relative to their experimental IC₅₀ values (Table 2). The error value was defined as the ratio between experimental and predicted activity value, and Hypo1 demonstrated remarkable consistency. The best pharmacophore model, Hypo1, was validated by various methods such as Fisher's randomization, a test set, and a decoy set to demonstrate its robustness and

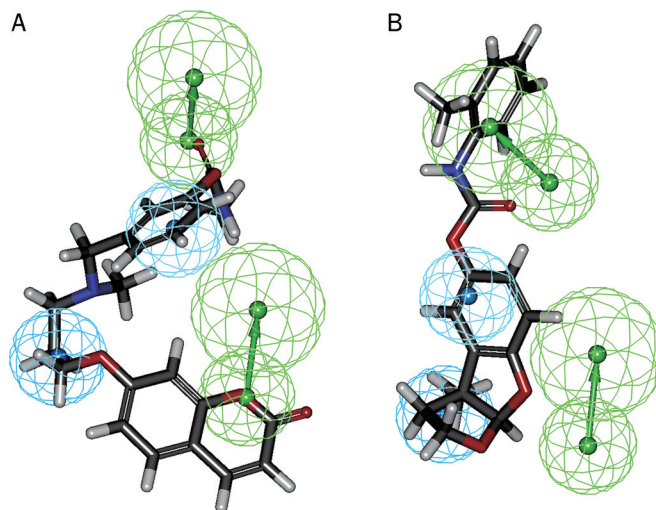


Figure 3. The best pharmacophore model Hypo1 aligned to training set compounds: A) active compound 1 (IC₅₀ 3.6 nmol/L) and B) low activity compound 26 (IC₅₀ 11400 nmol/L). The pharmacophore features are color coded (HBA, hydrogen bond acceptor: green; Hy-Ali, hydrophobic aliphatic: light cyan; Hy-Ar, hydrophobic aromatic: cyan).

statistical significance.

Validation of the pharmacophore model

Fischer's randomization test

Fischer's test was applied to evaluate the significance of Hypo1 based on statistical validation. A confidence level of 95% was chosen, and a total of 19 random spreadsheets were generated to produce the hypothesis. The significance of the hypothesis was calculated using the formula $S = \frac{1 - (1 + X) / Y}{1} \times 100$, where X is the total number of hypotheses having a total cost lower than the original hypothesis, and Y is the total number of HypoGen runs (initial+random runs). Here, X=0 and Y=(1+19), hence $95\% = \frac{1 - (1 + 0) / (19 + 1)}{1} \times 100$. The total cost of 19 random pharmacophore models compared with Hypo1 showed that the original hypothesis was far superior to the 19 other hypotheses, which indicated that the Hypo1 was not generated by chance (Figure 4). This result provided confidence that the Hypo1 could be a best hypothesis that contains all the necessary chemical features to inhibit BChE activity.

Test set validation

The test set contains 45 structurally distinct compounds from training set molecules. The test set was used to examine the ability of Hypo1 to predict the activity of external compounds in the same activity range. Except for one active compound that was underestimated as moderately active, all of the remaining compounds are predicted on their own activity range by Hypo1 (Table 3). Hypo1 shows the strong correlation coefficient of 0.94 between experimental and predicted BChE inhibitory activity values for the test set (Figure 5). This result also showed that Hypo1 fit not only for the training set compounds but also for the external compounds; this result

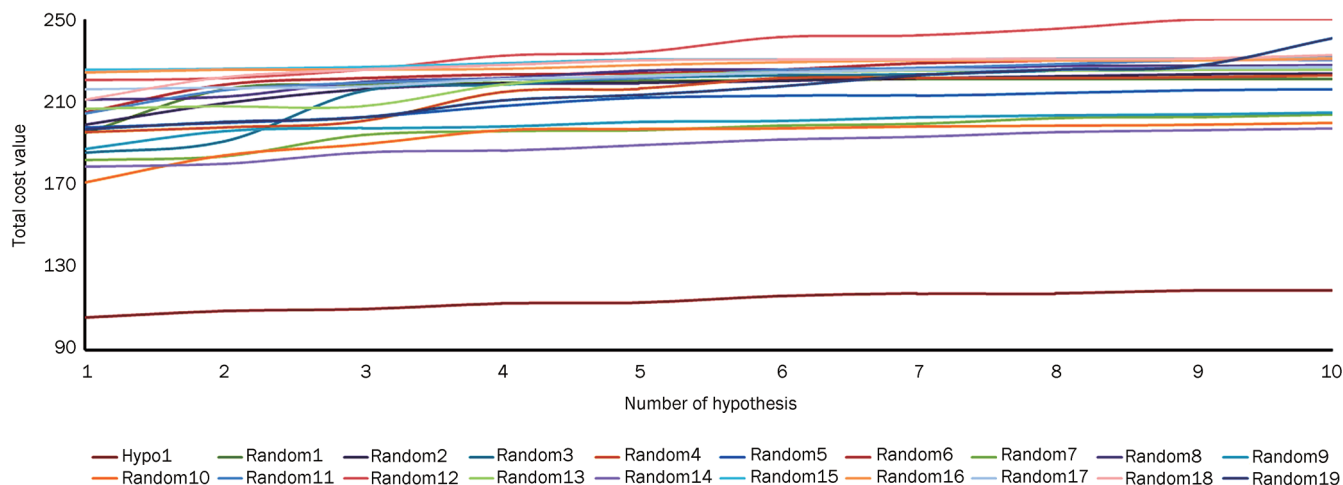


Figure 4. The difference in cost between 19 scrambled runs. The 95% confidence level was selected.

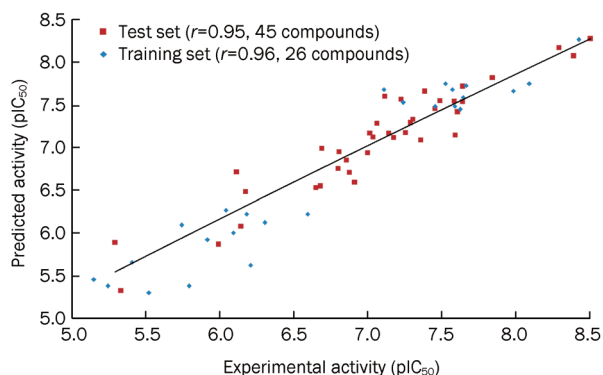


Figure 5. Plot of the correlation between the experimental activity and the activity predicted by Hypo1 for the test set molecules (in brown) and training set molecules (in blue).

also demonstrated the predictive ability of Hypo1 to differentiate the active and inactive BChE inhibitors.

Decoy set validation

As a final validation, decoy set screening was performed using the *Best Flexible* searching module/DS. To determine the robustness of Hypo1, four parameters were calculated: false positives, false negatives, enrichment factor (EF), and goodness of fit score (GF). EF and GF were calculated using the following set of parameters: hit lists (H_i), number of active percent yields (%Y), percent ratio of actives in the hit lists (%A), false negatives, and false positives (Table 4). Hypo1 succeeded in the retrieval of 76% of the active compounds from the decoy set. It predicted 6 active compounds to be inactive compounds (false negatives). Hypo1 showed a GH score of 0.86, indicating that Hypo1 had a greater tendency to show true positives. On the basis of the overall validations, we were strongly assured that the Hypo1 demonstrated excellent prediction of BChE inhibitor activities.

Virtual screening

The validated hypothesis, Hypo1, was used as a 3D structural query for retrieving novel candidate molecules from the Maybridge (60 000) and Chembridge (50 000) chemical databases. A total of 45 496 hit compounds were obtained from the first screening; among these, 1619 compounds were selected for further analysis by applying maximum fit value of greater than 8. Subsequently, these molecules were tested for ADMET and Lipinski's Rule of Five. ADMET properties calculated the values of blood-brain barrier (BBB) penetration, solubility, cytochrome P450 (CYP450) 2D6 inhibition, hepatotoxicity, HIA, plasma protein binding (PPB), and assessed a broad range of ligand toxicity. The drug should not cross the BBB, hence the level '3' was selected to represent low penetration of BBB. The value of 0 in CYP26 and hepatotoxicity indicates that the molecules are of low toxicity. The cutoff values of solubility and HIA were 3 and 0, respectively. Out of the 1619 molecules, 202 molecules passed the BBB level, absorption, solubility, and toxicity criteria. These hit compounds were subjected to further filtering by applying Lipinski's Rule of Five, which states that LogP should be less than 5, the molecular weight less than 500, the number of hydrogen bond donors less than 5, the number of hydrogen bond acceptors less than 10, and the number of rotatable bonds less than 10. The flexibility of the molecules and the total number of hydrogen bond acceptors and hydrogen bond donors are important predictors that a compound will have good oral bioavailability. Ultimately, 84 molecules were selected as hits based on drug-like properties. The hit compounds from the virtual screening process were subjected to molecular docking to reduce the false positive rate.

Molecular docking

A BChE complex with butanoic acid from PDB was chosen as the target protein for molecular docking. The establishment and reorganization of specific covalent or non-covalent

Table 3. Experimental and predicted IC₅₀ values of 45 test set molecules against Hypo1.

Compound No	Structure	Fit value	Exp IC ₅₀ (nmol/L)	Pred IC ₅₀ (nmol/L)	Error ^a	Exp Scale ^b	Pred Scale ^b
1		6.90	3.0	5.34	+1.78	+++	+++
2		6.36	3.3	8.51	+2.58	+++	+++
3		6.36	3.9	8.51	+2.18	+++	+++
4		6.07	4.9	6.85	+1.40	+++	+++
5		6.07	5.0	6.85	+1.37	+++	+++
6		5.93	13.9	15.31	+1.10	+++	+++
7		5.35	22.1	19.34	-1.14	+++	+++
8		6.05	24.0	38.57	+1.61	+++	+++
9		5.73	24.5	29.42	1.20	+++	+++
10		5.77	24.8	72.32	+2.92	+++	+++
11		6.69	25.2	28.84	+1.14	+++	+++
12		6.69	28.0	28.84	+1.03	+++	+++
13		5.17	31.0	29.62	-1.05	+++	+++
14		5.17	31.6	28.62	-1.10	+++	+++
15		7.08	34.1	35.36	+1.04	+++	+++

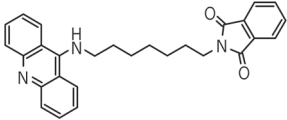
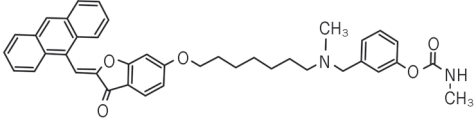
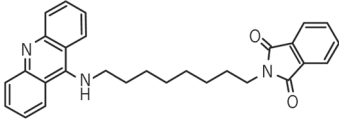
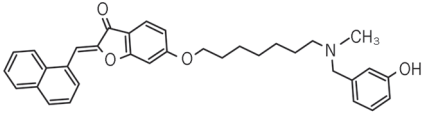
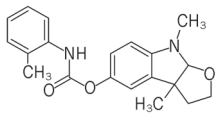
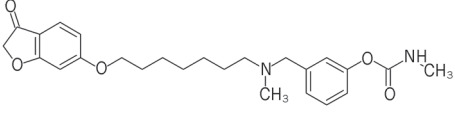
(to be continued)

Compound No	Structure	Fit value	Exp IC ₅₀ (nmol/L)	Pred IC ₅₀ (nmol/L)	Error ^a	Exp Scale ^b	Pred Scale ^b
16		5.33	40.0	22.05	-1.81	+++	+++
17		5.71	42.6	82.64	+1.94	+++	+++
18		5.71	44.3	82.64	+1.87	+++	+++
19		5.96	48.3	47.38	-1.02	+++	+++
20		5.92	50.0	51.57	+1.03	+++	+++
21		5.80	54.0	67.56	+1.25	+++	+++
22		5.96	54.6	47.38	-1.15	+++	+++
23		6.19	57.9	27.49	-2.11	+++	+++
24		5.75	65.0	76.99	-1.18	+++	+++
25		5.79	70.3	68.81	-1.02	+++	+++
26		5.28	74.8	25.39	-2.95	+++	+++
27		5.91	84.4	52.36	-1.61	+++	+++

(to be continued)

Compound No	Structure	Fit value	Exp IC ₅₀ (nmol/L)	Pred IC ₅₀ (nmol/L)	Error ^a	Exp Scale ^b	Pred Scale ^b
28		5.75	90	75.87	-1.19	+++	+++
29		5.30	98	115.96	+1.18	+++	++
30		5.22	120	257.32	+2.14	++	++
31		4.93	130	198.69	+1.53	++	++
32		5.10	136	142.40	+1.05	++	++
33		5.58	153	113.40	-1.35	++	++
34		5.74	155	178.64	+1.15	++	++
35		5.62	200	103.15	-1.94	++	++
36		5.70	205	284.84	+1.39	++	++
37		5.16	220	299.54	+1.36	++	++
38		5.70	237	244.84	+1.03	++	++
39		5.11	660	330.68	-2	++	++

(to be continued)

Compound No	Structure	Fit value	Exp IC ₅₀ (nmol/L)	Pred IC ₅₀ (nmol/L)	Error ^a	Exp Scale ^b	Pred Scale ^b
40		4.95	711	841	+1.18	++	++
41		4.35	761	194.74	-3.91	++	++
42		5.07	1010	1362.10	+1.35	+	+
43		4.74	4650	4776.95	+1.03	+	+
44		3.62	5100	1298.10	-3.93	+	+
45		3.59	11400	10400	-1.09	+	+

^a '+' indicates that the predicted IC₅₀ is higher than the experimental IC₅₀; '-' indicates that the predicted IC₅₀ is lower than the experimental IC₅₀; a value of 1 indicates that the predicted IC₅₀ is equal to the experimental IC₅₀.

^b Activity scale : IC₅₀<100 nmol/L=+++ (highly active); 100 nmol/L ≤ IC₅₀<1000 nmol/L=++ (moderately active); IC₅₀ ≥ 1000 nmol/L=+ (low active).

Table 4. Statistical parameter from screening test set molecules.

No	Parameter	Values
1	Total number of molecules in database (D)	2100
2	Total number of actives in database (A)	25
3	Total number of hit molecules from the database (Ht)	21
4	Total number of active molecules in hit list (Ha)	19
5	% Yield of active [(Ha/Ht) X 100]	90.47
6	% Ratio of actives [(Ha/A) X 100]	76
7	Enrichment Factor (EF)	76
8	False negatives (A-Ha)	6
9	False Positives (H _t -H _a)	2
10	Goodness of fit score (GF)	0.87

interactions between substrates or inhibitors play a crucial role in biological function. Three distinct domains in the active site confer selectivity of BChE inhibitors. The first domain is an acyl binding pocket that contains two residues (L286 and V288) responsible for the binding of larger substrates with

acyl groups^[43]. A second domain is found near the lip of the active site cavity, and a third domain is defined as the choline binding site (or cation-π site). The catalytic domain of BChE is composed of nucleophilic serine, histidine, and glutamate residues. The substrate was stabilized between the oxyanion hole and acyl binding pocket of the "catalytic triad" composed of S198, E197, and H438 of the active esteratic site. The mechanism of catalysis depends on the charge relay system, in which the imidazole ring of H438 relays electrons from E197 to S198 and causes the hydroxyl oxygen of S198 to become a nucleophile^[44]. A nucleophilic attack of this hydroxyl oxygen on the ester bond of the substrate leads to an acyl-enzyme intermediate and a free choline moiety. Then, the acyl group is hydrolyzed from S198 by the nucleophilic attack of a water molecule that is activated by taking a proton from H438 to form a catalytic triad.

Initially the co-crystal was docked in the active site of BChE to check whether the selected parameters are able to produce the most suitable binding orientation. The RMSD value of 0.79 Å was obtained when the best docked pose overlapped with the co-crystal, which revealed that the default parameters

are valid to find the best orientation of BChE in the active site. The same parameters were therefore employed to dock the candidate compounds. The selected candidate molecules from the virtual screening were docked in the BChE active site. The top-ranked 84 compounds based on the docking score were selected as the best potential inhibitors and were manually validated for critical interaction with vital amino acids in the active site of BChE. Intermolecular hydrogen bonding was observed between active residues S198, E197, and H438 in the active site of BChE (Figure 6). From the 84 compounds, 33 candidate molecules showed hydrogen bond interactions with S198 and H438, as well as reliable hydrophobic interactions with Y323 and F329.

Density functional theory

The orbital energies such as HOMO (highest occupied molecular orbital) and LUMO (lowest unoccupied molecular orbital) were calculated for 7 (5 active, one moderate and one inactive inhibitor) training set compounds and for the 33 hits from molecular docking. HOMO and LUMO are responsible for the charge transfer in a chemical reaction^[45]. The calculated orbital energies of the 33 hits and known inhibitors were compared to analyze the energy transfer and stability of small molecules in protein active site. Comparing the HOMO energy with the activity value of known BChE inhibitors shows an inverse correlation, indicating that the HOMO energy of the inhibitor may transfer its electrons to some critical residues in the active site of BChE. The highest energy value of the HOMO in the hit compounds implied the greatest likelihood of strong inhibition of BChE. Hence, correlation of the HOMO values of hits and the training set molecules showed that 10 hit compounds possessed greater values than the reported inhibitors (training set) of BChE (Table 5). A smaller energy gap (between the LUMO and HOMO) of the hit molecules illustrates that the molecule are more reactive^[46]. The wide energy gap in the hit

Table 5. Orbital energy value of hit leads and training set compounds.

Name	HOMO	LUMO	ΔE (eV)	IC ₅₀ (nmol/L)
SPB_07954	-8.31	-0.99	7.31	
Compound_Number_30238	-8.32	-0.23	8.08	
RJC_03502	-8.55	-0.44	8.11	
Compound_Number_14811	-8.62	-0.46	8.16	
BTB_07807	-8.65	-0.96	7.69	
Compound_Number_30080	-8.65	-1.19	7.46	
KM_03101	-8.69	-0.67	8.01	
KM_02281	-8.70	-0.94	7.76	
Compound_Number_15687	-8.76	-0.33	8.43	
Compound_Number_23227	-8.76	-0.97	7.79	
Training 1	-8.77	-0.89	7.89	3.6
Training 4	-8.80	-0.70	8.09	21
Training 5	-8.80	-0.10	8.70	22
Training 7	-8.92	-0.22	8.69	24.8
Training 8	-8.98	-0.78	8.21	26
Training 17	-9.18	-0.34	8.84	800
Training 26	-9.12	-0.28	8.83	11400

molecules is unfavorable for the electron to be excited from the HOMO to the LUMO, which consequently leads to a weak affinity of the inhibitor for BChE. Among the 10 compounds, 5 hit compounds (Figure 7) were selected based on their lowest energy gaps that suggested the molecules would be reactive. Table 5 clearly showed that the moderate and inactive compounds had high energy gaps that were not suitable for the reactivity of the molecules. The atomic orbital composition of the frontier molecular orbital for compound 30080 is shown in Figure 8. On the basis of the results above, we suggest that the hit compounds may possess equivalent or greater electronic properties compared with most active compounds and could

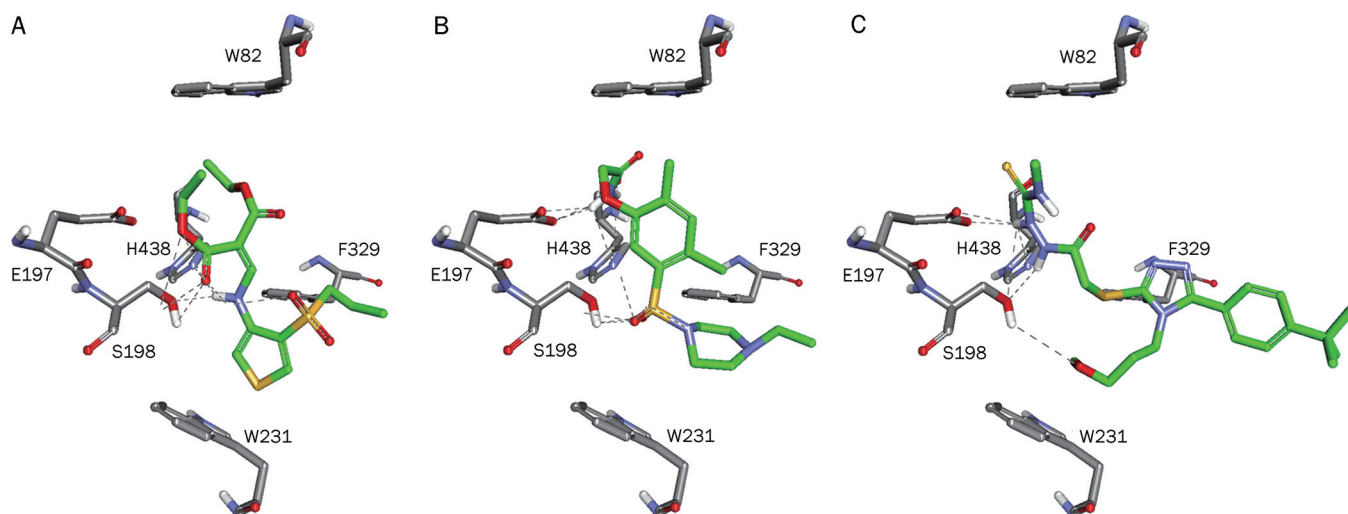


Figure 6. (A) Chembridge (compound 30080), (B) Maybridge (KM_02281), and (C) Maybridge (SPB_07954). The candidate compounds are represented as green sticks. Hydrogen bonds are shown in black. For the clarity of the docked view the Y323 was not shown.

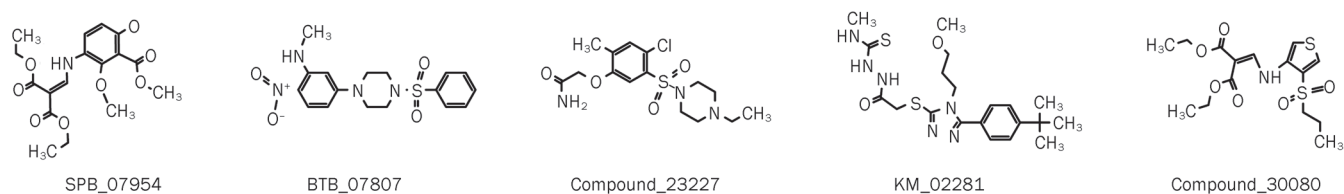


Figure 7. A 2D representation of the final 5 hit compounds.

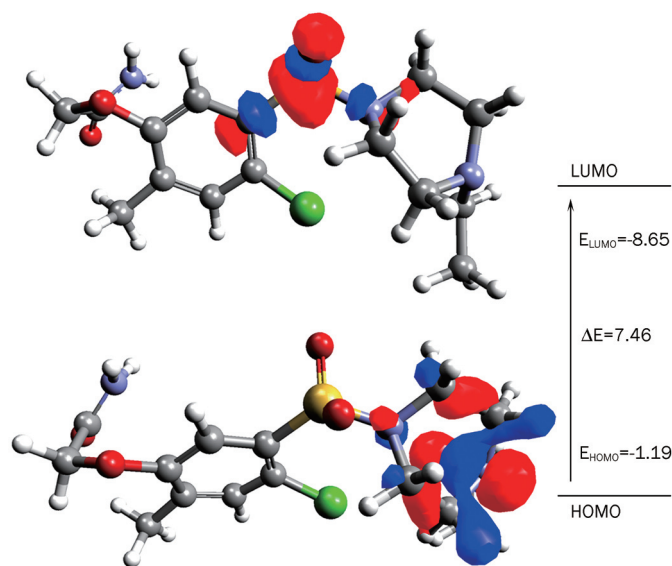


Figure 8. The orbital energy values and energy gap for compound 30080.

be used to design novel classes of BChE inhibitors.

Conclusions

In this study, pharmacophore models were generated based on a series of known BChE inhibitors. The main purpose of quantitative pharmacophore generation is to predict or differentiate the active inhibitors from inactive compounds. The best pharmacophore model, Hypo1, consisting of 2 HBA, 1 Hy-Ali, and 1 Hy-Ar, was validated by Fischer's randomization method, a test set, and decoy set. Fischer's method confirmed the 95% statistical confidence of Hypo1; the test set showed a fairly high correlation between experimental and predicted IC_{50} values (correlation coefficient of 0.96), indicating satisfactory predictive ability; additionally, good EF (0.76) and GF (0.87) values for Hypo1 were calculated from the decoy set. The three validation methods confirmed that Hypo1 was the best hypothesis to differentiate the active inhibitors from inactive inhibitors of BChE. Thus, Hypo1 was used as a 3D query to screen molecular structural libraries, including the Maybridge and Chembridge databases. The hit compounds were filtered using ADMET, Lipinski's Rule of Five, and molecular docking to reduce the number of false positive results. Finally, 33 compounds were selected based on their critical interactions with the significant amino acids in BChE's active site. To confirm

the inhibitors' potencies, we calculated the orbital energies, such as HOMO and LUMO, for hit compounds and 7 training set compounds. From among the 33 hit compounds, 10 compounds with the highest HOMO values were selected, and this set was further culled to 5 compounds based on their energy gaps, which is important for stability and energy transfer. From the overall results, we confirmed that 5 hit compounds satisfied all the pharmacophoric features in Hypo1 and are potential BChE inhibitors.

Acknowledgements

This research was supported by the Basic Science Research Program (2009-0073267), the Pioneer Research Center Program (2009-0081539), and the Management of Climate Change Program (2010-0029084) through the National Research Foundation of Korea (NRF) funded by the Ministry of Education, Science, and Technology (MEST) of the Republic of Korea. This work was also supported by the Next-Generation BioGreen21 Program (PJ008038) from the Rural Development Administration (RDA) of the Republic of Korea.

Author contribution

Sugunadevi SAKKIAH contributed to all parts of the work, including experimental design, conduct, and analysis, and preparation of the manuscript. Prof Keun Woo LEE analyzed the results.

References

- Massoulié J, Sussman J, Bon S, Silman I. Chapter 15: Structure and functions of acetylcholinesterase and butyrylcholinesterase. In: Cuellio AC editor. *Progress in Brain Research*; Elsevier; 1993. p 139–46.
- Sun H, El Yazal J, Lockridge O, Schopfer LM, Brimijoin S, Pang YP. Predicted michaelis-menten complexes of cocaine-butrylcholinesterase. *J Biol Chem* 2001; 276: 9330–6.
- Massoulié J, Pezzementi L, Bon S, Krejci E, Vallette FM. Molecular and cellular biology of cholinesterases. *Prog Neurobiol* 1993; 41: 31–91.
- Valle AM, Radić Z, Rana BK, Whitfield JB, O'Connor DT, Martin NG, *et al*. The cholinesterases: Analysis by pharmacogenomics in man. *Chem Biol Interact* 2008; 175: 343–45.
- Quinn DM. Acetylcholinesterase: enzyme structure, reaction dynamics, and virtual transition states. *Chem Rev* 1987; 87: 955–79.
- Li B, Sedlacek M, Manoharan I, Boopathy R, Duysen EG, Masson P, *et al*. Butyrylcholinesterase, paraoxonase, and albumin esterase, but not carboxylesterase, are present in human plasma. *Biochem Pharmacol* 2005; 70: 1673–84.

- 7 Satoh T, Hosokawa M. Structure, function and regulation of carboxylesterases. *Chem Biol Interact* 2006; 162: 195–211.
- 8 Duysen EG, Li B, Darvesh S, Lockridge O. Sensitivity of butyrylcholinesterase knockout mice to (–)-huperzine A and donepezil suggests humans with butyrylcholinesterase deficiency may not tolerate these Alzheimer's disease drugs and indicates butyrylcholinesterase function in neurotransmission. *Toxicology* 2007; 233: 60–69.
- 9 Gardiner SJ, Begg EJ. Pharmacogenetics, drug-metabolizing enzymes, and clinical practice. *Pharm Rev* 2006; 58: 521–90.
- 10 Doctor BP, Saxena A. Bioscavengers for the protection of humans against organophosphate toxicity. *Chem Biol Interact* 2005; 157–158: 167–71.
- 11 Masson P, Froment MT, Gillon E, Nachon F, Darvesh S, Schopfer LM. Kinetic analysis of butyrylcholinesterase-catalyzed hydrolysis of acetanilides. *Biochim Biophys Acta* 2007; 1774: 1139–47.
- 12 Vitorovic-Todorovic MD, Juranic IO, Mandic LM, Drakulic BJ. 4-Aryl-4-oxo-N-phenyl-2-aminylbutyramides as acetyl- and butyrylcholinesterase inhibitors. Preparation, anticholinesterase activity, docking study, and 3D structure-activity relationship based on molecular interaction fields. *Bioorg Med Chem* 2010; 18: 1181–93.
- 13 Burgen AS. The mechanism of action of anticholinesterase drugs. *Pharmac Ther* 1979; 6: 579–628.
- 14 Mesulam MM, Guillozet A, Shaw P, Levey A, Duysen EG, Lockridge O. Acetylcholinesterase knockouts establish central cholinergic pathways and can use butyrylcholinesterase to hydrolyze acetylcholine. *Neuroscience* 2002; 110: 627–39.
- 15 Li B, Stribley JA, Ticu A, Xie W, Schopfer LM, Hammond P, *et al*. Abundant tissue butyrylcholinesterase and its possible function in the acetylcholinesterase knockout mouse. *J Neurochem* 2000; 75: 1320–31.
- 16 Jhee SS, Shiovitz T, Hartman RD, Messina J, Anand R, Sramek J, Cutler NR, *et al*. Centrally acting antiemetics mitigate nausea and vomiting in patients with Alzheimer's disease who receive rivastigmine. *Neuropharmacology* 2002; 25: 122.
- 17 Perry EK, Perry RH, Blessed G, Tomlinson BE. Changes in brain cholinesterases in senile dementia of Alzheimer type. *Neuropathol Appl Neurobiol* 1978; 4: 273–7.
- 18 Geula C, Nagykerly N. Butyrylcholinesterase activity in the rat forebrain and upper brainstem: postnatal development and adult distribution. *Exp Neurol* 2007; 204: 640–57.
- 19 Mehrani H. Protective effect of polyurethane immobilized human butyrylcholinesterase against parathion inhalation in rat. *Environmental Toxicol Pharmacol* 2004; 16: 179–85.
- 20 Schumacher I, Arad A, Margalit R. Butyrylcholinesterase formulated in liposomes. *Biotechnol Appl Biochem* 1999; 30: 225–30.
- 21 Lockridge O, Bartels CF, Vaughan TA, Wong CK, Norton SE, Johnson LL. Complete amino acid sequence of human serum cholinesterase. *J Biol Chem* 1987; 262: 549–57.
- 22 Nicolet Y, Lockridge O, Masson P, Fontecilla-Camps, Nachon F. Crystal structure of human butyrylcholinesterase and of its complexes with substrate and products. *J Biol Chem* 2003; 278: 41141–7.
- 23 Altamirano CV, Lockridge O. Association of tetramers of human butyrylcholinesterase is mediated by conserved aromatic residues of the carboxy terminus. *Chem Biol Interact* 1999; 120: 53–60.
- 24 Mack A, Robitzki A. The key role of butyrylcholinesterase during neurogenesis and neural disorders: an antisense-5' butyrylcholinesterase-DNA study. *Prog Neurobiol* 2000; 60: 607–28.
- 25 Darvesh S, Hopkins DA, Geula C. Neurobiology of butyrylcholinesterase [10.1038/nrn1035]. *Nat Rev Neurosci* 2003; 4: 131–8.
- 26 Guillozet AI, Smiley JF, Mash DC, Mesulam MM. Butyrylcholinesterase in the life cycle of amyloid plaques. *Ann Neurol* 1997; 42: 909–18.
- 27 Giacobini E. Cholinesterases: New roles in brain function and in Alzheimer's disease. *Neurochem Res* 2003; 28: 515–22.
- 28 Bisi A, Belluti F, Gobbi S, Valenti P, Andrisano V, Cavrini V, *et al*. Acetylcholinesterase inhibitors for potential use in Alzheimer's disease: molecular modeling, synthesis and kinetic evaluation of 11H-indeno-[1,2-b]-quinolin-10-ylamine derivatives. *Bioorg Med Chem* 2000; 8: 497–506.
- 29 Wadkins RM, Tsurkan L, Hicks LD, Hatfield MJ, Edwards CC, Ross CR 2nd, *et al*. Planarity and constraint of the carbonyl groups in 1,2-diones are determinants for selective inhibition of human carboxylesterase 1. *J Med Chem* 2007; 50: 5727–34.
- 30 Moak T, Hatfield MJ, Tsurkan L, Edwards CC, Wierdl M, Danks MK, *et al*. Selective inhibition of carboxylesterases by isatins, indole-2,3-diones. *J Med Chem* 2007; 50: 1876–85.
- 31 Luo W, Yu QS, Kulkarni SS, Parrish DA, Holloway HW, Tweedie D, *et al*. Inhibition of human acetyl- and butyrylcholinesterase by novel carbamates of (–) and (+)-tetrahydrofurobenzofuran and methanobenzodioxepine. *J Med Chem* 2006; 49: 2174–85.
- 32 Fernandez-Bachiller MI, Perez C, Hernandez-Ledesma B, Bartolome B, Novel tacrine-melatonin hybrids as dual-acting drugs for Alzheimer disease, with improved acetylcholinesterase inhibitory and antioxidant properties. *J Med Chem* 2006; 49: 459–62.
- 33 Sakkiah S, Thangapandian S, John S, Kwon YJ, Lee KW. 3D QSAR pharmacophore based virtual screening and molecular docking for identification of potential HSP90 inhibitors. *Eur J Med Chem* 2010; 45: 2132–40.
- 34 Debnath AK. Pharmacophore mapping of a series of 2,4-diamino-5-deazapteridine inhibitors of mycobacterium avium complex dihydrofolate reductase. *J Med Chem* 2002; 45: 41–53.
- 35 Kansal N, Silakari O, Ravikumar M. Three dimensional pharmacophore modelling for c-kit receptor tyrosine kinase inhibitors. *Eur J Med Chem* 2010; 45: 393–404.
- 36 Brogi S, Kladi M, Vagias C, Papazafiri P, Roussis V, Tafi A. Pharmacophore modeling for qualitative prediction of antiestrogenic activity. *J Chem Inf Model* 2009; 49: 2489–97.
- 37 Sakkiah S, Thangapandian S, John S, Lee KW. Identification of critical chemical features for aurora kinase-B inhibitors using Hip-Hop, virtual screening and molecular docking. *J Mol Struct* 2011; 985: 14–26.
- 38 Lipinski A, Lombardo F, Dominy BW, Feeney PJ. Experimental and computational approaches to estimate solubility and permeability in drug discovery and development settings. *Adv Drug Delivery Rev* 1997; 23: 3–25.
- 39 Venkatachalam CM, Jiang X, Oldfield T, Waldan M, LigandFit n. LigandFit: a novel method for the shape-directed rapid docking of ligands to protein active sites. *J Mol Graphics Model* 2003; 21: 289–307.
- 40 Brooks B, Brucoleri R, Olafson B, States D, Swaminathan S, Karplus M. CHARMM: A program for macromolecular energy, minimization, and dynamics calculations. *J Comput Chem* 1983; 4: 187–217.
- 41 Bartolott LJ, Flurchick K. (2007) An Introduction to Density Functional Theory, in *Reviews in Computational Chemistry, Volume 7* (eds Lipkowitz KB and Boyd DB), John Wiley & Sons, Inc, Hoboken, NJ, USA. doi: 10.1002/9780470125847.ch4.
- 42 Debnath AK. Generation of predictive pharmacophore models for CCR5 antagonists: study with piperidine- and piperazine-based compounds as a new class of HIV-1 entry inhibitors. *J Med Chem* 2003; 46: 4501–15.
- 43 Cokugras AN. Butyrylcholinesterase: structure and physiological importance. *Turk J Biochem* 2003; 28: 54–61.
- 44 Darvesh KV, McDonald RS, Mataija D, Walsh R, Mothana S, Lockridge

- O, *et al*. Carbamates with differential mechanism of inhibition toward acetylcholinesterase and butyrylcholinesterase. *J Med Chem* 2008; 51: 4200–12.
- 45 Li Y, Wang Y, Li W, Dong P, Ge G, Yang L, *et al*. Investigation of binding features: effects on the interaction between CYP2A6 and inhibitors. *J Comput Chem* 2010; 31: 1822–31.
- 46 Queiroz AN, Gomes BAQ, Moraes WM Jr, Borges RS. A theoretical antioxidant pharmacophore for resveratrol. *Eur J Med Chem* 2009; 44: 1644–49.

Letter to the Editor

Pretreatment with IFN- α increases resistance to imatinib mesylate in patients with chronic myelocytic leukemia

Yin XIAO^{1, #}, Hui-hua HU^{2, #}, Hong-xiang WANG³, Xiao-jian ZHU¹, Ping ZOU¹, Zhi-chao CHEN¹, Zhao-dong ZHONG¹, Wei-ming LI¹, Yong YOU^{1, *}

¹Union Hospital, Tongji Medical College, Huazhong University of Science and Technology, Wuhan 430022, China; ²Department of Hematology, Centre Hospital, Suizhou 441300, China; ³Department of Hematology, Centre Hospital, Wuhan 430014, China

Acta Pharmacologica Sinica (2012) 33: 979–980; doi: 10.1038/aps.2012.43; published online 11 Jun 2012

Dear Editor,

Chronic myeloid leukemia (CML) is a malignant hematopoietic stem cell proliferative disease driven by BCR-ABL tyrosine kinase, the product of the Philadelphia chromosome^[1]. Tyrosine kinase inhibitors (TKIs) have revolutionized the treatment of CML. Such molecule directed against BCR-ABL first introduced into clinical practice was imatinib mesylate (IM, Gleevec/Glivec, formerly STI571), which showed excellent efficacy in terms of prolonged major molecular response (MMR) and progression-free survival^[2]. Replacing hematopoietic stem cell transplantation, IM is currently recommended as the first-line therapy for CML by the National Comprehensive Cancer Network (NCCN) and European Leukemia Net (ELN).

At the pre-TKI stage, IFN- α was the major choice for CML patients who were not candidates for allogeneic stem cell transplantation, and its observed complete cytogenetic response (CCyR) rates were approximately 20%. Moreover, IFN- α extends the leukemia-free survival (LFS) of patients^[3, 4]. In China, many patients begin with IFN- α treatment instead of IM at diagnosis for economic reasons. Previous studies have shown that the therapeutic efficacy of IM treatment is not affected by prior IFN- α treatment^[5, 6]. The results of our retrospective analysis of 137 CML cases suggest that IFN- α treatment before IM therapy is a risk factor associated with loss of MMR.

In this study, 137 CML outpatients (from June 2008 to May 2010) were retrospectively analyzed. CML diagnosis was confirmed by cytology, immunophenotyping, chromosome (Ph⁺)

and BCR-ABL genetic analysis. Among these patients, 122 had CML in the chronic phase (CP), whereas 15 were in accelerated phase or blast phase (AP/BP). A total of 69 CP patients and 8 AP/BP patients received IFN- α treatment before IM, and the other patients began IM treatment at diagnosis or shortly thereafter. The median period of disease before IM treatment was 3 years for both CP (1–6.6 years) and AP/BP (1–5 years) patients. IM treatment was continued for 3.5 \pm 1.5 years for CP and 3.33 \pm 1.33 years for AP/BP patients. The median follow-up time was 36 (6–57) months up to May 2010.

The IM dose (administered orally) was initially 400 mg/d for CP patients and 600 mg/d for AP/BP patients and was adjusted according to tolerance. Complete molecular remission (CMR) was determined by the absence of BCR-ABL detection. In patients with MMR, the ratio of BCR-ABL and ABL1 was reduced by more than 3 logs after treatment. BCR-ABL transcript levels in patients receiving IM were analyzed every 3 months within the first 12 months of treatment. If MMR was observed, monitoring occurred every 6 months. Quantitative RT-PCR analysis of the kinase domain of the ABL gene from peripheral blood mononuclear cells was performed when the patients lost MMR or did not acquire CMR within 18 months.

The overall 36-month MMR rates for IFN- α -treated and untreated CP and AP/BP patients are shown in Table 1. The MMR rate of IFN- α -treated CP patients (78.3%) was significantly lower than IFN- α -untreated CP patients (97.3%). In AP/BP patients, the MMR rates of IFN- α -treated and untreated patients (50% and 60.0%, respectively) did not differ significantly. Furthermore, the MMR rates of patients were analyzed for the association of IFN- α treatment with prolonged disease progression. A chi-square analysis showed that the MMR rate did not differ significantly in CP patients within the first two years of the disease but was significantly lower in CP patients

[#] These two authors contributed equally to this paper.

^{*} To whom correspondence should be addressed.

E-mail youyongunion@163.com

Received 2011-12-30 Accepted 2012-04-05

Table 1. Effect of IFN- α treatment on MMR rate.

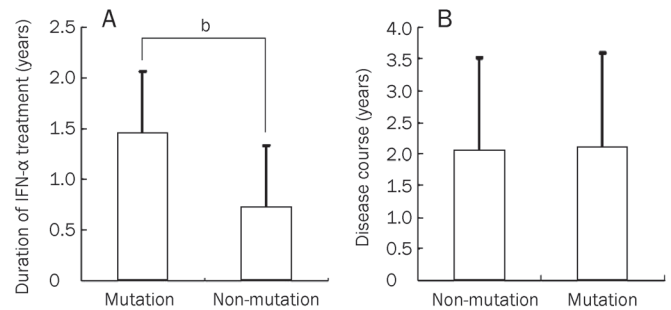
IFN- α treatment	n	CML-CP		CML-AP/BP		
		Overall MMR	%	n	Overall MMR	%
No	37	36	97.3	5	3	60
Yes	69	54	78.3	8	4	50

who had the disease for more than 2 years ($P=0.0001$), suggesting relatively reduced IM efficacy in patients with prolonged disease progression. A Cox regression showed that prolonged disease progression was an independent risk factor for IM efficacy [$P=0.006$, Exp (B)=0.625, SE=0.170]. However, IFN- α was used for all of the patients with disease durations of more than two years, making it impossible to distinguish the effects of disease course and IFN- α treatment on the MMR rate.

In this study, 38 patients (29 CP and 9 AP/BP) were resistant to IM, of which 20 CP and 8 AP/BP patients (disease course, 3.56 ± 2.38 years; average IFN- α treatment duration, 1.2 ± 0.79 years) did not acquire CMR within 18 months (primary resistance to IM). A total of 10 patients (9 CP and 1 AP/BP; disease course, 2.09 ± 1.33 years; average IFN- α treatment duration, 0.67 ± 0.43 years) lost MMR during the treatment (acquired resistance to IM). The disease course of patients with drug resistance (3.56 ± 2.49 years) was significantly longer than those with persistent MMR ($P=0.0001$). The IFN- α treatment duration in patients with primary drug resistance (3.56 ± 2.49 years) was significantly longer than in patients with persistent MMR (1 year) ($P=0.0002$). In patients with acquired drug resistance, the length of the disease course did not significantly correlate with MMR ($P=0.36$) or IFN- α treatment duration ($P=0.24$).

Point mutations in the BCR-ABL gene are the most frequent mechanisms of IM resistance in CML patients and were identified in 38 cases without MMR in our results. These mutations were identified in the kinase region of the ABL fusion gene in 55.3% (21/38) of the patients. Imatinib-resistant BCR-ABL mutants comprising 8 different amino acid locations were identified: P-loop (11 cases, including Y253F/H, E255K/V, G250E, Q252H, and M244V), H396P/R (2 cases), T315I (6 cases) and F359V (2 cases). These mutations were predominantly T315I, Y253H, and E255K/V mutations, in accordance with previous reports^[7]. The median IFN- α treatment duration for patients with mutations (1.45 ± 0.61 years) was significantly longer than for patients without mutations (0.72 ± 0.61) ($P<0.05$) (Figure 1A). The median pre-IM disease course of the 21 cases with point mutations (1.5 years) was similar to persistent MMR ($P=0.07$) (Figure 1B). The pre-IM disease course, IM treatment and IFN- α treatment duration did not differ significantly between AP/BP and CP patients. These results suggest that the duration of pre-TKI IFN- α treatment but not the pre-TKI disease course is associated with ABL point mutations and drug resistance.

In summary, IM therapeutic efficacy correlates with the

**Figure 1.** Duration of IFN- α treatment (A) and disease course (B) in patients with or without point mutations. ^b $P<0.05$.

disease course and duration of IFN- α treatment. The duration of pre-IM IFN- α administration in CP patients significantly impacts drug resistance, which is inconsistent with the results of previous studies. This study reveals that IFN- α affects IM resistance in CML patients via increasing the frequency of point mutations. Therefore, it is speculated that early diagnosis and IM administration combined with reduced durations of IFN- α treatment will effectively reduce the drug resistance rate, increase the MMR rate and prolong the leukemia-free survival time.

Acknowledgements

We thank Shi-ang HUANG and Xiao-qing LI for their skillful technical assistance. We also thank them for kindly providing reagents used in this study. This work was supported in part by grants from the Huazhong University of Science and Technology.

References

- Sengupta A, Arnett J, Dunn S, Williams DA, Cancelas JA. Rac2 GTPase deficiency depletes BCR-ABL⁺ leukemic stem cells and progenitors *in vivo*. *Blood* 2010; 116: 81–4.
- O'Brien SG, Guilhot F, Larson RA, Gathmann I, Baccarani M, Cervantes F, et al. Imatinib compared with interferon and low-dose cytarabine for newly diagnosed chronic-phase chronic myeloid leukemia. *N Engl J Med* 2003; 348: 994–1004.
- Melo JV, Hughes TP, Apperley JF. Chronic myeloid leukemia. *Hematology Am Soc Hematol Educ Program* 2003; 2003: 132–52.
- Simonsson B, Hjorth-Hansen H, Bjerrum OW, Porkka K. Interferon alpha for treatment of chronic myeloid leukemia. *Curr Drug Targets* 2011; 12: 420–8.
- Kiladjian JJ, Mesa RA, Hoffman R. The renaissance of interferon therapy for the treatment of myeloid malignancies. *Blood* 2011; 117: 4706–15.
- Kujawski LA, Talpaz M. The role of interferon-alpha in the treatment of chronic myeloid leukemia. *Cytokine Growth Factor Rev* 2007; 18: 459–71.
- Branford S, Rudzki Z, Walsh S, Parkinson I, Grigg A, Szer J, et al. Detection of BCR-ABL mutations in patients with CML treated with imatinib is virtually always accompanied by clinical resistance, and mutations in the ATP phosphate-binding loop (P-loop) are associated with a poor prognosis. *Blood* 2003; 102: 276–83.